DESIGN OF LEN LYE'S *BLADE* AT THE LARGEST ECONOMIC SIZE

A thesis submitted in partial fulfilment of the requirements for

the Degree

of Master of Engineering

in Mechanical Engineering

by Tim Spencer

University of Canterbury

2014

Abstract

Len Lye was born in Christchurch, New Zealand, in 1901. Lye was an avid enthusiast of kinetic sculpture and experimental film. In 1965 Lye built a prototype for a kinetic sculpture called *Blade* that he intended would be a much larger work.

In 1996, Dr. Shayne Gooch of the University of Canterbury embarked on a research contract that saw the fruition of Lye's *Blade* at a scale previously unachieved. This work was given the name *Big Blade*.

This thesis provides a study into the maximum realisable scale of *Blade* using technology and materials available today. A new pivoting clamp design is tested and assessed using a small scale *Blade* sculpture built at the University of Canterbury and used as a test rig.

Advancements in technology, material availability and manufacturing techniques lead to a comprehensive fatigue study of the new clamp design. Stresses are measured at the critical stress location in the blade material and a new maximum economic scale of *Blade* is suggested. The new sculpture requires a blade material that measures 10024mm x 1080mm x 22mm. The visible blade length is 8424mm. The new sculpture is called *Giant Blade*.

A critical aesthetic component for Len Lye's performance of *Blade* is the

mode shapes formed by the blade material. Specifically, the second and third bending modes (Lye's single and double harmonic) and the first torsional bending mode (Lye's shimmering frequency). These frequencies are calculated using the new pivoting clamp design to ensure that these sections of the performance are maintained in *Giant Blade*.

An important requirement of the new sculpture drive mechanism is the capability to reduce the amplitude of shuttle oscillation dynamically during *Blade* performances. This capability allows bending stresses in the blade material to be reduced in the third bending mode of vibration without halting the performance to adjust the shuttle oscillation amplitude. Four dynamically adjustable variable stroke mechanisms are presented and compared using the methods of Pahl and Beitz. A suitable mechanism for *Giant Blade* is selected and a proposed arrangement for the new sculpture is provided.

An embodiment design is presented for *Giant Blade*. This embodiment design consists of a new pivoting clamp design and the proposed variable stroke mechanism. Further work includes the design of a mechanism to support the ball and wand assembly.

UNIVERSITY OF CANTERBURY
Te Whare Wānanga o Waitaha
CHRISTCHURCH NEW ZEALAND

Deputy Vice-Chancellor's Office
Postgraduate Office

Co-Authorship Form

This form is to accompany the submission of any thesis that contains research reported in co-authored work that has been published, accepted for publication, or submitted for publication. A copy of this form should be included for each co-authored work that is included in the thesis. Completed forms should be included at the front (after the thesis abstract) of each copy of the thesis submitted for examination and library deposit.

Please indicate the chapter/section/pages of this thesis that are extracted from co-authored work and provide details of the publication or submission from the extract comes:

Chapter 3

SPENCER, T. D. & GOOCH, S.D. 2014. Fatigue Life Study of the Kinetic Sculpture Blade. 13th International Design Conference, 19-22 May 2014 Dubrovnik, Croatia.

Please detail the nature and extent (%) of contribution by the candidate:

75% CONTRIBUTION BY CANDIDATE

Certification by Co-authors:

If there is more than one co-author then a single co-author can sign on behalf of all

The undersigned certifys that:

- The above statement correctly reflects the nature and extent of the PhD candidate's contribution to this co-authored work
- In cases where the candidate was the lead author of the co-authored work he or she wrote the text

Name:	Signature:	Date:
SHANNE GOOCH		4 MAY 2014.

Acknowledgements

To John and Lynda Matthews, for the opportunity they provided me and their infectious passion for all things Len Lye. Their tireless efforts within The Len Lye Foundation have, and will continue to give, people everywhere the opportunity to appreciate one of New Zealand's most influential individuals.

To my supervisor, Dr. Shayne Gooch, his expertise in mechanical design and the kinetic sculpture of Len Lye have been invaluable throughout the project.

To Mr. Evan Webb, for his guidance in understanding the subtleties and sentiments of Len Lye's creations.

To my family and friends for their unwavering belief.

And finally, to my wife Casey, for her love and support which lifted me to new and unexpected heights. This is for you.

Table of Contents

List of Figures

List of Tables

Nomenclature

Algebraic symbols

A	Cross sectional area	(m^2)
b	Blade width	(m)
c	Power relationship coefficient	
C	Wave motion equation constant	
d	Blade thickness	(m)
D	Damage	
E	Elastic modulus	(N/m^2)
F	Force	(N)
g	Acceleration due to gravity	(m/s^2)
I	Second moment of area	(m^4)
k	Endurance limit modifying factor	
l	Blade length	(m)
m	S-N curve gradient	
M	Bending moment	(Nm)
n	Number of cycles	
N	Number of cycles	
n	Number of cycles seen by material	
P	Number of performances	
q	One-sided tolerance limit factor	
w	Mass per unit length	(kg/m)
S_e	Endurance limit	(MPa)

t	Time	(s)
T	Total time	(s)

Greek symbols

γ	Dimensionless stability factor	
δ	Sample coefficient of variation	
ε	Strain	
λ	Wave equation root	
v	Lateral beam displacement	(m)
ρ	Density	(kg/m^3)
σ	Stress	(MPa)
ω	Frequency	(rad/s)

Subscripts

0	Denotes 10^3 cycles
a	Denotes amplitude value
ar	Denotes the mean adjusted amplitude value
cr	Denotes the critical value
C	Confidence percentage
e	Denotes cycles to failure at endurance limit
f	Denotes cycles to failure
$\bar{f}$	Denotes mean performances to failure
i	Integer
$icpt$	Denotes stress value on S-N curve at 10^3 cycles
max	Denotes the maximum value
o	Refers to the ‘original’ size of the sculpture
R	Reliability percentage
s	Refers to the ‘scaled’ size of the sculpture

1 Introduction

1.1 Motivation

The purpose of this work is to investigate the feasibility of manufacturing Len Lye's sculpture, *Blade*, at a larger size than previously achieved.

"Today we have access to new forms of technology that can further enlarge the scope and potential of kinetic art. The powers of the computer can be used for… the production of large-scale versions of the sculptures Lye designed but could not realise during his lifetime" – Roger Horrocks, (Horrocks, 2009)

The Len Lye foundation is an entity in New Zealand that was formed to ensure that Len Lye's artwork has a place in the future of New Zealand citizens and that the artwork he envisaged materialises as technological advances permit. The Len Lye foundation is today responsible for bringing Len's visions for kinetic sculpture to life.

This thesis follows an earlier study by Gooch (S. D. Gooch, 2001) who designed and commissioned a large size version of Lye's Blade. The work was called *Big Blade* and was, according to Gooch, the largest economically possible size of *Blade* at the time of its completion.

Figure 1.1: Big Blade at the Christchurch Botanical Gardens in 1998 [courtesy of The Len Lye Foundation]

Gooch found that a constraining factor in increasing the scale of *Blade* was the reversed bending stress in the blade material at the clamp exit. This reversed bending stress increases with the scale of *Blade* and eventually results in fatigue failure of the blade material after a number of performances. This number of performances reduces as the scale of *Blade* increases, resulting in increasing cost per performance for the sculpture. Gooch suggested various avenues of further study for making *Blade* larger in the concluding comments of his thesis. One research avenue that was suggested involved the investigation of a pivoting (Figure 1.2), as opposed to rigidly vertical, base clamp for the blade material to reduce stress in the blade material.

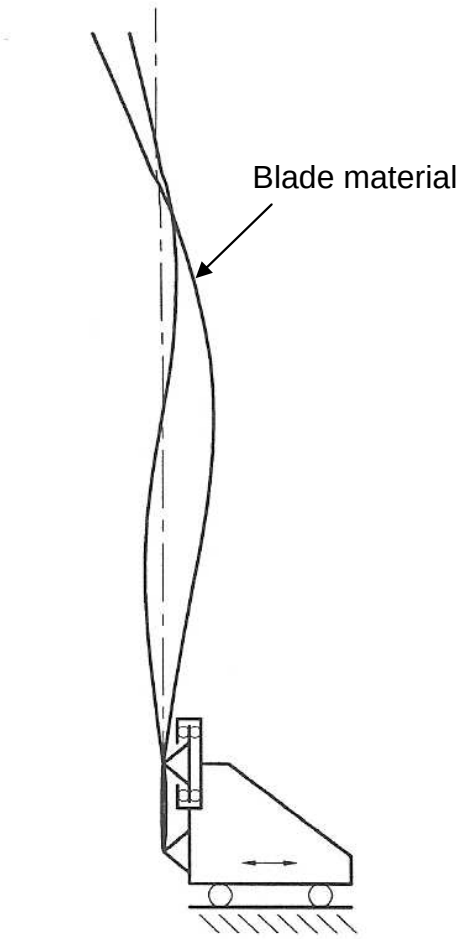

Figure 1.2: Pivoting clamp concept suggested by (S. D. Gooch, 2001)

Gooch also found that a significant constraining factor in building *Blade* at the largest economic size was the availability of the chosen material for the blade material. In the case of *Big Blade* this material was titanium alloy 6Al-4V. Since *Big Blade* was completed there have been significant advances in the demand for titanium alloy 6Al-4V resulting in larger and more readily available options for blade material. Therefore, this thesis will attempt to answer, among others, two key questions:

1. Will a pivoting base clamp in the artwork *Blade* reduce the stress induced at the base of the blade material sufficiently to increase the

size of the artwork whilst maintaining the artistic intentions of the piece?

2. Is there a piece of titanium 6Al-4V available that is sufficiently large enough to be suitable as the blade material, should the pivoting base clamp (or any alternative design) reduce the reversed bending stress enough to allow for a larger *Blade* artwork?

1.2 Historical Background

1.2.1 Len Lye

Len Lye was born in Christchurch, New Zealand in 1901. Lye was an exuberant man, his interests in avant-garde art and culture led him to Sydney, Samoa, London, and finally New York. Lye's interests lay in kinetic sculpture and experimental film techniques, both areas in which he is now considered a pioneer. The kinetic sculptures Len designed were rarely completed to the scale he intended they would exist – by Lye's own admission, it was a belief at the time of his ideas that the technology required for the sculptures to be built would not be available until the 21st century (Lye, 1968). Today, many of Len's visions are coming to fruition in New Zealand courtesy of the Len Lye Foundation and the advancements of manufacturing technology. Examples of Len's visions today can be seen as the 'Wind Wand' in New Plymouth and 'Water Whirler' on Wellington's waterfront.

1.2.2 Lye's Blade Prototype

Lye was inspired when he held a carbon steel wood saw with the blade orientated vertically and shook the blade into its natural vibratory modes. Lye

wanted to harness and amplify the same light and sound in a kinetic sculpture. The prototype, *Blade*, seen in Figure 1.3 was the result and consists of a large vertically standing rectangular carbon steel strip that is excited into various modes of vibration by a vibrating clamp at the base of the strip. A vertical wand, with a cork ball attached, is then enticed into contact with the blade when the amplitude of vibration reaches a sufficient level. The base platform of the work also rotates to complete the work giving viewers a mechanically composed symphony of sound and light. Lye envisaged that *Blade* would stand 50-100ft high (Horrocks, 2001), sufficient to intimidate and instil a sense of awe among its spectators. Other sources (Raine & Gooch, 1998) suggest a desired free blade length of 9m. The kinetics of this sculpture make Lye's wish of scale difficult to achieve, due to the large reversed stresses that occur at the base of the blade material where it is clamped during its motion.

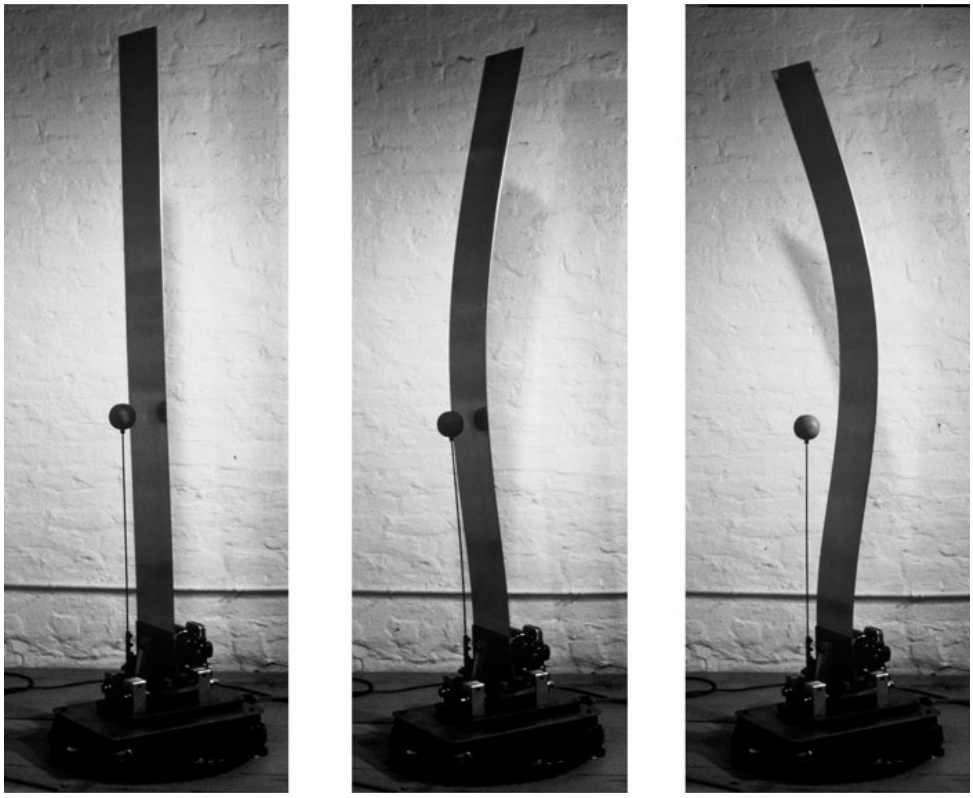

Figure 1.3: Len Lye's Blade prototype kinetic sculpture [courtesy of The Len Lye Foundation]

Blade was first exhibited at Lye's *'Bounding Steel Sculptures'* exhibition at the Howard Wise Gallery in New York from March to April in 1965. The blade material in the original prototype consists of a 1730 x 200 x 1.85mm carbon steel strip, commonly used in band saws for cutting timber. 100 mm of the strip length is clamped. The blade material in this prototype has failed and been subsequently replaced multiple times since its conception, due to the high reversed bending stresses at the clamp exit in the carbon steel blade material. Fatigue cracks tend to initiate and propagate in a direction parallel to the width dimension of the blade material at the clamp exit.

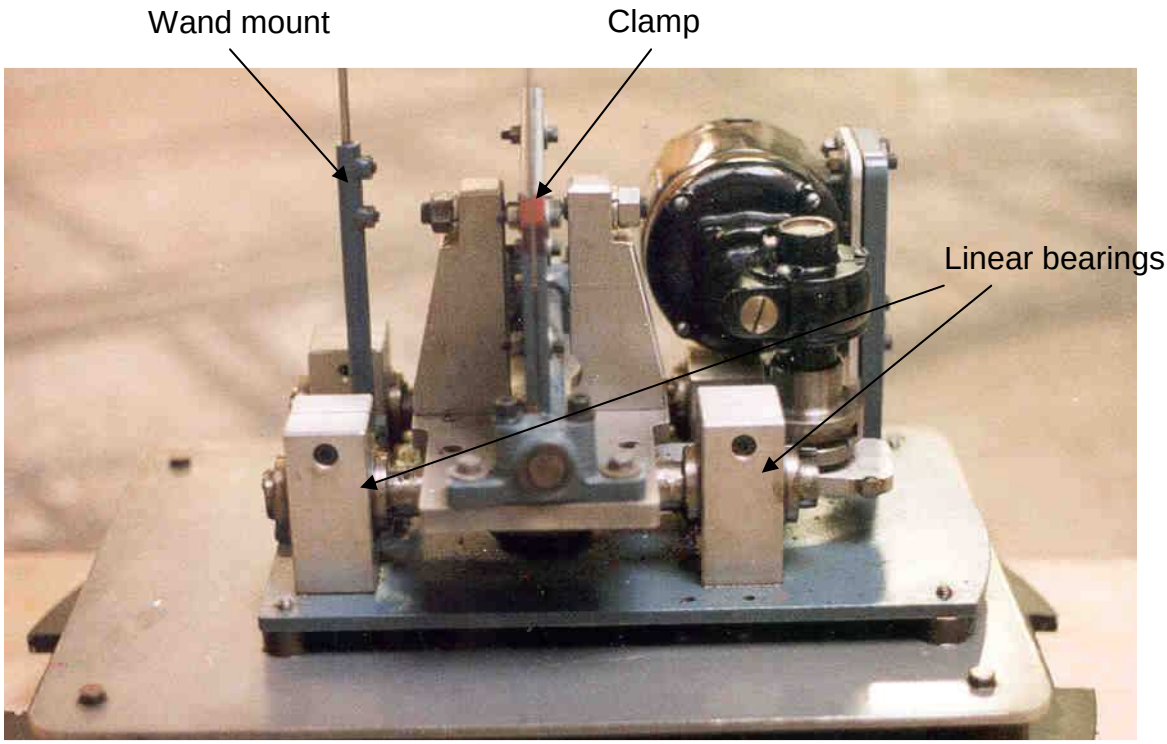

Figure 1.4: Len Lye's Blade prototype drive mechanism [courtesy of The Len Lye Foundation]

The drive mechanism, seen in Figure 1.4, consists of a rigid clamp in which 100mm of the blade material is clamped. The clamp is driven on 4 linear bearings by a 300mm connecting rod through a 5:1 reduction gearbox attached

to a Bodine 0.05hp DC electric motor. The crank offset is 5.58mm. Lye set the length of blade material protruding out of the rigid clamp (the *unclamped length*) by experimentally finding the scenario where buckling stability no longer exists due to self weight of the blade. Lye then reduced the unclamped length until the blade material would just remain standing vertically in the clamp under its own strength. Adjacent to the blade material is a vertical pendulum made up of a 5mm diameter stainless steel wand and a 75mm cork sphere with a mass of 85g. Lye controlled the electric motor using a Veriac type rheostat.

Modifications were made to Lye's prototype to aesthetically complete the sculpture for use in exhibitions and to optimise mechanical operation. These modifications were made by the Len Lye Foundation and were based on the artist's wishes before he died. The following list summarises these changes as explained by Gooch (S. D. Gooch, 2001).

- An electronic control system utilising PLC technology was added to control the system remotely.
- The control mechanism was concealed by a black cylindrical housing.
- The drive mechanism was repowered with a 0.125hp permanent magnet permanent magnet DC electric motor.
- The entire work was mounted on a vertical steel axle as in Figure 1.5 to provide the rotational aspect of the sculpture that Lye stipulated it should have.

- Copper slip rings and carbon brushes were installed into the sculpture to transmit power to the oscillation drive. These have since proven to be a problematic solution for power transmission to the electric motor.
- A mechanical spring actuated disc brake reduces the occurrence of whipping in the chain drive as a result of the twisting vibration mode of the blade material.

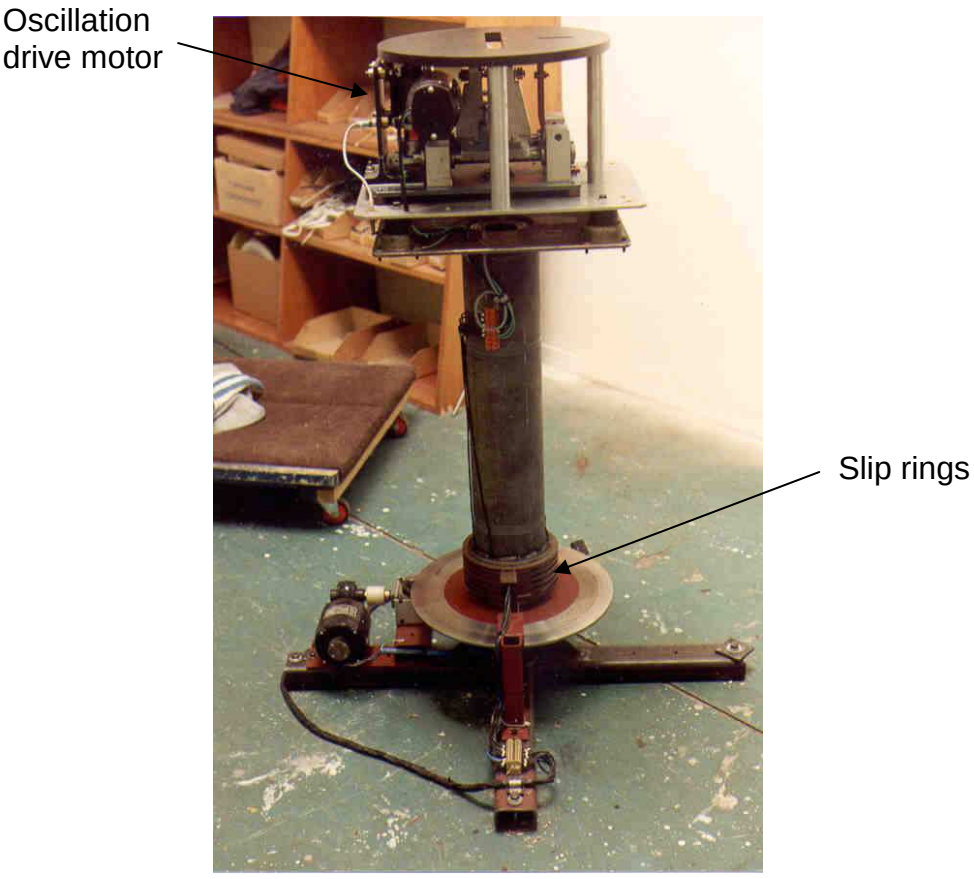

Figure 1.5: Vertical steel axle addition to Lye's Blade prototype [courtesy of The Len Lye Foundation]

The PLC control system was programmed to give the required output (Figure 1.6) to *Blade* remotely.

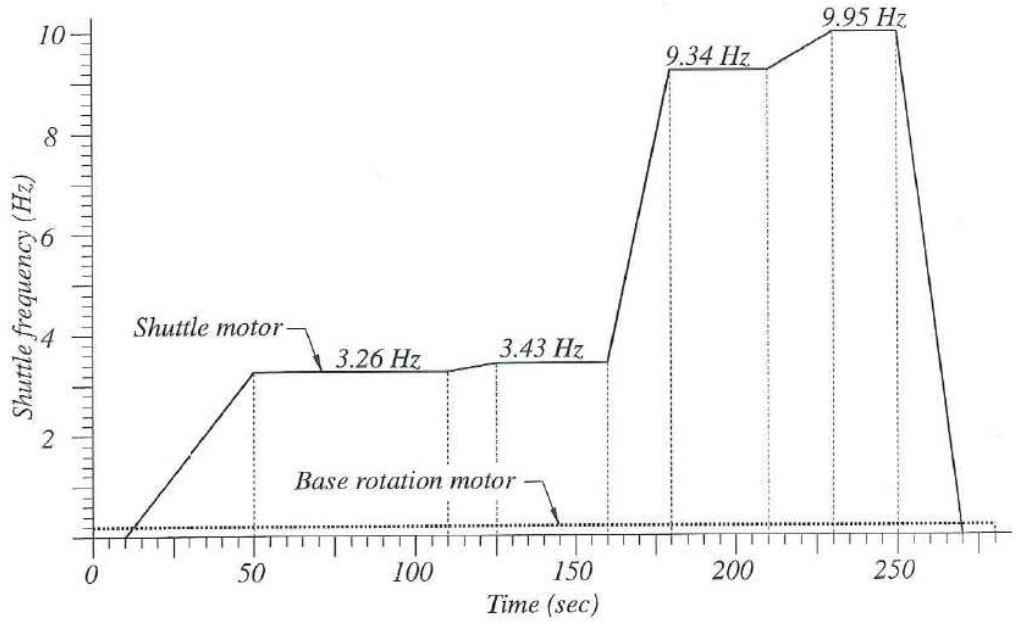

Figure 1.6: Control system program for Original Blade (S. D. Gooch, 2001)

The modifications listed above result in the kinetic sculpture which will, from this point onwards, be referred to as the original *Blade.*

1.2.3 Big Blade

Big Blade was the result of a research contract completed by Dr. Shayne Gooch at the University of Canterbury from 1996 to 1998. Gooch summarised his work in a thesis submitted in 2001 for a Doctor of Philosophy in Mechanical Engineering. This work will be frequently referred to in this thesis.

Gooch used Buckingham's Pi Theorem to develop scaling laws for the sculpture *Blade* and predict structural properties, system dynamics, life and cost of the blade material as the scale of the sculpture increases. Important results of this work that affect the scaling of *Blade* are listed as follows:

- The reversed bending stress at the clamp exit increases with the scale of the sculpture. Fatigue life therefore reduces until the blade material will only last one performance. Cost per performance based on blade material cost increases with scale and therefore is a constraining factor on the realisable size of *Blade.*
- Titanium alloy 6Al-4V is the preferred choice for blade material. The low elastic modulus compared to carbon steel results in a significant reduction in reversed bending stress in the blade material for equal scale blade materials made of titanium and steel. Titanium also has the advantage of maintaining the aesthetic and acoustic characteristics of carbon steel which are an important aspect of the kinetic sculpture.
- The availability of 6Al-4V in the plate size required for a larger sculpture also restricts scaling of the sculpture.

Big Blade was manufactured at a scale approximately twice that of the original *Blade*. The visible blade material measured 3355 x 430 x 5.53mm with an extra 200mm of blade material inside the clamp. The steel axle base rotation mechanism was replaced by a combination of tapered roller bearings, similar to the arrangement in the stub axle of a car, with a synchronous belt driven by a 0.25kW 4-pole induction motor as shown in Figure 1.7.

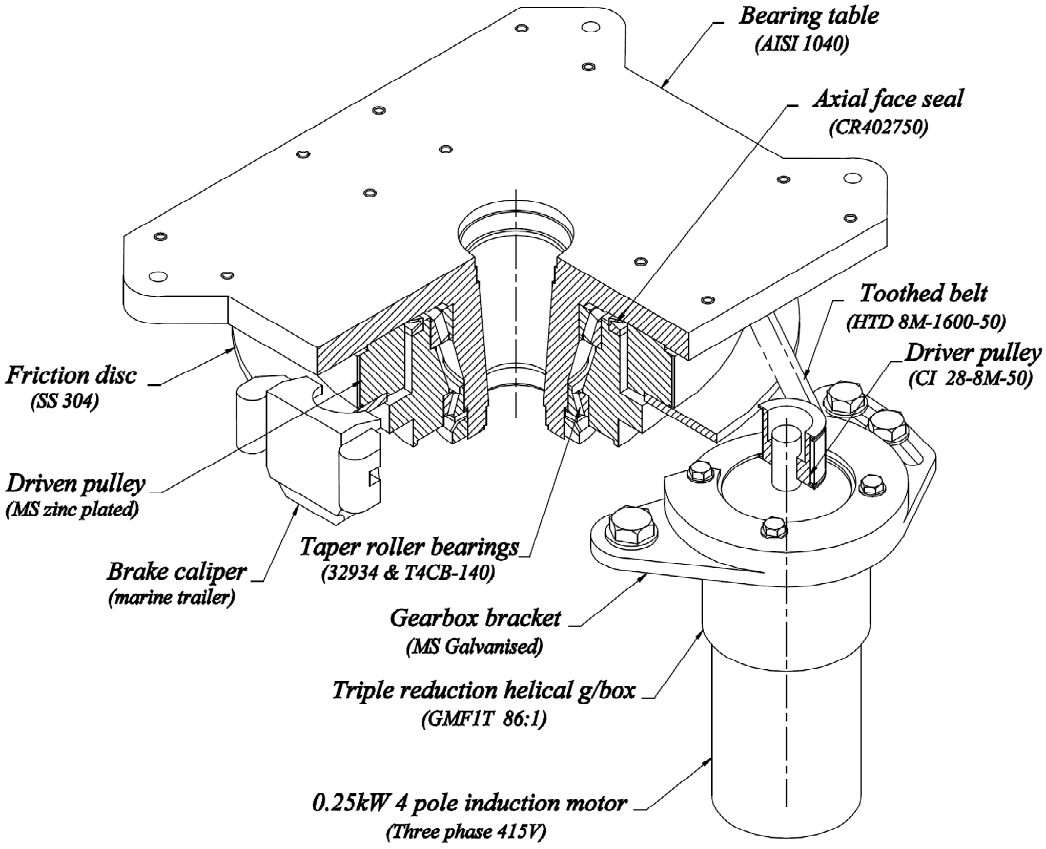

Figure 1.7: Base rotation mechanism of Big Blade from (S. D. Gooch, 2001)

The rigid clamp design of the original *Blade* is retained in *Big Blade* as shown in Figure 1.8.

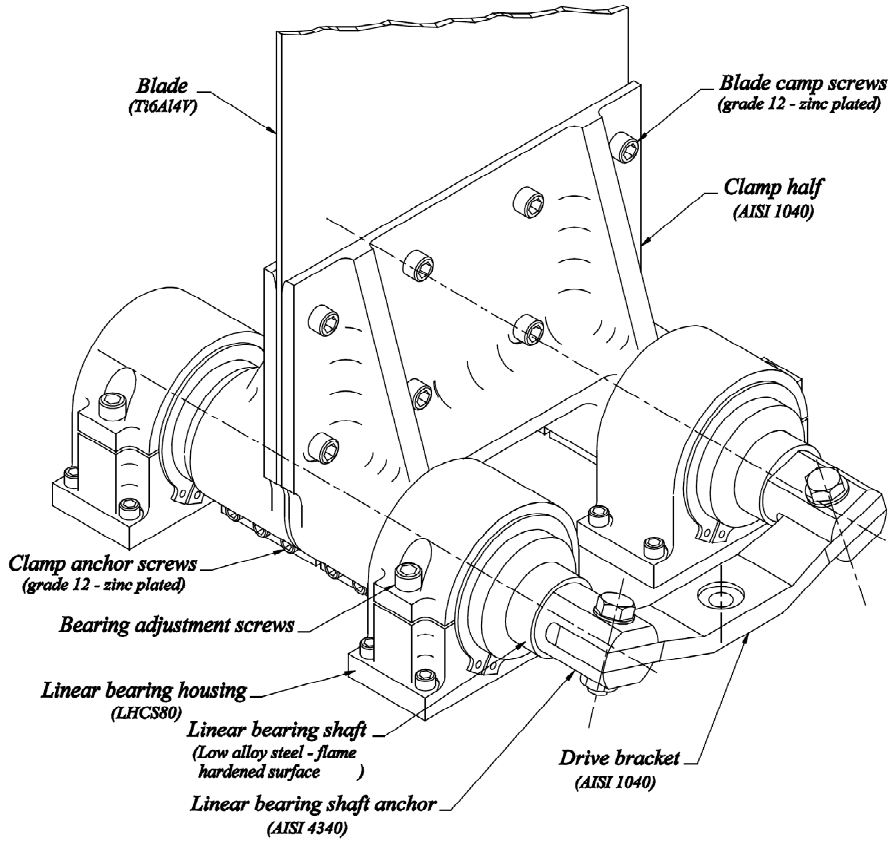

Figure 1.8: Clamp design for Big Blade from (S. D. Gooch, 2001)

Linear bearings are utilised to provide a shuttling motion to the clamp. The shuttle is driven by a 3kW 4-pole induction motor through a reducing helical gearbox and a crank-slider arrangement as shown in Figure 1.9.

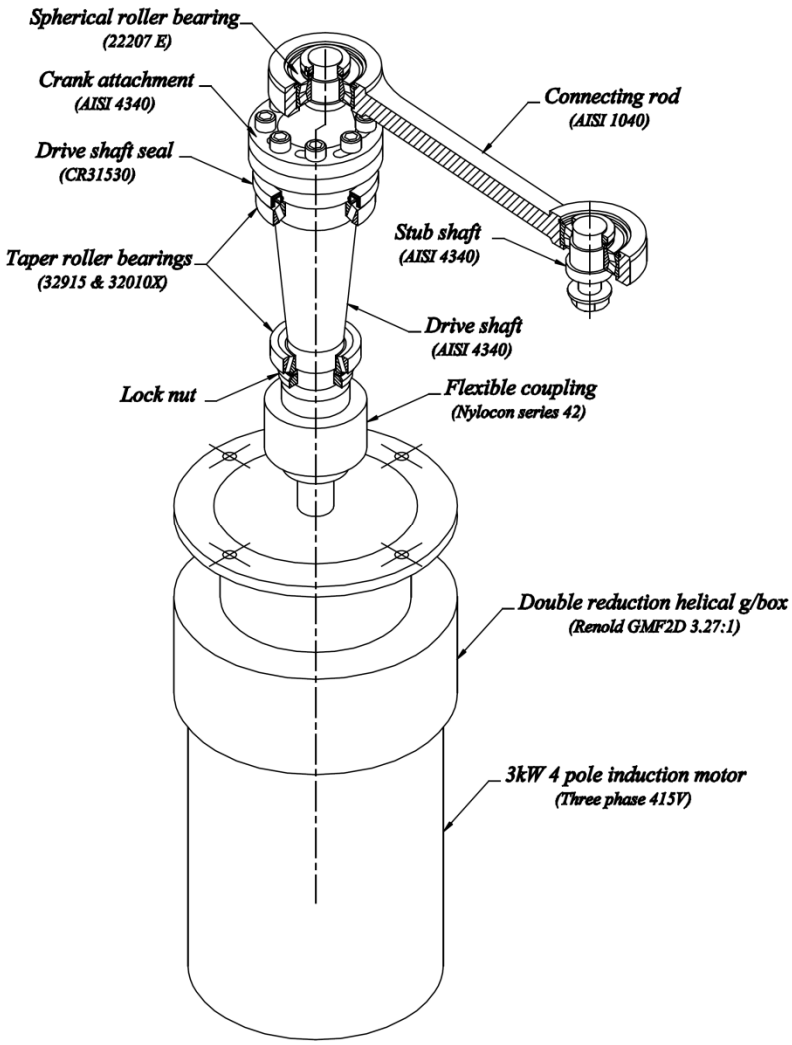

Figure 1.9: Oscillation drive mechanism for Big Blade from (S. D. Gooch, 2001)

A more sophisticated program for *Big Blade* performances was implemented to the control system for *Big Blade*. This program can be seen in Figure 1.10.

Observations of the original *Blade* are the reason for the addition of stepping functions and S-curve type speed ramping (not shown) in this program. These findings are summarised as follows:

- An undesirable disturbance occurs in the third mode of vibration (double harmonic – see Figure 4.1) of the blade material. This disturbance was found to be the excitation of the first mode of vibration during the third mode of vibration and was subsequently termed the ‘swinging phenomenon’ (S. D. Gooch, 2001) (Figure 5.1). The causes were the interaction between the blade and the wand, combined with abrupt changes in ground motion frequency. Introducing an S-type base motion acceleration ramping function significantly reduced this disturbance and resulted in a more stable ‘double harmonic’ in *Big Blade* performances.
- An unstable ‘breathing’ of vibration amplitude in the blade material occurred during the third mode of vibration. This was due to the non-linear jump phenomenon as outlined by Gooch (Figure 2.13). The minor steps down to the blade material natural frequency from a position above the natural frequency minimises the ‘breathing’ that occurs during the non-linear jump phenomenon.

The modifications outlined above characterise the development and lessons learned in the scaling of *Blade* from the original prototype up to what is now known as *Big Blade.*

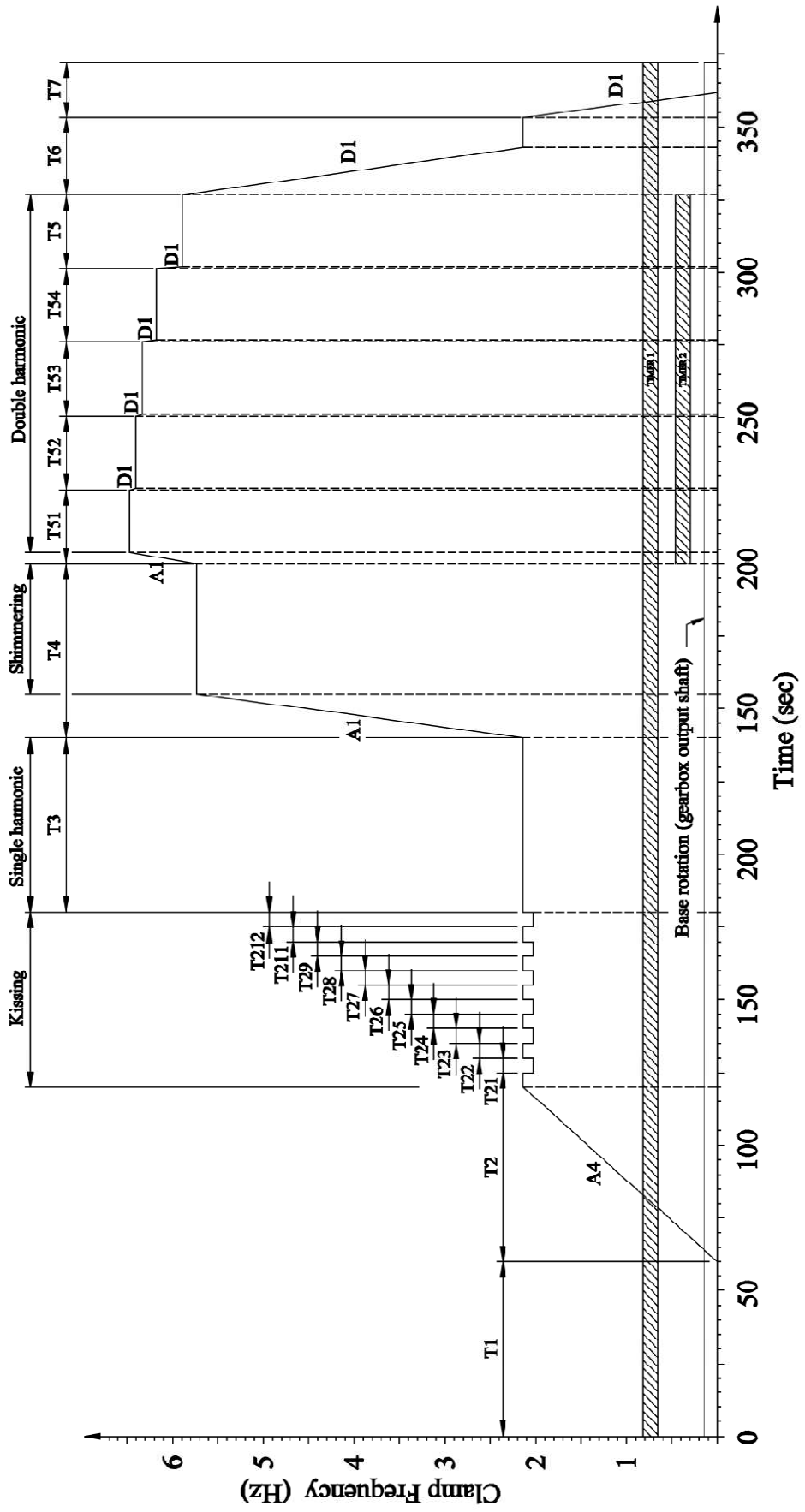

Figure 1.10: Control system program for Big Blade (S. D. Gooch, 2001)

1.2.4 Keeping the Vision Alive

Lye left behind detailed literature and drawings of his sculpture when he died in 1980. This collection was handed over to the Len Lye Foundation for careful curation to ensure that Lye's visions would materialise when the technology became available and/or economically viable.

Steel Henge (Figure 1.11) is how Lye intended to display the *Blade* sculptures, ranging in size from the original *Blade*, to the largest possible size. This work will endeavour to make a step towards fulfilling Lye's grand vision by determining the maximum economic size of *Blade* today and providing a new embodiment design to drive the sculpture. The sculpture of maximum possible scale will be known from here as *Giant Blade*.

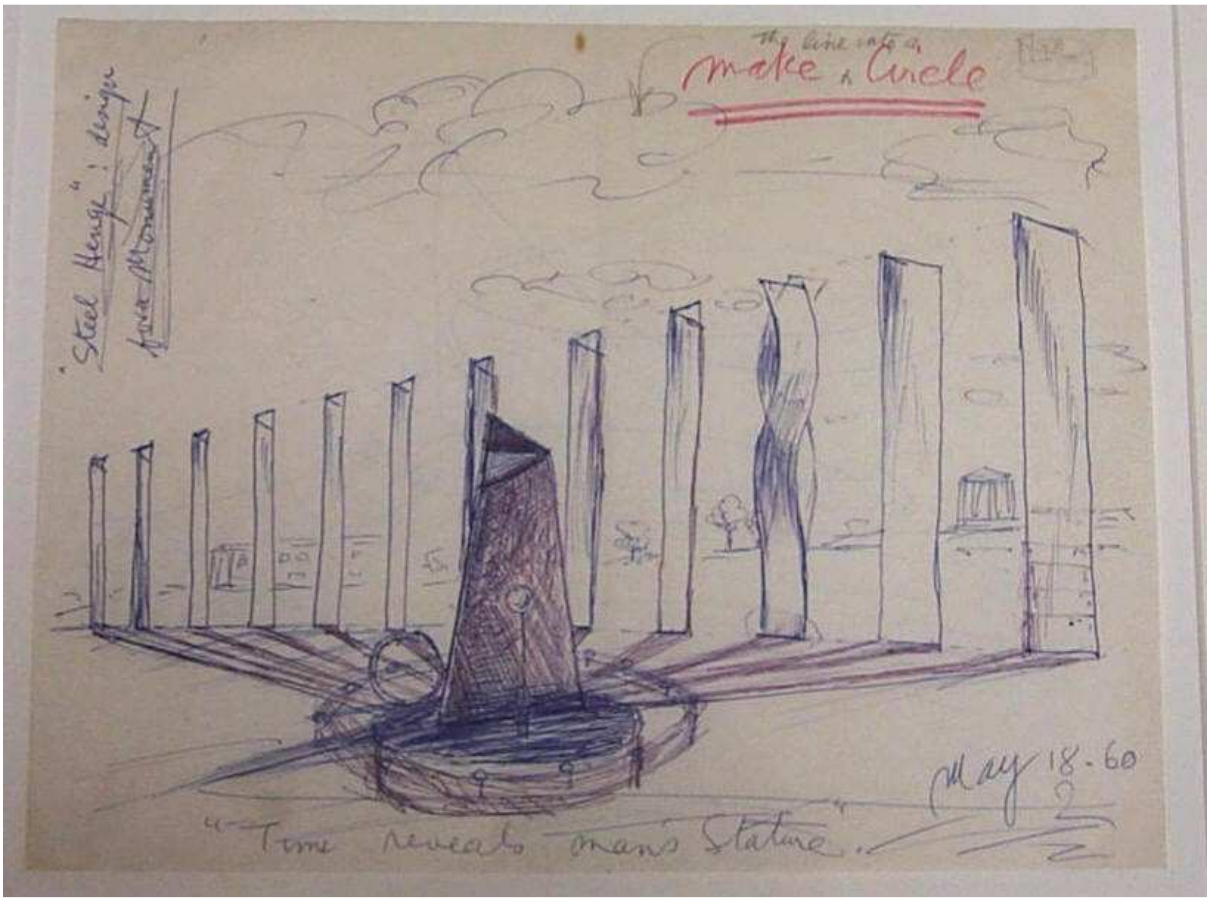

Figure 1.11: Steel Henge as drawn by Len Lye [courtesy of The Len Lye Foundation]

1.3 Thesis scope and structure

The scope of this work is to determine the largest economic size of *Blade* possible using currently available materials. An embodiment design will be presented at this size and the issues that are evident in previous versions of the sculpture will be considered in this design.

Chapter 2 of the thesis evaluates the predicted effectiveness of the pivoting clamp concept, suggested by Gooch, in reducing the reversed bending stress in the blade material at the clamp exit.

Chapter 3 is concerned with determining the maximum economic scale of *Blade* based on the fatigue life and the commercial availability of the titanium blade material.

Chapter 4 investigates the effect on the natural frequencies of the relevant modes of vibration for the blade material in changing the clamp design from a cantilever to pivoting clamp arrangement.

Chapter 5 compares various dynamically adjustable variable stroke mechanisms and presents a final solution that is most appropriate for implementation on the scaled *Blade*.

Chapter 6 will present a functional embodiment design for the scaled sculpture at the largest economic scale.

Chapter 7 discusses a suggested work plan to progress the project successfully forward into the manufacturing stage and realise Len Lye's vision for *Blade*.

2 Pivoting Clamp Stress Reduction

2.1 Introduction

The purpose of this chapter is to determine the feasibility of implementing the pivoting clamp concept through quantification of the stress reduction provided by the suggested clamp design.

Intuitively, the pivoting clamp concept is an improvement over the rigid cantilever type clamp of previous *Blade* sculptures by the well-known theory of replacing a cantilever support with a pinned support. However, the degree of stress reduction is unknown. The degree of stress reduction provided by the pivoting clamp concept, compared to the original cantilever type clamp, will be required to make an informed decision as to whether the pivoting clamp concept is beneficial to implement in a new *Blade* sculpture. From this point forward, the pivoting clamp concept suggested by Gooch (S. D. Gooch, 2001) in Figure 1.2 will be referred to as the *pivoting clamp.* The rigid clamp design used in the original *Blade* and *Big Blade* will be referred to as the *cantilever clamp*.

2.2 Test Facilities

A *Blade* sculpture, at the scale of the original *Blade*, was designed and built in the Mechanical Engineering Department of the University of Canterbury. This sculpture was built to serve as a test rig for measuring and determining

scalable dynamic properties of the blade material using the scaling laws developed by Gooch. The test rig is capable of measuring reversed bending stress at the clamp exit for both the pivoting clamp and cantilever clamp arrangement. The test rig consists of a base frame that supports an oscillating carriage driven by an electric motor through a crank slider mechanism. The carriage consists of an assembly that supports the pivoting clamps and blade material.

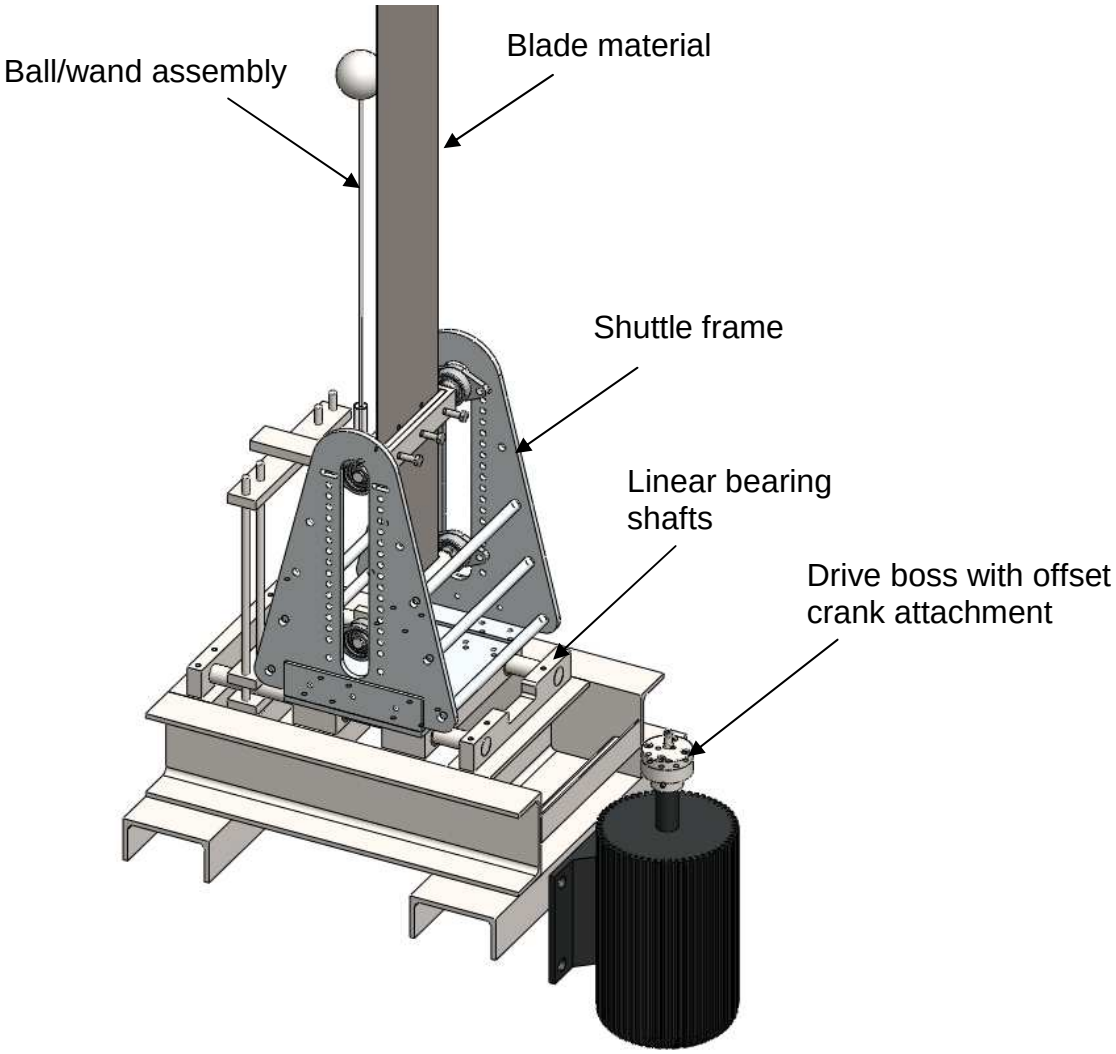

Figure 2.1: 3D CAD model of Blade test rig omitting support legs and crank between electric motor and shuttle

Figure 2.2 shows the test rig in situ in the mechanical engineering department at the University of Canterbury.

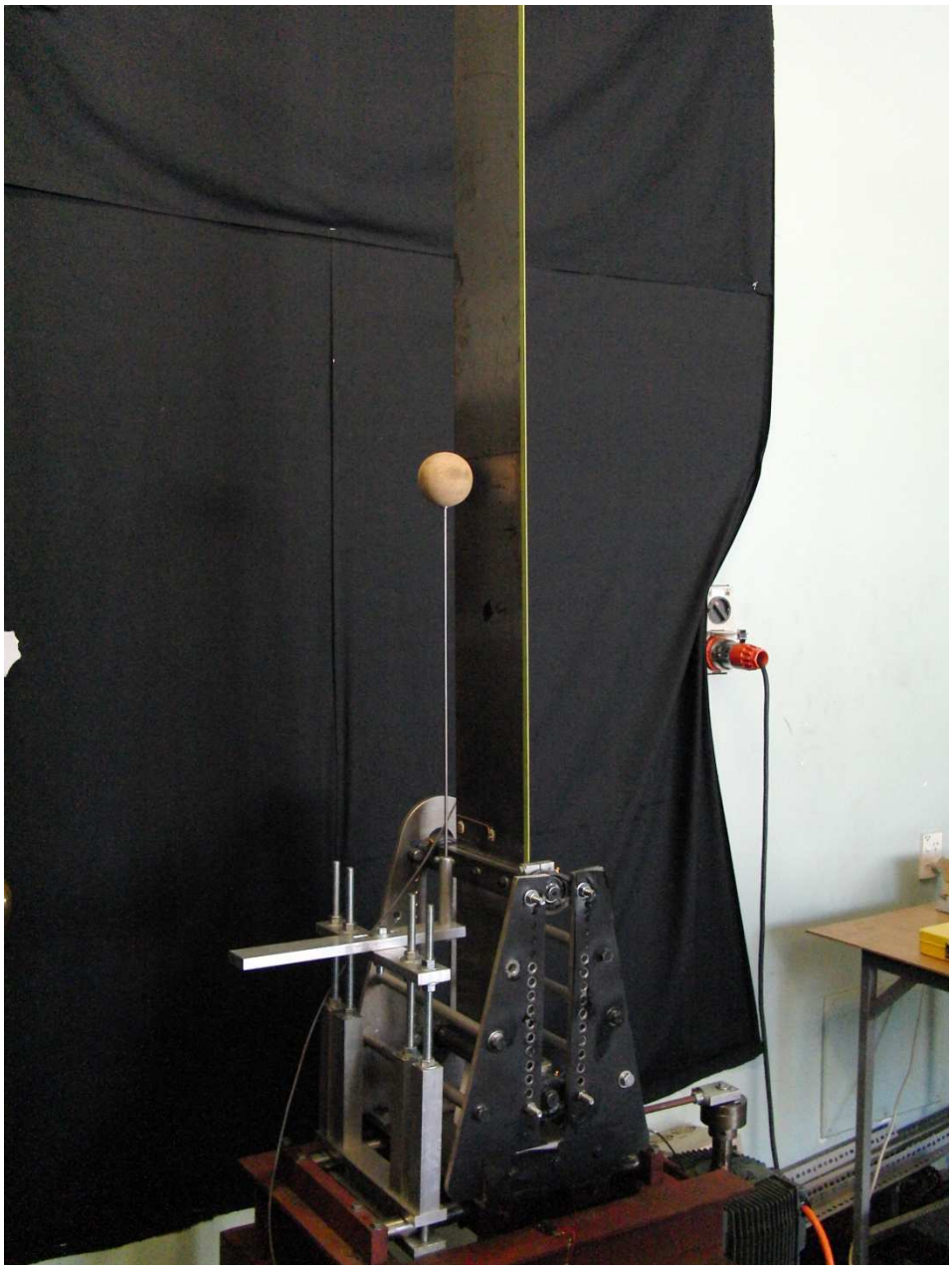

Figure 2.2: Blade test rig sculpture as completed at the University of Canterbury

2.2.1 Clamp Design

A key requirement of the clamp assembly was that the mass added to the oscillating carriage should be minimised while maintaining enough strength to ensure the clamp structure retained sufficient stiffness during operation. The

clamp structure was fabricated using aluminium alloy 6061 due to the wide availability and desirable strength to weight ratio.

The clamp structure consists of two shafts with adjustable separation (Figure 2.3). These two shafts perform the function of the simple supports in Figure 1.2. The top shaft (termed the *upper pivot*) clamps the blade material while the bottom shaft (termed the *lower pivot*) constrains the blade material in the vertical plane. The lower pivot (Figure 2.3) consists of a wire cut slot that fits closely to the blade material to allow the required relief movement of the blade material between pivots during deflection while still maintaining the stable vertical orientation of the blade material. This solution is noisy due to the clearance between the slot and blade material. However, this was deemed acceptable due to the simplicity of the solution for manufacture and the fact that the sculpture would only be used for testing purposes.

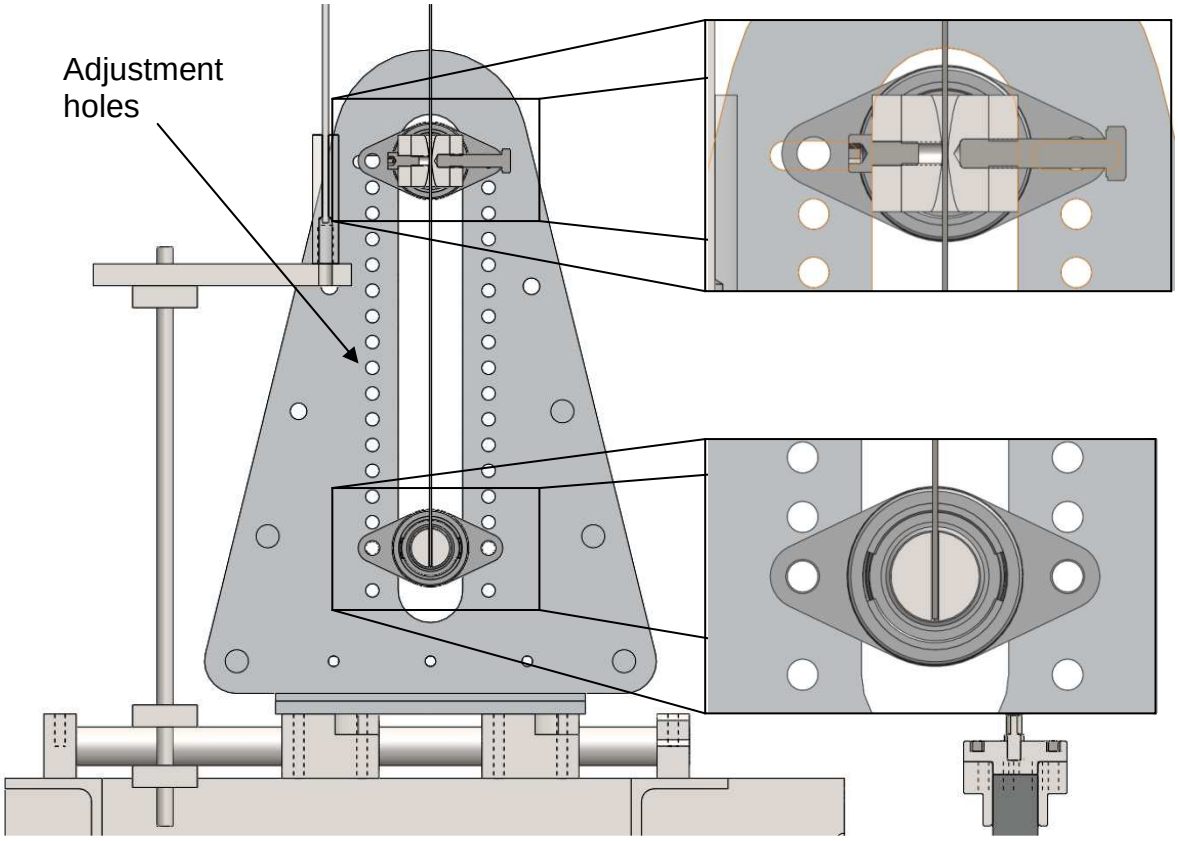

Figure 2.3: 3D CAD section view showing clamp detail on Blade test rig

The upper pivot was designed to clamp the blade material in place using two opposing jaws (Figure 2.3). One jaw is fixed to the shaft while the other floats on 3 cap screws for clamping the blade material in place. The jaw profiles were manufactured using a CNC mill to be parabolic ensuring the geometric stress concentration at the clamp exit was minimised. It is anticipated that the jaw design for a larger sculpture will also incorporate this feature.

Strain measurement at the clamp exit was taken into account in the design of the upper pivot jaws. Notches were machined out of the jaws in the location of the strain gauges to ensure no damage occurred in any scenario of the blade material and jaws interacting.

2.2.2 Pivot Separation

As mentioned previously, the pivoting clamp concept is hypothesized to reduce the reversed bending stress in the blade material at the clamp exit by allowing a larger radius of curvature to exist in the worst case scenario of blade material deflection. To maximise this reduction in stress, it was decided that the pivot separation should be adjustable to give larger ratios of clamped length to unclamped length (Figure 2.4) than that which exists in original *Blade* and *Big Blade*.

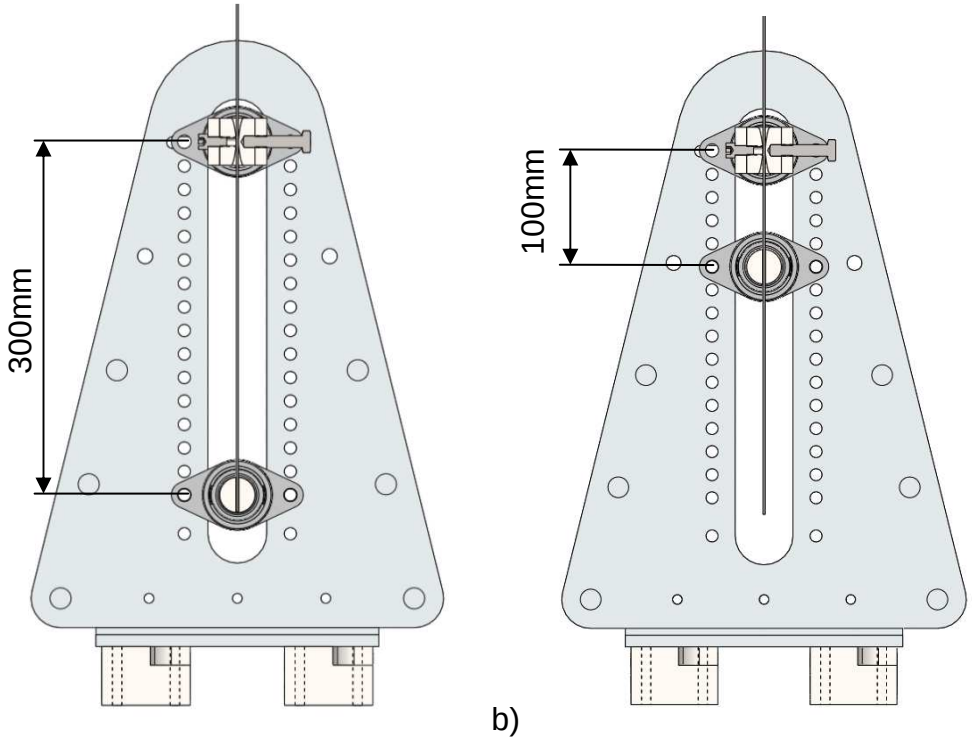

Figure 2.4: 3D CAD section views of Blade test rig clamp shuttle showing a) 300mm clamp separation and b) 100mm clamp separation (as seen in previous Blade sculptures)

The bending moment existing at the upper pivot depends directly on the separation (*l)* of the pivots in the clamp structure by Equation (2.1) and Figure 2.5 (Shigley, Mischke, Budynas, Liu, & Gao, 1989) for small displacements.

$$M_{AB} = -\frac{Fax}{l} \tag{2.1}$$

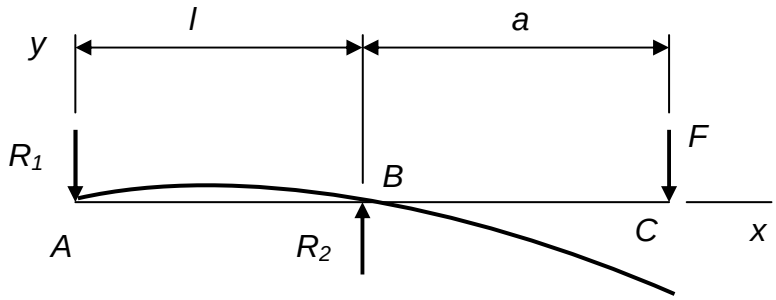

Figure 2.5: Simple supported beam with an overhanging load

Theoretically, up to a practical limit, increasing the pivot separation should decrease the reversed bending stress in the blade material. The disadvantage of increasing the pivot separation is the requirement of more blade material and hence the increase in cost per performance of the sculpture.

To investigate the effect of pivot separation on stress reduction the clamp assembly was designed to incorporate adjustable pivot mounting points giving a range of pivot separations between 100mm and 300mm in increments of 20mm (Figure 2.4). 300mm was chosen as a maximum length of clamped blade material. This translates to approximately 19% of the unclamped (or free) blade material length. This ratio was deemed to be the largest practical ratio for a scaled *Blade* work, with the risk of the supporting structure and mechanism becoming too tall to be feasible. The mounting plates were cut using a waterjet at Fabrum Solutions, Christchurch.

A carbon steel strip, of similar thickness to the original *Blade* was obtained for testing. As mentioned in Chapter 1, Lye experimented to find the unclamped

length in the original *Blade*. The approximate solution for buckling of a thin cantilever under self weight was found by A.G. Greenhill in 1881 (Frisch-Fay, 1961) to be,

$$\gamma = \frac{wgl_{cr}{}^{3}}{EI} = 7.84 \tag{2.2}$$

Where, instead, Lye used the value of 5.65 for the stability parameter, γ. This led Gooch to develop an equation relating thickness of the blade material to unclamped length of the form,

$$d = \sqrt{\frac{12\rho g l^{3}}{\gamma E}} \tag{2.3}$$

For an available gauge thickness of band saw steel of 1.8mm, Equation (2.3) gives a required unclamped length of 1599mm. An extra 335mm was added to the length of the blade material to account for a maximum pivot separation of 300mm (the top clamp has a height of 40mm and the bottom clamp has a height of 30mm with the rotational axis at half the height in each clamp giving a total extra required length of 335mm). The blade material has final measurements of 1934mm x 200mm x 1.8mm.

2.2.3 Allowance for a Cantilever Clamp Configuration

The inclusion of a cantilever clamp configuration on the test rig was considered important since this would be the baseline for comparison to the results in the pivoting clamp configuration. The pivots were designed to incorporate a cylindrical section that would accommodate an adjustable clamp at

the same axial position on each pivoting shaft. To transform the clamp assembly from pivoting to cantilever, these clamps are simultaneously fixed together by a length of 50mm x 25mm x 4mm 5052 alloy rectangular hollow section as in Figure 2.6.

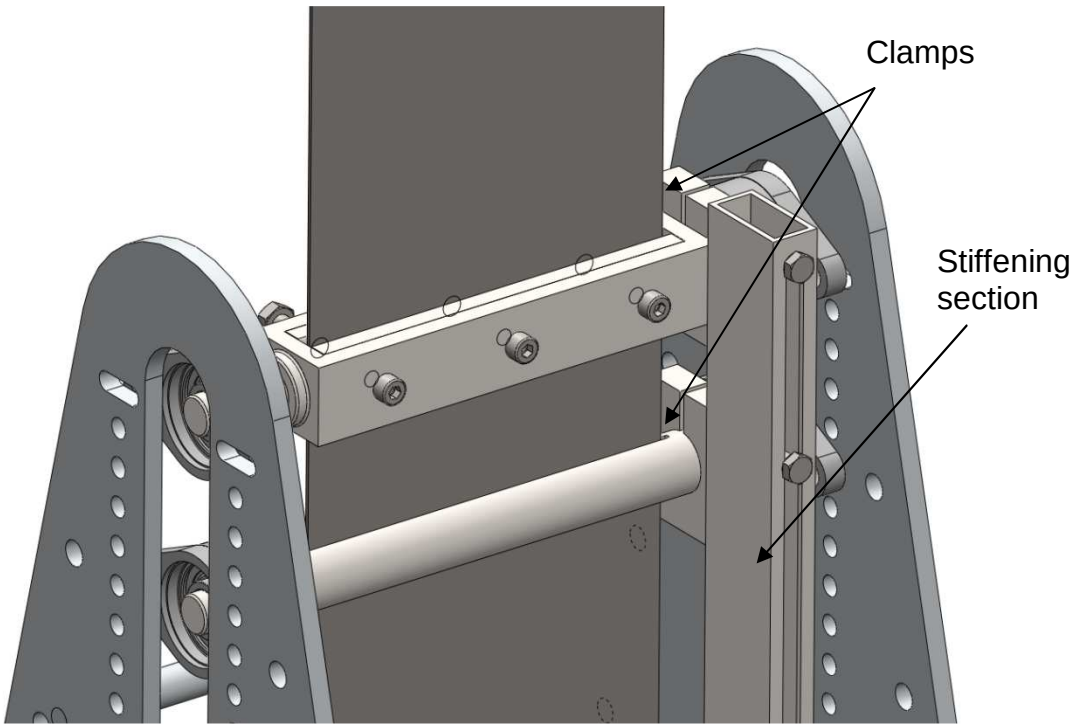

Figure 2.6: Blade test rig clamp in the 100mm cantilever configuration

The configuration of 100mm pivot separation clamped as a cantilever arrangement is equivalent to the clamping systems used in both the original *Blade* and *Big Blade*. This will provide a baseline for the comparison of results of bending stress measurement in the pivoting clamp arrangement at varying pivot separation.

2.2.4 Adjustable Ball and Wand

Gooch (S. D. Gooch, 2001) found that a significant factor in causing the 'swinging phenomenon' mentioned in Chapter 1 was the interaction of the ball

and wand with the blade material during performances. A ball and wand were therefore designed for the test rig with the purpose of experimenting with ball/wand materials and locations to find and optimal arrangement. The support structure for the ball and wand is clamped onto the linear bearing shafts that support the clamp structure as in Figure 2.7.

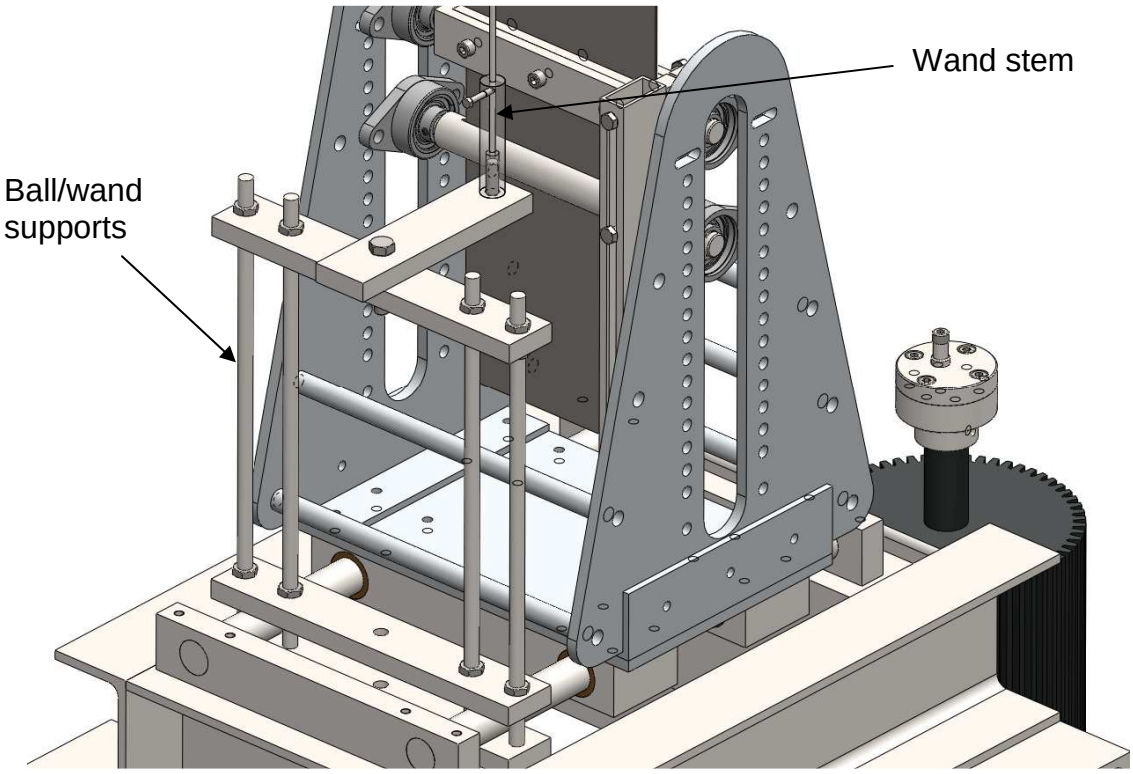

Figure 2.7: Ball and wand mounting arrangement on Blade test rig

The ball can be adjusted to be a specified distance from the blade. The collet design that clamps the wand was drilled through completely to allow infinite adjustment for the vertical striking location of the ball on the blade material. The clamping structure also allows adjustment of the ball height via the use of threaded rods. The ball and wand will be utilised in the study of Chapter 3, however they have been deliberately omitted for this particular study.

2.2.5 Strain Gage Measurement and Calibration

Strain gages were installed on to the blade material to measure the reversed bending stress at the clamp exit as in Figure 2.8. The strain gages were aligned to measure stress in the direction parallel to the long dimension of the blade material. The strain gages used were of the uniaxial type with designation N11-FA-2-120-11.

a) 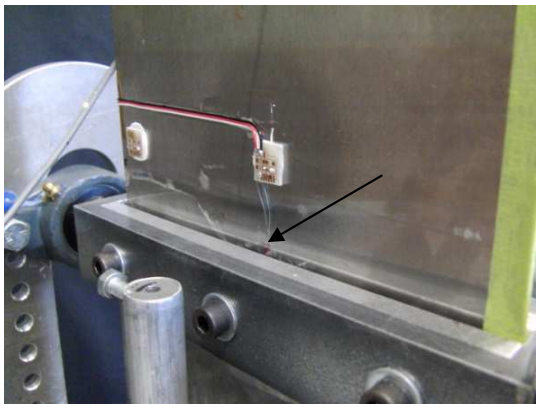 b) 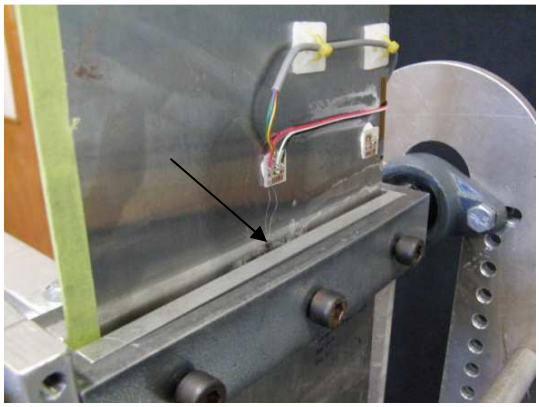

Figure 2.8: Strain gage locations on blade material

Zeroing the strain gages was performed by clamping two known straight edges on either side of the blade material to ensure that the neutral bending plane of the blade is completely flat. The gages were then zeroed using the Labview program that will be discussed in Section 2.2.9.

Calibration of the strain gages was performed using two different methods. The first method involved setting the blade material in fixtures to simulate a horizontal cantilever and allowing the free end to hang under self weight as in Figure 2.9.

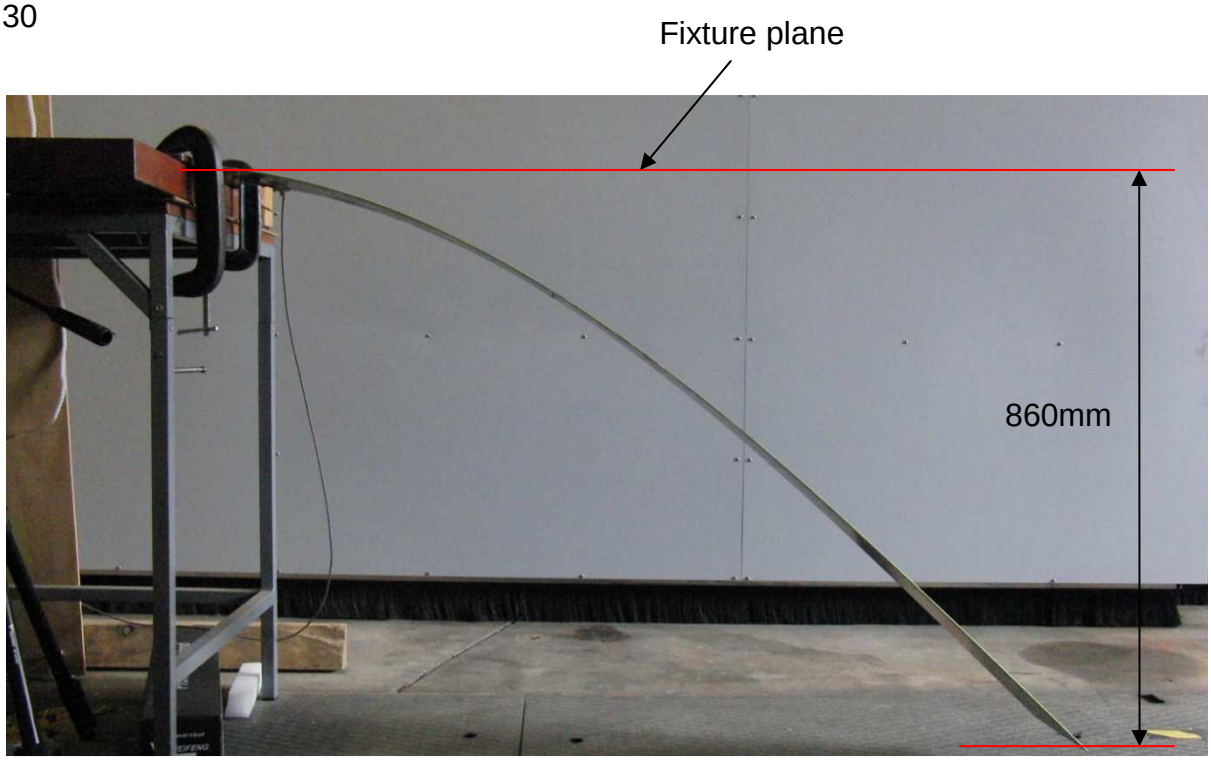

Figure 2.9: Hanging cantilever test performed on blade material

The measured strain was converted to a bending stress using the elastic modulus of the carbon steel and then compared to the result of MATLAB script tipdeflection.m (see Appendix B) for the code using theory from (Wang, 1986)). The measured strain for the carbon steel blade in the horizontal cantilever arrangement was 1304 microstrain. The tip deflection was measured to be approximately 860mm from the fixture plane. 1304 microstrain converts to 273.84MPa using,

$$\sigma = E\varepsilon \tag{2.4}$$

The results of tipdeflection.m calculated the bending stress to be 279.5MPa. The maximum tip deflection was calculated to be 876.3mm from horizontal (Figure 2.10).

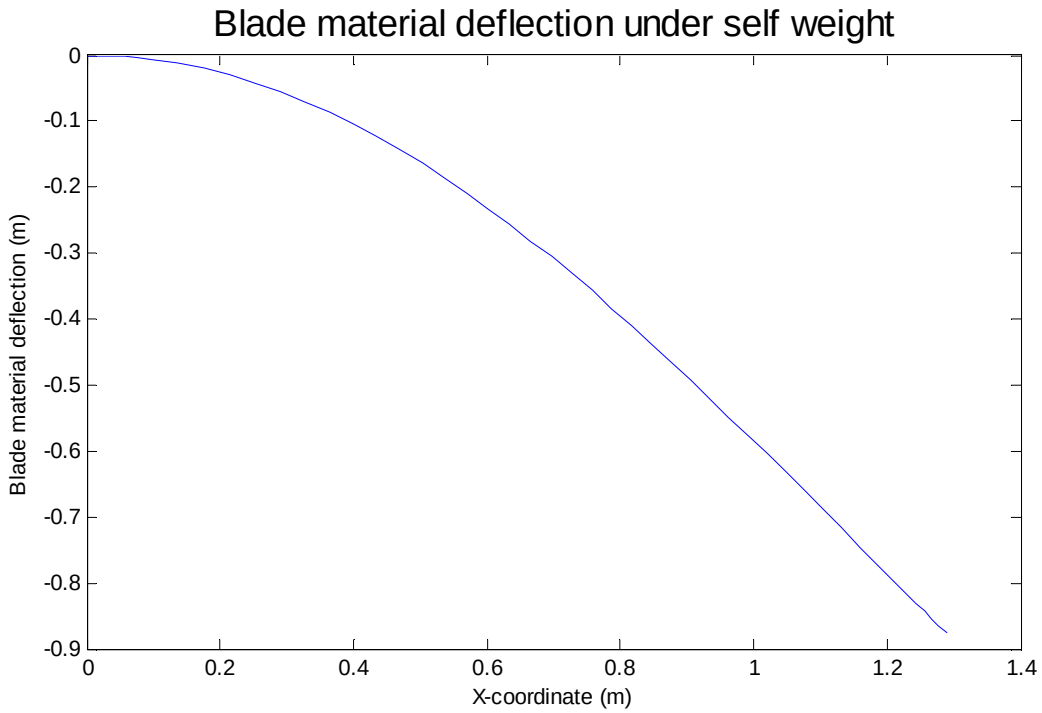

Figure 2.10: Output of tipdeflection.m showing the deflection of the blade material under self-weight along the axis of the un-deflected length

The errors in the measured bending stress and deflection values are 2.1% and 1.9% respectively. This error was deemed acceptable for testing purposes considering the possible sources of error in this calibration method. These sources of error include:

- Temperature effects on the carbon steel blade
- Residual stresses left in the blade material by the manufacturing process
- The flatness/level of the cantilever platform fixtures
- The position of the strain gage relative to the clamp exit
- The alignment of the strain gage with the direction of true normal bending stress in the surface of the blade material
- The clamping method for the cantilever

- The actual elastic modulus versus the value used in tipdeflection.m

The second method used to calibrate the strain gages was a shunt calibration. This procedure involves placing a resistor of known resistance across the strain gage terminals and comparing the result to a known stress that this resistor is simulating.

2.2.6 Frequency Measurement

An important aspect of the testing to be carried out is the ability to determine the experimental values of the clamp oscillation frequencies at crucial points during *Blade* performances. These values will be useful for the investigation of Chapter 4 in determining the required frequencies of clamp oscillation for the *Giant Blade* performances. The test rig employed an LVDT (linear variable differential transformer) displacement sensor (Figure 2.11) to measure the relative displacement of the clamp assembly and hence frequency oscillation of the clamp.

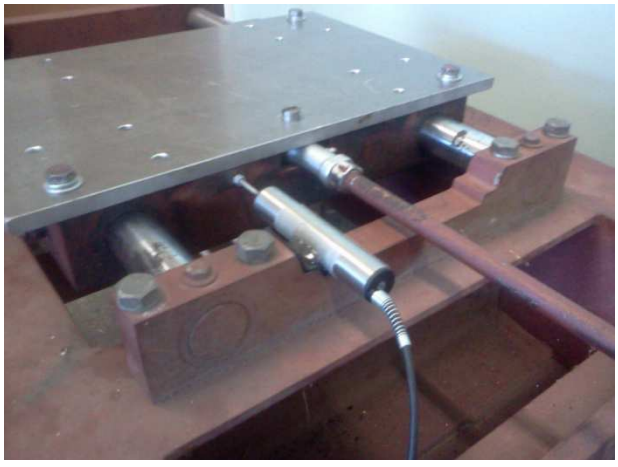

Figure 2.11: LVDT sensor for frequency measurement in situ on Blade test rig

2.2.7 Clamp Motion

Simple harmonic was required in the motion of the clamp assembly to ensure that the acceleration profile of the base motion remained uniform and produced the correct formation of natural bending modes in the blade material during performances. Several precautions were taken to ensure that the base motion of the carriage in the test rig obeyed simple harmonic motion as closely as possible. Den Hartog (Den Hartog, 1956) suggests that for an infinitely long connecting rod, the motion of a piston (clamp assembly) will follow simple harmonic motion (SHM). For short connecting rods the acceleration will deviate from SHM which would be undesirable in a *Blade* sculpture due to the resulting unbalanced inertial forces. Therefore, the crank arm on the test rig was manufactured of sufficient length with the intention of ensuring the clamp oscillation follows approximately SHM. This was later verified by comparing displacement sensor output to theoretical SHM displacement (Figure 2.12).

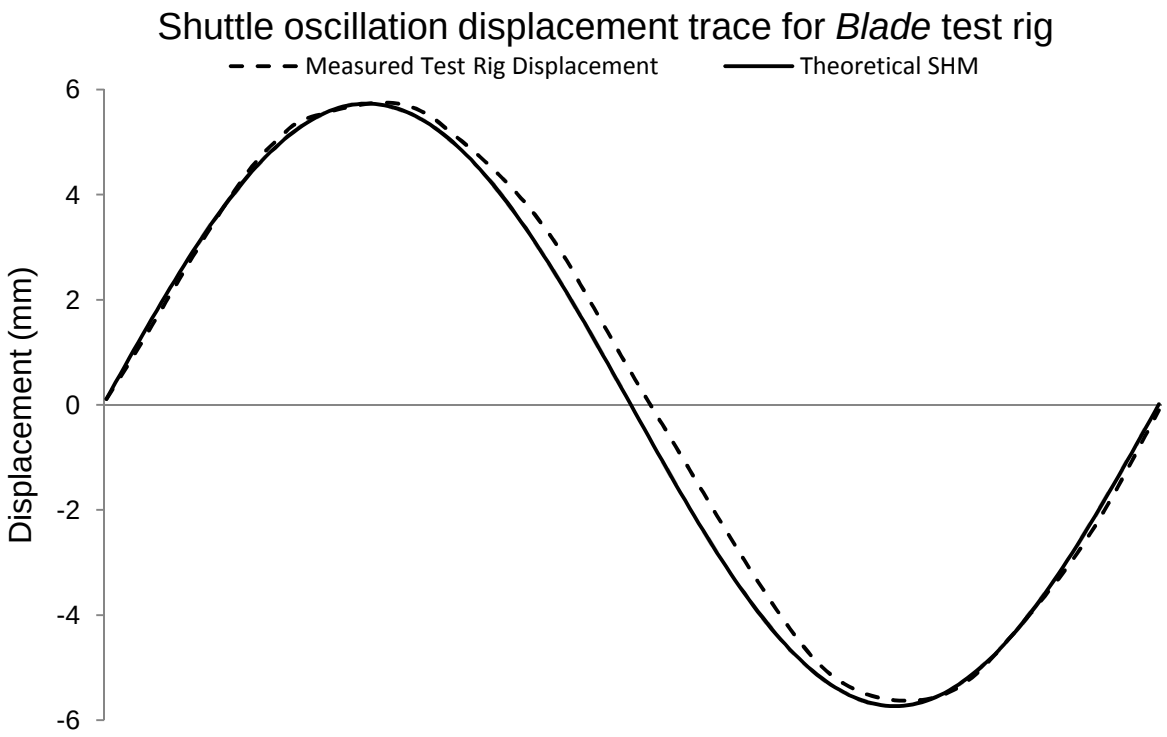

Figure 2.12: Comparison of the test rig shuttle oscillation profile with the theoretical case of simple harmonic motion

The displacement amplitude required for this scale of *Blade* sculpture is very close to the *Original Blade* displacement amplitude. The drive hub for attaching the driving crank to the electric motor was machined to mount a steel pin at 5.55mm offset from centre to give the correct oscillation displacement. The variation of the test rig profile from the theoretical SHM profile can be attributed to the clearances in the linkages of the drive mechanism and also inertial forces of the shuttle.

The friction of the linear bushes was of concern to ensure uniformity of clamp oscillation. Bronze bushes were selected and designed with grease galleries to ensure adequate lubrication could be provided evenly to the sliding surfaces.

The electric motor selected was a readily available 5kW 4-pole 3 phase squirrel cage unit to ensure the inertial effects of the vibrating blade material did not affect the clamp motion. In earlier sculptures there was a tendency for *'the tail to wag the dog'* (S. D. Gooch, 2001) in terms of the electric motor relationship with the dynamic components of Lye's sculpture. In larger sculptures, such as *Giant Blade*, a compromise of control over unpredictability was agreed upon for failure purposes. More control allows more accurate prediction of the life of the sculpture. Hence, the test rig sculpture was designed to provide the same control of clamp motion as would be in *Giant Blade* by providing sufficient drive power.

2.2.8 Pivot Friction

The selection of the simple support solution for the pivots required consideration of various factors. Stiffness was of high importance as any damping would introduce undesired vibrations and impulses into the blade motion. Friction opposing rotation would reduce the ability of the clamp to ensure a maximum bending stress reduction in the blade material. Ultimately, flange mounted ball bearing units were selected as the most simple and readily available solution with the least amount of friction and damping. Grease lubrication was specified for the bearing inserts. Oscillatory motion, such as that of the inner raceway on the simple supports of the clamp assembly, is generally not a good application for ball bearings. However, considering the relatively low loading for the size of the bearing selected there were no anticipated wear issues in the bearings.

2.2.9 Data Acquisition

Labview 2011 version 11.0 was used to measure the incoming signals from the displacement sensors and strain gages. The program was designed to write data to a text file as output for further post-processing in MATLAB. Time, displacement, and strain were all measured at a rate of 1kHz in blocks of 100 data points. Clamp oscillation frequency was measured through the LVDT using an average of instantaneous frequencies from each 100 data point block.

The Labview program also controlled the electric motor on the test rig through a Teco motor controller. The ability to gradually change the clamp oscillation frequency was an important feature of the Labview program. As mentioned in Chapter 1, Gooch found that the worst case scenario for bending stress in the blade material occurred during the ‘swinging’ phenomenon which was a direct result of the profile of the ramping function used to alter the clamp oscillation speed. Gooch also found that by forming the natural frequency mode shapes in the blade material by entering the corresponding clamp oscillation frequency from above, rather than below, there was more stability in the dynamics of the blade material. This was due to a concept of vibration called the non-linear jump phenomenon (Den Hartog, 1956). For a softening spring, as the blade material behaviour was found to obey, Figure 2.13 illustrates the dynamics that occur during the jump phenomenon for increasing and decreasing clamp oscillation frequency.

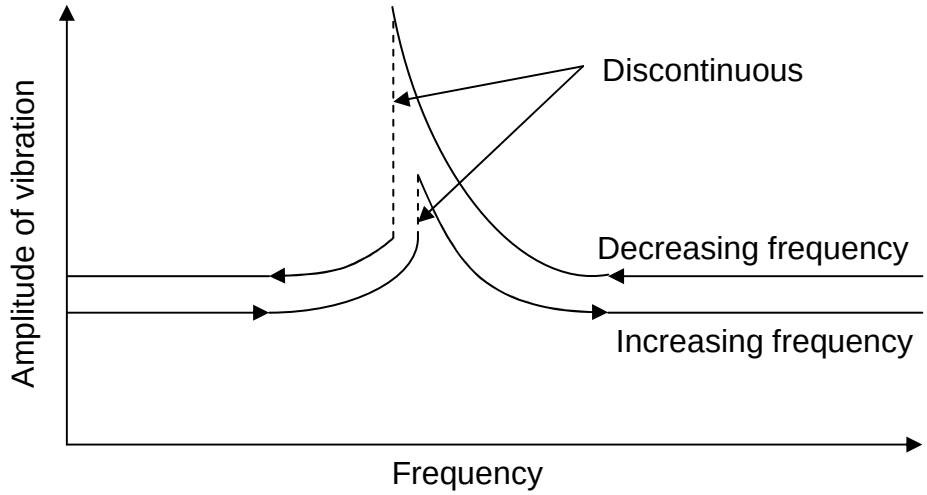

Figure 2.13: Non-linear softening spring effect and jump phenomenon (Nayfeh & Mook, 1995)

Each performance for the test rig was programmed to be as close to the performance program for *Big Blade* (Figure 1.10). A notable difference was that the sections of *Big Blade* performance Lye named ‘kissing’ and ‘shimmering’ were omitted and the blade material was excited into the second mode and third mode (Figure 4.1) respectively for these sections. This resulted in a program that excited the test rig blade material into the second mode for approximately 130 seconds and the third mode for approximately 220 second - a total test performance time of 350 seconds.

2.3 Average Stress Reduction of Pivoting Clamp

2.3.1 Method

In this experiment the ball and wand were removed from the test rig to minimise any swinging that may occur in the blade material. This was intended to ensure each performance was as repeatable as possible (at least in terms of measuring an average stress in each vibratory mode). Strain data was measured

for one performance at each pivot separation and also at the 100mm cantilever configuration. Strain data was then processed in MATLAB using compare.m (Appendix B) to determine the average stress during each of the second and third modes of vibration.

2.3.2 Results

Table 2.1 presents the results of the average stress reduction measurements for varying pivot separation and the 100mm cantilever configuration.

Table 2.1: Average percentage stress reduction for varying pivot separation on the Blade test rig

	Average measured bending stress (MPa)		**Percentage reduction (%)**	
	2nd Mode	3rd Mode	2nd Mode	3rd Mode
100	*141*	*97.0*	*(Cantilever)*	
100	116	91.6	17.23	5.60
120	130	78.8	8.94	18.76
140	128	71.3	4.50	26.47
160	125	79.3	5.68	18.19
180	120	71.9	5.87	25.89
200	118	69.5	9.23	28.32
220	112	66.6	13.86	31.33
240	112	65.0	10.53	32.94
260	99.2	63.8	27.16	34.19
280	111	55.3	21.35	42.97
300	102	56.8	27.70	41.46

Pivot separation (mm)

Figure 2.14 illustrates the trend of stress reduction for the varying pivot

separations compared to the 100mm cantilever configuration.

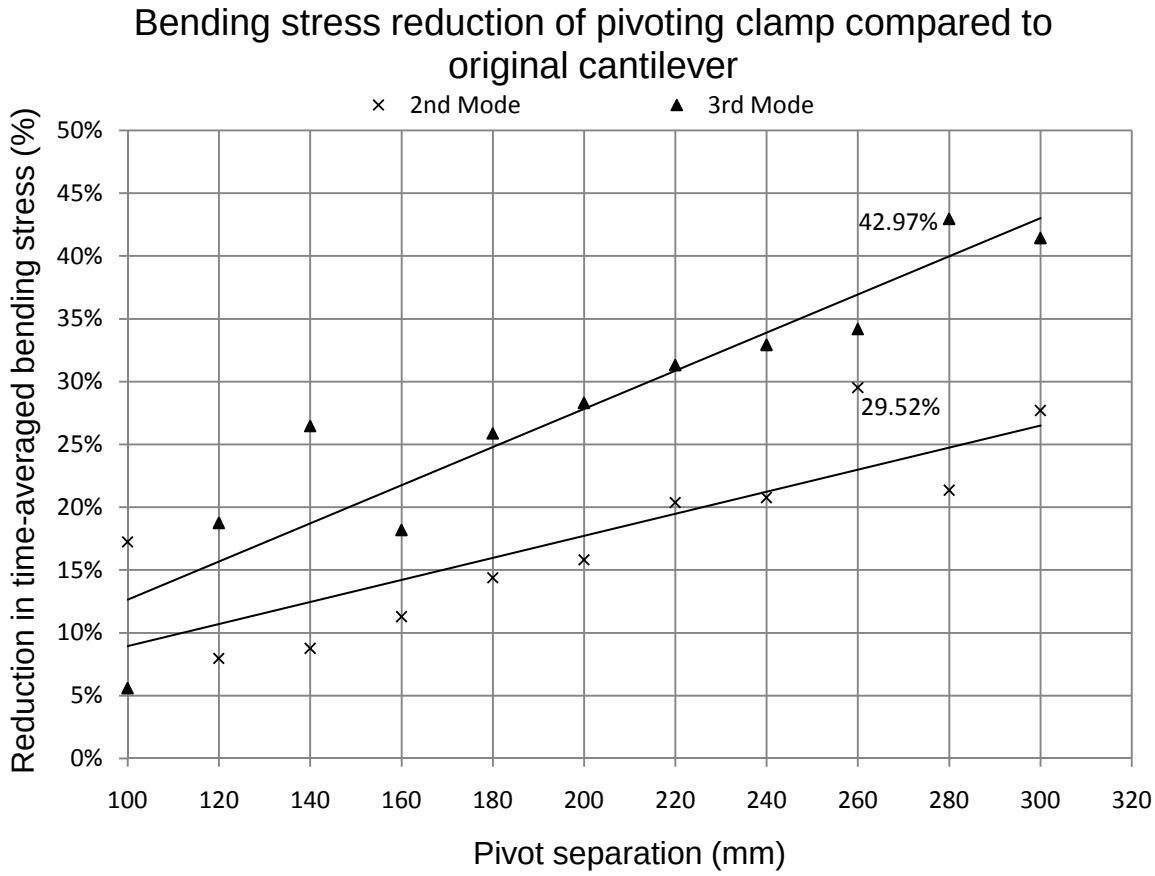

Figure 2.14: Measured trends of stress reduction provided by the pivoting clamp for the two relevant bending modes in the blade material

2.3.3 Discussion

It is clear from Figure 2.14 that as the pivot separation increases, so too does the stress reduction capability of the pivoting clamp concept. This is an intuitive and expected result. The trend lines indicate that the maximum stress reduction of average stress in the second mode of vibration is approximately 27% and in the third mode of vibration, 43%. The trend of increasing reduction in stress is obvious with some outliers present (42.97% and 29.52% as indicated in Figure 2.14). This can be attributed to the unpredictable nature of the blade material during vibration. Some performances developed the swinging previously

mentioned, despite efforts to avoid this, and the results would have been affected.

An interesting result of this testing is that, without the ball and wand present, the average stresses in the second mode of vibration are higher than in the third mode. The reason for this is the visibly increased amplitude of vibration evident in the second mode compared to the third mode (Figure 2.15).

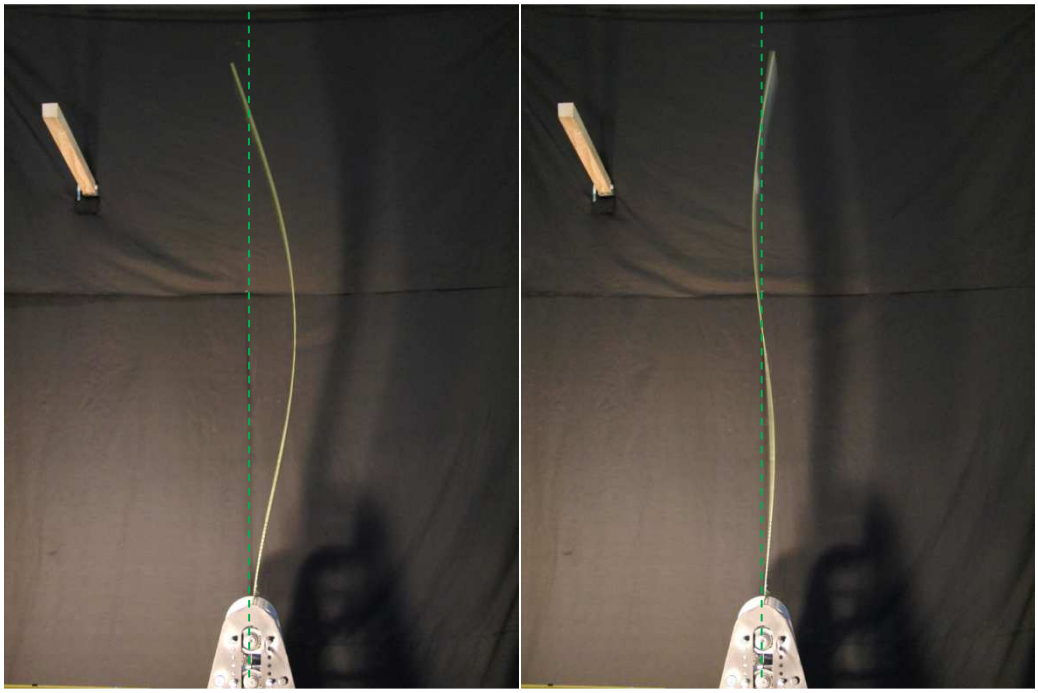

Figure 2.15: Illustration of the difference in amplitude of vibration between the 2nd and 3rd mode during testing

This would suggest that the pivoting clamp is more effective in reducing stress at larger bending radii at the clamp exit rather than equally effective across the whole range of bending radii possibilities. It was envisaged that the stress reduction capability of the pivoting clamp concept would reduce for decreasing bending radius at the clamp exit as the pivoting clamp concept tended more towards the behaviour of the cantilever clamp. This experiment has confirmed

that the maximum pivot separation of 300mm provides the most stress reduction at the clamp exit for each mode of vibration. Further investigation is required to understand the full benefits of the pivoting clamp concept.

2.4 Clamp Stress Profiles for Varying Bending Radii

2.4.1 Method

This experiment involved reducing the bending radius of the blade material at the clamp exit and measuring the bending stress in the blade material at each various bending radii. A temporary frame was attached to the test rig base frame to hold the blade material in its deflected state at each bending radius (Figure 2.16). This was carried out for the 300mm pivot separation as well as the 100mm cantilever clamp configuration. Bending strain was measured at each stage of blade material deflection and the results were compared.

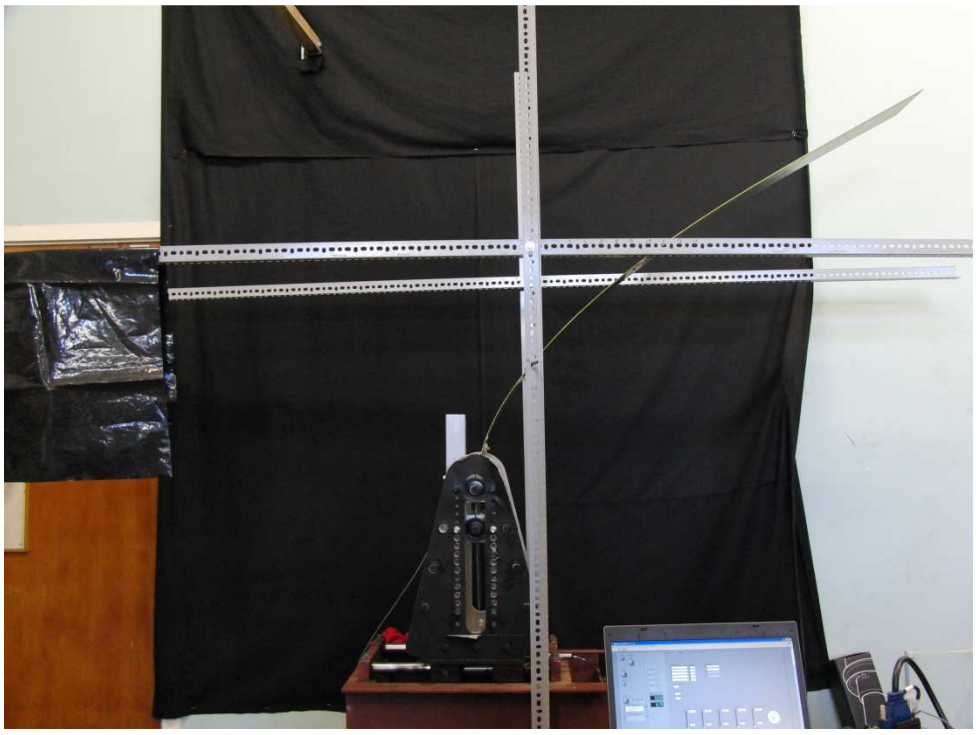

Figure 2.16: Test rig set up for clamp stress profile testing

2.4.2 Results

The stresses in the blade material measured at each bending radii are presented in Figure 2.17.

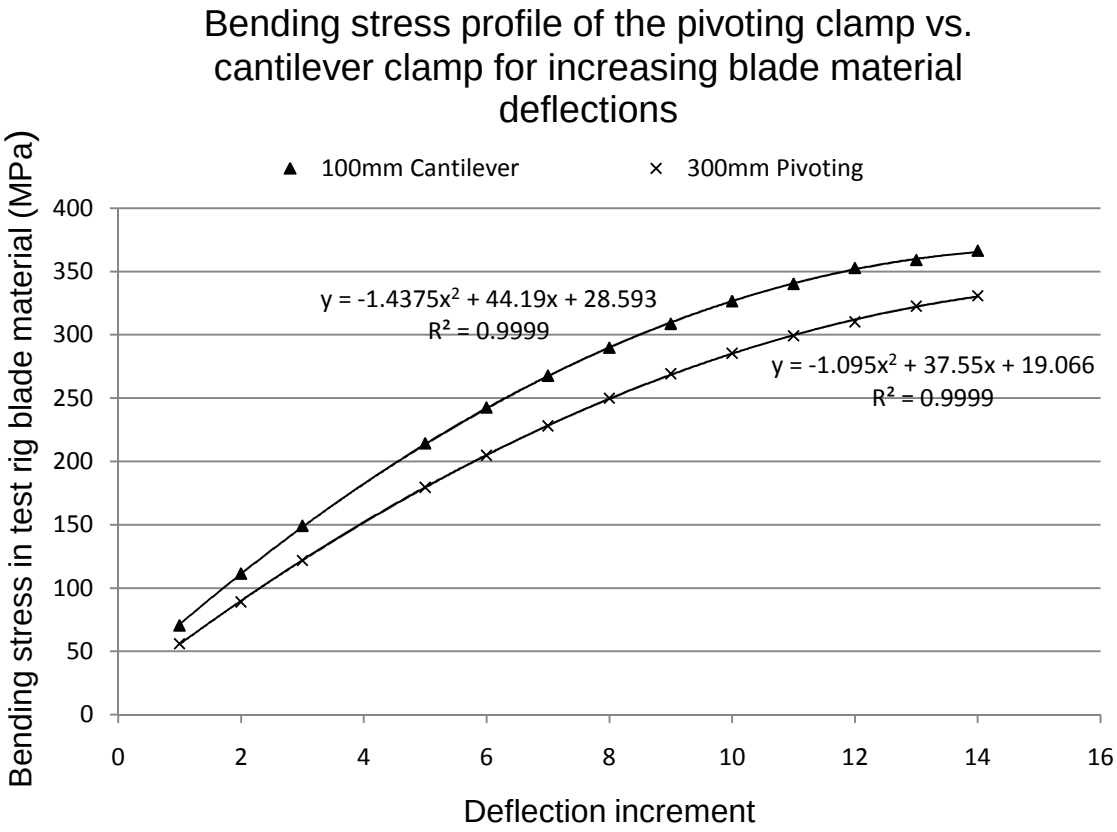

Figure 2.17: Bending stress profiles of the pivoting clamp at 300mm separation and the 100mm cantilever clamp

Although it may appear the greatest stress reduction occurs at the higher values of bending stress, the opposite is actually true due to the relative values of stress in each clamp configuration for a specific blade material deflection. Figure 2.18 represents the stress reduction in percentage for increasing bending stress levels of the 300mm pivoting clamp configuration compared to the cantilever clamp configuration.

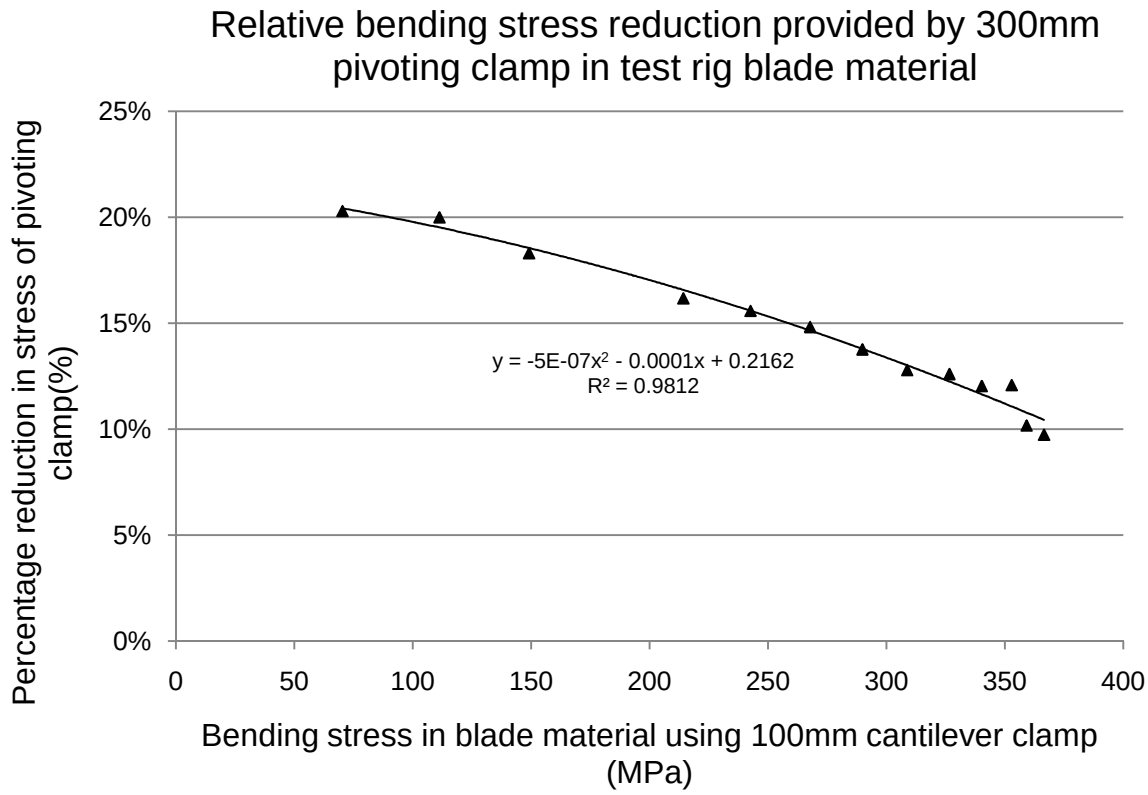

Figure 2.18: Bending stress reduction provided by the implementation of a pivoting clamp for various measured bending stresses in the blade material of a cantilever clamp sculpture

The reason for the decreasing stress reduction effect of the pivoting clamp is thought to be due to the material stiffness between the pivots of the clamp. As the deflection of the material between pivots increases, the clamp tends towards the behaviour of a cantilever clamp configuration.

2.4.3 Discussion

The information presented in Figure 2.18 is useful in predicting the percentage reduction in stress that the pivoting clamp configuration would achieve in a larger sculpture. Gooch (S. D. Gooch, 2001) developed a scaling law for bending stress to predict stresses in larger sculptures that takes the form,

$$\frac{\sigma(x/l)_o}{\sigma(x/l)_s} = \sqrt{\frac{\rho_o E_o l_o}{\rho_s E_s l_s}} \tag{2.5}$$

It can be seen from Equation (2.5) that scaling the bending stresses in the blade material depends only on the material properties and geometry of the blade material. Therefore, all values of relative percentage reductions in stress will remain constant as the scale of the sculpture increases. In other words, because static similarity is maintained in scaling the sculpture (S. D. Gooch, 2001), the relative difference in bending stress in the blade material between a cantilever version and a pivoting version will remain equal at all scales. Equation (2.5) can therefore be used to scale the x axis in Figure 2.18 to obtain a useful chart for predicting stress reduction for the scale of sculpture in question.

Average stress reductions do not necessarily provide a definitive indication as to whether the pivoting clamp will provide enough advantage in extending the life of the sculpture to warrant implementation. In building *Big Blade*, Gooch predicted the number of performances until failure for this sculpture to be 261 performances. This was based on observations of the mathematical model that Gooch developed where a worst case reversed bending stress of 383MPa was observed to occur 785 times per performance. The maximum reversed bending stress in the test rig during testing was measured to be 249MPa in the cantilever clamp configuration. This scales to a reversed bending stress of 203MPa at the scale of *Big Blade* using Equation (2.5). The fatigue data for Ti-6Al-4V used in the analysis of Gooch (Hempel & Hillnhagen, 1969) is now dated. Using the S-N curve of Chapter 3, a reversed bending stress of 203MPa occurring 785 times per performance predicts 273 performances until failure for *Big Blade*. Here, it

will be assumed that the reversed bending stress of 203MPa (248MPa at test rig scale) is the dominant stress cycle in the blade material in terms of fatigue. Using the Equation in Figure 2.18, a stress reduction of approximately 15% (at 248MPa) on the maximum reversed bending stress is obtained by implementation of a pivoting clamp. This results in a new dominant fatigue stress cycle of 173MPa in *Big Blade*. The performances to failure of *Big Blade* with a pivoting clamp would now be 827, an increase of approximately 300% on the life of the blade material in *Big Blade* and a savings of 25NZD per performance in terms of the blade material cost in 1998.

2.5 Conclusions

A quantitative measure of the stress reduction qualities of the pivoting clamp concept compared to the cantilever clamp concept has been obtained.

> ***At any scale of Giant Blade, introducing a pivoting clamp in place of a cantilever clamp would reduce bending stress seen by the blade material in the second and third modes of vibration by approximately 27% and 43% on average respectively.***

A quantitative measure of the advantage in sculpture life provided by the implementation of a pivoting clamp was required so a blade material deflection experiment was carried out to determine the stress profiles of each clamp configuration.

> ***Based on an assumption for the dominant stress cycle during Blade performances, and the occurrence of this***

cycle per performance, it was found that the implementation of a pivoting clamp on to Big Blade would result in a 300% increase in sculpture life and a blade material cost savings of approximately 25NZD per performance.

There are important implications for design as a result of the testing in this chapter. The 300mm pivot separation is equivalent to approximately 19% of the blade material free length in the test rig.

The blade material obtained for Giant Blade should have a length dimension equal to the correct blade free length found in Chapter 3 plus 19% of this length to ensure that the same stress reduction achieved in testing is maintained in the larger sculpture designed with a pivoting clamp.

The results of this chapter indicate that the pivoting clamp configuration would result in a significant improvement in the life cycle of *Big Blade*. However, the assumption of a dominant bending stress cycle is inaccurate for larger scales of the sculpture, since all cycles have some effect on the endurance limit and life cycle of a material (Manson, Nachtigall, Ensign, & Freche, 1965). The assumption of 785 cycles per performance is also questionable. Finally, the 300% increase in sculpture life will only hold for the sculpture at the scale of *Big Blade* due to the logarithmic nature of S-N curves. Therefore, an investigation into the cyclic nature of the reversed bending stress in the blade material is required to gain an accurate understanding of the maximum possible scale of the sculpture.

3 Largest Economic Scale of Giant Blade

3.1 Introduction

The purpose of this chapter is to determine an accurate fatigue life of a scaled version of Blade based on the largest piece of blade material commercially available.

Chapter 2 explained the conservative assumptions used in obtaining a fatigue life for *Big Blade*. To ensure the scale of the new sculpture is optimised, a method of accounting for every reversed bending stress cycle in a performance is required to determine an accurate fatigue life. The same testing apparatus used in Chapter 2 is used in this study with the addition of the ball and wand.

3.2 Material Availability

As explained in Chapter 1, Gooch (S. D. Gooch, 2001) found that one of the most influential constraining factors in building *Blade* as large as possible is the availability of the blade material at the correct dimensions. A useful measure of the size of a scaled sculpture is the scale ratio, defined as,

$$s = \frac{l_s}{l_o} \tag{3.1}$$

It was decided that a scale ratio of 3 would be the minimum scale required

to justify the build of a larger *Blade.*

Similarity conditions require that static similarity be maintained between the *Original Blade* and a scaled sculpture. Similarity rules developed by Gooch require that the thickness of the blade material scales as follows,

$$\frac{d_o}{d_s} = \sqrt{\frac{l_o^3}{l_s^3}} \tag{3.2}$$

This equation takes the form of Figure 3.1,

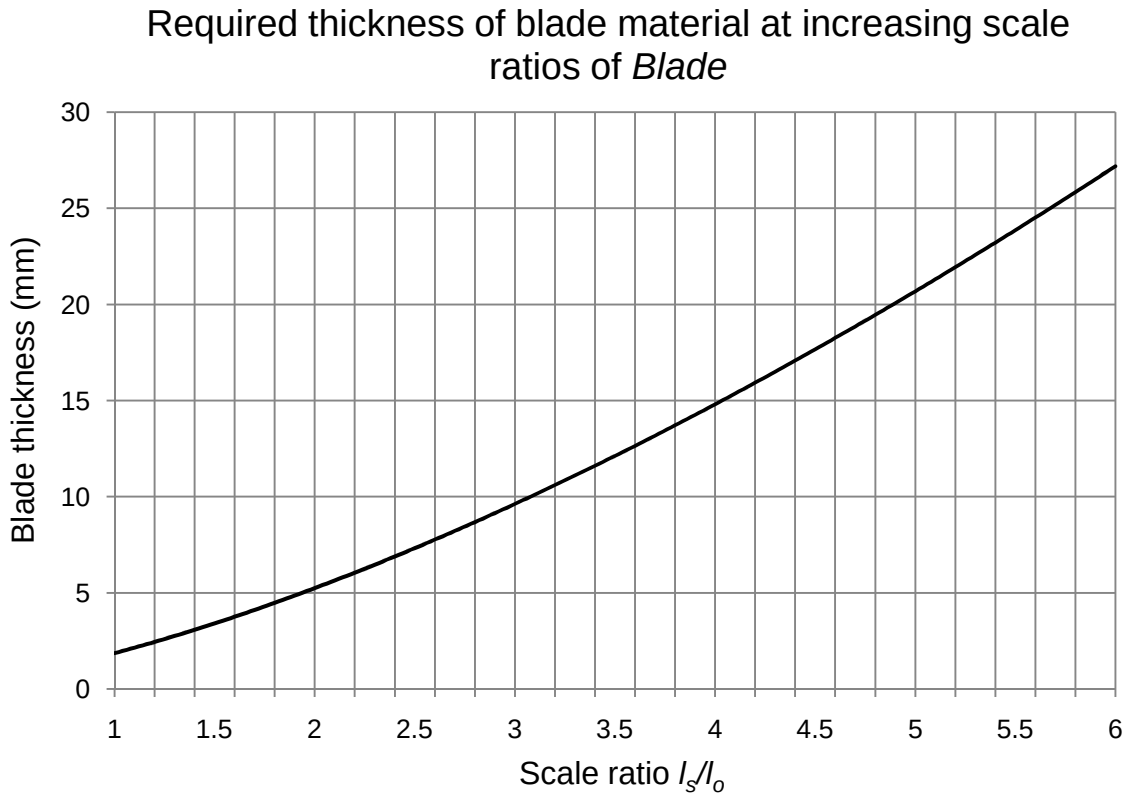

Figure 3.1: Influence of Blade size on required thickness of blade material

Using Equation (3.1), a scale ratio of 3 would give the required thickness of a new piece of titanium blade material to be approximately 10mm as is

confirmed in Figure 3.1 above. Most material suppliers form catalogues for plate on the basis of thickness. Therefore, a more useful result would be a required length of blade material for a given thickness. The basis of Lye's method for finding the correct free length of blade material is explained by Gooch to obey the theory of the stability of a vertical cantilever beam. The solution for the critical weight at the onset of buckling is given in Equation (2.2). Using Equations (2.2) and (3.2) Gooch developed an equality constraint that allowed the free length of blade material to be determined from a given thickness.

$$l = \sqrt[3]{\frac{d^2 \gamma E}{12 \rho g}} \tag{3.3}$$

Equation (3.3) was used to develop a list of viable blade free lengths based on standard titanium plate thicknesses. The width of the blade material was calculated using the geometric similarity rule developed by (S. D. Gooch, 2001) that states the aspect ratio of the blade material should remain constant through all scales,

$$\left(\frac{b}{l}\right)_o = \left(\frac{b}{l}\right)_s \tag{3.4}$$

Chapter 2 results in the conclusion that, additional to the free length of blade material required at a particular thickness, there should be 19% of the free length to make up the total required length of the titanium plate. Using Equations (3.3) and (3.4) for example, a standard 10mm thickness plate of titanium 6Al-4V for *Blade* would result in a blade material 5926mm long and 638mm wide.

A worldwide search for titanium 6Al-4V was carried out. The areas where the likely suppliers were located included Russia, the United States, Singapore, China and Korea. Two sizes were requested from approximately 50 suppliers. The plate sizes corresponded to 10mm (x 5926mm x 638mm) and 15mm (x 7766 x 836mm) thicknesses as a first attempt. The largest supplier of titanium worldwide, VSMPO, was included in this search. 20 of the original 50 suppliers that were contacted returned the correspondence and the majority of these suppliers were only willing to quote on sizes that were currently available in stock. The thickness and the width requirements of the plate were easily met. However, the length dimensions of the plates being offered reached an upper limit of 144 inches (3657.6mm) for all suppliers. This was explained by various sales representatives to be a limitation of the hot rolling process used to manufacture the titanium plates.

Welding of two plates was investigated as a solution to the length limitations. However, this was discounted due to the visible weld seam that would result in the blade material. The required sanding surface treatment (Table E.1 Appendix E) would reduce the appearance, but the heat affected zone of the weld would always be visible. Due to the aesthetic requirements of the artwork this was not a viable option.

Trans World Alloys was the first supplier to respond positively to the suggestion that the plate could be custom manufactured. Several iterations and discussions led to a maximum size of plate agreed on being 8769mm x 944mm x 18mm providing a visible blade free length of 7369mm. Unfortunately,

subsequently during the process of securing a purchase order, the mill advised that they were not willing to manufacture the size of plate agreed on. As the titanium is drawn through the final dies the plate begins to cool and can bind to the rollers that support the finished plate. The mill was not willing to risk the shutdown and repair period required should this occur.

China was deemed the next best option for a supplier of the blade material for a scaled sculpture. This involved a visit to Shanghai in August of 2013. A blade material size of 10024mm x 1080mm x 22mm was discussed and China Special Metals advised that manufacture was possible, although with a lead time of approximately 8 months. Investigation into competing suppliers was undertaken and several factories were visited. At the time of writing, Baoti Titanium has been selected as supplier of the blade material. Price and quality of factory facilities were factors in this decision. The blade material that can be supplied is 10024mm x 1080mm x 22mm which corresponds to a scale ratio for *Giant Blade* of 5.17 with 8424mm of visible blade material in the scaled sculpture.

3.3 Fatigue Life Prediction Method

The general approach to establishing fatigue life used in this study is presented in the logical flow diagram of Figure 3.2.

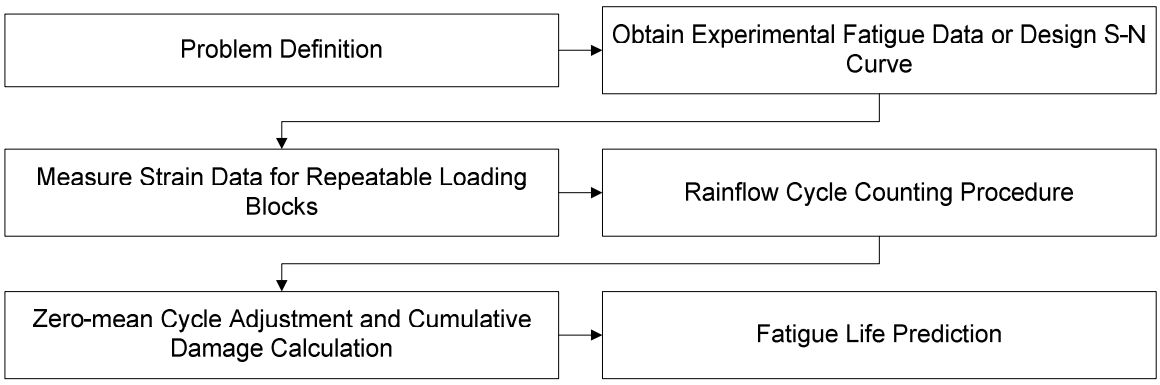

Figure 3.2: Flow chart showing the approach for fatigue life prediction in this study (adapted from (Baek, Cho, & Joo, 2008))

3.3.1 Scaling Laws

Gooch (S. D. Gooch, 2001) established the relationship between bending stress, material properties and size of the sculpture as in Equation (2.5). It can be shown that for similar material properties, the bending stress in the blade material increases with increasing size of the sculpture.

3.3.2 Rainflow Cycle Counting

Matsuishi and Endo (Matsuishi & Endo, 1968) are credited with developing the rain-flow cycle counting method while Downing and Socie (Downing & Socie, 1982) present an algorithm for rain-flow cycle counting. This method of variable amplitude load history cycle counting allows extraction of all major and minor stress-strain hysteresis loops from a stress-time loading history.

This method of cycle counting begins with a stress-time history of a typical loading block as shown in Figure 3.3: Example of a load history data block

.

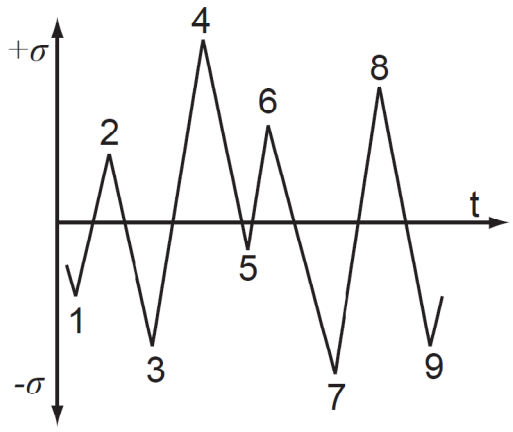

Figure 3.3: Example of a load history data block

This plot is rotated through 90 degrees. Peaks are identified and sorted into compressive troughs (negative stress) or tensile peaks (positive stress). In Figure 3.4 the odd numbers are compressive troughs and even numbers are tensile peaks. Visualise the stress-time history as a multi tiered roof with water cascading over each tier. Stress half-cycles are identified by the following rules:

1. The ‘flow’ from a tensile peak (or compressive trough) meets an imaginary horizontal line that intersects a tensile peak (or compressive trough) of greater magnitude.
2. The ‘flow’ from a tensile peak (or compressive trough) meets the ‘flow’ from a tensile peak (or compressive trough) that originated earlier.
3. The ‘flow’ reaches the end of the stress time history.

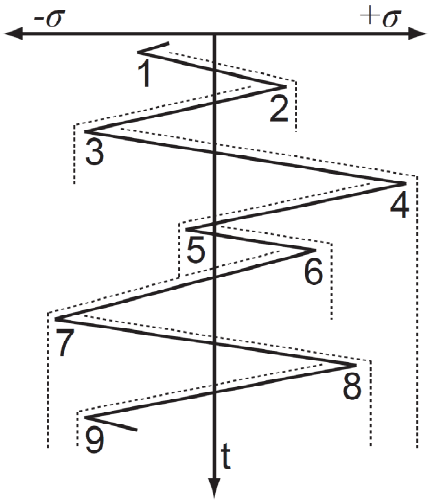

Event	*Cycles*
1-2	0.5
2-3	0.5
3-4	0.5
4-7	0.5
5-6-5	1.0
7-8	0.5
8-9	0.5

Figure 3.4: Rain-flow cycle counting method illustrated for loading clock in Figure 3.3

Half cycles are counted according to the magnitude of their range. The amplitude and maximum value of each half cycle is recorded and the zero-mean equivalent stress of the half cycle is calculated using the Smith-Watson-Topper method. Manson's method is then used to determine the damage sustained during a typical loading block (1 performance in the case of the sculpture).

3.3.3 Smith-Watson-Topper Method

Obtaining reliable fatigue data without performing lengthy fatigue tests on material samples can be difficult. Fortunately, 6Al-4V is widely used in the aerospace industry and there exists extensive data on the failure behaviour of the alloy. Dowling (Dowling, 2004) has also performed extensive work on equivalent zero-mean adjustments of stress cycles to allow the use of a single S-N curve in fatigue life analysis in the case of variable mean stress loading, as occurs in *Blade.* Dowling suggests the use of the Smith-Watson-Topper method for 6Al-4V

in obtaining zero-mean adjusted values for stress cycles. For an S-N curve that takes the assumed form,

$$\sigma_{ar} = cN_f^m \tag{3.5}$$

The SWT method states that for a non-zero-mean stress cycle, the equivalent zero-mean adjusted stress amplitude of the cycle is,

$$\sigma_{ar} = \sqrt{\sigma_{max}\sigma_a} \tag{3.6}$$

3.3.4 Titanium 6Al-4V S-N Curve

Data for titanium 6Al-4V in the annealed state was obtained from the USAF High Cycle Fatigue program (Gallagher, van Stone, deLaneuville, Gravett, & Bellows, 2001). This set of data (Figure 3.5) is relevant to test conditions where the stress ratio is R=-1 (zero-mean stress cycles) and adjusted to fit the Smith-Watson-Topper regression by (Dowling, 2004).

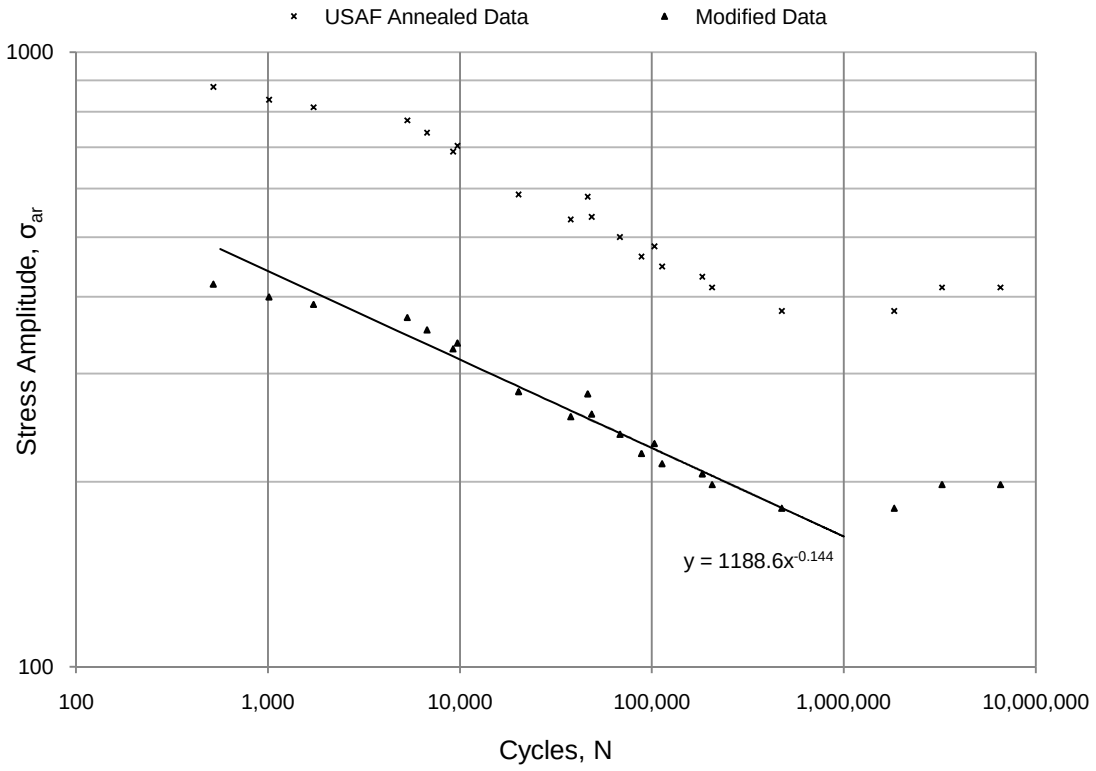

Figure 3.5: S-N curve for annealed 6Al-4V

A regression line has been added to the modified S-N curve (see Section 3.3.5 for modification factor) to determine the equivalent form of Equation (3.5) for the curve. This is the equation used in the post-processing of measured strain data and the prediction of the fatigue life of the blade material. Cycles counted using the rain-flow counting technique were zero-mean adjusted using Equation (3.6) for use in the S-N curve presented.

3.3.5 Endurance Limit Modification

A factor of safety on fatigue data is required due to uncertainties and irregularities that arise in the manufacture and treatment of all engineering materials. (Shigley et al., 1989) suggests the use of endurance limit modifying factors to account for such discrepancies. As a conservative approach to this

fatigue life study, the resulting endurance limit modifying factor has been applied to all S-N curve data as in Figure 3.5. Table 3.1 lists the modifying factors, and the reasons for their selection.

Table 3.1: Endurance limit modification factors

Surface modification factor, k_a	0.7163	Blade material is to be belt sanded to 0.8μm (32Ra)
Size factor, k_b	0.9259	Rectangular cross section, non-rotating bending
Load modification factor, k_c	1	Bending load
Temperature modification factor, k_d	1	No adverse temperature effects
Reliability factor, k_e	0.814	99% required reliability
Stress concentration factor, K_f	1.13	Worst case fatigue stress concentration factor at 900MPa tensile strength (Hosseini, 2012)
Endurance limit modification factor, k	0.4778	$S_e = \underbrace{k_a k_b k_c k_d k_e \frac{1}{K_f}}_{k} S'_e$

3.3.6 Modified Miner's Rule for Stress Condition

It has been suggested (Kang, Jang, Park, Han, & Kim, 2012) that stress cycles below the endurance limit still have some effect on the life of a material. In practice, the modified Miner's rule shows superior agreement over Miner's rule in experimental life testing (Baek et al., 2008) (Kang et al., 2012). This rule involves extrapolating the linear section of the log-log S-N curve below the endurance limit in a collinear direction as in Figure 3.6. Manson's method can then used to determine the damage caused to the material for all stress cycles below the

endurance limit.

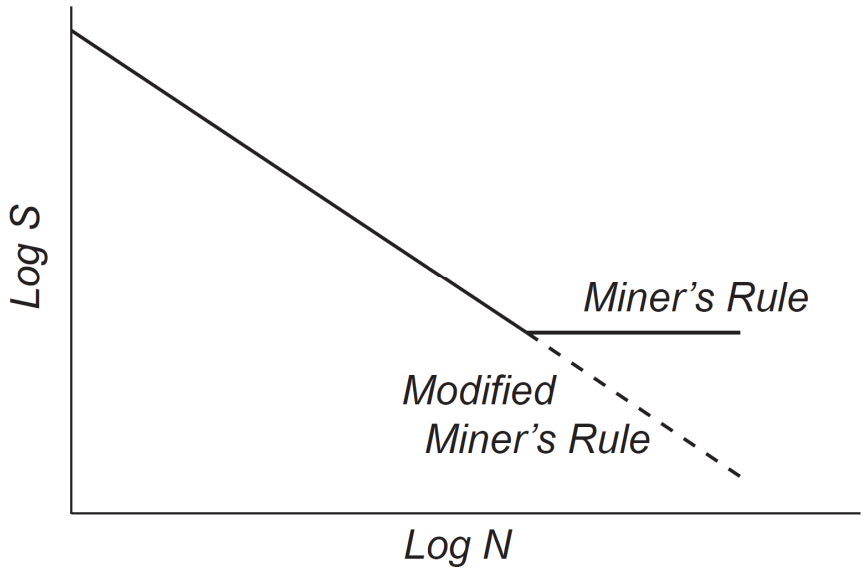

Figure 3.6: Modified Miner's rule used to account for the effect of cyclic stresses with amplitudes below the endurance limit of the material

3.3.7 Manson's Method for Cumulative Damage

Use of the Palmgren-Miner theory can lead to non-conservative life estimates (Kang et al., 2012). Considerations for the effect of cyclic loading on the endurance limit itself and also cyclic loads below the endurance limit are required. Once a virgin material undergoes a stress cycle above its endurance limit, the endurance limit of that material is somewhat reduced (Shigley et al., 1989). This reduction is dependent on the order of the applied stress cycles. Manson's method (Shigley et al., 1989) is used in this study to predict the damage done, if any, to the endurance limit during each stress cycle. The Palmgren-Miner rule assumes that the ultimate tensile strength of a material is damaged to the same extent as the endurance limit. Experiments have failed to confirm this assumption (Manson et al., 1965). Instead, Manson's method assumes an intersection of the S-N curve at $N_0 = 10^3$ cycles and the new S-N

curve after each damaging cycle pivots around this intersection as in Figure 3.7. The intersection point is best found from experimental data.

If a virgin material is subjected to cyclic stress amplitude, σ_i, for a number of cycles, n_i, the damage inflicted in the material is defined as

$$D = \frac{n_i}{N_{f,i}} \tag{3.7}$$

Where $N_{f,i}$ is the number of cycles until failure of the material at stress amplitude σ_i. Calculation of $N_{f,i}$ in the first step of Manson's method with knowledge of the S-N curve is simple. For an S-N curve that obeys the relationship in (3.5), the number of cycles to failure at σ_1 is

$$N_{f,1} = \left(\frac{\sigma_1}{c}\right)^{\frac{1}{m}} \tag{3.8}$$

It is here that Manson's method deviates from the Palmgren-Miner rule. A new gradient of the S-N curve and endurance limit is required for the next calculation if σ_1 is above the endurance limit of the material.

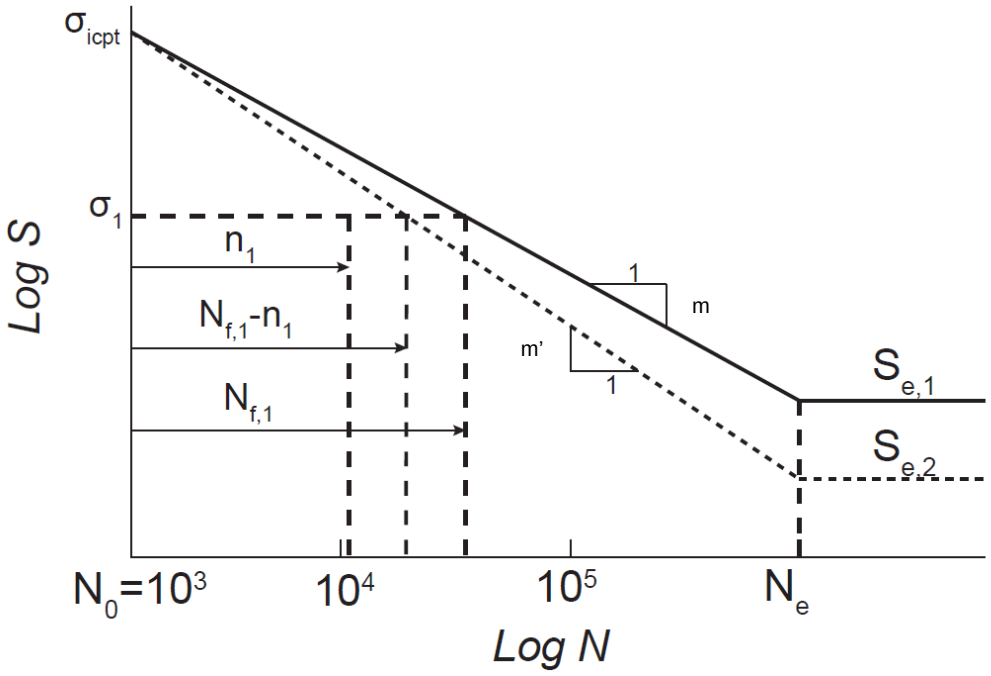

Figure 3.7: Manson's method used to predict the new endurance limit of an overstressed material

The gradient of the new S-N curve (dotted line in Figure 3.1) is defined as

$$m' = \frac{\log(\sigma_1) - \log(\sigma_{icpt})}{\log(N_{f,1} - n_1) - \log(N_0)} \tag{3.9}$$

The new endurance limit for the material is

$$S_{e,2} = \sigma_{icpt} 10^{m'(\log(N_e) - \log(N_0))} \tag{3.10}$$

The gradient *m'* becomes *m* for the next step and now, for a new stress amplitude σ_2, with the material exposed to n_2 cycles, the cycles to failure $N_{f,2}$ is defined as

$$N_{f,2} = N_0 10^{\frac{\log(\sigma_2) - \log(\sigma_{icpt})}{m}} \tag{3.11}$$

If σ_2 is greater than endurance limit $S_{e,2}$ (i.e. a damaging cyclic stress) then the calculation for an additional stress amplitude should begin at (3.9). If σ_2 is less than $S_{e,2}$ then (3.11) can be used to find the cycles to failure of the additional stress amplitude (i.e. the S-N curve is not affected by σ_2).

The total damage inflicted in the material by cyclic stresses σ_1 and σ_2 is

$$D = \frac{n_1}{N_{f,1}} + \frac{n_2}{N_{f,2}} \qquad (3.12)$$

$$If\ D \geq 1\ Failure\ Occurs$$

For the blade material specifically, if D is the damage done to the blade material during a performance, and t is the duration of a performance, then the total time the blade material will last is defined as

$$T = \frac{t}{D} \qquad (3.13)$$

The number of performances the blade material will last based on the loading history of the test rig is defined as

$$P_{f,o} = \frac{T}{t} = \frac{1}{D} \qquad (3.14)$$

The natural frequencies of the blade material also change as a function of the scale of the sculpture (S. D. Gooch, 2001). This has a direct effect on the number of stress cycles occurring in the blade material during each performance. The scaling laws developed by Gooch illustrate how natural frequencies change as the sculpture is scaled by

$$\frac{\omega_o}{\omega_s} = \frac{d_o l_s^2}{d_s l_o^2} \sqrt{\frac{\rho_s E_o}{E_s \rho_o}} \tag{3.15}$$

Therefore, the number of performances the blade material will last in the scaled sculpture is defined as

$$P_{f,s} = P_{f,o} \frac{\omega_o}{\omega_s} \tag{3.16}$$

3.4 Results

3.4.1 Fatigue Life Prediction

Labview was used to measure and process strain data in addition to controlling the test rig electric motor. The ball and wand were installed onto the blade test rig of Chapter 2. The load history was measured in real time during a typical *Blade* performance.

Hooke's law and Equation (2.5) via strainconv.m (Appendix B) was used to convert the strain-time history of the test rig performance into a predicted scaled stress-time history as shown in Figure 3.8. Bladefatiguefinalv3.m (Appendix B) was then used to post process the stress-time history using the theory presented in Section 3.3. An example of the resulting stress cycle history of a *Blade* performance is presented in Figure 3.9. Half cycles were counted by the rain-flow method according to the magnitude of their range. The amplitude and maximum value of each half cycle were recorded and the zero-mean equivalent

stress of the half cycle was calculated using the Smith-Watson-Topper method. Manson's method was then used to determine the damage done during a typical loading block (1 performance in the case of the sculpture).

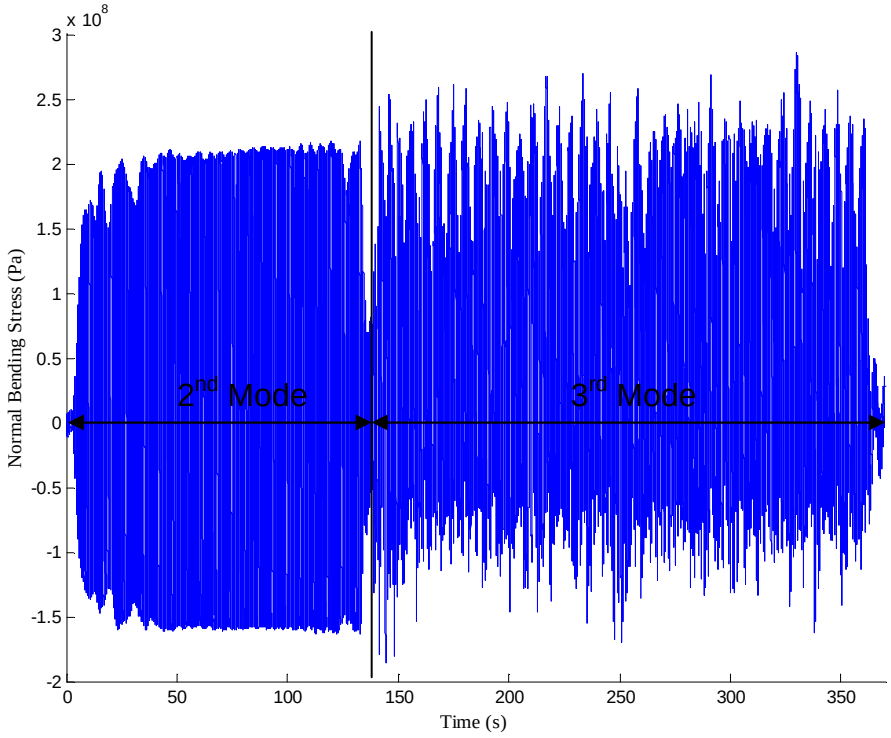

Figure 3.8: Stress-time loading block from a typical Blade performance. This data shows the predicted loading history for a blade free length of 8.424m.

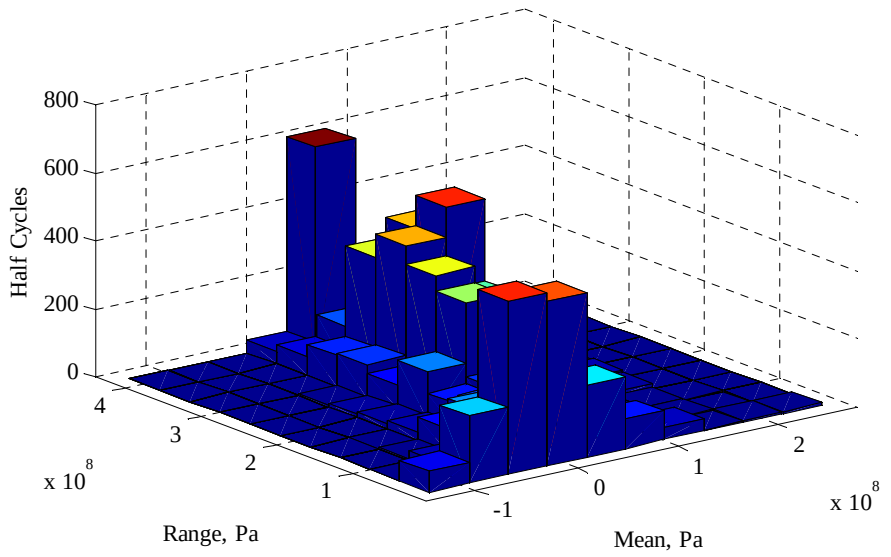

Figure 3.9: Histogram example of the scaled Blade loading history

Ten performances of the test rig were carried out and the load history for each performance was measured. The load history was scaled for various blade material sizes ranging from approximately 5m to 8.5m in free blade length. Fatigue lives were calculated for each of the ten performances according to the free blade length. The mean, standard deviation and the sample coefficient of variation (SCOV) of the ten fatigue lives were calculated for each free blade length and are presented in Table 3.2. For comparison, the sculpture built by Gooch has a scale ratio equal to 2.12.

Table 3.2: Statistical values for fatigue lives calculated at various blade material sizes

Free Blade Length, l_s (m)	Scale Ratio, l_s/l_o	Mean Fatigue Life, $\bar{P}_{f,s}$	Standard Deviation, $SD_{\bar{P}}$	SCOV, $\delta_{\bar{P}}$
8.424	5.17	443	15	3.39%
8.167	5.01	484	16	3.35%
7.905	4.85	532	18	3.34%
7.64	4.69	589	20	3.43%
7.369	4.52	654	22	3.33%
7.094	4.35	730	24	3.34%
6.813	4.18	821	28	3.35%
6.526	4.00	932	31	3.33%
6.232	3.82	1065	35	3.31%
5.932	3.64	1231	41	3.31%
5.624	3.45	1423	48	3.39%
5.307	3.26	1704	56	3.28%
4.980	3.06	2051	66	3.23%

The use of a normal distribution is only accurate for large sample sizes (Dowling, 1993). Dowling suggests the use of one-sided tolerance limits to account for small sample sizes such as this case. The number of performances for the scaled sculpture exceeded *R* percent of the time at a confidence level of *C* is,

$$P_{f,s} = \bar{P}_{f,s} - q_{R,C} SD_{\bar{P}} \tag{3.17}$$

The one-sided tolerance limit factor, $q_{R,C}$, for a reliability level of 99% and a confidence level of 95% is (Dowling, 1993),

$$q_{99,95} = 3.98 \tag{3.18}$$

The fatigue lives of the blade material at various free lengths, with 95% confidence that the lives predicted will be exceeded 99% of the time, are presented in Table 3.3.

Table 3.3: Predicted fatigue lives of the scaled sculpture at various blade material free lengths

Free Blade Length, l_s (m)	Total Blade Material Length (m)	Blade Thickness (mm)	Performances to Fatigue Failure, $P_{f,s}$	Cost Per Performance Chinese Supplier ($NZD)	Cost Per Performance US Supplier ($NZD)
8.424	10.024[1]	22	384	$163.91	N/A
8.167	9.718	21	420	$134.44	N/A
7.905	9.407	20	462	$109.07	N/A
7.64	9.091	19	509	$87.83	N/A
7.369	8.769[2]	18	567	$69.50	$118.93
7.094	8.441	17	633	$54.48	$93.23
6.813	8.107	16	712	$42.05	$71.95
6.526	7.766	15	809	$31.83	$54.47
6.232	7.416	14	925	$23.70	$40.56
5.932	7.059	13	1069	$17.25	$29.52
5.624	6.692	12	1231	$12.43	$21.27
5.307	6.315	11	1482	$8.43	$14.42
4.980	5.926	10	1789	$5.59	$9.56

1. Maximum blade material size available in China
2. Maximum blade material size available in the United States

Figure 13 shows the various predicted fatigue lives of blade material for increasing scale ratio of the sculpture. Figure 13 also shows the price per

performance of each scale of blade material based solely on the price of titanium per kilogram at the time of this study.

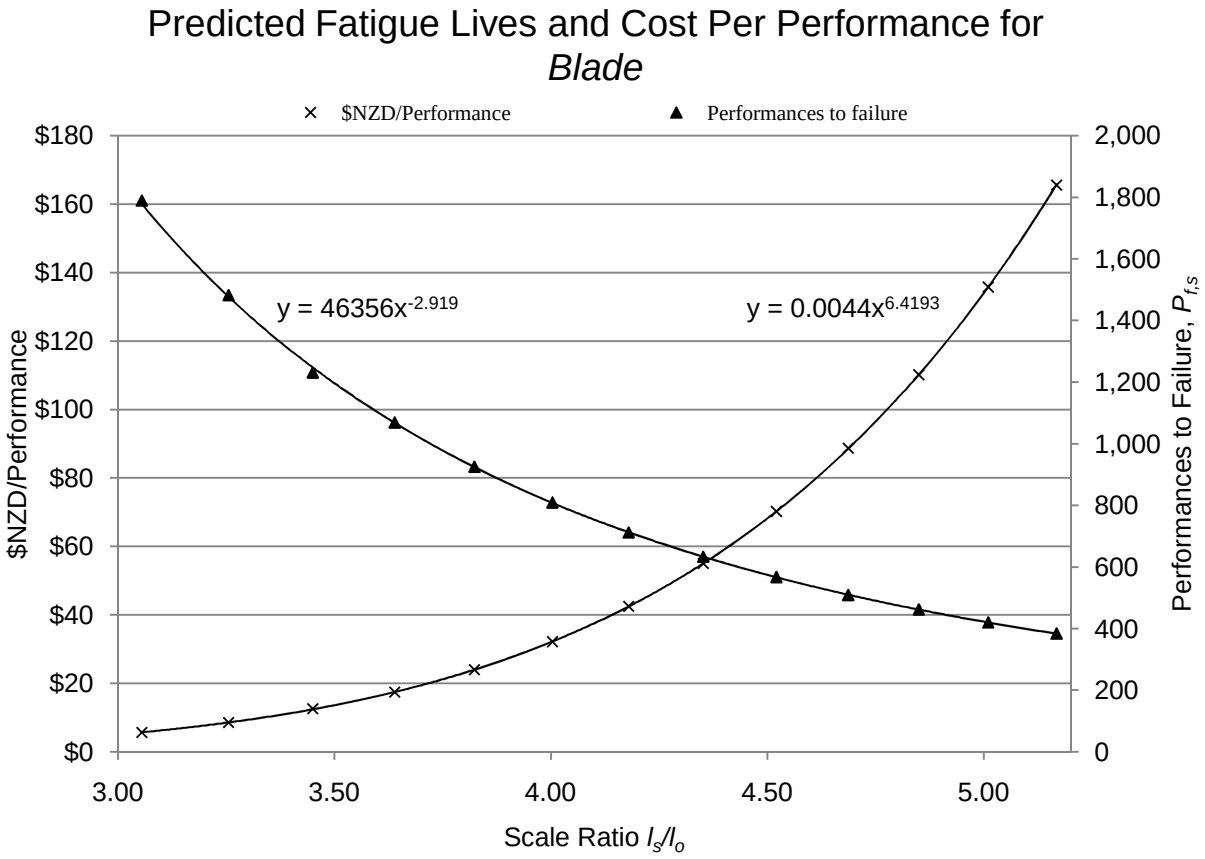

Figure 3.10: Trends for the predicted fatigue lives and cost per performance for increasing size of the scaled sculpture (based on price of titanium in China).

3.5 Discussion

3.5.1 Statistical Results

The sample coefficient of variation is a measure of the uncertainty in the values of $P_{f,s}$ (Dowling, 1993). The SCOV remains around a value of 3.3% for all free lengths of the blade material. This suggests that the consistency of the sculpture performances in the sample data is high i.e. the loading history experienced by the blade material during a performance is sufficiently repeatable.

This result gives additional confidence to the one-sided tolerance limit lives presented in Table 3.3.

The one-sided tolerance limit lives account for the small sample size for fatigue life calculations. Each life predicted is three standard deviations below the mean life predicted to give a predicted fatigue life with 95% confidence of 99% reliability for the blade material. The results in Table 3.3 suggest that, at the appropriate blade free length, the predicted fatigue lives of the blade material presented will be exceeded 99% of the time.

3.5.2 Maximum Scale

Several factors must be taken into account to determine a maximum possible scale for the *Blade* sculpture. A combination of material availability and a target price per performance will determine the practicality of building the maximum economic scale of *Blade*. The largest length of titanium material available at the correct thickness is 10024mm as mentioned in Section 3.2. This would correspond to a free length for *Blade* of 8424mm as determined in Equation (3.3). At this size of blade material the cost per performance to the Len Lye Foundation in 165NZD. Compare this to the target cost per performance for Gooch's *Blade* of less than 500NZD per performance (in 1996) (S. D. Gooch, 2001). This would suggest that building *Blade* using the largest piece of titanium currently available is certainly practical in terms of the fatigue life of the blade material.

The maximum theoretical economic scale of *Blade* can be determined if

manufacturing limitations are ignored. The equation for the cost per performance trend in Figure 3.10 closely follows a power relationship of the form

$$C_P = 0.0044\left(\frac{l_s}{l_o}\right)^{6.4193} \tag{3.19}$$

Using Lye's artistic target of a 9m blade free length, extrapolating the data using Equation (3.19) gives a cost per performance of approximately 255NZD. Therefore, based on the results of this fatigue life study, it is apparent that Lye's grand vision of a 9m *Blade* is a theoretical possibility.

3.5.3 Increasing the Fatigue Life of the Blade Material

A large number of post manufacture heat treatments exist for the titanium 6Al-4V alloy. Generally, the material is supplied in the mill annealed form where the optimum combination of strength and fatigue properties is obtained. Further heat treatments result in a trade-off of one of these properties in the material (Boyer & Collings, 1993). Solution treating and aging the alloy will increase the endurance limit of the alloy along with its ultimate tensile strength at the expense of damage tolerance properties i.e. the alloy becomes brittle through the age hardening process. A re-crystallization anneal will improve damage tolerance properties at the expense of material strength. The re-crystallization anneal has surpassed beta annealing in industry for fracture critical airframe components which would suggest this heat treatment would be an ideal option for the blade material, should an increase in fatigue resistance properties be desired.

However, it would be prudent to investigate the effects of wind loading and

any other unforeseen circumstances using a mill annealed blade for a new scaled sculpture before deciding on the usefulness of a further heat treatment. The loading measured in the test rig scales to significantly less than the yield strength of a mill annealed material. However, if any unforeseen loading was experienced by the blade material in a larger sculpture, the re-crystallization annealed item would have a lower material strength to sustain the loading. A mill annealed blade would have comparable properties to that of the material used in the S-N curve data source for this study and is, therefore, a sufficient heat treatment for the scaled sculpture using the largest piece of material available.

3.6 Conclusions

A test rig was built at the scale of the original *Blade* prototype and the loading history of a typical performance was measured at the critical stress location in the blade material using strain gages. Fatigue lives were predicted for various scale ratios of the sculpture.

The maximum economic scale ratio of Blade is 5.17:1, the scale which corresponds to a blade free length of 8.424m. The Len Lye Foundation can be 95% confident that the sculpture will have a 99% reliability of lasting 384 performances. This corresponds to a cost per performance of 165NZD.

The maximum theoretical economic scale ratio of Blade is 5.52:1, the scale which corresponds to a blade free length of 9m. This is the artistic scale of Blade which Len Lye intended. The cost per performance is predicted to be 255NZD.

The mill annealed heat treatment will be sufficient for the sculpture to be built to the maximum economic scale ratio.

4 Predicted Natural Frequencies of Giant Blade

4.1 Introduction

The purpose of this chapter is to confirm that the relevant vibratory modes for Blade are maintained in the modification of clamp design from a cantilever type clamp to the pivoting clamp concept.

The natural vibratory mode shapes that occur in a material when it is excited at the correct frequency are a phenomenon that Lye utilised in many of his sculptures. Without this interesting and tangible facet of physics, many of Lye's sculptures would not have been physically possible. *Blade* utilises the second and third beam bending mode of the long strip that is the blade in the sculpture to provide the dynamics desired for a *Blade* performance.

Gooch (S. D. Gooch, 2001) studied the vibratory behaviour of both the blade material as a uniform beam/plate and the ball/wand combination as a uniform beam with an end mass. Gooch also developed a model for the dynamic interaction of the two systems in a gravity field. In this chapter, the natural frequencies of the scaled sculpture will be calculated for the largest economic size of titanium available using basic Euler-Bernoulli vibration theory. An FEA model will be developed in Solidworks and this will be used to verify the

mathematical results and experimental observations using an eigenfrequency study. The results of this investigation can be used to tune the control system of the scaled sculpture.

4.2 Lateral Natural Frequencies of Simply Supported Beam with Overhang

A key element of the *Blade* performance is the shapes that the blade material forms due to base excitation. These shapes are summarised in Figure 4.1. In changing the clamp arrangement to that of a pivoting clamp configuration from the original cantilever configuration there is a need for confirmation that the shapes formed during a *Blade* performance are preserved. The bending mode shapes and natural frequencies can be determined using Euler-Bernoulli beam theory.

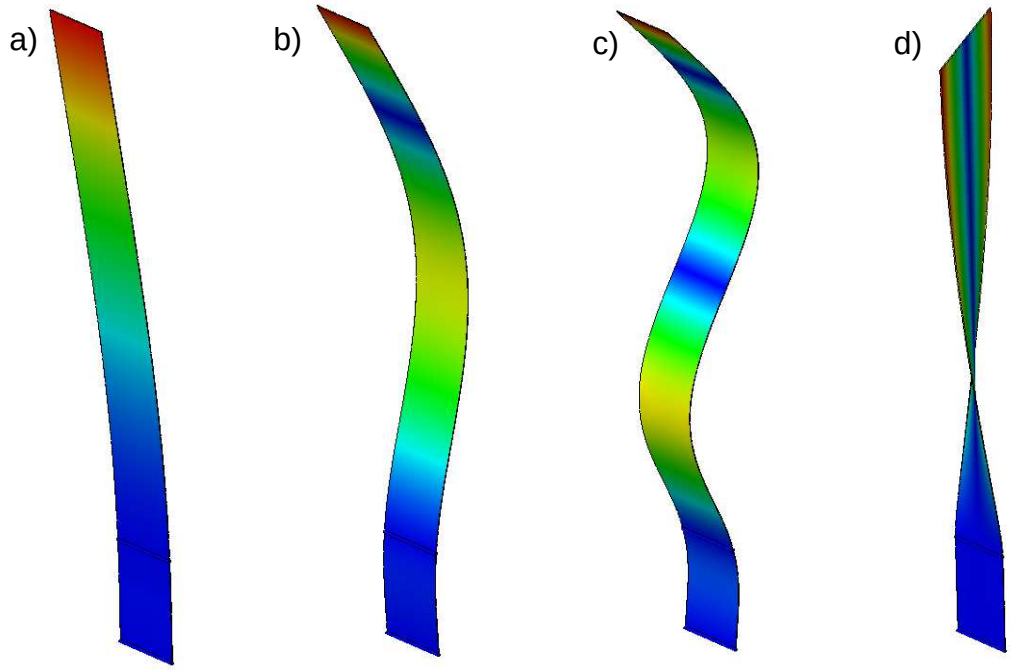

Figure 4.1: FEA results from Solidworks for a) First bending mode, b) second bending mode (Lye's single harmonic), c) third bending mode (Lye's double harmonic), d) torsional plate mode

4.2.1 Mathematical Solution

The solution for the natural frequencies of the free vibration of the beam in Figure 4.2 excluding gravitational effects is as follows (McCallion, 1973).

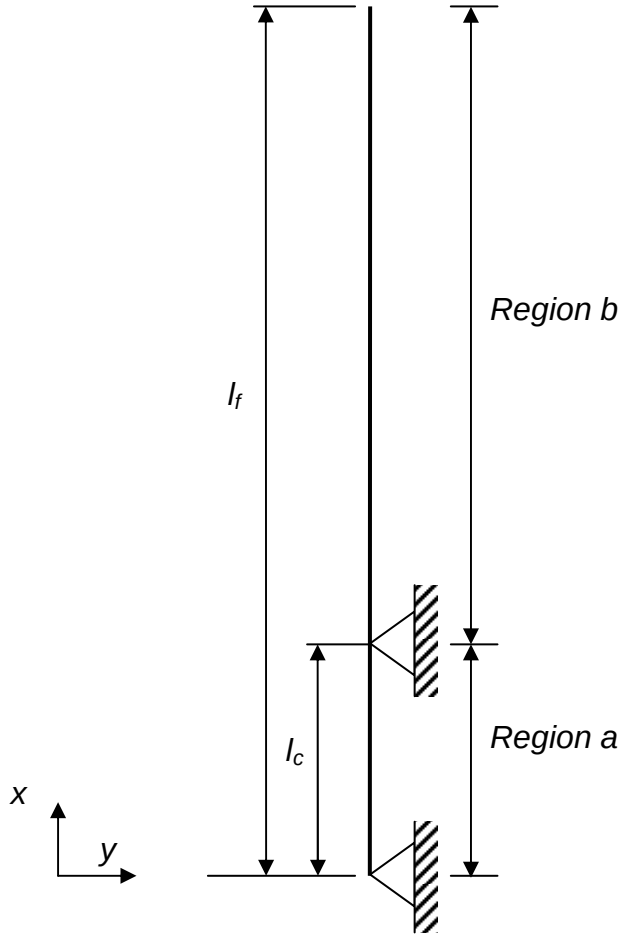

Figure 4.2: Schematic of the pivoting clamp as in the proposed Blade sculpture

Figure 4.2 shows the simplified schematic of the pivoting clamp configuration to be utilised in the scaled sculpture. Two simple supports are separated by a distance l_c, and the combined length of both beam regions is l_f. Assume the beam in Figure 4.2 is undergoing planar deflection. It is also assumed the beam follows Euler-Bernoulli beam behaviour, that is, the neutral fibre is only deflected and the orthogonal cross sections to the neutral fibre

remain orthogonal during deflection. For an infinitesimally small element the free body diagram is illustrated in Figure 4.3.

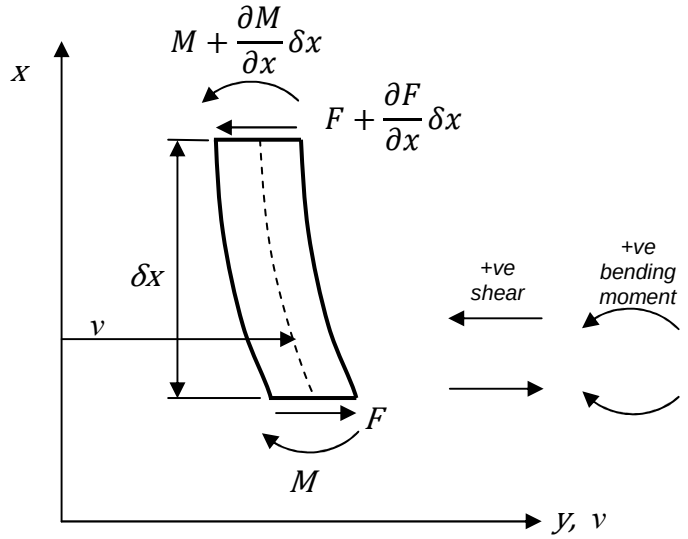

Figure 4.3: Free body diagram and sign conventions for a beam element of the beam in Figure 4.2

For motion in the y direction, the sum of forces is,

$$-F + F + \frac{\delta F}{\delta x}\delta x = \rho A \delta x \frac{\delta^2 v}{\delta t^2} \tag{4.1}$$

Rearranging gives,

$$\frac{\delta F}{\delta x} = \rho A \frac{\delta^2 v}{\delta t^2} \tag{4.2}$$

For motion in the rotational direction, the sum of moments is,

$$-M + M + \frac{\delta M}{\delta x}\delta x + F\delta x = 0 \tag{4.3}$$

Rearranging gives,

$$F = -\frac{\delta M}{\delta x} \tag{4.4}$$

Substituting the result of Equation (4.4) into equation (4.2) gives,

$$\frac{\delta^2 M}{\delta x^2} + \rho A \frac{\delta^2 v}{\delta t^2} = 0 \tag{4.5}$$

Euler-Bernoulli beam theory states that the bending moment at any point in an Euler-Bernoulli beam is proportional to the radius of curvature of the beam at that point by the relationship,

$$M = EI \frac{\delta^2 v}{\delta x^2} \tag{4.6}$$

Substituting Equation (4.6) into Equation (4.5) gives,

$$EI \frac{\delta^4 v}{\delta x^4} + \rho A \frac{\delta^2 v}{\delta t^2} = 0 \tag{4.7}$$

It is well known that the solution to Equation (4.7) consists of the wave motion solution in the space and time domain,

$$v(x,t) = \sum_n V_n(x)\{A_n sin\omega_n t + B_n cos\omega_n t\} \tag{4.8}$$

Substituting Equation (4.8) into (4.7) gives,

$$\frac{\delta^4 V_n}{\delta x^4} + \frac{\rho A \omega_n^2}{EI} V_n = 0 \tag{4.9}$$

The general solution to (4.9) is well known as the following,

$$V_n = C_{1n} sin\lambda_n x + C_{2n} cos\lambda_n x + C_{3n} sinh\lambda_n x + C_{4n} cosh\lambda_n x \tag{4.10}$$

Where,

$$\lambda_n^4 = \frac{\rho A \omega_n^2}{EI} \tag{4.11}$$

These equations hold true for a uniform beam where the normal mode, V_n, is continuous along with its three derivatives. The subscript *n* denotes the

relevant mode of vibration. For a beam such as in Figure 4.2, where a discontinuity exists at the second pinned joint, the beam needs to be treated as two separate beams to determine the combined mode shapes of each beam. The mode shape for each beam region is described by the expression in Equation (4.10). The coefficients, C_{in}, will differ for each beam while the λ_n results will remain common between the two beam sections. For the section of the beam where $0 \leq x \leq l_c$ the equation for the mode shapes formed is,

$$V_{n,a} = C_{1n,a}sinh\lambda_n x + C_{2n,a}cosh\lambda_n x + C_{3n,a}sin\lambda_n x + C_{4n,a}cos\lambda_n x \tag{4.12}$$

Similarly for the section where $l_c \leq x \leq l_f$ the equation for the modes shapes formed is,

$$V_{n,b} = C_{1n,b}sinh\lambda_n x + C_{2n,b}cosh\lambda_n x + C_{3n,b}sin\lambda_n x + C_{4n,b}cos\lambda_n x \tag{4.13}$$

Boundary and continuity conditions are required to form the series of equations from which the frequency equation can be obtained, and hence the values of λ_n determined. The boundary conditions for the beam section *a* are as follows,

$$V_{n,a}(0) = 0 \tag{4.14}$$

$$\frac{d^2V_{n,a}(0)}{dx_a^2} = 0 \tag{4.15}$$

Similarly, the boundary conditions for section *b* are,

$$V_{n,b}(l_c) = 0 \tag{4.16}$$

$$\frac{d^2V_{n,b}(l_f)}{dx_b^2} = 0 \tag{4.17}$$

$$\frac{d^3V_{n,b}(l_f)}{dx_b^3} = 0 \tag{4.18}$$

The continuity conditions that are common to both beam sections are,

$$V_{n,a}(l_c) = V_{n,b}(l_c) \tag{4.19}$$

$$\frac{dV_{n,a}(l_c)}{dx_a} = \frac{dV_{n,b}(l_c)}{dx_b} \tag{4.20}$$

$$\frac{d^2V_{n,a}(l_c)}{dx_a^2} = \frac{d^2V_{n,b}(l_c)}{dx_b^2} \tag{4.21}$$

Substituting Equations (4.16) to (4.18) into Equations (4.12) and (4.13) results in the following series of equations,

$$C_{1n,a} + C_{3n,a} = 0 \tag{4.22}$$

$$C_{1n,a} - C_{3n,a} = 0 \tag{4.23}$$

$$C_{1n,b}cosh\lambda_n l_c + C_{2n,b}sinh\lambda_n l_c + C_{3n,b}cos\lambda_n l_c + C_{4n,b}sin\lambda_n l_c = 0 \tag{4.24}$$

$$C_{1n,b}cosh\lambda_n l_f + C_{2n,b}sinh\lambda_n l_f - C_{3n,b}cos\lambda_n l_f - C_{4n,b}sin\lambda_n l_f = 0 \tag{4.25}$$

$$C_{1n,b}sinh\lambda_n l_f + C_{2n,b}coshh\lambda_n l_f + C_{3n,b}sin\lambda_n l_f - C_{4n,b}cos\lambda_n l_f = 0 \tag{4.26}$$

$$C_{1n,a}sinh\lambda_n l_c + C_{2n,a}cosh\lambda_n l_c - C_{3n,a}sin\lambda_n l_c + C_{4n,a}cos\lambda_n l_c = C_{1n,b}sinh\lambda_n l_f + C_{2n,b}cosh\lambda_n l_f - C_{3n,b}sin\lambda_n l_f + C_{4n,b}cos\lambda_n l_f \tag{4.27}$$

$$C_{1n,a}cosh\lambda_n l_c + C_{2n,a}sinh\lambda_n l_c - C_{3n,a}cos\lambda_n l_c - C_{4n,a}sin\lambda_n l_c = C_{1n,b}cosh\lambda_n l_f + C_{2n,b}sinh\lambda_n l_f - C_{3n,b}cos\lambda_n l_f + C_{4n,b}sin\lambda_n l_f \tag{4.28}$$

$$\begin{aligned} &C_{1n,a}cosh\lambda_n l_c + C_{2n,a}sinh\lambda_n l_c + C_{3n,a}cos\lambda_n l_c + C_{4n,a}sin\lambda_n l_c \\ &\quad + C_{1n,b}cosh\lambda_n l_f + C_{2n,b}sinh\lambda_n l_f \\ &\quad + C_{3n,b}cos\lambda_n l_f + C_{4n,b}sin\lambda_n l_f = 0 \end{aligned} \tag{4.29}$$

This series of equations can be presented in the form of a matrix equation,

$$YC = 0 \tag{4.30}$$

For this relationship to hold true, the matrix *Y* must be singular and the frequency equation for the vibrating beam in Figure 4.2 is,

$$\begin{aligned} det(Y) = \Big(&(-4cosh(\lambda_n l_c)^2 - 4cos(\lambda_n l_c)^2) sin\big(\lambda_n l_f\big) \\ &+ \big(4cos(\lambda_n l_c) sin(\lambda_n l_c) \\ &- 4cosh(\lambda_n l_c) sinh(\lambda_n l_c)\big) cos\big(\lambda_n l_f\big)\Big) sinh\big(\lambda_n l_f\big) \\ &+ \big(4cosh(\lambda_n l_c) sinh(\lambda_n l_c) \\ &- 4cos(\lambda_n l_c) sin(\lambda_n l_c)\big) cosh\big(\lambda_n l_f\big) sin\big(\lambda_n l_f\big) \\ &+ (4cosh(\lambda_n l_c)^2 \\ &- 4cos(\lambda_n l_c)^2) cos\big(\lambda_n l_f\big) cosh\big(\lambda_n l_f\big) \\ &+ 8sin(\lambda_n l_c) sinh(\lambda_n l_c) = 0 \end{aligned} \tag{4.31}$$

The first three roots (λ_n) of this equation are relevant to the *Blade* performance. These roots were found to be 1.09, 2.74 and 4.62 respectively for the first, second and third lateral bending modes (Procedure B6 Appendix B). Substituting these values into Equation (4.11), and using the appropriate properties for the carbon steel test blade, the lateral natural frequencies (converted to Hertz from radians per second) were found to be 0.51Hz, 3.22Hz and 9.16Hz.

4.2.2 Finite Element Analysis

Solidworks Simulation 2012 was used to verify the natural frequencies that

were obtained analytically. The carbon steel test blade was modelled in Solidworks 2012, with appropriate geometry to simulate the simple supports where required.

The pivots were constrained as fixed hinges and a 1N force applied to the top edge of the blade material to provide the required physics for an eigenfrequency analysis. The mesh was refined until a convergence of 1% between consecutive results was achieved. The relevant natural frequencies were found to be 0.52Hz, 3.29Hz and 9.29Hz.

4.2.3 Experimental Observations

As mentioned in Chapter 2, the *Blade* test rig built at the University of Canterbury has the capability of measuring the frequency of oscillation of the shuttling clamp. Observations of the clamp shuttle frequencies required to excite vibratory modes of the blade material were made during the testing of Chapter 2. At the optimal pivot separation of 300mm the clamp shuttle frequencies to excite first, second and third modes respectively were observed to be 0.25Hz, 3.30Hz and 9.43Hz.

4.3 Discussion

Table 4.1 summarises the values obtained for the natural frequencies of the carbon steel test blade.

Table 4.1: Results of the bending mode natural frequencies (Hz) of the blade material at the test rig scale ratio

	First	Second	Third
Mathematical Solution (excluding gravity)	0.51	3.22	9.16
Finite Element Analysis (excluding gravitational effects)	0.52	3.29	9.29
Finite Element Analysis (*including* gravitational effects)	0.20	3.09	9.08
Experimental Observations	0.25	3.30	9.43

4.3.1 Error Analysis

The discrepancy between the theoretical solutions and the experimental observations can be attributed to the non-linear jump phenomenon (softening spring effect Figure 2.13) that occurs when increasing shuttle oscillation frequency from below the blade material natural frequency (S. D. Gooch, 2001). In the *Blade* test rig, it was necessary to avoid this phenomenon by entering the blade material natural frequencies from above rather than below to ensure stable blade motion and repeatable measurements. This resulted in a slightly higher measured shuttle frequency than the actual natural frequency of the blade material for each of the second and third bending modes. Aerodynamic damping will also play a part in the variance between calculated and experimental values.

Internal friction and body force damping can account for the discrepancies between the calculated values with and without gravitational effects. Increased body forces due to self weight decrease the stiffness of the vertical blade material as a whole and result in a reduced natural frequency for all bending modes.

4.3.2 Bending Modes

It is clear that the implementation of a pivoting clamp configuration does not adversely affect the spectrum of natural lateral bending frequencies for the blade material compared with the original cantilever clamp arrangement. Compare the natural frequencies calculated above to Lye's original prototype with tuned frequencies of 3.34Hz for the second mode and 9.95Hz for the third mode (Figure 1.6). The variation is small and will not require any remedial attention in the design of the *Giant Blade* mechanism to account for any unforeseen effects of using a pivoting clamp configuration in the scaled sculpture.

Knowledge of the natural frequencies of the blade material in the test rig using a pivoting clamp configuration allows prediction of the natural frequencies of the blade material in *Giant Blade*. Scaling laws developed by Gooch (S. D. Gooch, 2001) are also relevant for natural frequency,

$$\frac{\omega_o}{\omega_s} = \frac{d_o l_s^2}{d_s l_o^2} \sqrt{\frac{\rho_s E_o}{E_s \rho_o}} \tag{4.32}$$

Using the experimental observations in Equation (4.32), the required shuttle frequencies for the second and third mode respectively in *Giant Blade* are 1.42Hz, and 4.06Hz. These values have been validated using Solidworks Simulation using the same method as in Section 4.2.2, only changing the geometry to that of the largest scale of blade material possible as a result of Chapter 3. The results of the FEA simulation including gravitational effects for the second and third bending modes respectively are 1.42Hz and 4.17Hz.

4.3.3 Torsional Modes

Critical aspects of a Blade performance are the ‘kissing’ and ‘shimmering’ acts that occur before each relevant bending mode occurs in the blade material (Figure 1.10). These acts are designed to build suspense for the observer with delicate interaction of the blade and wand that builds into heavy complete interaction as the shuttle frequency is increased. The ‘kissing’ act is achieved simply by setting the clamp shuttle frequency just below the frequency required to excite the second bending mode of vibration. This causes the blade material to appear as though it is very nearly exciting the second bending mode and results in the aforementioned delicate blade/wand interaction. The ‘shimmering’ act, however, is a result of the first torsional mode existing very close to the third bending mode in the frequency spectrum of the blade material. This mode is not theoretically excited due to the design of the shuttling mechanism. However, out of balance mechanism forces do excite this mode in reality (S. D. Gooch, 2001) and it is a desirable part of the artistic performance. Equation (4.32) is applicable to scaling the lateral bending modes but is not appropriate to use in scaling the torsional vibration mode. Verification that the torsional mode is maintained in using a pivoting clamp was achieved using Solidworks Simulation. At the *Original Blade* size, the first torsional mode was found to be 9.19Hz. At the maximum possible scale, the first torsional mode was found to be 3.97Hz. It can be seen that for the *Original Blade* the torsional mode lies above the third bending mode (9.08Hz) and for *Giant Blade* the torsional mode lies below the third bending mode (4.17Hz). This has implications for the design of the control system. The *Giant Blade* control system should ramp to the shuttle oscillation

frequency required for the ‘shimmering’ act and then continue ramping to the third bending mode frequency and slowly step down to slightly above the third bending mode frequency to avoid the non-linear jump phenomenon as in Figure 2.13. If a sculpture was to be built at the *Original Blade* scale with a pivoting clamp, then the control system should increase the shuttle oscillation frequency to above the third bending mode frequency to achieve the shimmering dynamics and then slowly ramp down to the third bending mode frequency to excite Lye’s double harmonic.

4.4 Conclusions

The shuttle oscillation frequencies for the Original Blade scale do not change significantly with the implementation of a pivoting clamp. The torsional mode required to excite the ‘shimmering’ section of the performance in Giant Blade does shift from being above the third bending mode of vibration in the Original Blade to below in Giant Blade. Therefore, the control system in the scaled sculpture should take the form of the program for Big Blade with appropriate changes to account for the change in location of the torsional mode of vibration that gives the ‘shimmering’ section of a Blade performance. Tuned frequencies can be obtained from this point by trial performances.

5 Variable Stroke Mechanism

5.1 Introduction

The purpose of this chapter is to present a functional design for a variable stroke mechanism to be implemented in Giant Blade to drive the clamp shuttle.

Basic vibration theory states that for a case of base excitation the amplitude of the input vibration displacement is directly proportional to the amplitude of the output displacement via a transfer function (Palm, 2007). The critical failure mode for the *Blade* sculpture is fatigue of the blade material at the clamp exit due to high reversed bending stresses. The stresses at the clamp exit are a function of the radius of curvature and, therefore, the amplitude of vibration of the blade material i.e. the larger the amplitude of vibration, the smaller the bending radius and hence the higher the bending stress in the blade material. Chapter 3 was concerned with accurately predicting a fatigue life for the blade material based on stresses scaled from measurements of the *Blade* test rig. A requirement of the final sculpture mechanism design is a system that allows reduction of vibratory amplitude in the blade material should measured stresses be higher than predicted. The reduction in amplitude is most useful in the third bending mode due to the stress resulting from the small bending radius in the blade material at the clamp exit when the third mode is combined with the 'swinging' phenomenon (S. D. Gooch, 2001) as in Figure 5.1.

a) 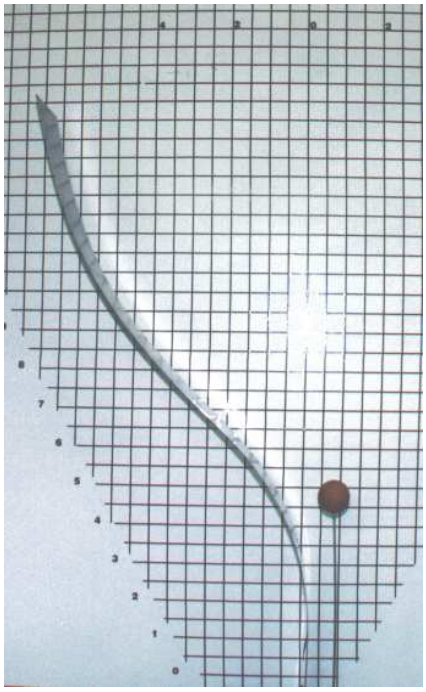 b) 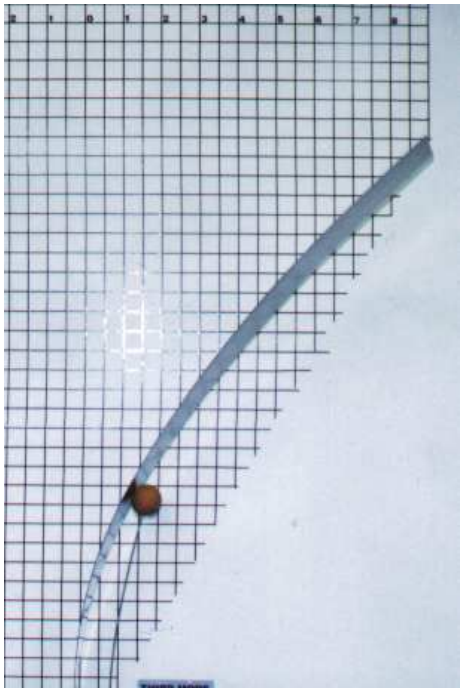

Figure 5.1: a) Swinging phenomenon observed at the third bending mode frequency, b) swinging dominating the third bending mode shape [from (S. D. Gooch, 2001)]

A mechanism is therefore required to remotely reduce the amplitude of vibration between the second mode and the third mode during a *Blade* performance. Current designs for variable stroke mechanisms will be researched and a suitable mechanism will be selected using the principle solution evaluation method of (Pahl & Beitz, 1996).

5.2 Known Variable Stroke Mechanisms

Dynamically adjustable variable stroke mechanisms have been an avenue of research in the automotive industry for decades. Variable compression ratio engines use variable stroke mechanisms to dynamically adjust the compression ratio of an engine to ensure fuel efficiency across a wider range of engine revolutions. Variable stroke mechanisms also have a significant role to play in

paper manufacturing as will be discussed in Section 5.2.3.

5.2.1 Generic Early Variable Stroke Engine (4-Link Mechanism)

The Autocar Handbook (1919) provides a schematic for a variable stroke engine presented in Figure 5.2.

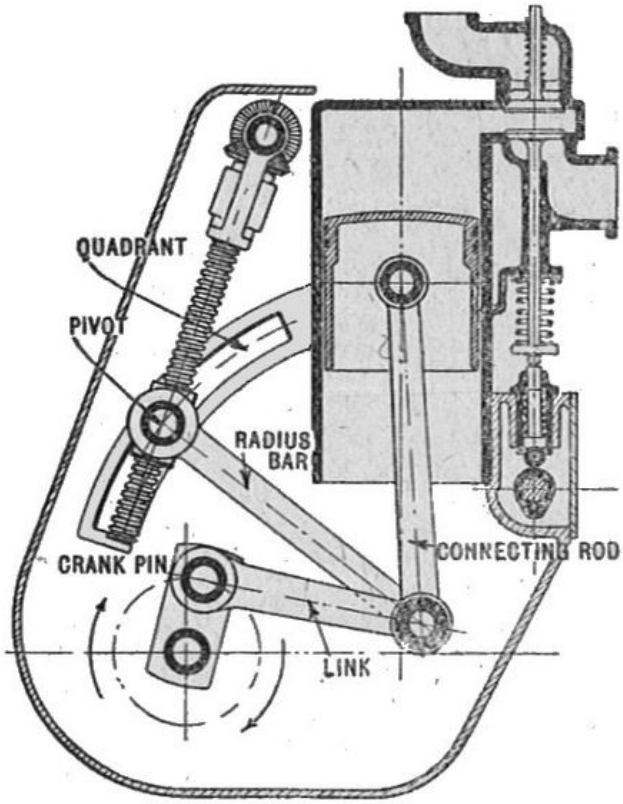

Figure 5.2: Early arrangement for a variable stroke combustion engine [Retrieved from http://commons.wikimedia.org/wiki/File:Variable_stroke_engine_(Autocar_Handbook,_Ninth_edition).jpg

The mechanism used in this engine concept consists of a traditional crankshaft, three connecting rods and a bevel gear actuated lead screw that is used to adjust the stroke the piston experiences in the cylinder. The lead screw effectively adjusts the location of where the three connecting rods meet through the radius bar as indicated in Figure 5.2. In researching this mechanism, the

author could not reproduce any instances where this mechanism had been implemented in a working combustion engine. Therefore, this mechanism will be classed as conceptual only in this study. This mechanism is a candidate for the Giant Blade oscillation mechanism due to the simplicity of manufacture and apparent resistance to high shock impact loading as seen in an internal combustion engine. Figure 5.3 shows the Solidworks model developed to simulate the motion of this mechanism for this comparison study.

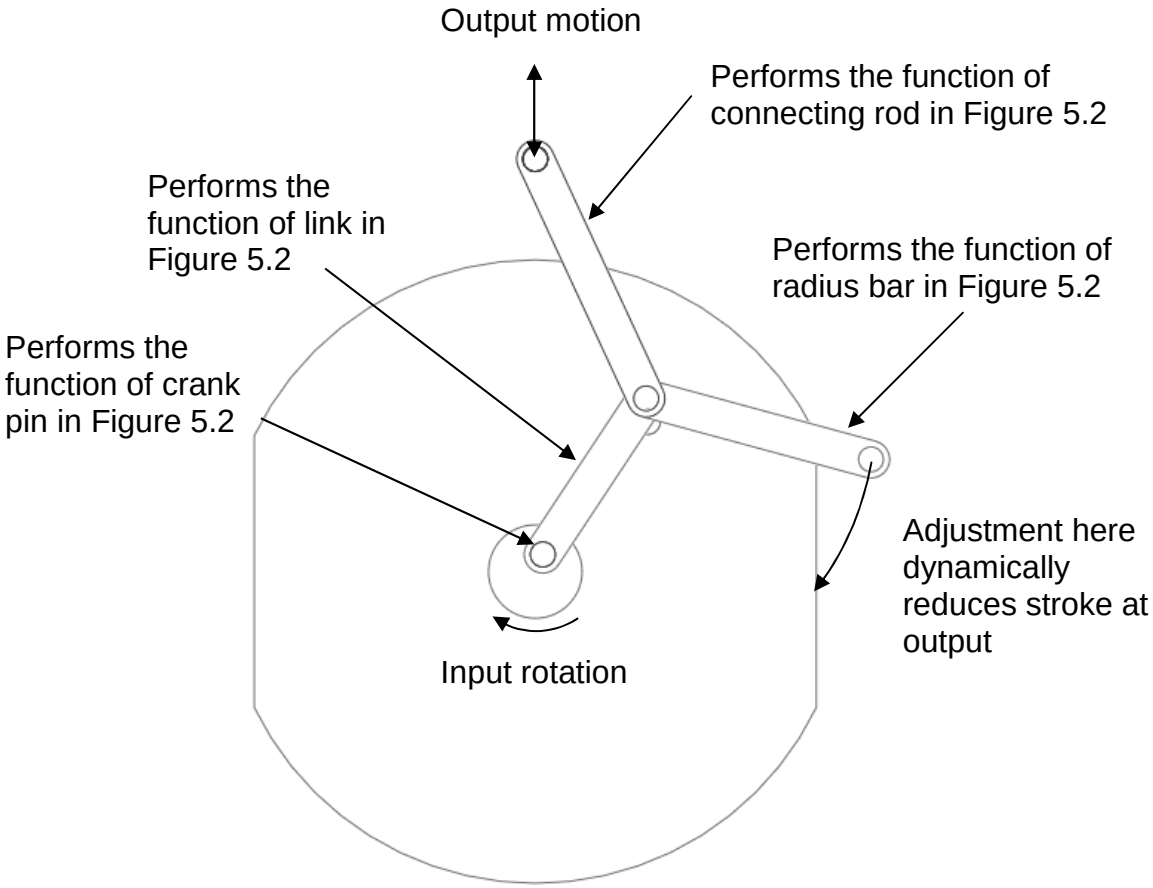

Figure 5.3: Solidworks model of the mechanism developed to assess the suitability of the 4-link mechanism

5.2.2 Nissan Variable Stroke Engine Mechanism (3-Link Mechanism)

Nissan (see Article C1 Appendix C) has developed a prototype variable

compression ratio (VCR) engine capable of increasing fuel efficiency for a non-turbocharged engine and increasing power in a turbocharged engine. The design reduces 2nd order vibrations that are usually mitigated by a balanced crank shaft by allowing the piston displacement to resemble simple harmonic motion i.e. acceleration extremes of the piston are distributed more evenly. Figure 5.4 shows the layout of the Nissan VCR engine. The control shaft is rotated by an actuator which is driven by engine revolutions. The C-link is connected to the control shaft via an eccentric journal bearing. As the control shaft rotates, the eccentric journal bearing causes the L-link to change position and hence adjust the stroke of the piston similarly to the generic variable stroke mechanism outlined in Section 5.2.1.

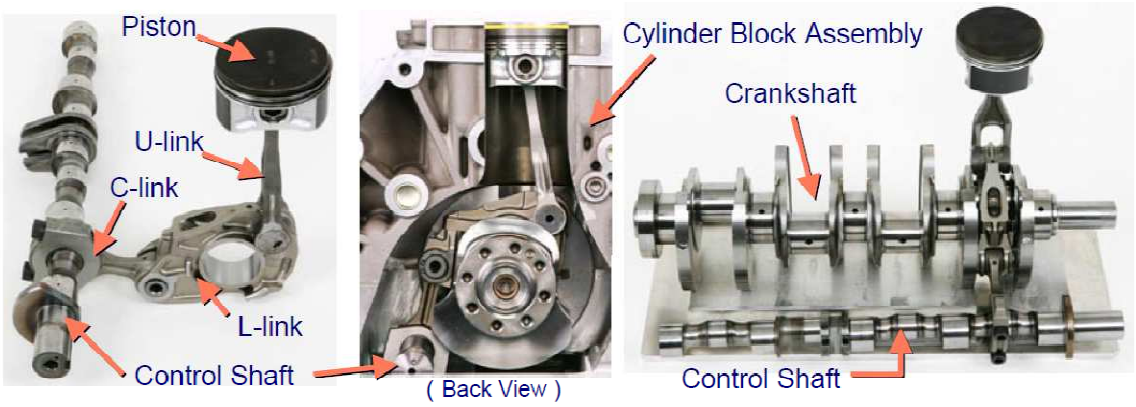

Figure 5.4: Nissan's variable compression ratio engine

Figure 5.5 presents the Solidworks model developed for this comparison study to simulate the dynamics and forces involved in the 3-link mechanism.

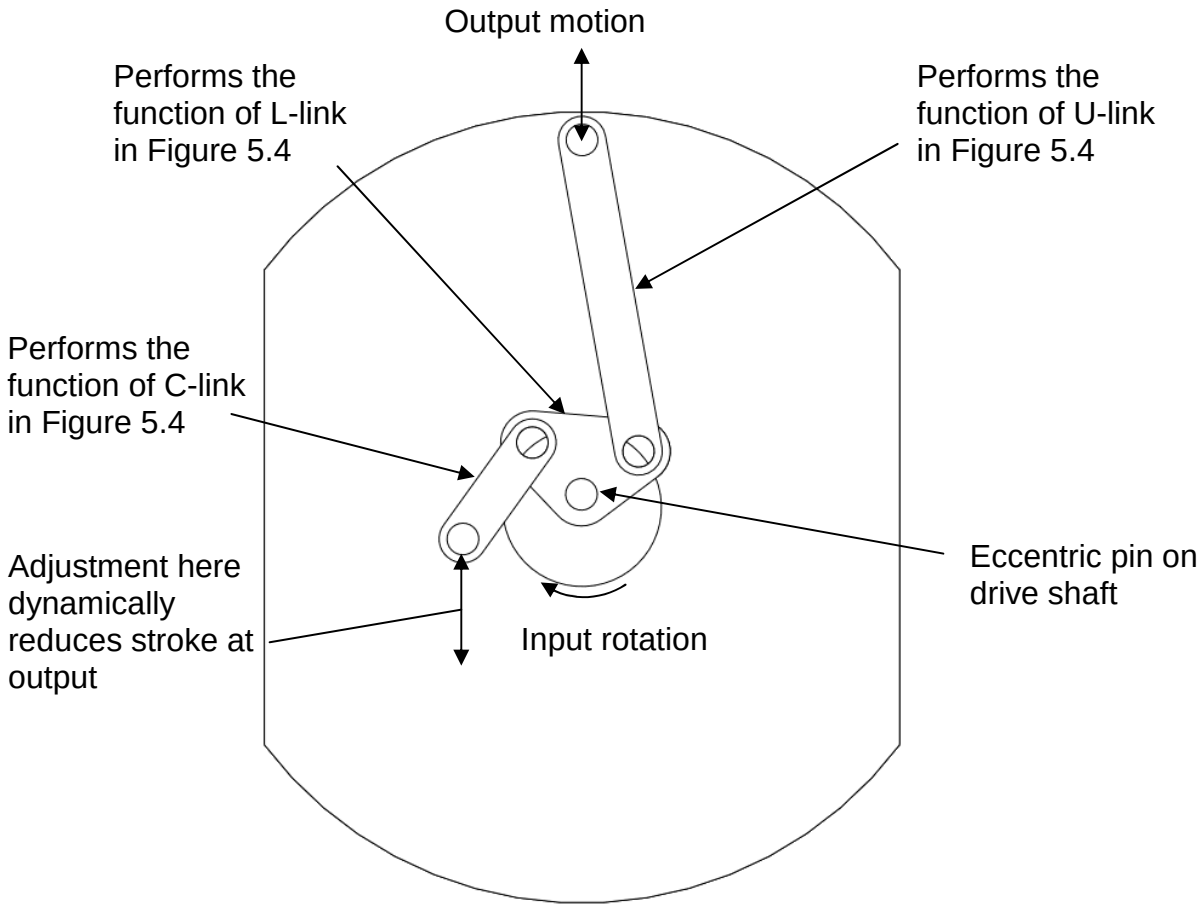

Figure 5.5: Solidworks model of the mechanism developed to assess the suitability of the 3-link mechanism

5.2.3 Variable Stroke Shaker Mechanism for Paper Making Machines (Fourdrinier Mechanism)

A patent search was carried out by the author. This search revealed a mechanism used to shake the fourdrinier table in a paper manufacturing line. Originally these tables were actuated using a fixed-displacement crank with an adjustable toggle to provide the required oscillating motion. There are various disadvantages of this mechanism for paper manufacture, namely:

- The motion deviates from simple harmonic at large displacements
- The mechanism cannot be run at zero stroke
- At smaller displacements the output frequency tends towards twice the input frequency

These undesirable aspects of the original design result in a reduced service life of the fourdrinier table components. Therefore, the mechanism presented in Figure 5.6 was developed to overcome these drawbacks.

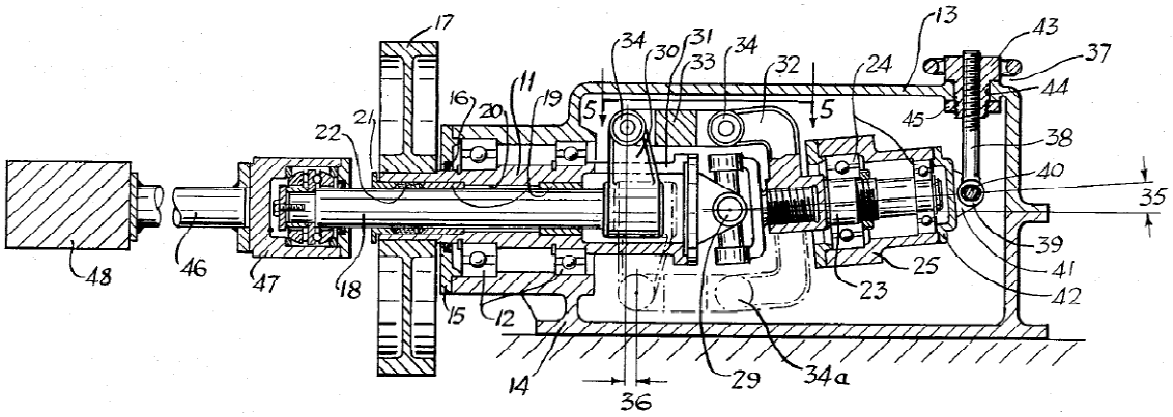

Figure 5.6: Variable stroke mechanism for paper making machines

In short, the linear displacement at 48 is adjusted by actuation of the shaft 38. Rotational motion is applied at input shaft 11 through the input pulley 17. This rotational motion is converted to linear motion of output shaft 18 through the series of linkages made up by 30, 32, and 33. The linkages are asymmetric whenever the adjusting system is outside of its neutral position. This asymmetry causes the linear motion of shaft 18 as the input shaft 11 rotates. For a more in-depth explanation of these workings, please see the patent C2 regarding this mechanism in Appendix C.

5.2.4 Variable Stroke Design from Ingenious Mechanisms for Designers and Engineers (Dovetail Slide)

A useful source of information, published as a series of four volumes, Ingenious Mechanisms for Designers and Engineers presents conceptual mechanism for various purposes. The chapter on variable stroke reciprocating mechanisms provides many novel and elegant solutions to the problem of converting rotational to linear motion with varying displacement. The most appropriate solution for the scaled sculpture from this source is presented in Figure 5.7.

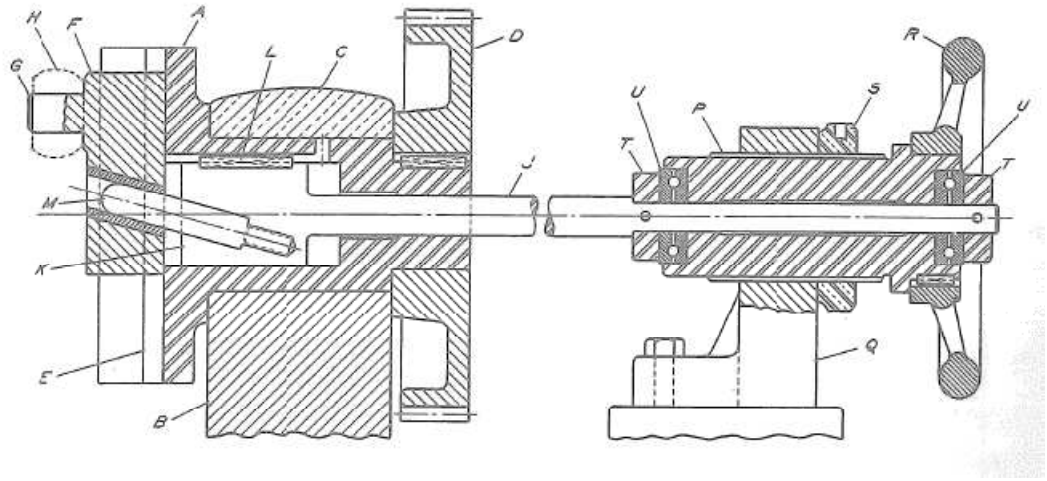

Figure 5.7: Revolving the hand wheel R adjusts the eccentricity of pin G

Rotational motion is applied to pulley D. Housing Q supports the housing P in a threaded hole. Lock nut S is loosened and the hand wheel R is used to adjust the shaft J left or right (as oriented in Figure 5.7) inside the housing A. The angled pin M consequently moves left or right and causes dovetail slide M to move up or down as in Figure 5.7. Pin G is therefore offset from the centre of rotation depending on adjustment. Pin G is connected to a crank that provides reciprocating motion through a crank slider arrangement. The amplitude of

displacement of this crank slider arrangement being controlled by the workings explained above and equal to the offset of pin G from the centre of rotation of pulley D. This mechanism has the advantage of the potential to be manufactured with a high level of strength to withstand the shock loading that will exist in *Giant Blade*.

5.3 Evaluating Principle Solution Variants

To select an appropriate variable stroke mechanism for the scaled sculpture, a quantitative comparison of the mechanism candidates is required. Pahl and Beitz (Pahl & Beitz, 1996) recommend the following method for evaluating solution variants for a particular application.

5.3.1 Evaluation Criteria

Standard technical and economical evaluation criteria apply to this study such as:

- Production – can the mechanism be made using readily available machining processes and tools
- Proven Design – Has the design been manufactured previously and used successfully or is it simply conceptual?

There are also characteristics of the *Blade* shuttling mechanisms that dictate requirements of the variable stroke mechanism in *Giant Blade*.

- Simple Harmonic Motion – do the dynamics of the mechanism result in a simple harmonic oscillation of the driven component.
- Strength – What are the forces, stresses, motor torque requirements in each of the components?
- Stroke Centre – In dynamically adjusting the amplitude of displacement in the mechanism, does the centre of this stroke shift significantly?
- Compactness – As specified in Table 6.1, the variable stroke mechanism should be as low profile as possible to meet the requirements of the mechanism as a whole.
- Retrofit – How easily can the mechanism be reverted back to a simple crank slider mechanism if there are unforeseen issues with the design?

5.3.2 Weighting the Criteria

Due to the fact some of the above requirements are critical to the functioning of the scaled sculpture mechanism as a whole, weighting factors will be introduced to the evaluation criteria here. Each evaluation criteria will be assigned a value ranging from the following scale:

1. Inconsequential
2. Moderate
3. Critical

This scale can be interpreted as:

1. Being of minimal importance to the functioning of the sculpture mechanism as a whole
2. Can be considered somewhat desirable in the function of the sculpture, but not critical.
3. Being of the utmost importance to the proper function of the sculpture.

5.3.3 Comparing Concept Variants

The mechanisms summarised in Section 5.2 will be scored based on how they meet the various criteria outlined in Section 5.3.1. The scoring values will be based on the following scale:

1. Significantly worse compared to datum
2. Moderately worse compared to datum
3. Equal in performance to datum mechanism
4. Moderately better compared to datum
5. Significantly better compared to datum

The dovetail slide mechanism has been selected as the datum for the comparison study – the three alternative mechanisms can perform better or worse than this mechanism in the evaluation criteria. Many of the evaluation criteria in Section 5.3.1 can be scored and commented on without in-depth analysis using standard engineering theory and experience. However, other criteria such as strength, stroke centre, and simple harmonic motion will require some analysis to make an educated scoring decision. For these criteria, the

capabilities of Solidworks Motion will be utilised. Each mechanism for comparison was modelled as a working structure in Solidworks by utilising the Motion Study Mates that allow the user to define pivoting joints as theoretical bushes. This allowed analysis of the dynamics and forces of each structure for a fixed oscillating mass. This mass was equal to the mass of the shuttle designed in Chapter 6 to give realistic dynamic conditions in this study.

To achieve a score for a particular criterion of evaluation, the weightings stated in Section 5.3.2 applicable to the criterion in question are multiplied by the score achieved by the mechanism for that criterion. The overall score for a mechanism is the sum of these products for all criteria of the particular mechanism being assessed. Each criterion will now be discussed in terms of how the mechanisms compare with each other.

Production

The linkages and the connections of the 3-link and 4-link mechanisms can be manufactured using standard procedures and tools. The connection points could be made using a combination of spherical roller and deep groove ball bearings and would allow elimination of play in the mechanism. The dovetail slide mechanism does not perform well in this area. Machining the dovetail to ensure that there is no play would be a challenge. Adjustment of stroke for the 3-link and 4-link mechanisms can be achieved by actuating the relevant link along the path of the black arrows show in Figure 5.3 and Figure 5.5 respectively. The 3-link mechanism would require a linear actuator with a shaft that is supported to protect the actuator form side loading. The 4-link mechanism would only require

a linear actuator to be mounted in the normal simply supported manner due to the system being pin jointed. This allows forces to be transmitted to the actuator in only tension and compression. The fourdrinier mechanism is the most complicated in terms of production of all the variable stroke mechanisms. The implementation of a fourdrinier mechanism would best suit a slewing ring base rotation mechanism rather than the chosen tapered roller arrangement of Chapter 6. Slewing rings are expensive when manufactured with the clearances required to reduce noise caused by the vibration transmitted from the blade material. Therefore, the fourdrinier mechanism performs equally with the dovetail slide in terms of production.

Proven Design

The 3-link mechanism was implemented into an experimental Nissan variable compression ratio engine with promising results of more evenly distributed piston accelerations, lower vibration, increased power and efficiency. Durability was not mentioned in the publication. The 4-link mechanism was sourced as a concept design for a variable stroke engine in a dated automotive handbook. Both mechanisms work on the same principle of adjusting stroke but achieve the results with subtly different methods. Therefore, the 4-link mechanism is expected to function without unforeseen design issues. The 4-link mechanism does contain a weak point in where the links meet in a 3 high link stack as in Figure 6.3. The dovetail slide mechanism performs poorly in this comparison. The mechanism was found in a dated publication and an example of its use in industry could not be found. There was also no evidence that the fourdrinier mechanism ever made its way into production on paper making

machines.

Simple Harmonic Motion

Trial and error simulations were carried out on both the 4-link and 3-link mechanism to optimise the dimensions of the links to give motion agreeing with SHM as closely as possible across the entire stroke range. This optimisation gave motion of the oscillating mass very close to simple harmonic motion (Figure 5.8 to Figure 5.11). The maximum oscillation stroke for each mechanism was set at 60mm as found in Section 2.2 Appendix D. The minimum oscillation stroke for the link mechanisms was set at approximately 2/3 of the maximum oscillation stroke. The final minimum stroke was dependent on a reasonable value at which SHM was still achieved. Since the dovetail slide solution is effectively a simple crank slider mechanism, this option would only require the crank connecting the drive shaft and shuttle to be sufficiently long to achieve SHM (Den Hartog, 1956). The fourdrinier mechanism has also been designed to provide SHM motion to the oscillating output.

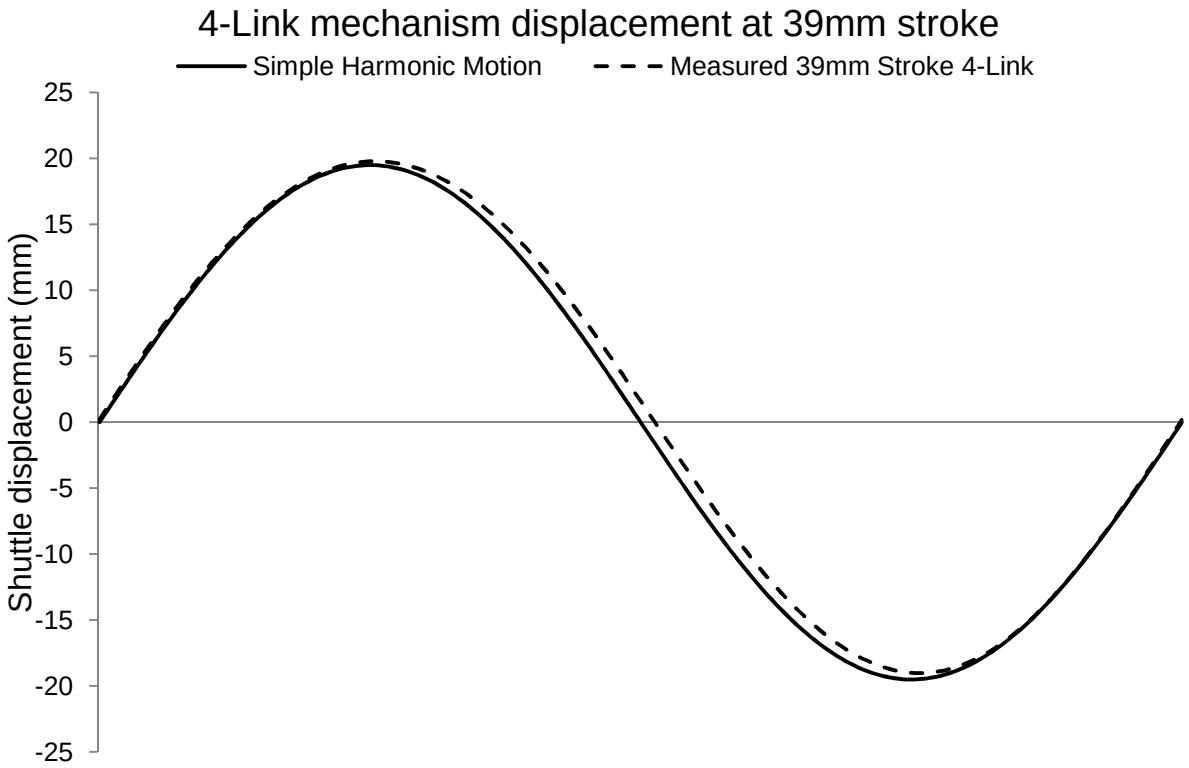

Figure 5.8: Displacement trace of the 4-link mechanism at 39mm stroke compared to the ideal case of simple harmonic motion

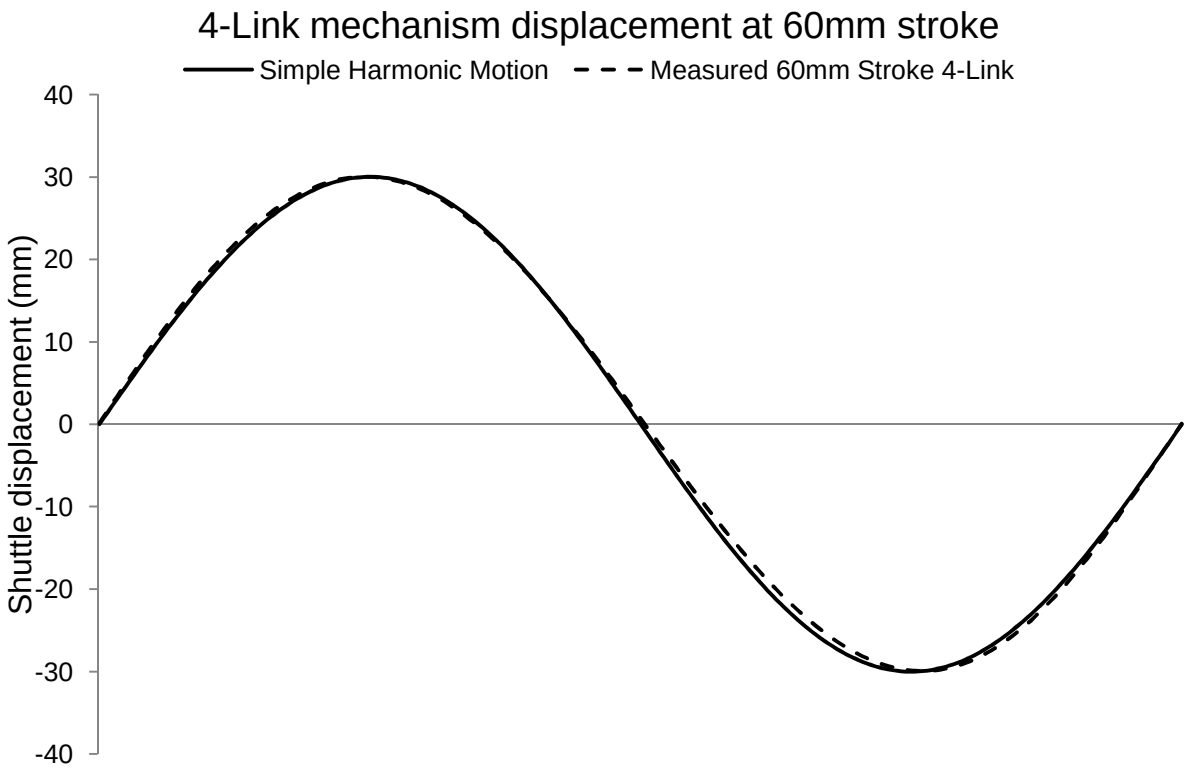

Figure 5.9: Displacement trace of the 4-link mechanism at 60mm stroke compared to the ideal case of simple harmonic motion

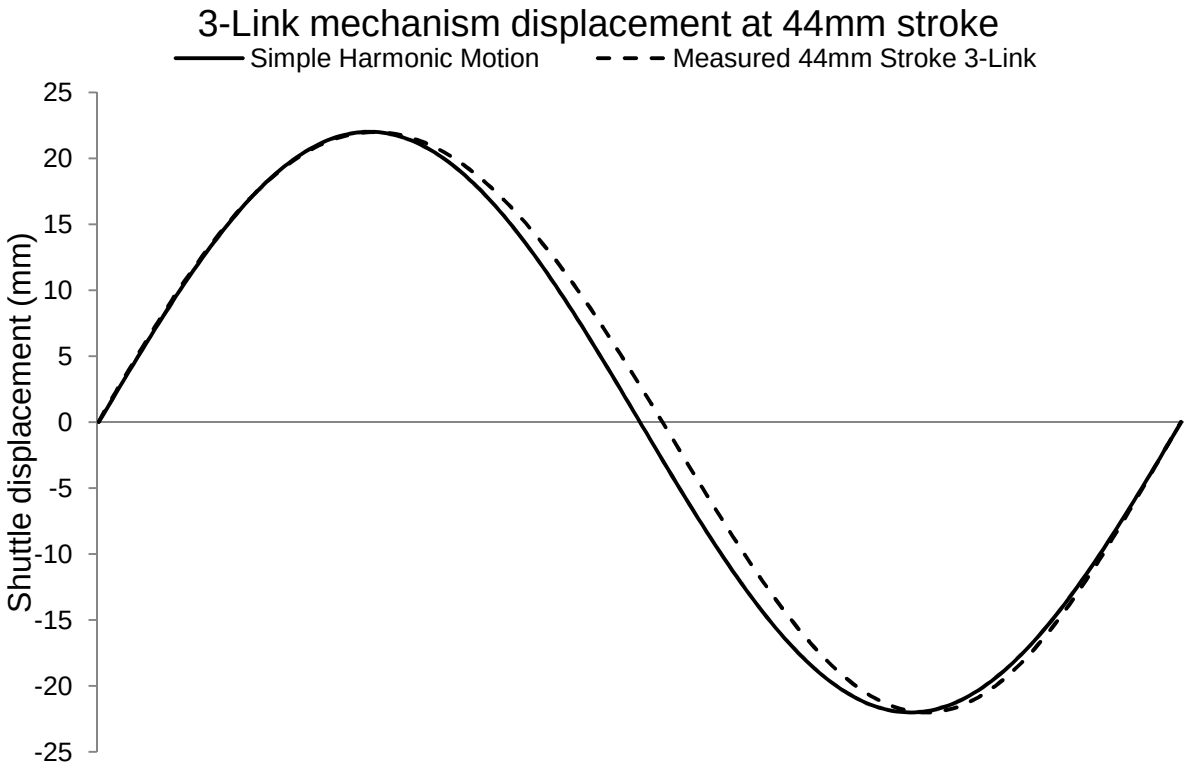

Figure 5.10: Displacement trace of the 3-link mechanism at 44mm stroke compared to the ideal case of simple harmonic motion

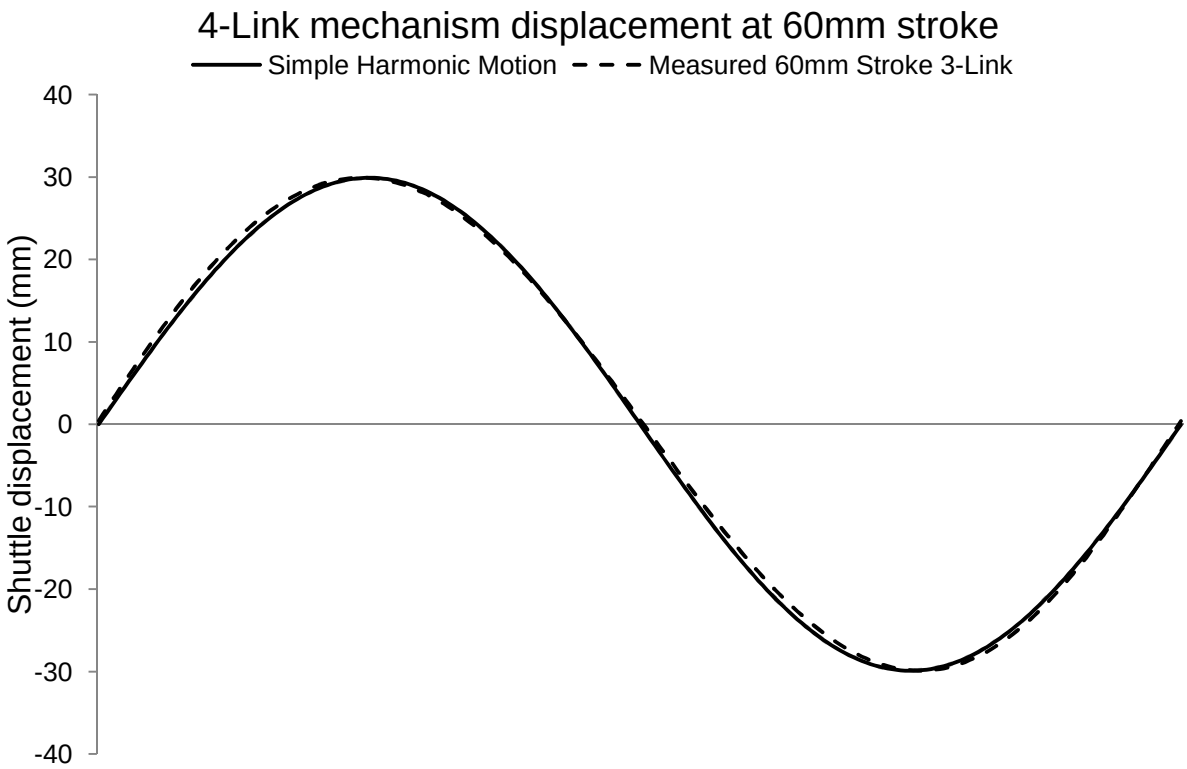

Figure 5.11: Displacement trace of the 3-link mechanism at 44mm stroke compared to the ideal case of simple harmonic motion

Strength

Reaction forces, motor torques and stresses were calculated for each mechanism in order to compare strength characteristics and optimise dimensions. Calculations for the dovetail slide showed that the pin in the sliding shaft would see high levels of bending stress due to the unsupported length of the pin at the minimum stroke location of adjustment (see Figure 5.12).

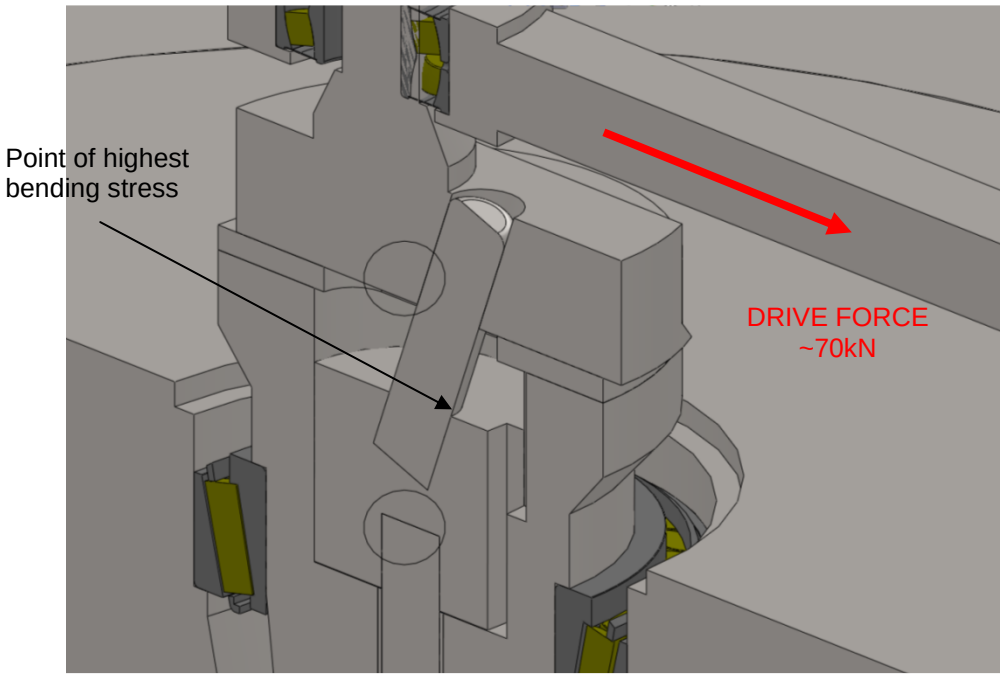

Figure 5.12: Point of highest bending stress at minimum stroke in the dovetail slide variable stroke mechanism

The fourdrinier mechanism is designed for light loads that are experienced by the fourdrinier tables used in paper manufacture. These components could be designed and selected to withstand the shock loading in a *Blade* sculpture but the cost would be prohibitive. Reaction forces and motor torques for the 3-link and 4-link mechanisms were obtained from Solidworks Motion. Figure 5.13 and Figure 5.14 show the reaction forces measured in each mechanism and their locations.

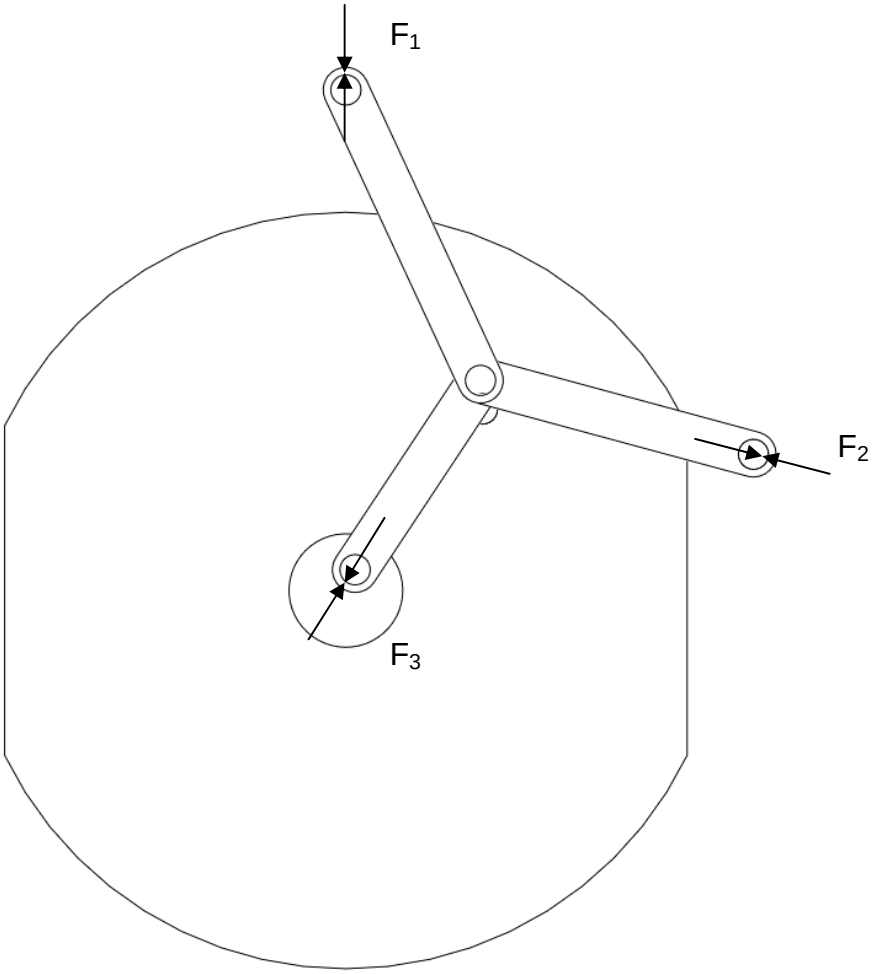

Figure 5.13: Forces measured in the 4-link variable stroke mechanism

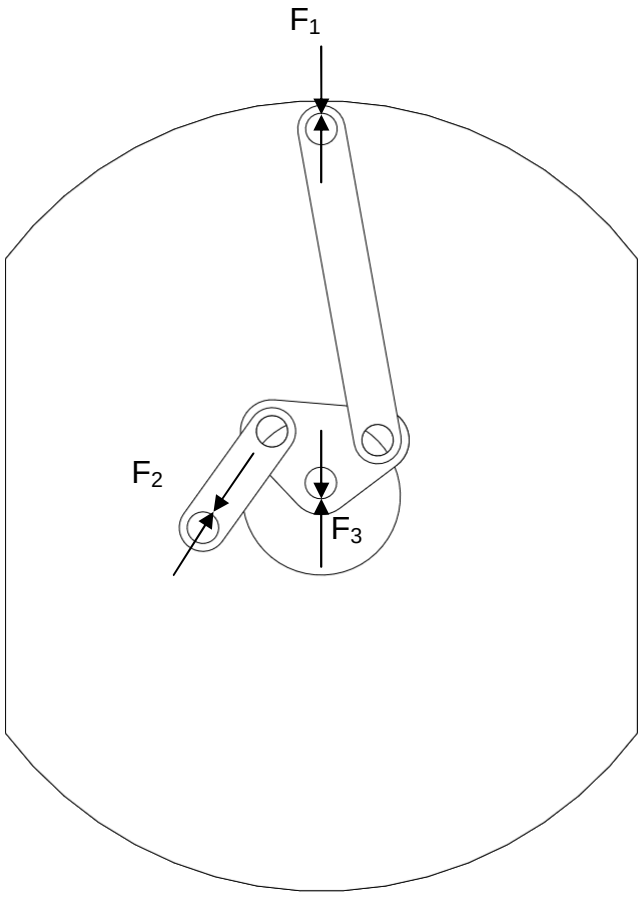

Figure 5.14: Forces measured in the 3-link variable stroke mechanism

Table 5.1 and Table 5.2 summarise the results of the Solidworks Motion studies.

Table 5.1: Reaction forces measured using Solidworks for 4-link variable stroke mechanism

	F1 (kN)	**F2** (kN)	**F3** (kN)	**Motor Torque** (Nm)
60mm	64	75	75	1094
39mm	41	38	31	422

Table 5.2: Reaction forces measured using Solidworks for 3-link variable stroke mechanism

	F1 (kN)	**F2** (kN)	**F3** (kN)	**Motor Torque** (Nm)
60mm	64	69	118	1106
44mm	51	28	77	593

The 3-link mechanism can be seen to perform poorly in the strength category. The force on the drive pin is larger by a factor of approximately 2 compared to the inertial force transmitted to the mechanism by the oscillating mass. The motor torque requirements for the 4-link mechanism are less than for the 3-link mechanism at the minimum stroke displacement. A lower motor torque requirement will reduce manufacturing cost of the scaled sculpture mechanism.

Stroke Centre

The shift in stroke centre refers to the distance that the centre of oscillation of the shuttle moves along the axis of oscillation when adjusting between the minimum and maximum strokes. The dovetail slide mechanism does not cause a shift in stroke centre and therefore performs optimally for this category as does the fourdrinier mechanism. The 3-link inherently requires a shift in stroke centre due to its geometry. The shifts in stroke centre for the optimised mechanism was found to be approximately 49mm. The 4-link mechanism geometry allowed optimisation to a point where no shift in stroke centre was evident providing performance equal to the dovetail and fourdrinier mechanisms.

Clearly the 4-link mechanism is superior to the 3-link mechanism in this

comparison. The change in stroke centre requires a longer length of track for linear bearings hence the 3-link variable stroke solution would result in a more expensive mechanism for *Giant Blade*. A mechanism to adjust the location of the ball and wand relative to the blade material may also be required, further increasing cost. A shift in stroke centre may be desirable in reducing reversed bending stresses in the blade material if it is used to move the blade material away from the ball and wand in the third mode. For the purposes of this study, the stroke shift will remain as a disadvantage unless further information comes to light.

Compactness

Compactness refers to the circular area of footprint that the mechanism will require. It is assumed that the maximum distance from driveshaft centre to the furthermost extremity of the mechanism (not including the shuttle attachment point) will define the radius of the circular footprint of the mechanism (see Figure 5.15).

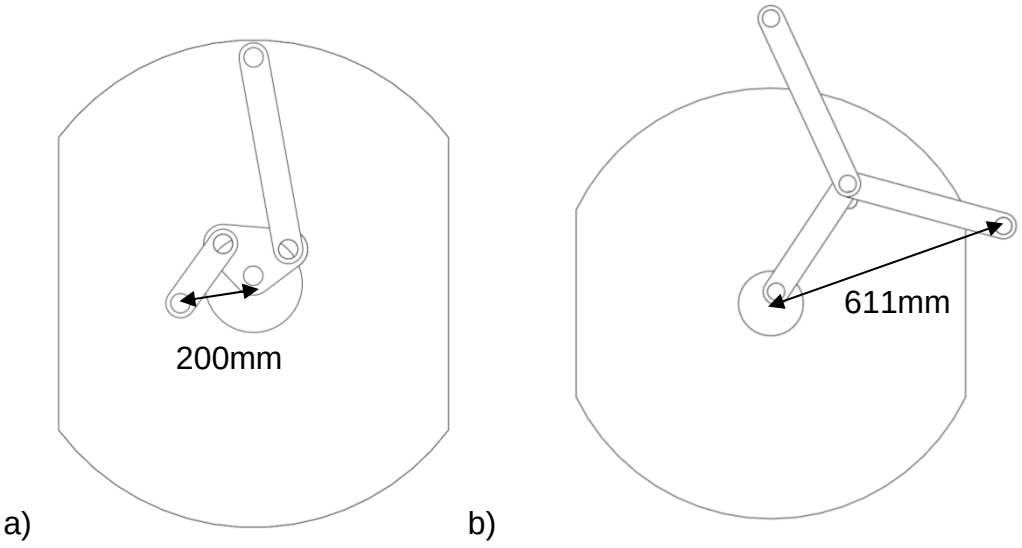

Figure 5.15: Definition of footprint radius for a) 3-link mechanism and b) 4-link mechanism

The 3-link mechanism has a footprint radius of approximately 200mm at maximum stroke. The 4-link mechanism has a footprint of 611mm. Therefore, the 3-link mechanism is the more desirable of the two multiple link mechanisms. The dovetail slide footprint requires a radius which is dependent completely on the size of the shuttle structure and where the mechanism attaches to the shuttle. Therefore, the dovetail slide effectively has negligible footprint. It is difficult to determine the area of footprint for the fourdrinier mechanism without completing at least an embodiment level of design. This mechanism will therefore be scored equally with the dovetail slide mechanism.

Retrofit

The retrofit evaluation criterion refers to the ability of the mechanism to accommodate a retrofit with a simple crank slider mechanism should any unforeseen dynamic issues arise in whichever mechanism is implemented in *Giant Blade*. Both multiple link mechanisms outperform the dovetail slide

mechanism equally. Each mechanism utilises the same connection method to the drive shaft and shuttle frame as a simple crank slider mechanism. Therefore, each multiple link mechanism could be changed to a simple crank slider by disassembling the various links and replacing them with a single link between the driveshaft and shuttle frame. The drive shafts of the 3-link and 4-link mechanisms already have an eccentric drive pin at the correct offset for shuttle oscillation. The dovetail slide mechanism performs poorly in this comparison because the entire sculpture mechanism would need to be disassembled and the drive shaft replaced with a solid version as opposed to the hollow item (see Figure 5.16). The fourdrinier mechanism would require a slewing ring base rotation mechanism and therefore would not allow retrofit of a crank slider mechanism without substantial alteration of the *Giant Blade* mechanism structure.

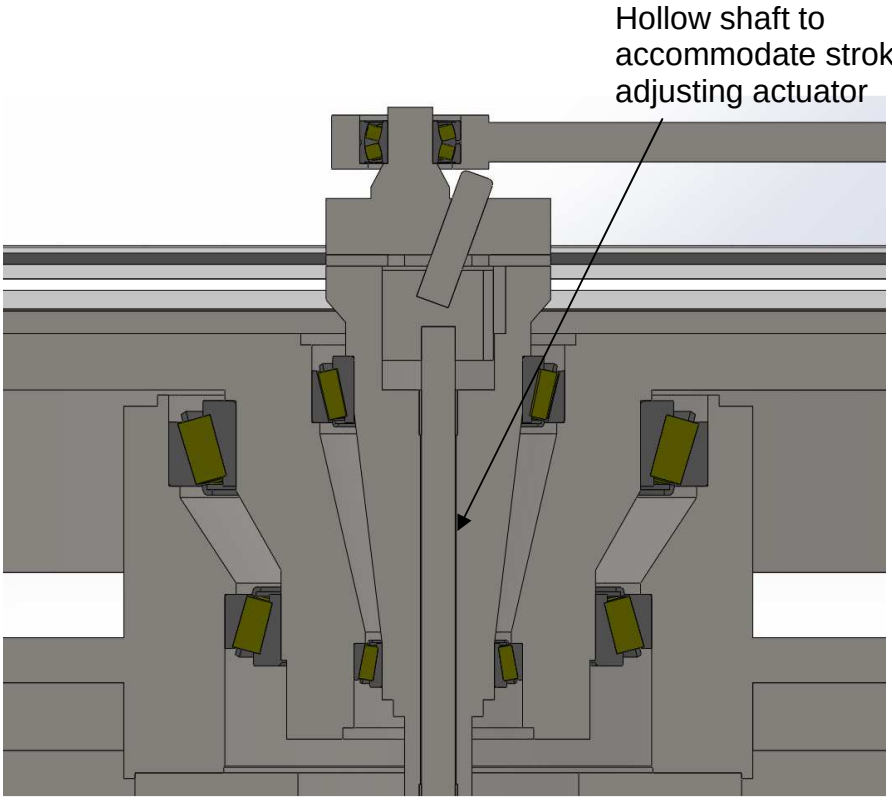

Figure 5.16: 3D CAD model of early concept showing hollow drive shaft required for the dovetail slide mechanism

5.4 Comparing Concept Variants

Table 5.3 presents quantitative results of the above study into an appropriate variable stroke mechanism for the scaled sculpture.

Table 5.3: Selection matrix for the variable stroke mechanism candidates

		3-Link	4-Link	Fourdrinier	Dovetail Slide (Datum)
Production	**3**	4	5	3	3
Proven Design	**2**	5	4	3	3
Simple Harmonic Motion	**3**	2	2	3	3
Strength	**3**	3	5	2	3
Stroke Centre	**2**	1	3	3	3
Compactness	**2**	2	1	3	3
Retrofit	**2**	5	5	2	3
	Totals	53	62	46	51

The 4-link mechanism has been found to be superior in comparison to alternative variable stroke mechanisms. Experimental verification is required to ensure that there are no unforeseen dynamics that exist in the mechanism that would inhibit the scaled sculpture to produce a typical *Blade* performance.

5.5 Small Scale Verification

5.5.1 Miniature Blade Design

A miniature version of the *Blade* sculpture was built at the University of Canterbury. The design the miniature *Blade* is based on the embodiment design

of Chapter 6. This sculpture was utilised for two purposes:

1. To test the 4-link mechanism chosen for implementation on the scaled sculpture as a result of the study in Section 5.3.
2. To test the pivoting clamp arrangement where the upper clamp pivot is free to move in the vertical direction and the lower clamp pivot is fixed as in Figure 5.17. Please note the blade material in the test rig is bolted to the upper pivot. This would not be the case in the scaled sculpture and was done so for ease of manufacture.

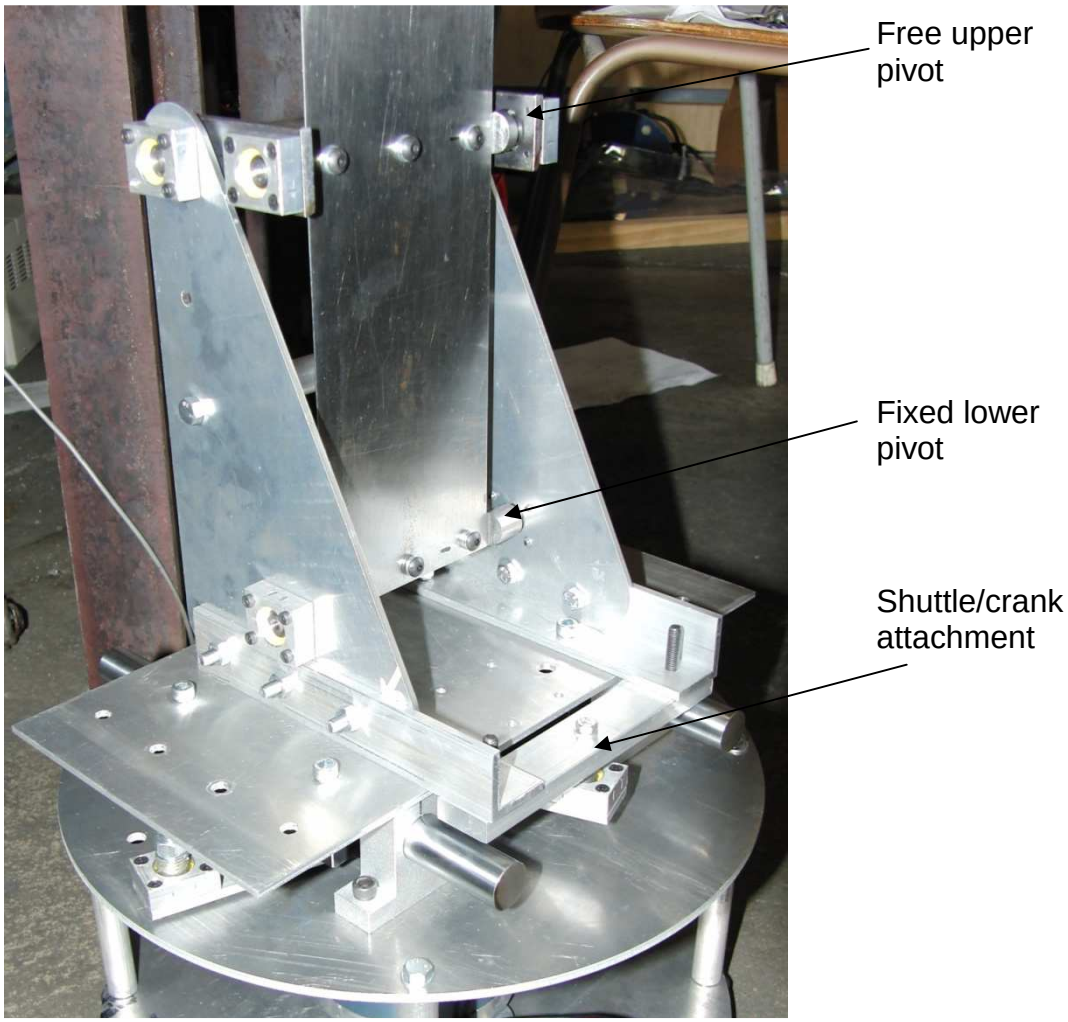

Figure 5.17: Shuttle arrangement of variable stroke test rig showing the pivot arrangement intended for use on the scaled sculpture

The sculpture was designed around an excess piece of carbon steel that was surplus to the requirements of another Len Lye sculpture based project. The blade material measures 1100mm x 100mm x 0.8mm. This provides an unclamped length of blade material measuring 925mm if the ratio of clamped to unclamped blade material found in Chapter 3 is used.

A DC electric motor was sourced to drive the mechanism. Laser cut aluminium made up the majority of the structure of the mechanism due to the ease and speed of manufacture. Mass was also kept to a minimum by using aluminium to reduce any inertial effects that the shuttling clamp would have on the motor drive.

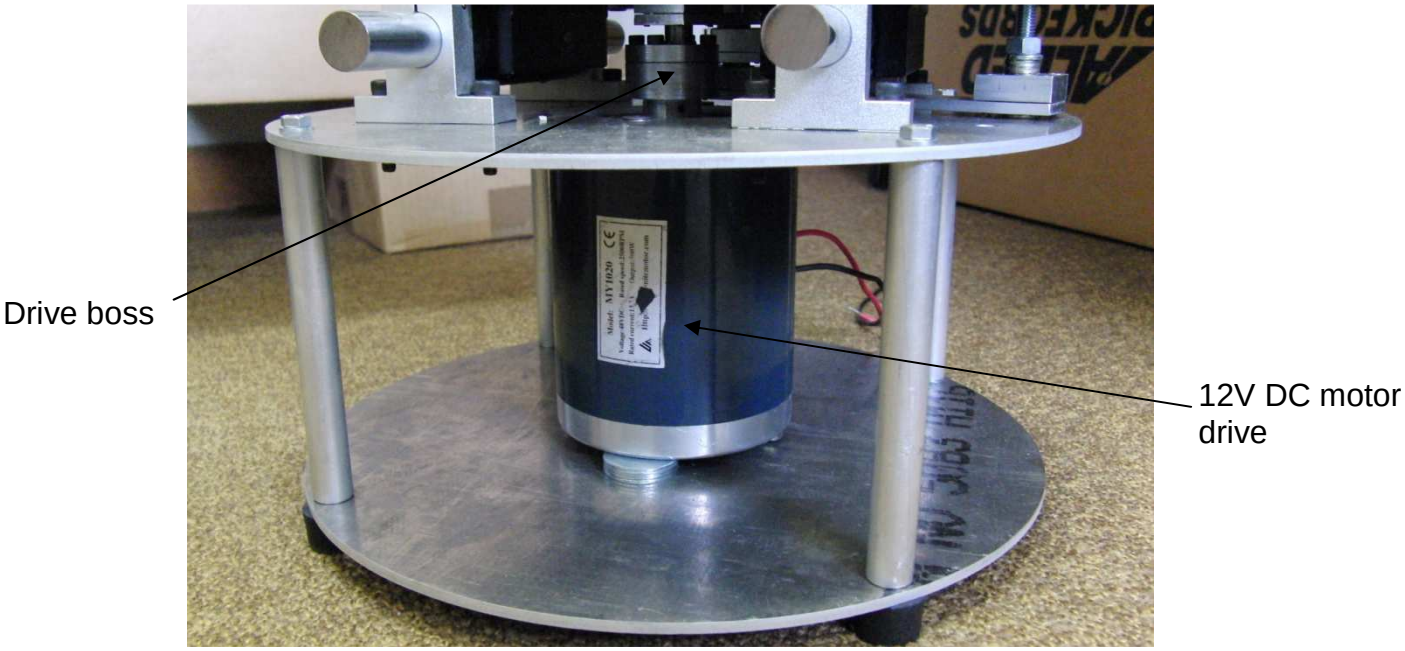

Figure 5.18: Base structure and electric motor on the variable stroke mechanism test rig

The pivoting clamp shafts were manufactured from mild steel to provide enough stiffness to the pivot points for each pivoting clamp shaft.

Figure 5.19: Upper pivot of variable stroke mechanism test rig

Figure 5.20: Lower pivot of variable stroke mechanism test rig

Deep groove ball bearings were utilised in the clamp pivots and variable stroke mechanism cranks. Generic bearing housings were designed to allow the same housing to be used at every bearing location in the sculpture mechanism. Re-circulating ball type linear bearings were utilised for the clamp shuttle.

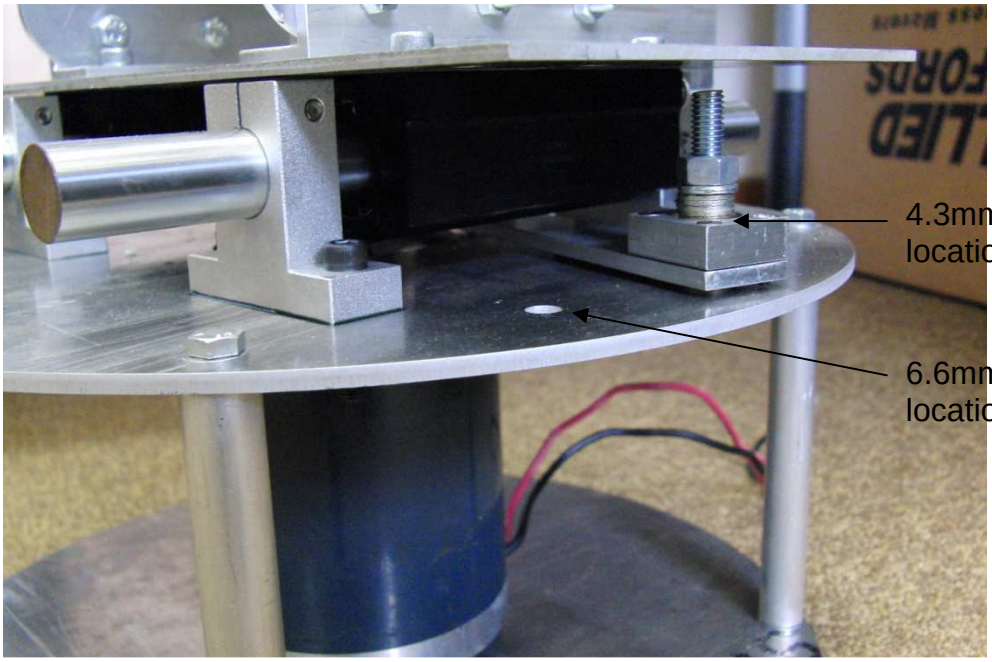

Figure 5.21: Locations of stroke adjustment mounting points

The variable stroke mechanism links were fabricated from aluminium flat bar and the standardised bearing housings. The drive mechanism is identical to the 4-link mechanism of Section 5.2.1. The oscillation stroke of the shuttle is adjusted by bolting the link shown in Figure 5.21 into one of the two adjustment locations on the upper plate of the base frame. The maximum and minimum strokes were found using the following calculation. The scale ratio for the original *Blade* compared to the proposed size for *Giant Blade* is,

$$\frac{l_{s1}}{l_o} = \frac{8.424m}{1.630m} = 5.17$$

The scale ratio for the original *Blade* compared to the miniature *Blade* is,

$$\frac{l_{s2}}{l_o} = \frac{0.925m}{1.630m} = 0.57$$

Therefore, the scale of the miniature *Blade* compared to *Giant Blade* is,

$$\frac{\frac{l_{s2}}{l_o}}{\frac{l_{s1}}{l_o}} = \frac{l_{s2}}{l_{s1}} = 0.11$$

Therefore, for the miniature blade to be tested to similar operating conditions as the scaled sculpture, the values of stroke oscillation should be,

$$39mm \times 0.11 = 4.3mm$$

$$60mm \times 0.11 = 6.6mm$$

The geometry of the variable stroke mechanism on the miniature blade was optimised to ensure that the stroke displacements calculated above were achieved. The resulting variable stroke mechanism on the test rig sculpture is presented in Figure 5.22.

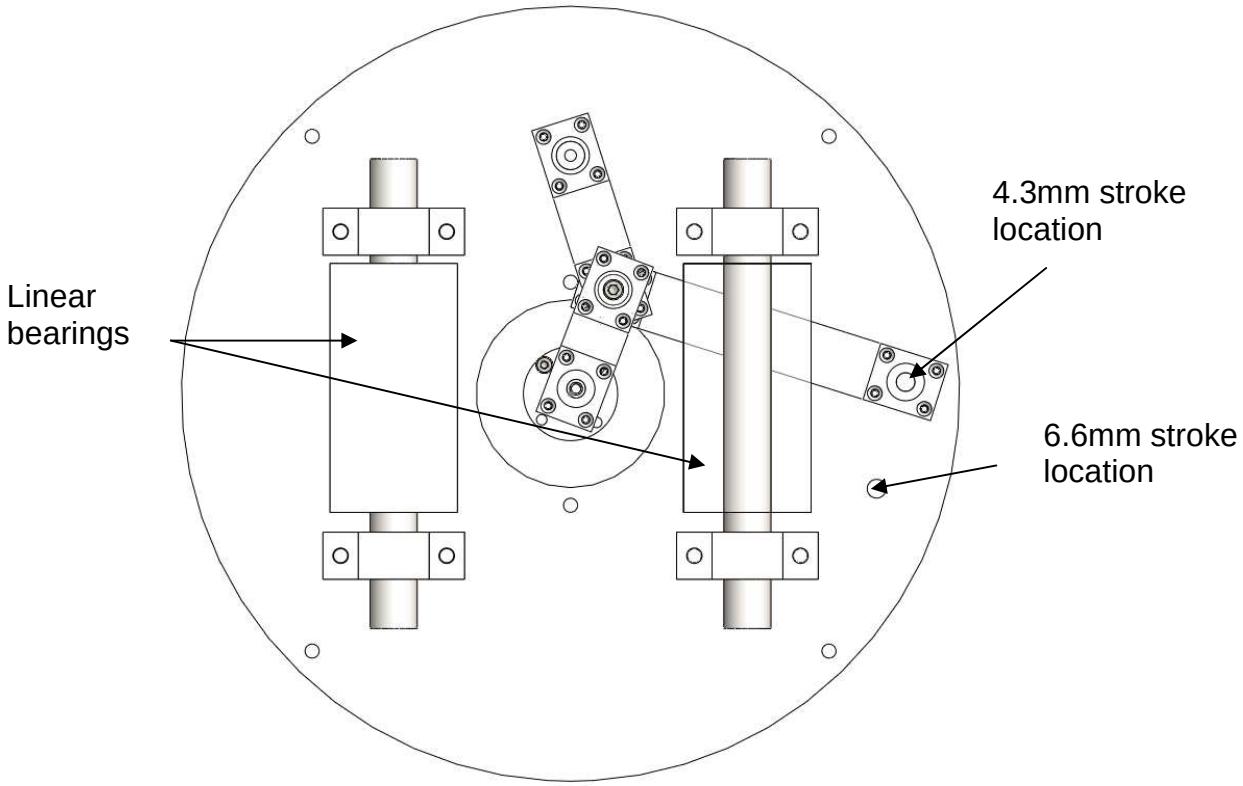

Figure 5.22: 4-link variable stroke mechanism on test rig.

5.5.2 Observations

Simple harmonic motion of the mechanism was verified again using Solidworks Simulation and the results presented in Figure 5.23 and Figure 5.24. There is obvious agreement with theoretical SHM which is expected from the study of Section 5.3.

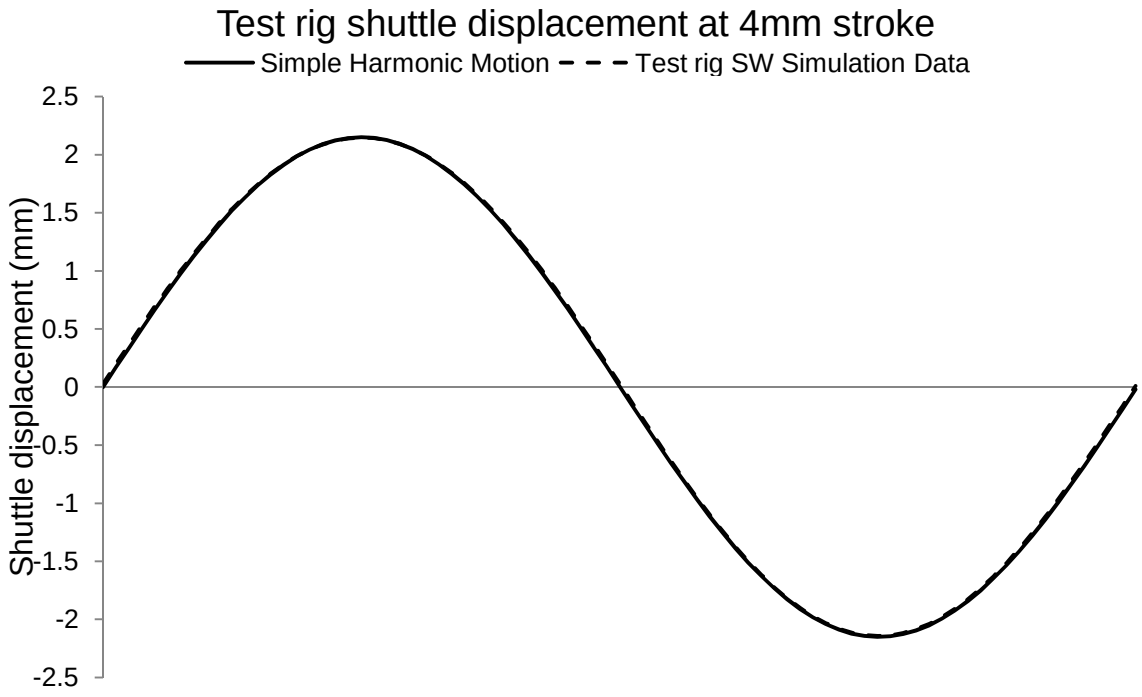

Figure 5.23: Displacement trace of the 4-link mechanism at 4.3mm stroke on test rig compared to the ideal case of simple harmonic motion

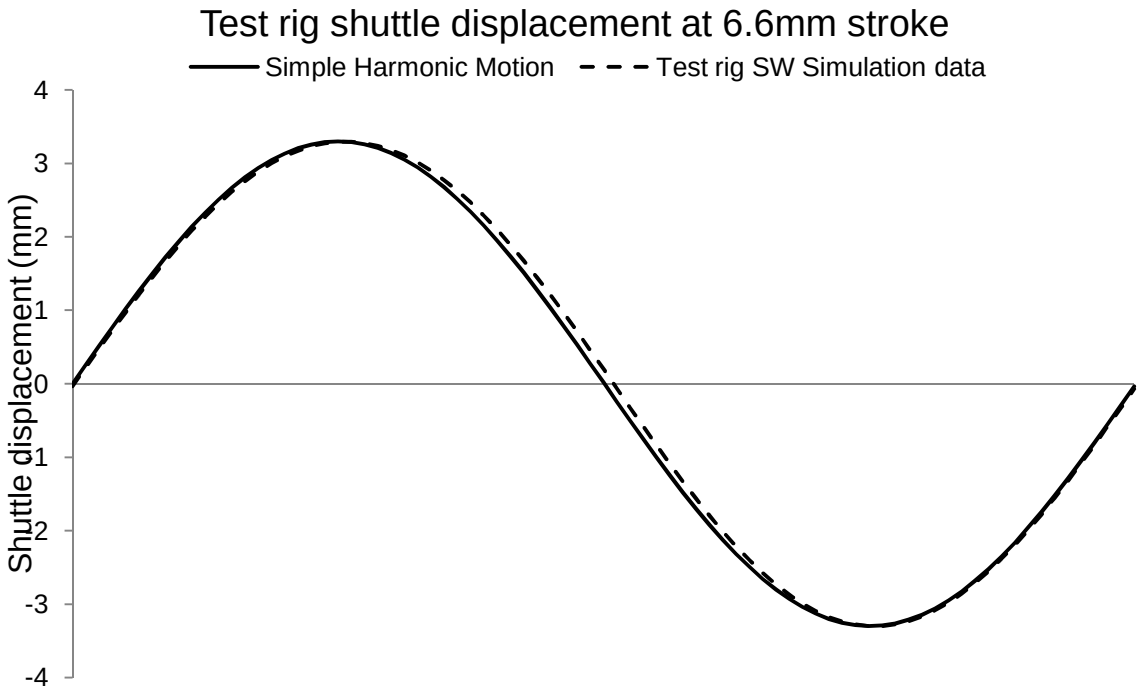

Figure 5.24: Displacement trace of the 4-link mechanism at 6.6mm stroke on test rig compared to the ideal case of simple harmonic motion

Testing on a variable power supply produced good results in terms of the mode shapes formed by the small blade at maximum and minimum strokes. Figure 5.25 and Figure 5.26 present the mode shapes captured using a high speed camera and show less displacement for the minimum stroke configuration as expected. The blade material does not stand perfectly vertical due to the parent material being stored in a coil for the majority of its life. The first image in each figure is used to determine the uppermost node location and hence provide a reference point for the imaginary line of the stationary blade material to compare deflections.

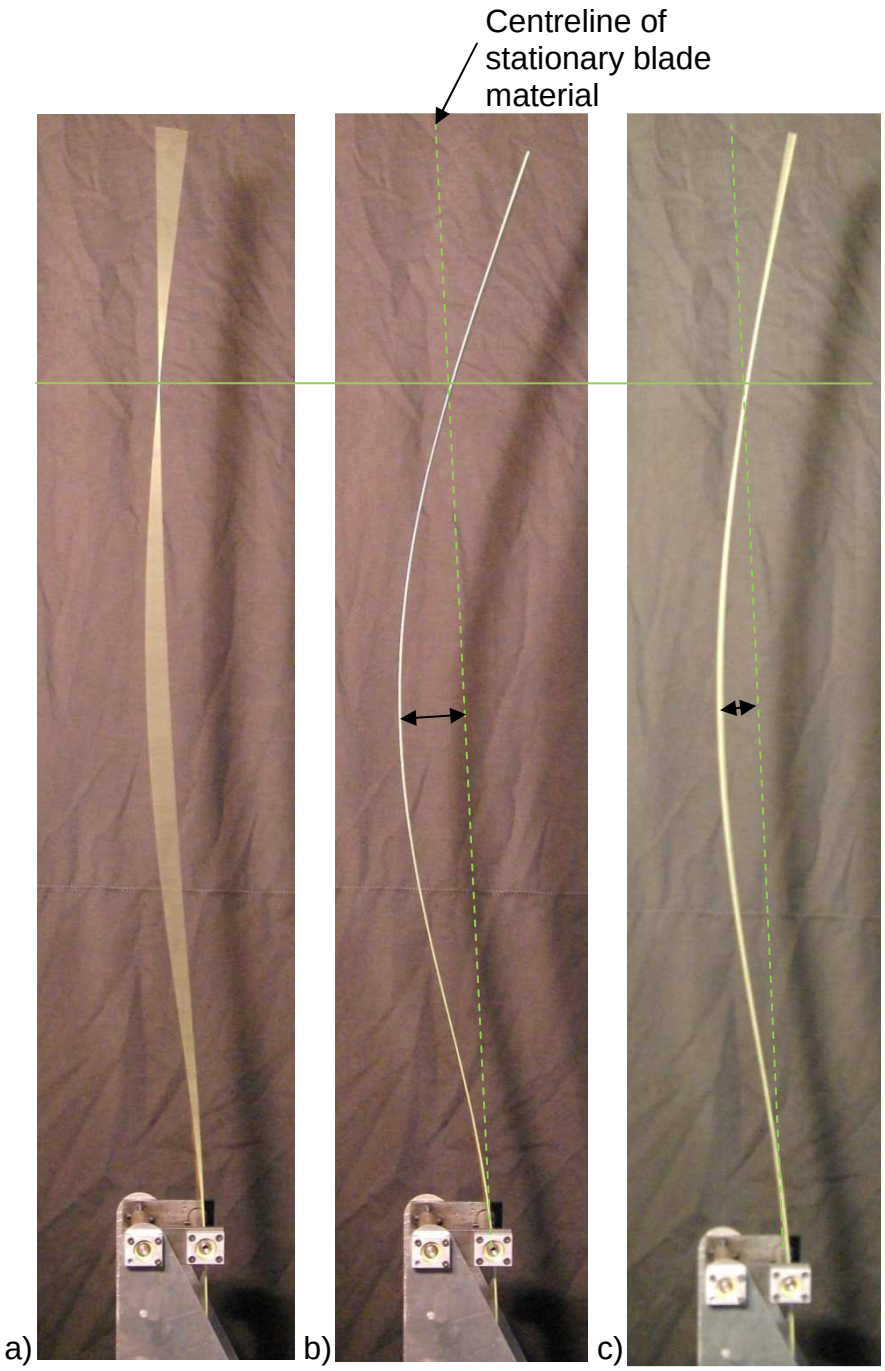

Figure 5.25: Lye's single harmonic excited in the variable stroke test rig at b) 6.6mm and c) 4.0mm. Image a) is used to determine the location of the top node for displacement comparison

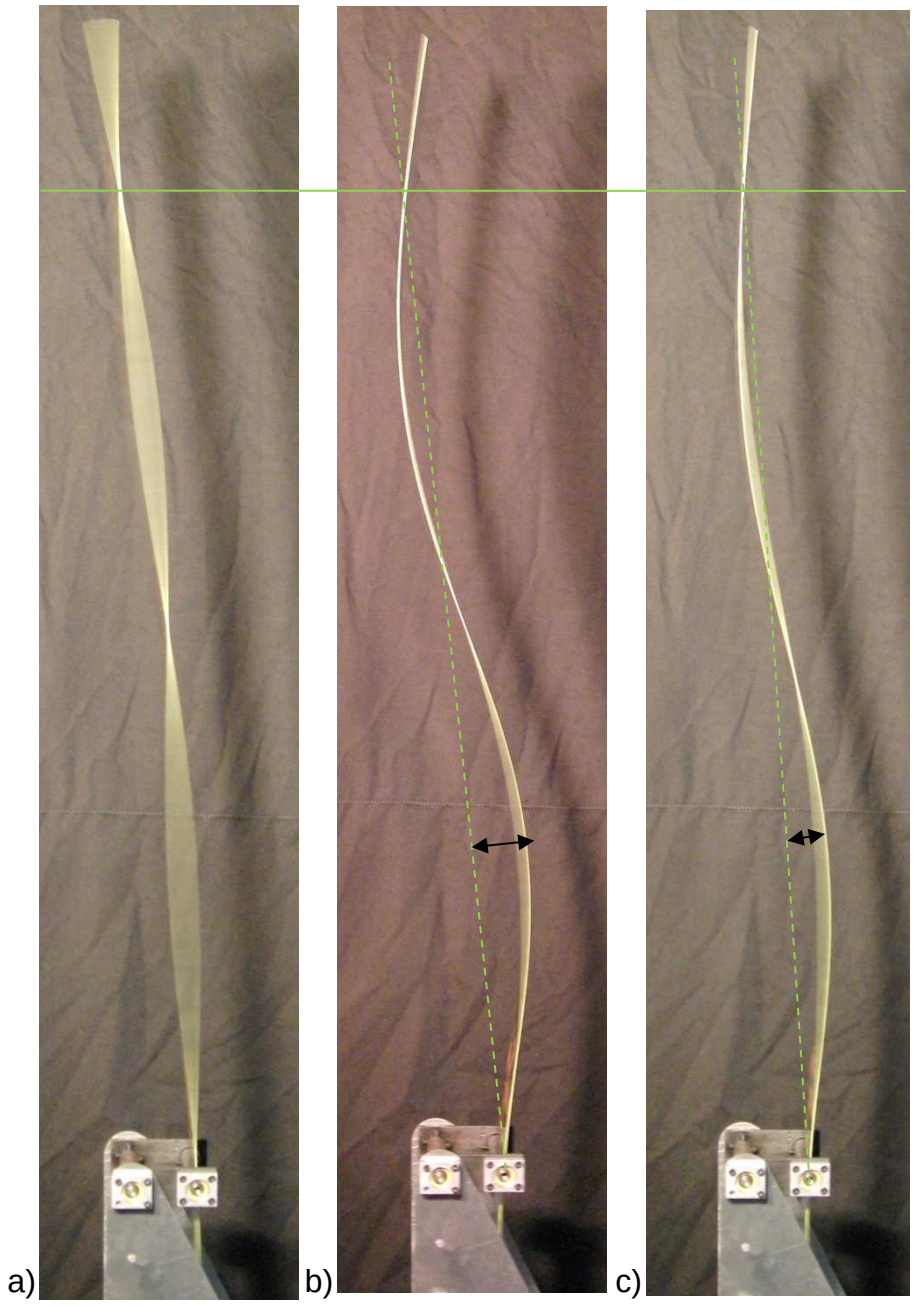

Figure 5.26: Lye's double harmonic excited in the variable stroke test rig at b) 6.6mm and c) 4.0mm. Image a) is used to determine the location of the top node for displacement comparison

This sculpture could easily be modified to rotate. An enclosure and wand could be fabricated and installed to create the *Small Blade* work outlined in the original scope of works. During testing, the variable power supply indicated a voltage draw of just under 10V in the third mode. This suggests that the work could easily be made wireless and be powered by a 12V battery of sufficient amperage. The inertial forces in the work were found to be significant and the sculpture was unstable without restraint in the third mode. A wider mounting frame should be fabricated and used as an anchor to mount the sculpture. This could be completed in conjunction with implementing a base rotation mechanism.

No adverse effects were observed in terms of the mode shapes formed during vibration due to the pivoting clamp arrangement. In the scaled sculpture, the upper pivot would only clamp the blade material (no through bolts) in an effort to reduce stress concentrations at the clamp exit. In the miniature blade, bolts were utilised at the clamp exit because fatigue failure is negligible at this scale and it significantly simplified the build procedure.

5.6 Conclusions

This chapter has presented and assessed four designs of mechanism that are capable of converting oscillating output motion from a rotational input motion, with the capability of varying the oscillation amplitude. Each mechanism has been assessed using the method of (Pahl & Beitz, 1996) against various important requirements the mechanism must meet to be a successful solution in *Giant Blade*. The 4-link mechanism has been selected as the most appropriate mechanism for *Giant Blade*.

The 4-link mechanism is the most suitable to implement in the design of the Giant Blade drive mechanism to give dynamically variable stroke of shuttle oscillation during performances. Figure 6.3 and Figure 6.4 present a proposed layout for the implementation of the 4-link variable stroke mechanism in the scaled sculpture. A linear actuator is used to adjust stroke by shifting the radius arm (crank 4) between two fixed locations. This pinned arrangement is optimal for service loading since the linear actuator is always subjected to tensile or compressive forces.

6 Design of the Scaled Blade

6.1 Introduction

Chapters 2 to 5 have established the design information for the sculpture to be built at a larger size. Chapter 2 assessed the advantage of implementing a pivoting clamp on *Giant Blade* to replace the original cantilever design. Chapter 3 determined the maximum economic scale at which the sculpture could be built based on current titanium prices, the largest commercially available piece of titanium, and the predicted fatigue life of the blade material. Chapter 4 outlines the required shuttle oscillation frequencies to achieve the correct mode shapes with the implementation of a new pivoting clamp design. Chapter 5 has presented a suitable variable stroke mechanism to ensure that bending stresses in the blade are controllable should there be any unforeseen dynamic effects in the sculpture.

The purpose of this chapter is to establish whether the Giant Blade drive mechanism can be built using standard mechanical components. This chapter will also establish the size of the mechanical components required for the drive mechanism of Big Blade. The new concept should address problems associated with the design of Big Blade.

6.1.1 Original Blade Optimisation

The original *Blade* was driven through a mechanism that transmitted electrical power to the shuttle drive motor through the base rotation mechanism via slip rings (Figure 1.5). This solution proved to be problematic in that the inertial effects of the blade material caused the electrical connection between the slip rings to become intermittent during operation of the sculpture. Gooch (S. D. Gooch, 2001) solved this problem by designing a nested drive system in which the base rotation driveshaft and shuttle oscillation driveshaft had concentric rotational axes (Figure 1.7). This allowed the shuttle oscillation drive motor to be mounted below the base rotation mechanism and hence be powered by a drive motor fixed to the support frame. All input for sculpture motion was mechanical removing the requirement of slip rings to transmit power to the bearing platform.

Another undesirable characteristic of the original *Blade* was the tendency of the blade material to flare out during a performance. This phenomenon was termed ‘swinging’ by Gooch and was found to be caused by the excitation of the first natural bending frequency of the blade material (Figure 5.1). This caused by the interaction of the blade and the ball/wand assembly and also abrupt changes in the shuttle oscillation frequency. In order to reduce the swinging phenomenon as much as possible, Gooch optimised the ball/wand assembly and added ‘S curve’ characteristics to the ramping sections of the control program.

6.1.2 Design Issues in Big Blade

The shuttle oscillation in both *Original Blade* and *Big Blade* is achieved through the use of re-circulating ball type linear bearings on a circular shaft. At

the size of the original *Blade* noise made by these bearings is negligible. However, the linear bearings on *Big Blade* emit an unsatisfactorily high level of noise. There are three sources of noise in the linear bearings:

1. The rubber bellows used for sealing the bearing/shaft interface displace air as they expand and contract.
2. The ball bearing elements inside the linear bearings make contact with each other during load reversals and produce a rattling noise.
3. The shuttle drive gearbox also developed a high degree of backlash which and contributes to the mechanism noise.

Len Lye had specific requirements for the performances of his kinetic sculptures. He believed that the technology used to produce the motion in his sculptures should not overshadow the performance. In other words, the mechanism for actuating his sculptures should be hidden from sight and not heard. Hence, in designing *Giant Blade*, a solution to the noise issues in *Big Blade* should be found.

The systematic approach to engineering design recommended by (Pahl & Beitz, 1996) will be used to achieve a suitable solution for the scaled sculpture mechanism.

6.2 Task Clarification

To begin a design problem, Pahl and Beitz (Pahl & Beitz, 1996) recommend forming a solution neutral problem statement to ensure that all

avenues of design are considered. The problem statement made by Gooch (S. D. Gooch, 2001) in designing *Big Blade* is applicable to this design procedure. The following problem statement will be used to develop conceptual morphological matrices for each sub-system of the entire scaled sculpture mechanism.

Problem Statement: To support the blade and the wand as vertical cantilever beams when at rest. To apply a base motion at the supported end of the blade material that achieves Len Lye's intended vibratory form for the blade and the intended interaction between the blade material and the wand. The blade and wand are to rotate about the vertical axis. The mechanism is to operate automatically and concealed within a cylindrical cover.

6.3 Design Requirement Specification

Hales and Gooch (Hales & Gooch, 2004) suggest the use of a design requirement specification to monitor design progress. The design requirement specification phase ensures that all requirements of the final design solution are recorded and suitability can be assessed as the design progresses through its natural stages. In terms of a Len Lye kinetic sculpture, there are important requirements that must be fulfilled to preserve the experience that the artist intended for his audiences. The design requirement specification for the scaled sculpture will be similar to that which Gooch developed for *Big Blade* with some modifications.

Table 6.1: Design requirements specification for Giant Blade adapted from (S. D. Gooch, 2001)

Demand/ **W**ish	*Giant Blade* sculpture drive mechanism requirements
	Functional requirements for the mechanism
D	The oscillating/driving mechanism should be silent with respect to all observers
D	The amplitude of blade base excitation should be dynamically variable between reasonable limits to account for unforeseen high bending stresses in the blade material during 'swinging'
D	The oscillating mechanism must be capable of reciprocating the blade material to produce the single (second bending mode) and double (third bending mode) harmonic frequencies
D	The mechanical drive and the support structure is to be designed to safely withstand all loading conditions of the performance
D	The blade material should be mounted such that it stands vertical when at rest
D	The blade and wand are to rotate smoothly at a speed set by the control system < 1rpm
D	The oscillating mechanism is to follow simple harmonic motion
W	The geometric stress concentration factor at the clamp should be $k_t < 1.2$
W	The ball/wand should have control sufficient to move vertically and inwards and outwards perpendicular to the blade material
W	The oscillation mechanism should be capable of producing the third harmonic frequency (fourth bending mode)
W	The oscillating mechanism and enclosure height should be minimised
W	The ball/wand should be supported in such a way that the wand stands vertically
	Functional requirements for the control system
D	Accurate speed control for the shuttle drive motor
D	Control system must be capable of storing at least four set speeds and eight ramped speed changes for the shuttle drive

Table 6.1 cont.

D	Control system to allow an ‘s-curve’ when increasing/decreasing shuttle motor speed
D	Variable speed control setting for the base rotation drive motor
D	Include an indicator light to show the state of the program (e.g. green for running and red for complete)
W	The power supply and electronic control signals to be transmitted to the mechanism without the use of slip rings
W	Control system to have sufficient capacity for control parameter settings during performance
W	Include a speed transducer on shuttle drive for a positive feedback signal
W	Control system should have the ability to store more than one program for performances
Safety requirements	
D	Include an emergency stop button to isolate power supply in the event of an emergency *(to be positioned at a clearly identifiable location)*
D	Maintain a minimum safe spectator distance $> 2l$
Quality requirements	
D	Design life for mechanism components $> 10\ years$
D	Wiring for electric machines to comply with AS/NZS 3000:2007
D	All manufactured components to be inspected to comply with tolerances specified on manufacturing drawings
D	Sculpture to be fully tested in working environment before release to end user
Manufacturing requirements	
D	Mechanism to be bolted to heavy foundation

Table 6.1 cont.

W	Use manufacturing methods that will allow all components to be manufactured in the University of Canterbury mechanical engineering workshop
W	Ensure that all components can be assembled/disassembled using simple hand tools
Ergonomic requirements	
D	Allow independent on-site adjustment of control system variables
D	‘Start’ and ‘stop’ performance using remote control
D	Display shuttle drive motor speed
D	User interface to clearly identify key performance control functions (start/stop/program number)
W	Allow removal of the blade material without disassembly of any mechanism components
W	Allow adjustment of control system variables while program is running (helpful for tuning set frequencies)
W	Control system to incorporate times to record total running time and total time spent operating at the double harmonic frequency
W	Display program cycle parameters
Timing requirements	
D	Allow 1 week minimum for in-house testing before commissioning
D	Coordinate manufacture with planning schedule at mechanical engineering workshop (UoC)
Economic Requirements	
W	Total materials and labour project cost less than $200k
Ecological requirements	
D	Provide adequate protection to mechanism and electrical equipment from the outside environment (salt air, dirt, grit, water and temperature extremes)

Table 6.1 cont.

D	Include fusible links and/or circuit breakers to protect control system from power supply surges
Life cycle requirements	
D	Service after each blade material life or 50 performances, whichever occurs first (check for bearing noise, environmental damage, and components that may have vibrated loose)
W	Obtain second use from blade material by turning end for end after first failure

6.4 Establishing Function Structures

As was the case with *Big Blade*, the overall function of the scaled sculpture mechanism can be broken down into sub-functions for concept generation. This method allows the designer to separately address the specific requirements of each sub-function to determine the optimal solution. Each chosen solution to a sub-function is then combined to form the overall optimal solution to the design problem. The *Giant Blade* mechanism can be divided into the sub functions presented in Figure 6.1

.

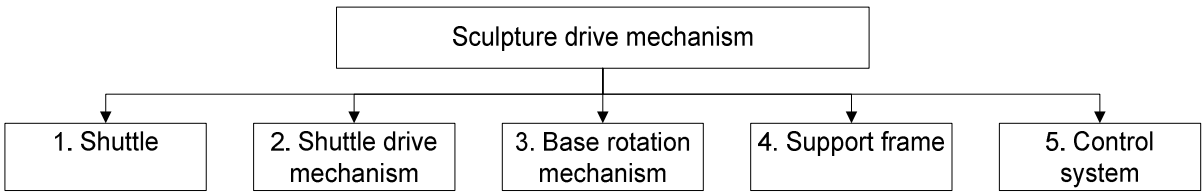

Figure 6.1: Sub-system map of the scaled Blade sculpture (S. D. Gooch, 2001)

6.5 Conceptual Design of the Drive Mechanism

The purpose of this section is to establish a new concept for the drive mechanism of the scaled *Blade* that eliminates the issues discussed in Section

6.1.2. The shuttle, shuttle drive and the base rotation mechanism will be assessed and an appropriate solution found for each sub-function. The support structure will be manufactured of standard steel sections and hot dip galvanised. Most current motor drive systems have PLC capabilities which will be sufficient for the control system.

The method used here will be similar to that used by Pahl and Beitz (Pahl & Beitz, 1996). The solutions to some of the sub-functions in Figure 6.1 will remain identical to the solutions found by Gooch. Others, such as the variable stroke mechanism and the pivoting clamp concept have been pre-selected by the studies of Chapters 2 and 5. The remaining sub-function solutions will differ from the solutions found by Gooch due to the varying requirements of increasing the scale of the sculpture from *Big Blade* to the scale found in Chapter 3.

6.5.1 Shuttle

The shuttle sub-system has been partially solved by the decision to employ a pivoting clamp arrangement. However, the configuration of the pivoting clamp and the components to be used is still unknown. Figure 6.3 illustrates the working principles considered in the development of the shuttle on the scaled sculpture.

At first glance, the pivot arrangement selection would seem inconsequential. It is not until the assembly of the sculpture is considered that the subtleties of the decision become apparent. If the sculpture was to employ a free lower pivot there would be a requirement for ‘through’ bolt supports at the

upper pivot. This would increase the geometric stress concentration to above the required 1.2 at the upper pivot (Table E.1 Appendix E) and hence reduce the fatigue life of the blade material unnecessarily. Therefore, the sculpture should consist of a free upper pivot as in A1, Figure 6.2, with through bolt supports in the lower pivot shaft to support the blade material.

Two solutions were considered regarding the manufacture of the clamp pivots. The fabricated solution of B1, Figure 6.2, would have an optimal strength to weight ratio. However, the amount of welding required would likely distort the concentricity of the stub shafts at each end. Machining out the centre of the shaft could also cause the final product to bow due to the amount of material being removed. Solution B2 is more suitable, and should be manufactured from a high strength carbon steel alloy plate with sufficient thickness.

The preferred solution for the rotating elements of the pivoting shafts is plain DU bushes with thrust washers (solution C3, Figure 6.2). It was found that the lining in the plain spherical bearings is not suitable for the load reversals seen by these components. The ball bearing solution would not be suitable due to the noise generated by the interaction of the ball bearing elements. There is always some clearance present in ball/roller bearings, unless the preload is adjustable. The ball bearing pivot mounts selected for the test rig of Chapter 2 emit some noise and it is predicted that at a larger scale this would be exacerbated. These bearings have also worn prematurely, resulting in increased clearance in the bearing and increased noise. The DU bush solution allows clearances to be minimised by careful machining of the pivot shafts.

The optimal solution for the shuttle frame supports is linear guides (solution D1, Figure 6.2). Linear guides are produced with customisable preload, which reduces the possibility of noise due to clearance. Linear guides today are also capable of accommodating significantly high radial loads as seen in *Giant Blade*. They provide a simple, off-the-shelf solution to the oscillating movement of the shuttle frame. A bogie type system was also considered, similar to that found on roller coasters. Operating clearance was an issue here, along with wear of the rollers that most likely would have been manufactured by some type of urethane. The hinged solution of D3 provides an elegant option for achieving the small oscillation displacement of the shuttle frame. However, the sheer amount of material required to manufacture this, along with the long load paths and out of balance forces, deemed this solution inadequate.

The attachment of the shuttle frame to the variable stroke mechanism is achieved through the use of a simply supported shaft (made as a spigot for assembly and shown in Figure 6.6). This solution provides far better load handling capability than a cantilever stub shaft attached to the shuttle frame. The connection of the oscillation drive shaft to the variable stroke mechanism will be through a pair of tapered roller bearings (Figure 6.22) due to the significant bending moment about the top of the drive shaft due to the dynamics of the variable stroke mechanism. Two separated tapered rollers are optimal for bending moments when compared to deep groove ball bearings and cylindrical roller bearings.

Morphological Matrix – Sub-system 1 Shuttle mechanism				
Solution / **Sub-system Sub-functions**		1	2	3
A	Pivot arrangement	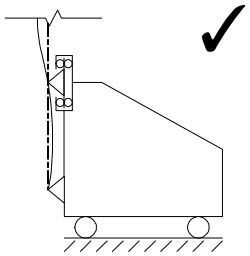 ✓ Free upper pivot	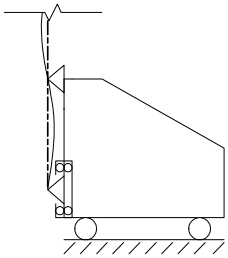 Free lower pivot	
B	Pivot clamps	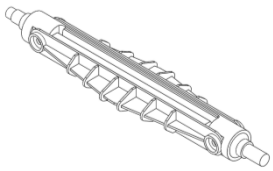 Fabricated clamp	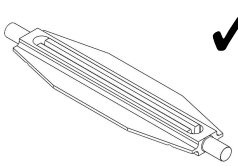 ✓ Machined clamp (one piece with jaws)	
C	Pivot rotating elements	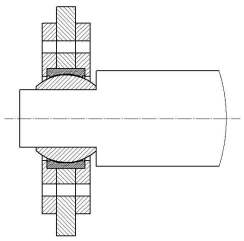 Spherical plain bearings	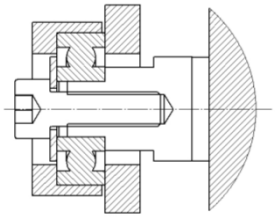 Ball bearings	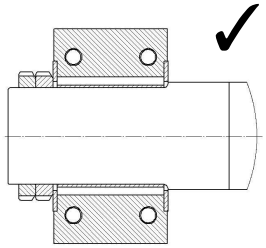 ✓ Plain DU bushes with thrust washers
D	Shuttle frame support	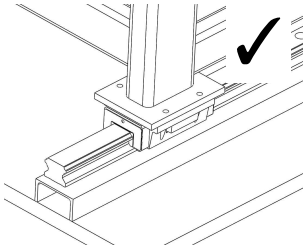 ✓ Linear guides (Re-circulating ball type)	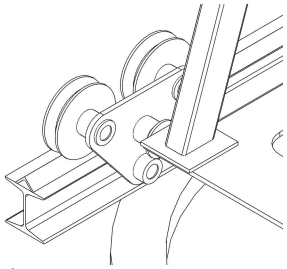 Bogie	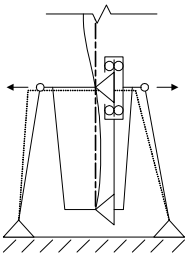 Leaf sprung supports/Hinged structure

Figure 6.2: Working principles considered in the development of a concept for the shuttle in the Giant Blade design

6.5.2 Shuttle Drive Mechanism

The concept design of the shuttle drive mechanism has been largely investigated in Chapter 5. The solutions to each sub-function of the shuttle drive mechanism found by Gooch will be adopted in this exercise (see Figure E.1). A solid 1-piece shaft will be employed as opposed to a bolted cam crank arrangement as in *Big Blade*. This section will largely deal with the selection of appropriate bearing arrangements for the variable stroke mechanism.

There are 7 potential bearing locations in the variable stroke mechanism of Chapter 5 (Figure 6.3).

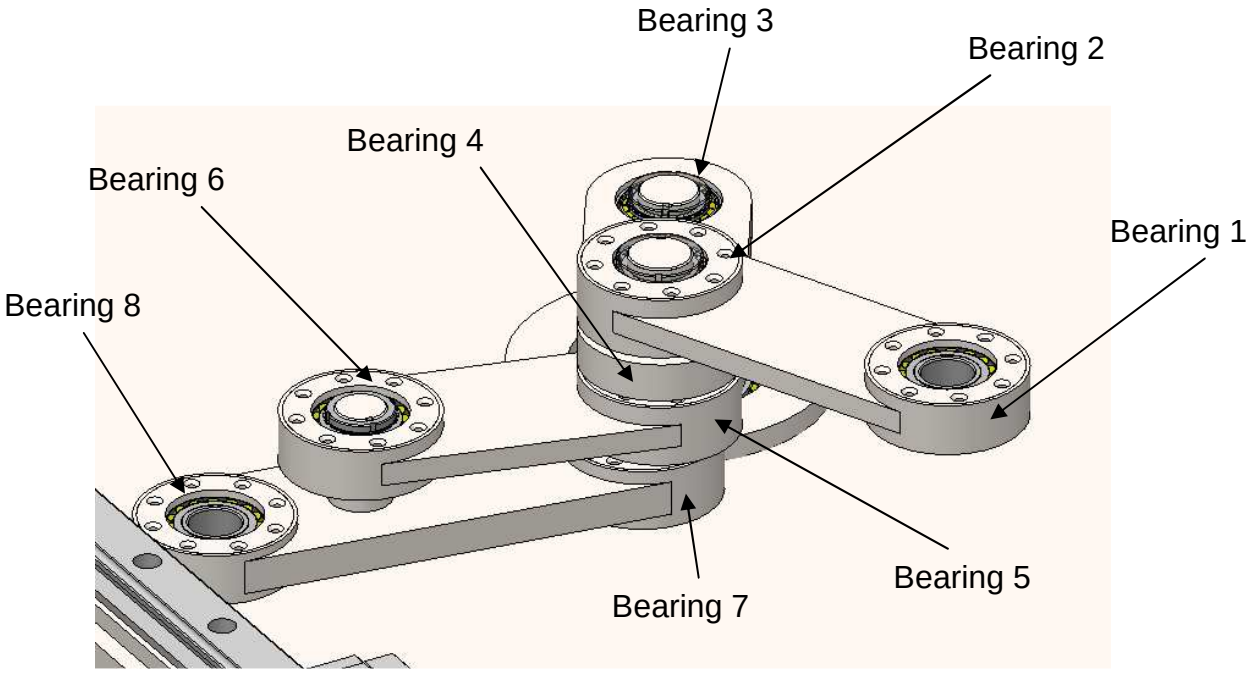

Figure 6.3: Variable stroke mechanism arrangement proposed for Giant Blade indicating bearing locations (bearing stack consists of bearings 2, 4 and 5)

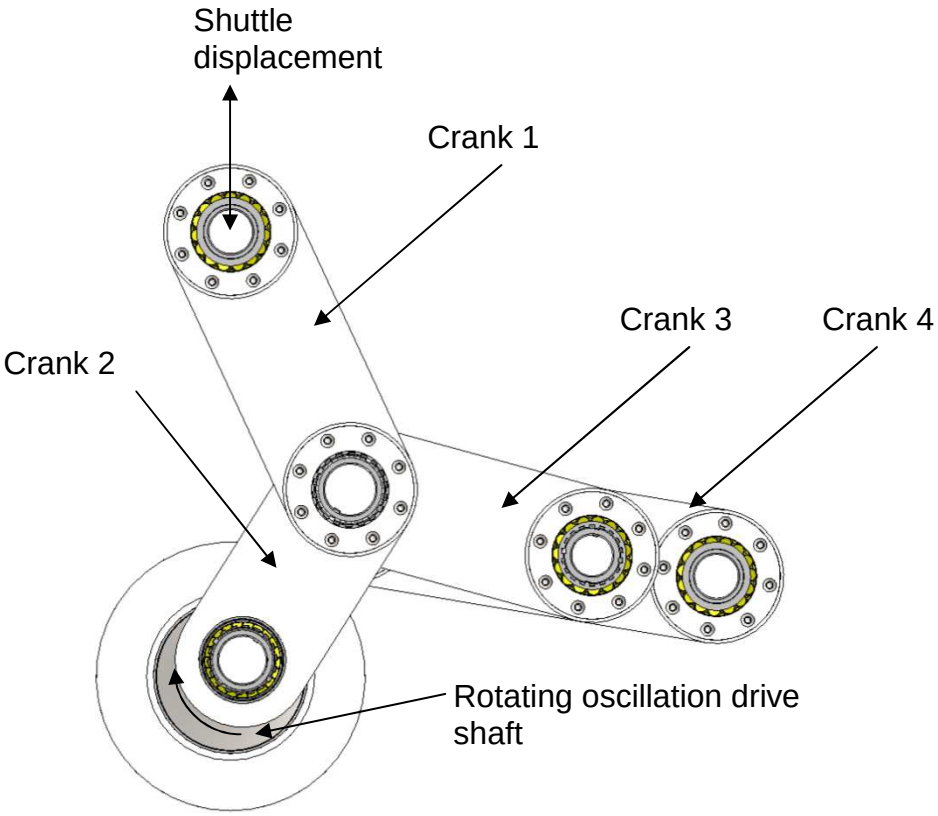

Figure 6.4: Variable stroke mechanism proposed for Giant Blade indicating crank locations

The weakest point of the mechanism is the bearing stack as shown in Figure 6.3 consisting of bearings 2, 4 and 5. This bearing stack is subject to a large bending moment caused by cranks 1 and 3 applying a force couple around the centre of the stack. If the stack consisted of 3 bearings in each crank then the central bearing (bearing 4) would require a high capacity of facilitating bending moment loading. A better solution would be to introduce a welded shaft onto crank 2 in place of bearing 4 as in Figure 6.5.

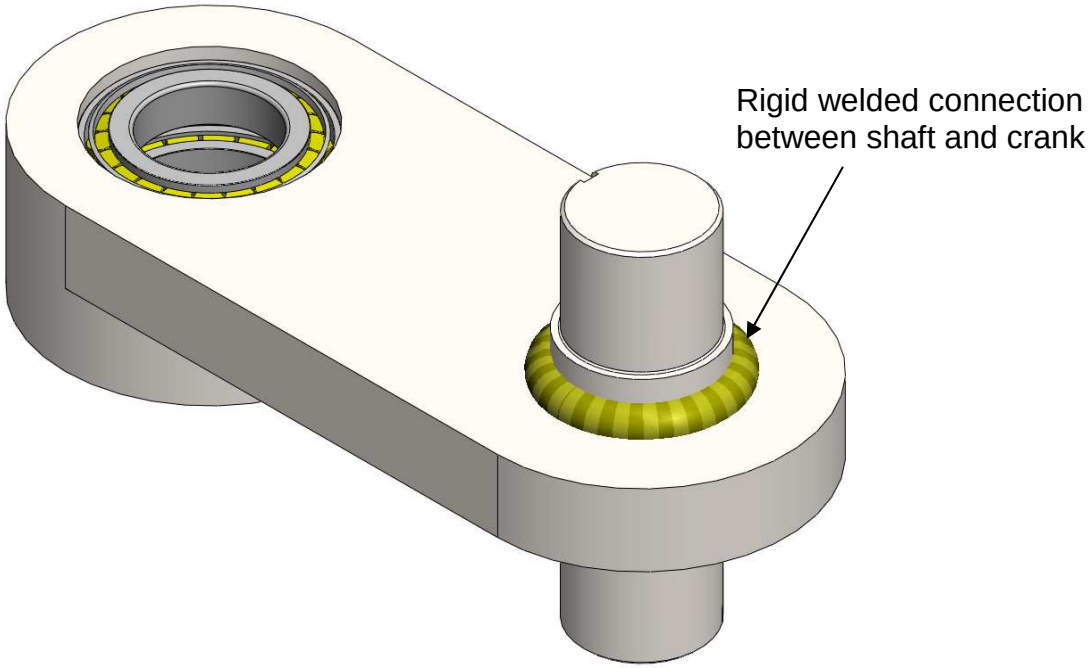

Figure 6.5: Isometric view of crank 2 showing the suggested welded shaft arrangement to overcome the high bending moments at this bearing location

This transfers the bending moment applied by cranks 1 and 3 directly to the shaft and crank 2. These components can be designed to be large enough to resist the bending moment loading. The other bearings in the stack are double row cylindrical roller bearings to maintain the stiffness of this bearing stack.

The connection of the variable stroke mechanism to the shuttle frame at bearing location 1 is a sealed spherical roller unit pre packed with LGHB grease for vibratory applications (see Figure 6.6). This bearing is required to sustain high loading whilst undergoing oscillatory motion. Roller bearings are designed to operate under full rotation of roller elements. The slow and incomplete rotational speed results in inadequate oil film dispersion inside the bearing. Therefore, this bearing has been selected based on the static load rating of the bearing with a safety factor as opposed to the dynamic load rating as

recommended by SKF. LGHB grease is also selected due to it possessing good characteristics under high load and heavy impact conditions.

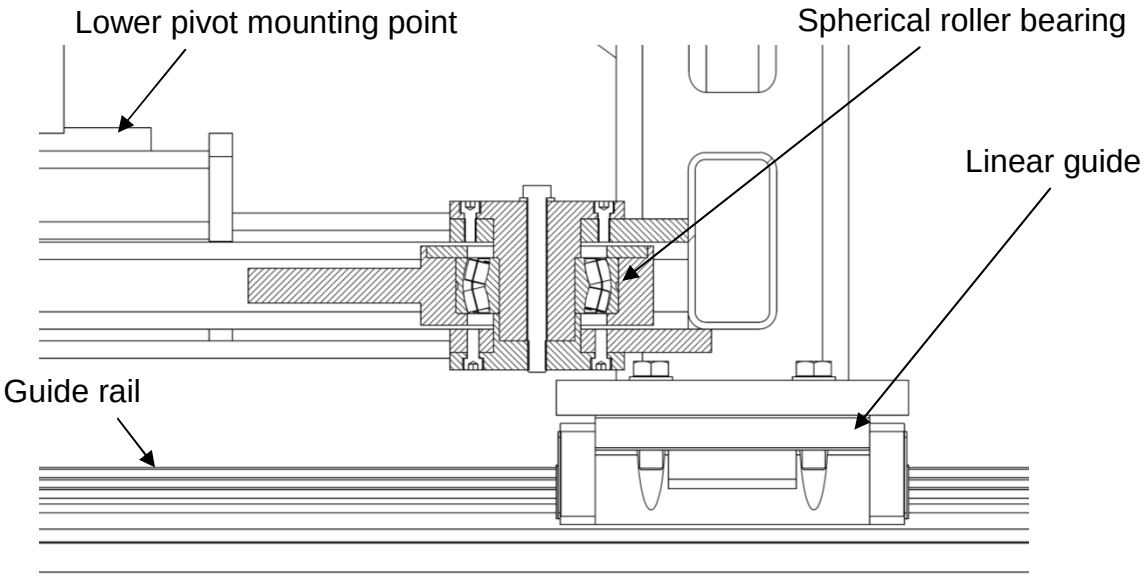

Figure 6.6: Shuttle frame to variable stroke mechanism connection

A double row cylindrical roller bearing has also been selected for the pedestal mount (bearing 7) of the stroke adjusting crank. Bearing 3 consists of two tapered roller bearings to support the bending moment transmitted through crank 2. Spherical roller bearings were selected for the remaining bearings to avoid over-constraining the mechanism.

6.5.3 Base Rotation Mechanism

The base rotation mechanism provides rotation of the entire ball/wand/blade material combination during a *Blade* performance. The original *Blade* consists of a chain drive mechanism and a disc brake as shown in Figure 6.7.

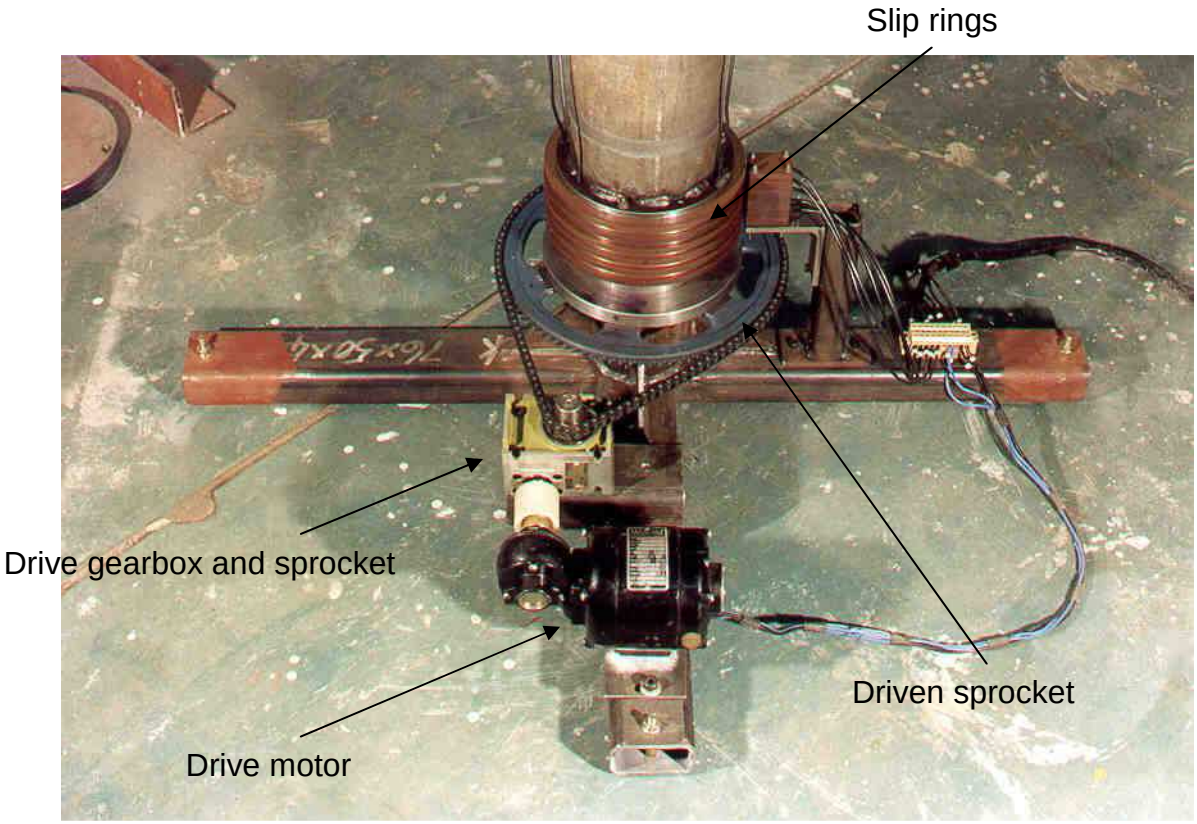

Figure 6.7: Base rotation mechanism used in the original Blade (disc brake removed)

Big Blade utilises a synchronous belt drive system as shown in Figure 1.7. Many of the same solutions for the base rotation sub functions were considered for the scaled sculpture in this study. Referring to Figure E.2 for the morphological matrix of Gooch the solution to the base rotation drive for the scaled sculpture is also a belt/chain drive. Due to the requirement of low noise and the possibility of exposed grease in a chain system, a belt drive has been selected for *Giant Blade*. The worm drive solution of L1 is unsuitable in this application due to the requirement of braked rotation to withstand torsional inertia of the vibrating blade material. Gear backlash noise would also be an issue with this solution. The spur and helical combination of L3 would be unsuitable for the same reasons.

The table support solution of tapered roller bearings M2, Figure E.2, has

also been chosen for the scaled sculpture. The plain bearing solution of M1 would be unsuitable due to the high bending moment loading about the base rotation mechanism. Slewing rings were also considered but were discounted due to the non-zero clearances inside these bearings. It is envisaged that these clearances will eventually develop into rattling of the sculpture mechanism causing undesirable noise pollution during performances. Solution M2 allows adjustment for wear in the bearings which is advantageous in reducing mechanism noise to a minimum.

The bearing table trunnion joint has been selected to be the same design as *Big Blade*. The welded arrangement of N2, Figure E.2, provides the required strength for the high bending moment loads evident at this location. The bearing table is required to possess a high degree of flatness and will likely be required to be milled before having the linear guides mounted. This flatness can be maintained in a rigid welded arrangement. However, the bolted arrangement of N1 is likely to move during operation which will increase wear in all bearing elements due to the resulting misalignment. The press fit of N3 will not be suitable for the high bending loads.

The friction damper solution of O2, Figure E.2 has been chosen for the scaled sculpture and provides the required friction to counteract out-of-balance forces. The disc with floating calliper is the most suitable solution to the combination of tapered roller bearings and belt/chain drive solution of P2. Worm gear driven slewing rings such as the item in Figure 6.8 were also considered for the base rotation mechanism. These worm gear drives can be purchased in a

zero backlash configuration with minimised clearances in the slewing ring bearing. This solution would likely be more compact and less complicated to manufacture than the tapered roller bearing and belt/chain drive, but cost made this option prohibitive.

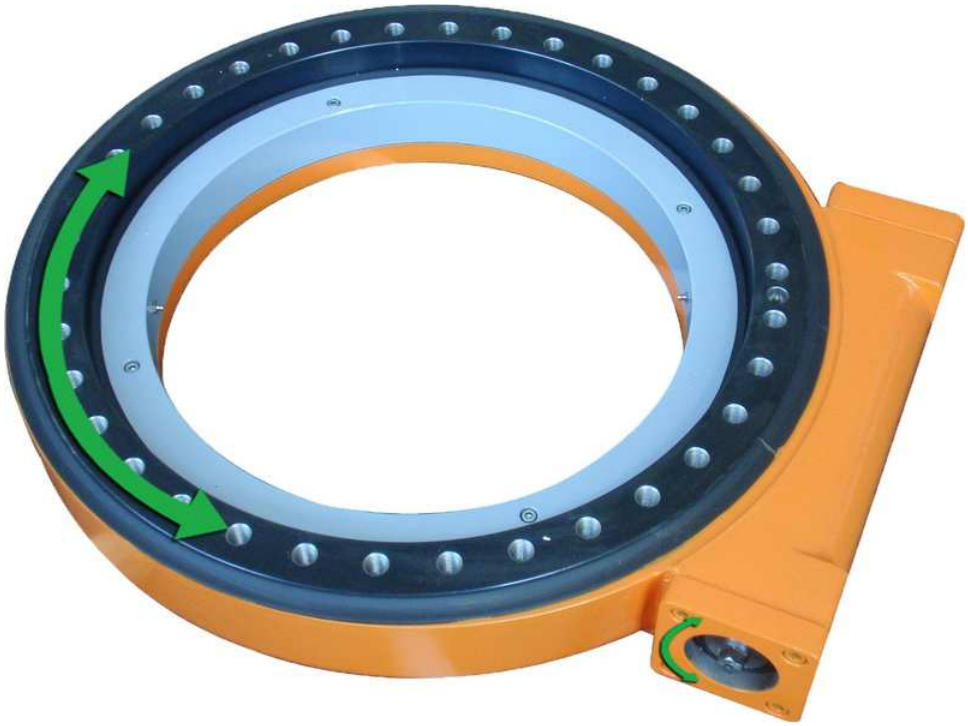

Figure 6.8: Worm drive slewing ring with green arrows illustrating actuation [Retrieved from http://www.h-fang.com.cn/]

6.5.4 Assessment of the conceptual design stage

The current design has been assessed according to the method recommended by Hales and Gooch (Hales & Gooch, 2004). Figure E.3 presents the confidence in meeting each category of the design requirement specifications in a general sense. The worksheet indicates that there is good confidence in the functional requirements of the sculpture mechanism at this stage. Areas of concern consist of the manufacturing requirements and the quality requirements. Specifically, locating a company that has the facilities to build the components for

the mechanism at the size required. Ensuring that the blade material quality meets the relevant standards ((ASTM International, 2013)) will also be important. Further development will see improvement in manufacturing requirements and therefore, it was decided to proceed with the embodiment design phase. Ergonomic requirements show low confidence due to the requirement of a control mechanism for the ball and wand arrangement. Timing requirements have been affected by the search for a suitable piece of titanium.

6.6 Embodiment Design of the Drive Mechanism

This section will present the embodiment design for the blade material drive mechanism of the scaled sculpture using the combinations of sub-systems selected in Section 6.5. A design for the support structure will also be presented. The final embodiment design will be assessed using the embodiment design work sheet from Hales and Gooch. The calculation set in Appendix D will be referred to throughout this section.

6.6.1 Predicted System Loads and Forces

The worst case scenario identified by Gooch of ‘swinging’ (Figure 5.1) has been used as a basis for the drive mechanism design. A maximum blade material bending stress value was obtained from the testing of Chapter 2 to be 331MPa. The drive mechanism and its support structure have been designed to withstand this worst case scenario for the predicted number of cycles the mechanism is subjected to this loading.

6.6.2 Shuttle: Upper Pivot

A machined pivot shaft was selected in the concept design of Section 6.5. Hand calculations in MathCAD were carried out to determine the rough geometry of the pivot in Section 4.0 Appendix D. Once the rough geometry was obtained, the pivot was modelled in Solidworks. The geometry was then optimised using Solidworks Simulation FEA capabilities.

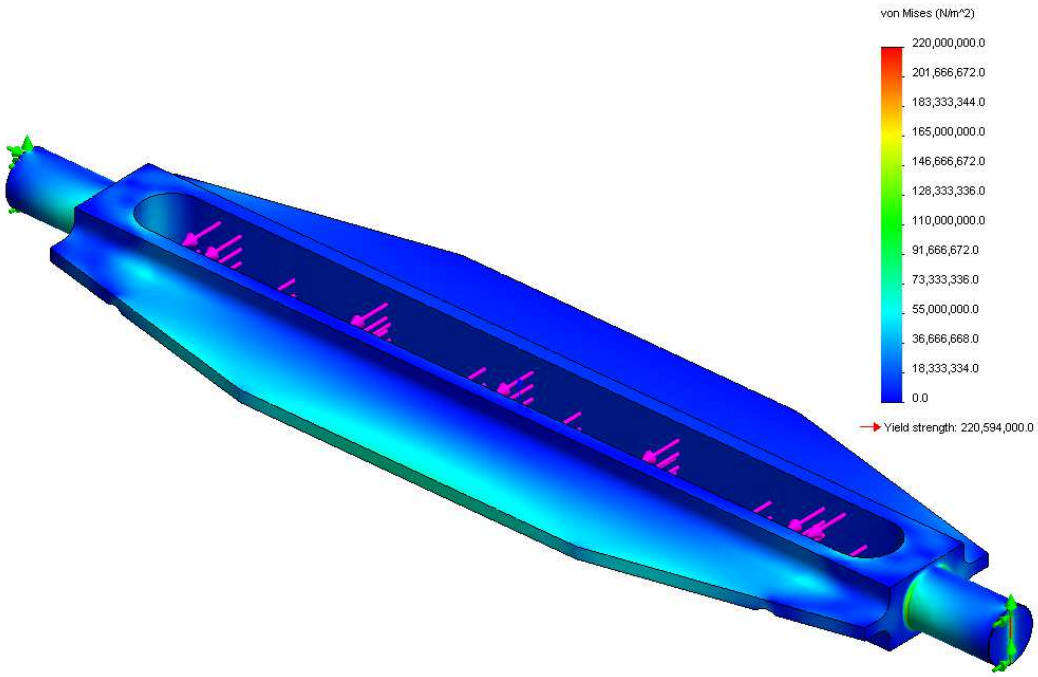

Figure 6.9: Finite element analysis von-Mises stress plot for the upper pivot clamp on the Giant Blade

The pivot is to be manufactured from 100mm Bisalloy 80 wear resistant plate. This material provides the high strength required in this application in plate form. The pivot should first be roughed out with an oxy-acetylene gas cutter. Then, the major dimensions should be milled. The stub axles should then be turned and finally the cavity for the blade material entry should be profile cut using wire electrical discharge machining.

The pivot clamp jaws (Figure 6.10) should be manufactured of the same Bisalloy 80 material. These jaws have a parabolic profile to minimise the geometric stress concentration factor in the blade material. Titanium and steel are at risk of fretting fatigue when the two materials are in dynamic contact. The interface of the blade material and the steel jaws should be coated in an anti-fretting coating such as Sulzer Metco (specification sheet provided in storage media).

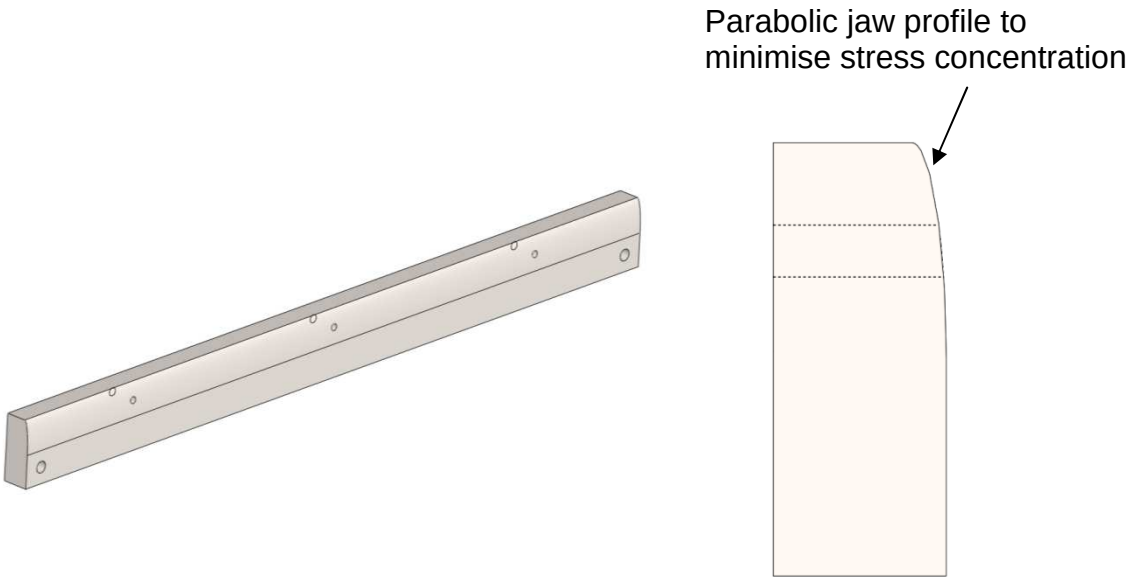

Figure 6.10: 3D CAD image of pivot clamp jaw and cross section illustrating parabolic profile

The blade material mass is supported by the lower pivot. Therefore, the upper pivot is only required to clamp the blade material using a friction grip. One jaw is floating and the other jaw is fixed. The two bolts mounted either side of the blade material (Figure 6.11) are used to tighten the floating jaw against the fixed jaw and the blade material.

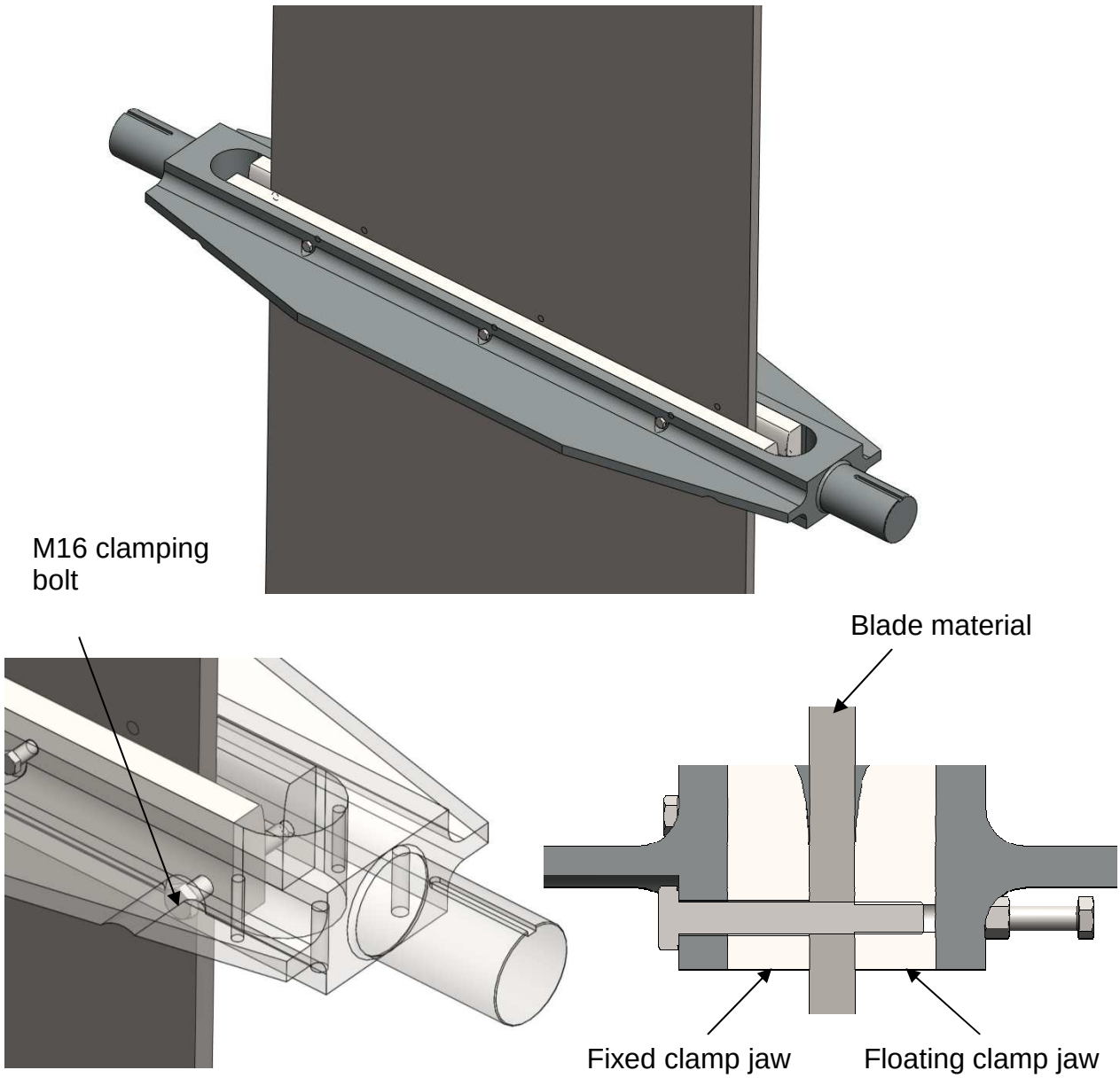

Figure 6.11: 3D CAD image of upper pivot showing the clamping bolts for blade material

The bolts that support the floating jaw in blind holes (Figure 6.12) are used to evenly distribute the clamping force across the blade material and ensure the entire floating jaw remains in contact with the blade material at all times.

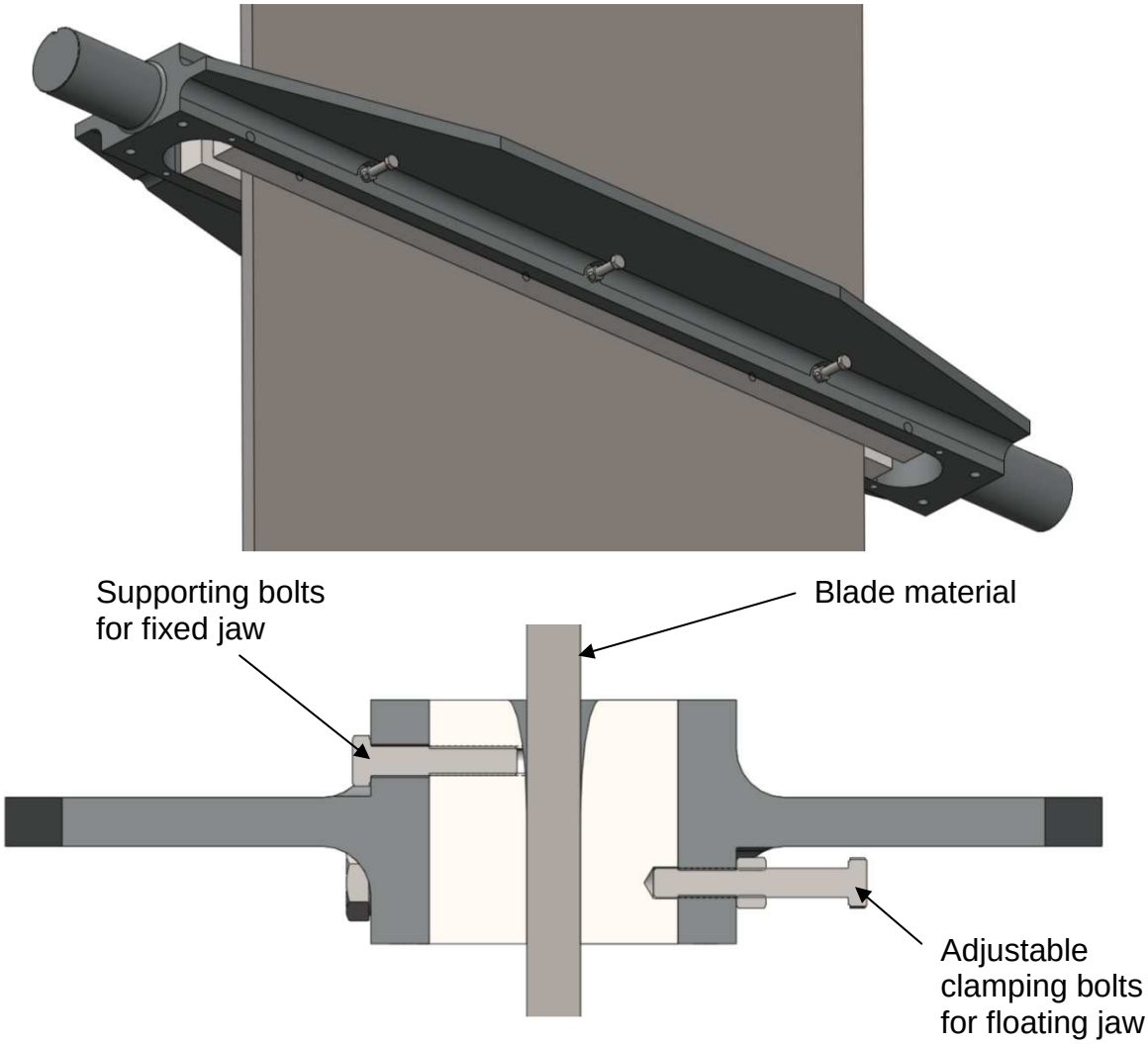

Figure 6.12: 3D CAD cross section of the upper pivot illustrating the adjustable bolts for floating jaw load distribution

For assembly purposes, there are two plates that support the jaws from sliding through the upper pivot as in Figure 6.12.

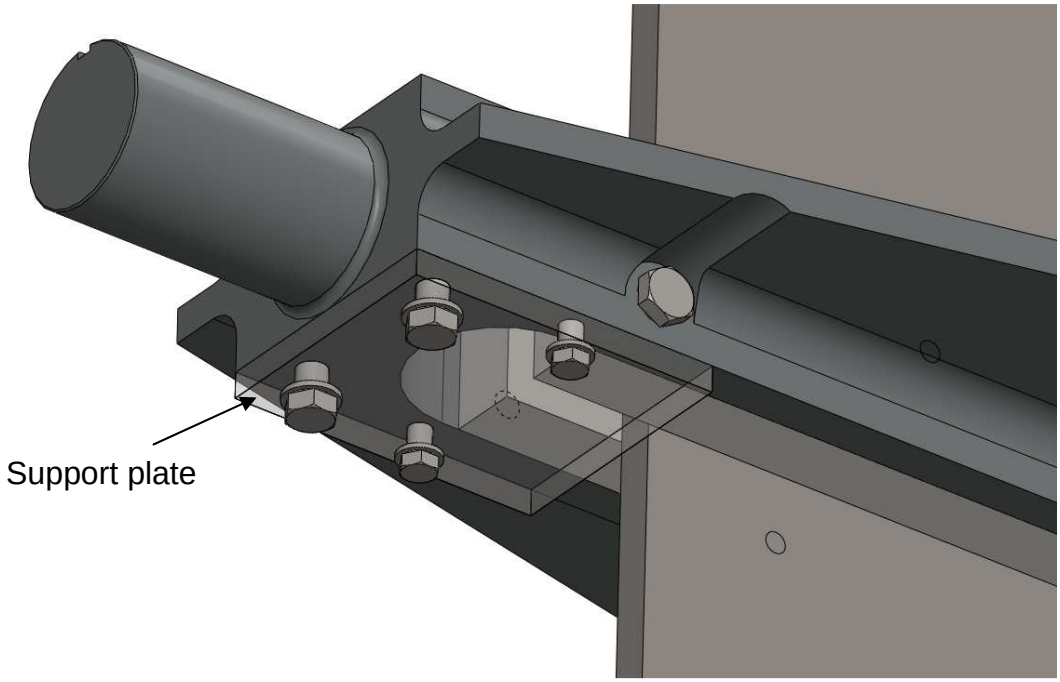

Figure 6.13: 3D CAD image of upper pivot jaw supporting plates

6.6.3 Shuttle: Upper Pivot Frame

The upper pivot frame performs the function of allowing the upper pivot shaft to move in the vertical direction as the blade material deflects between the pivot shafts. If the pivot shafts were fixed relative to one another, the blade material would be over-constrained and the stress relieving effect of the pivoting clamp design would be substantially reduced. The frame pivots on a 150mm seamless line pipe shaft (Figure 6.14) to ensure maximum stiffness and, therefore, minimal deflection between the two pillow blocks when the tube is under load from the blade material reaction forces (Appendix D Sections 7.0, 8.0 and 9.0).

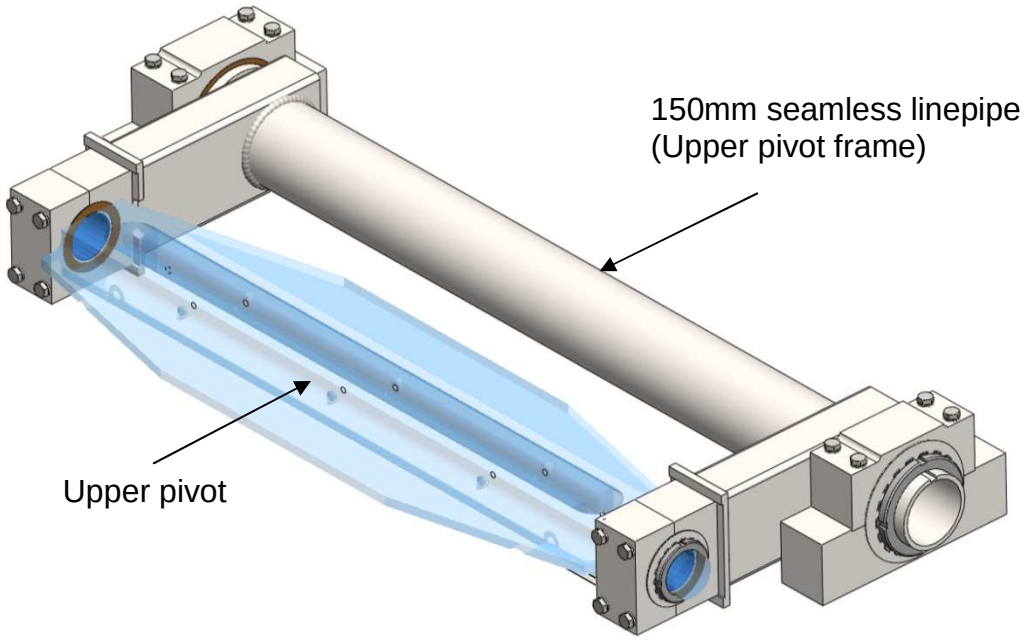

Figure 6.14: 3D CAD image of upper pivot frame

6.6.4 Shuttle: Lower Pivot

The lower pivot has been designed using the same method as the upper pivot. There is less of a reaction to blade material forces required at this pivot compared to the upper pivot (Section 11.0 Appendix D). However, this is countered by the requirement of the pivot to support the mass of the blade material. The lower pivot design for the scaled sculpture is presented in Figure 6.15.

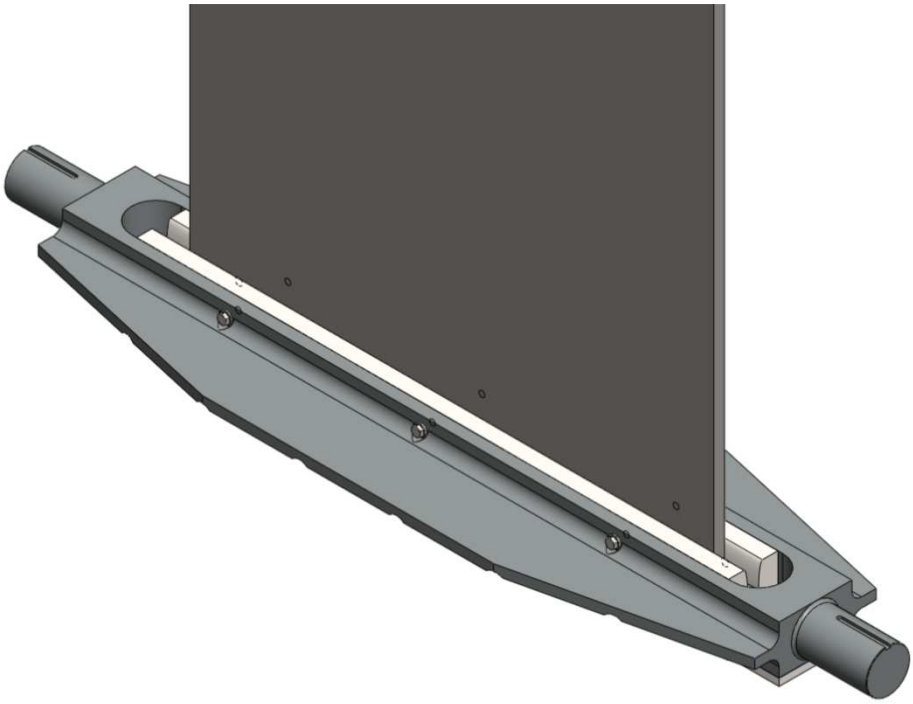

Figure 6.15: 3D CAD image of lower pivot clamp

There are various differences in the lower pivot when compared to the design of the upper pivot. All supporting bolts are bolted through the blade material to support the mass of the blade (Figure 6.16). There is effectively no bending stress in the blade material in the lower pivot, therefore fatigue of the titanium at this location due to the stress concentration of bolt holes can be ignored.

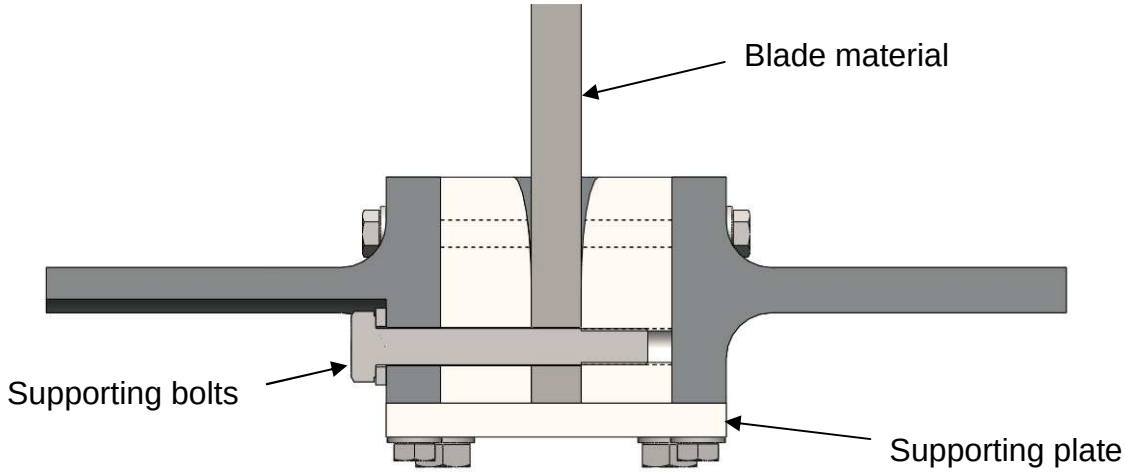

Figure 6.16: 3D CAD cross section of lower clamp illustrating the function of the blade material supporting bolts and plate

Another addition to the lower pivot is the presence of a capping plate across the cavity for the blade material (Figure 6.16). This works as a failsafe for the blade material should the supporting bolts fail for any reason.

6.6.5 Shuttle: Pivoting Media

The concept design phase of Section 6.5.1 resulted in bushes being selected for the rotating media of the pivoting shafts in the shuttle clamp. PTFE/Lead impregnated steel DU bush items have been selected for all rotating media in the pivoting clamp. These will be housed in custom mild steel pillow blocks as shown in Figure 6.17. The M16 bolts used to mount the top half of each pillow block are to be tightened to a torque of 224Nm (Section 6 Appendix D).

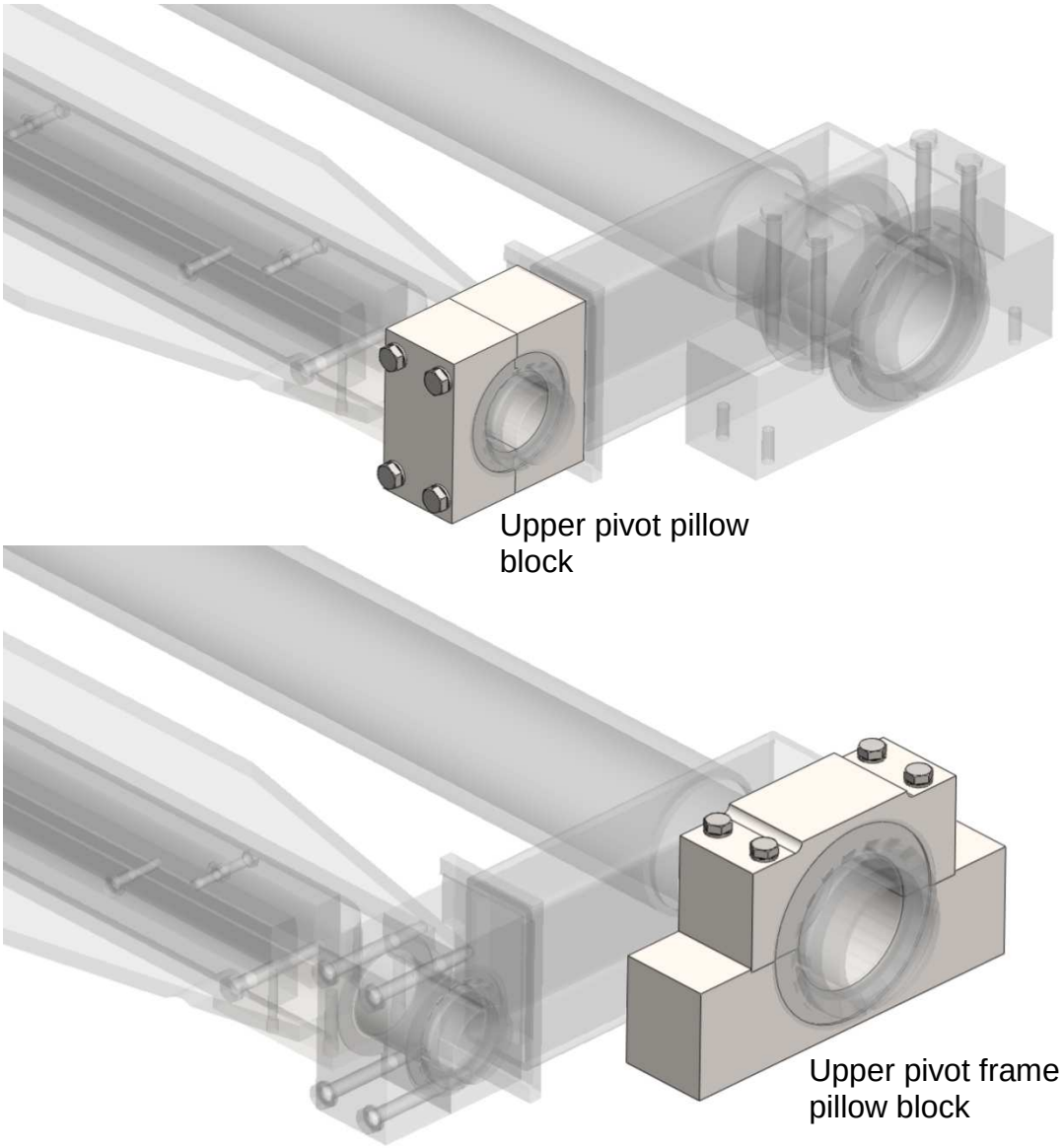

Figure 6.17: The two designs of pillow blocks utilised in the upper pivot of the Giant Blade design

All shafts will be restrained axially using thrust washers of the same material as the DU bushes and locking nuts as shown in Figure 6.18.

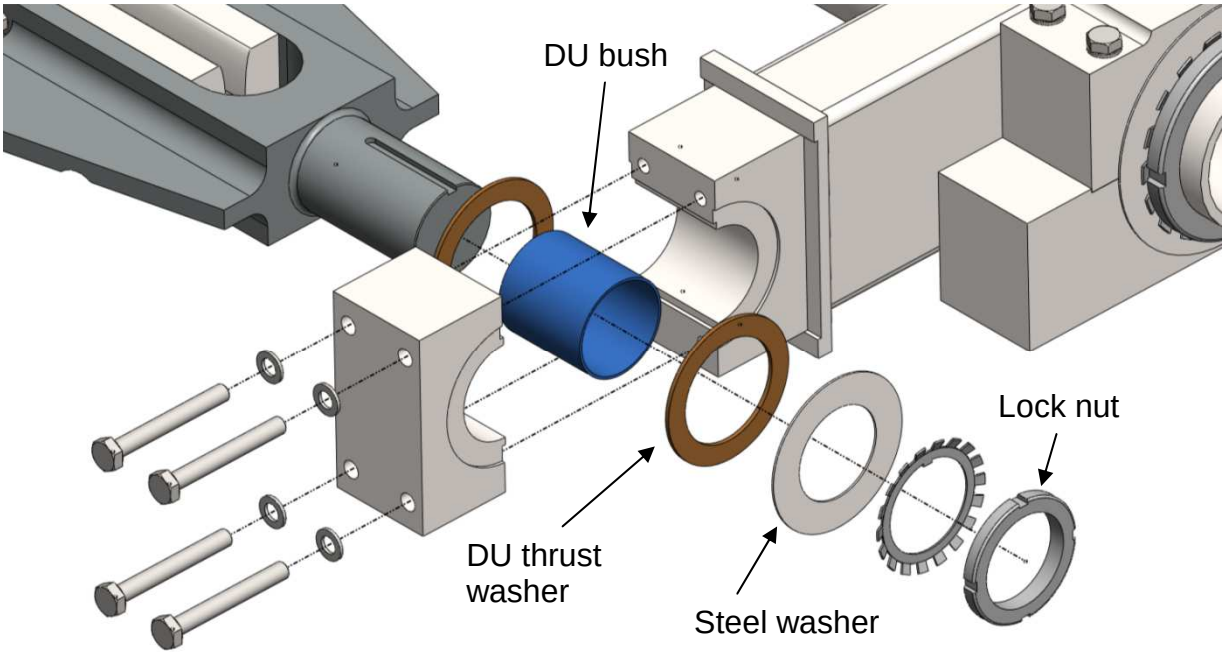

Figure 6.18: Exploded view of the rotating media used in the pivoting components of Giant Blade

The steel washer on the lock nut side of the assembly protects the thrust washer from the locking washer and provides a flat, consistent bearing surface for the thrust washer.

6.6.6 Shuttle: Frame

The shuttle frame is a welded structure made up of a combination of square and rectangular hollow sections to maximise stiffness and minimise mass (Figure 6.19).

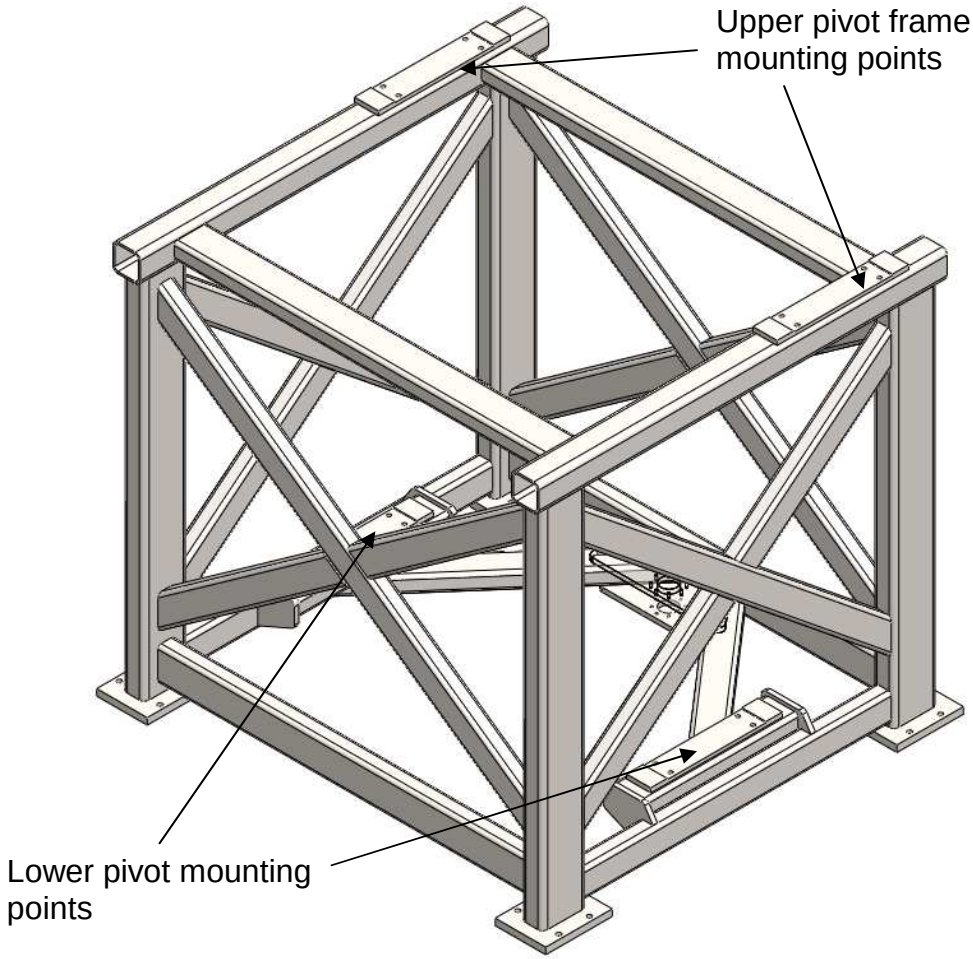

Figure 6.19: Shuttle frame structure

The mass of this frame is the dominating factor in selecting the size of motor required to oscillate the shuttle hence optimising the strength to weight ratio will minimise cost in this area of the mechanism design. FEA studies were carried out in Solidworks Simulation until the maximum stresses were within the safe cyclic loading limits as specified in BS5400 (BS, 1982) (Section 10.0 Appendix D). The optimum strength to weight ratio, while achieving all mounting requirements, was achieved by employing a cube type frame with diagonal bracing. The horizontal bracing at the base of the shuttle frame in Figure 6.20 is designed to give direct load paths from the frame to shuttle drive connection to the lower pivot support of the blade material.

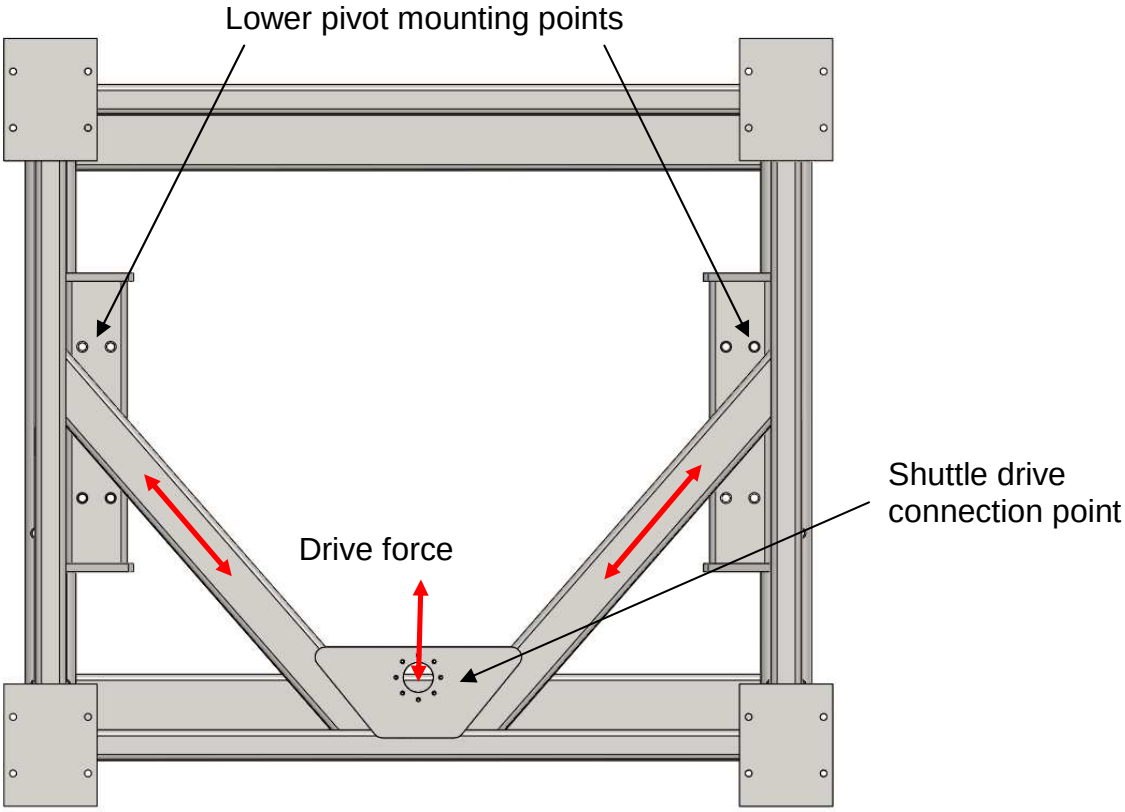

Figure 6.20: Base of the shuttle frame indicating the bracing to transfer drive forces directly to the blade material

The shuttle frame should be heat treated and galvanised before the mounting pads for the pillow blocks and linear guides are milled flat to ensure accuracy of all mounting points on the frame. This is highly important to ensure that the linear guides are mounted in such a way that they do not bind and/or develop premature wear.

6.6.7 Shuttle Drive Mechanism: Linear Guides

Linear guides from THK have been chosen (specification sheet in storage media) and are a 4-way equal load full ball roller type guide. Caged rollers were considered in this aspect of the design but it was found that the load reversals are detrimental to the longevity of the separating cages. Load conditions were

calculated in Section 12.0, Appendix D and provided to THK sales representatives in New Zealand. This information was then provided to THK in Japan and the HSR65-LR model was recommended to meet these requirements (see storage media for correspondence). During the development of the shuttle frame, the size of these linear guides was found to be insufficient to provide enough space for mounting bolts. The model of linear guide was then upgraded to the HSR85-LA to provide enough space around the structural member and welded area on the frame mounting pad (Figure 6.21).

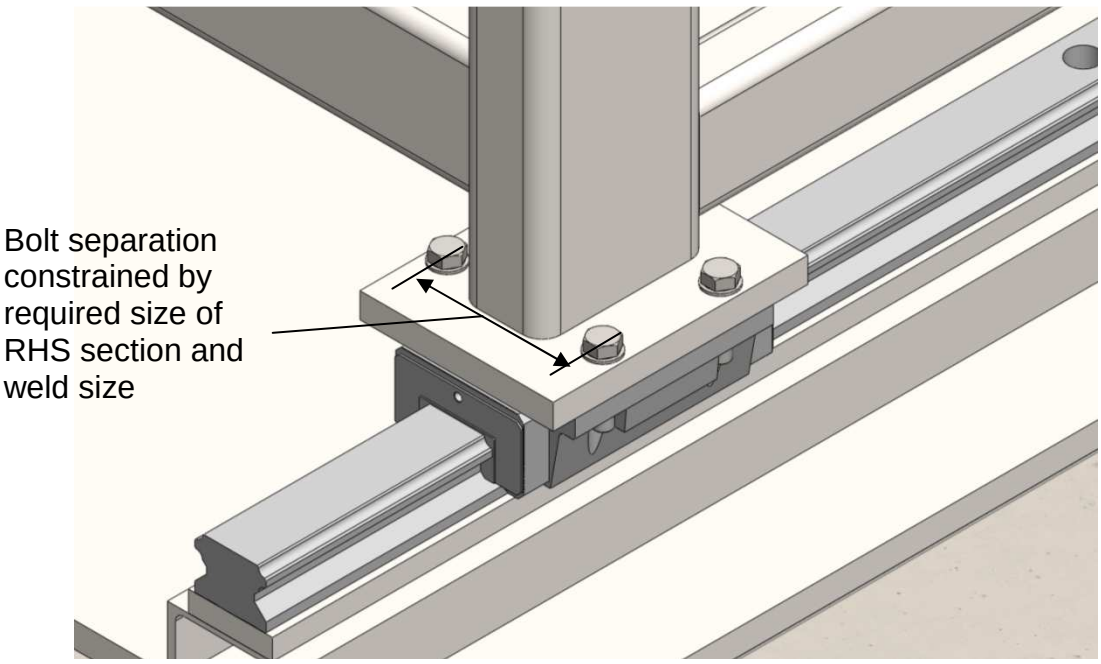

Figure 6.21: Shuttle frame structure supported by THK linear guide. Note the bolting arrangement constrained by the size of the RHS section in view.

This model of linear guide has approximately twice the static and dynamic load ratings of the HSR65-LR. Therefore, it will be sufficient in meeting the loading requirements of the scaled sculpture. The HSR85-LA is provided with anti-corrosion modifications for use in an outdoor environment. The guides are available in a pre-loaded arrangement to ensure minimum clearance and, hence,

operating noise. A continuously pressurised plunger type grease system will be employed to ensure adequate lubrication and minimum noise at all times of operation. This arrangement of linear guides will eliminate the requirement of bellows in the mechanism and solve the problem of noise being generated by displaced air in the mechanism for *Big Blade*. The linear guides are provided with low profile seals that seat against the guide rail with no trapped air.

6.6.8 Shuttle Drive Mechanism: Variable Stroke Mechanism Bearings

Section 6.5.2 outlines the desired arrangement of bearings in the variable stroke mechanism. These bearings all undergo oscillatory rotation and therefore have been selected based on their static load rating as recommended by SKF. They will be sized according to the loading conditions predicted in the mechanism. Hand calculations in Section 13.4 show that the spherical bearing unit SKF 22313 E/VA405 (see storage media for SKF catalogue) should be used for all spherical bearings in the variable stroke mechanism. The double row full complement cylindrical roller bearing SKF NNCF5016 (SKF catalogue) has been selected for the bearing locations where a high resistance to moment loading is required. Bearing 3 has been selected to be a set of tapered roller bearings for the reasons mentioned in Section 6.5.2. The upper bearing as in Figure 6.22 has been selected to be SKF 30215 J2/Q according to the calculations in Sections 13.5 and 13.6, Appendix D. Similarly, the lower bearing has been selected as SKF T2EE 100. These tapered roller bearings are expected to last at least 16 blade material lives before replacement. The spherical and cylindrical bearings should be replaced after each blade material life. The oscillatory motion that these bearings are subjected to is not traditionally what roller bearings are

designed for. Therefore, although the bearings have been selected based on a safety factor applied to their static load rating, the wear in these bearings will be accelerated and replacement will eliminate any noise that may develop in the mechanism.

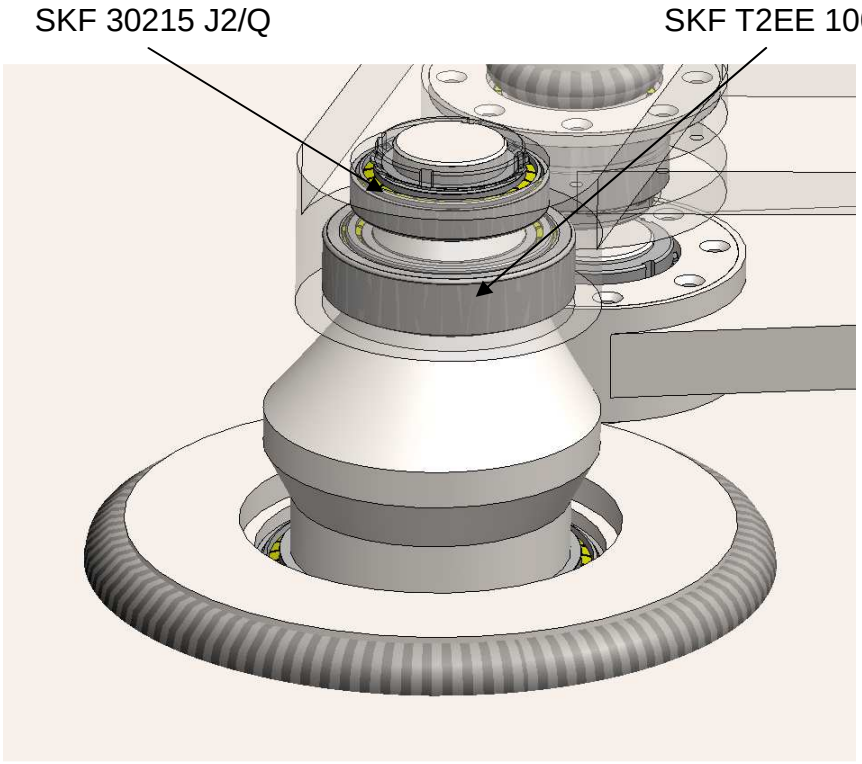

Figure 6.22: Tapered roller bearing arrangement for bearing location 3

Referring to Figure 6.3, the following table will summarise the bearing selections for the variable stroke mechanism.

Table 6.2: Summary of selected bearings for proposed variable stroke mechanism on scaled sculpture (refer to SKF catalogue on storage media)

Bearing	Type	Designation
1	Sealed spherical roller	SKF 22313 E/VA405
2	Full-complement double row cylindrical roller	SKF NNCF5016
3	Tapered roller bearings	SKF 30215 J2/Q SKF T2EE 100
4	Replaced by solid shaft	-
5	Full-complement double row cylindrical roller	SKF NNCF5016
6	Sealed spherical roller	SKF 22313 E/VA405
7	Full-complement double row cylindrical roller	SKF NNCF5016
8	Sealed spherical roller	SKF 22313 E/VA405

6.6.9 Shuttle Drive Mechanism: Bearing Table

The platform that supports the linear guides for shuttle oscillation has been termed the support table. The bearing trunnion for the base rotation mechanism is welded to the centre of this platform as shown in Figure 6.23.

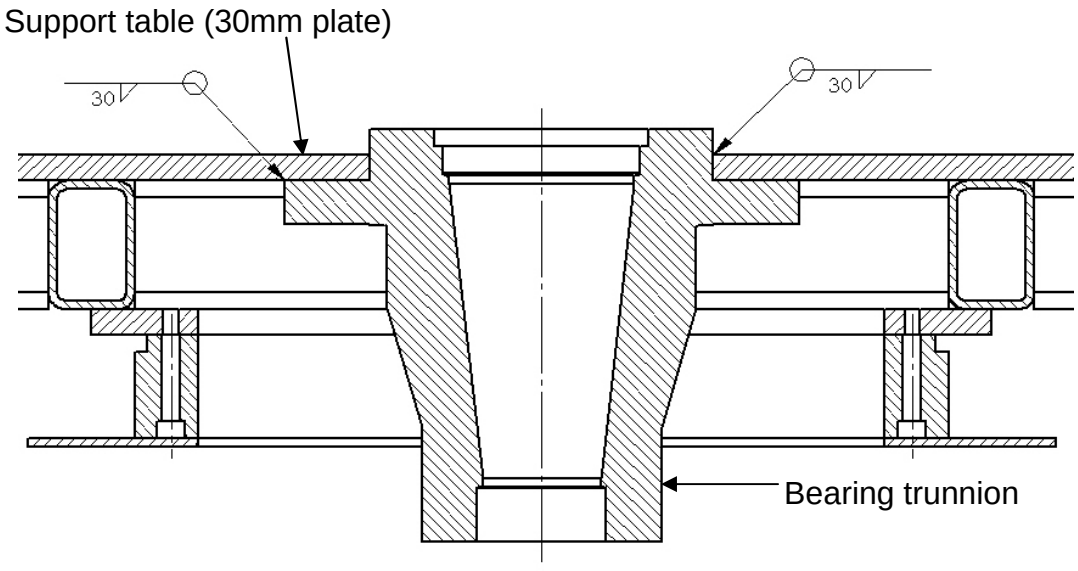

Figure 6.23: Section view of the support table showing bearing trunnion arrangement

The support structure of this platform will be manufactured of rectangular hollow steel sections which provide a stiff frame for the mild steel plate that forms the top of the bearing table. Hand calculations in Section 15.0, Appendix D were carried out to ensure that the deflection and stresses of the bearing table were within suitable limits. Another 30mm plate will be welded to the RHS frame on the underside of the bearing table to add stiffness to the platform and also provide a mounting location for the brake disc and base rotation drive pulley.

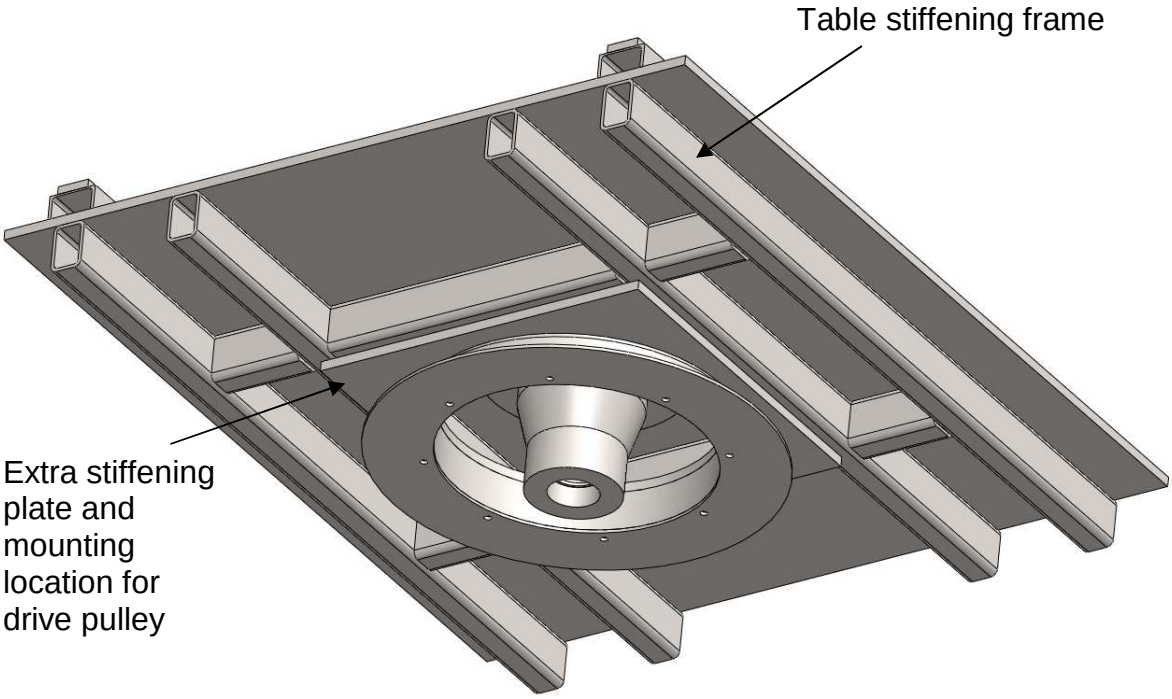

Figure 6.24: Bearing support table viewed from beneath showing the RHS frame and bearing trunnion

6.6.10 Shuttle Drive Mechanism: Oscillation Drive Shaft

The function of the oscillation drive shaft is to convert rotational motion from the drive motor to oscillatory motion of the shuttle frame. The drive shaft will be manufactured from 4140 high carbon steel and will be machined from a solid piece of 220mm diameter bar stock. The pin offset of 30mm provides 60mm of

stroke at the maximum stroke setting of the variable stroke mechanism as required (Section 2.2, Appendix D). Hand calculations in Section 14.0 were carried out to determine the minimum diameter of the shaft at the point where the bending and torsional stresses combine to give a worst case Von-Mises stress. A spreadsheet (see storage media) was generated to predict shaft deflections and the slope of the shaft at each bearing location. The maximum deflection of the shaft was calculated to be approximately 0.15mm in the worst case bending plane as seen in Figure 6.25.

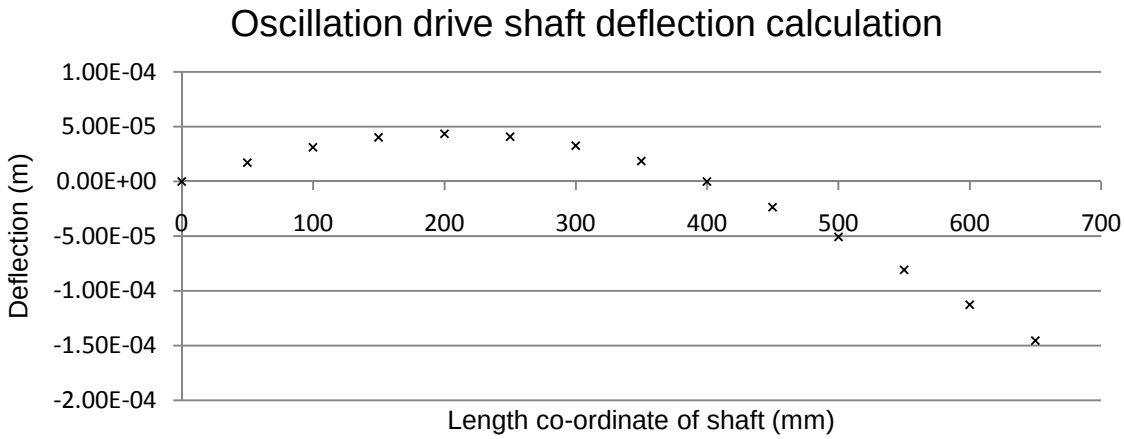

Figure 6.25: Calculated worst case scenario deflection of the oscillation drive shaft during operation

The slope values were optimised to be within safe limits specified for the tapered roller bearings chosen for the drive shaft (Sections 14.3 and 14.4, Appendix D).

6.6.11 Shuttle Drive Mechanism: Oscillation Drive Bearings

The tapered roller bearings for the oscillation drive shaft were sized using the worst case forces calculated for the variable stroke mechanism (Section 13.0, Appendix D). The bearing selection process is presented in Sections 14.3 and

14.4 of Appendix D. The top bearing has been selected as SKF item T4DB170 and the bottom bearing as SKF item 32020X/Q. These bearings are expected to outlast the blade material by at least 44 of the predicted blade material service periods (Section 14.3, Appendix D). This result is a function of the minimum diameter required by the shaft, as opposed to selecting a bearing too large for the application.

6.6.12 Base Rotation Mechanism

Section 6.5.3 resulted in tapered roller bearings being chosen as the best solution to this sub-function, as was the case with *Big Blade*. The constraining factor in selecting the size of these bearings was not the loading conditions experienced by the bearings as in the case of the oscillation drive mechanism drive shaft. The constraining factor in this case was the required critical OD of the bearing housing due to the bending moment in the bearing trunnion and the available steel bar stock. The bearing trunnion should be manufactured from 600mm bar stock. This size of stock steel is most commonly available in low strength grade steels and this was considered in strength calculations (Section 16.0, Appendix D). In this case, instead of calculating a critical diameter for the shaft as was carried out in Section 6.6.10 for the oscillation drive shaft, the factor of safety on the size of the bearing trunnion was calculated by the theory of Deutschman (Deutschman, Michels, & Wilson, 1975) (Section 16.0, Appendix D). Due to the nested nature of the base rotation mechanism, the size of the tapered roller bearings required meant that the loading conditions were more than sufficiently met, resulting in large factors of safety on the life of these bearings (Sections 16.1 and 16.2, Appendix D). The philosophy of designing the bearing

trunnion was to maintain a consistent wall thickness in the bearing trunnion itself that continues to the point where the trunnion is welded to the bearing platform while ensuring that the bending moment loading is spread across as large an area as possible. Proportions were taken from the design of the bearing trunnion in *Big Blade*. The resulting factor of safety for fatigue on the bearing trunnion is 18 (Section 16.0, Appendix D). Although this is a large safety factor, the importance of providing a large area over which the bending moment of the vibrating blade can be distributed took precedence over reducing the size of the trunnion. See Figure 6.26 for the resulting design of the bearing trunnion and the appropriate tapered roller bearings.

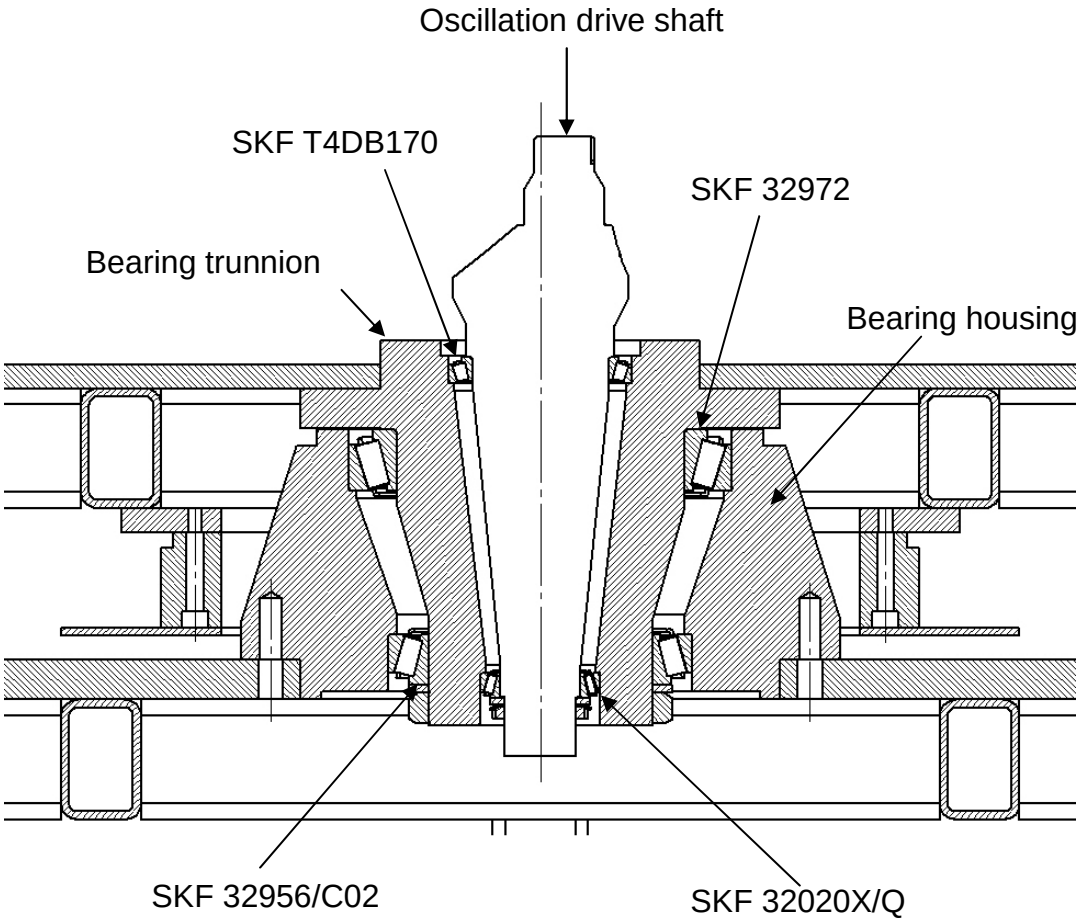

Figure 6.26: Nested drive shafts in the drive mechanism of Giant Blade

Deflections and slopes of the bearing trunnion at critical locations were calculated using the same method as in Section 6.6.10 (see shaft deflection spreadsheet in storage media). The design of the trunnion has ensured a stiff structure where deflection is close to zero and the slope at each bearing is negligible. The tapered roller bearings will also provide some stiffness to the assembly. The top bearing has been chosen as SKF 32972 and the bottom bearing has been chosen as SKF32956/C02. The life of these bearings is effectively infinite due to the required size of the bearing trunnion. The bearing housing will be manufactured from 800mm steel bar stock and has been designed for an infinite working life.

6.6.13 The general assembly

The embodiment design of the scaled *Blade* drive mechanism is presented in Figure 6.27 at the current stage of completion and consists of the sub-systems discussed in Sections 6.5.1 to 6.6.12.

6.6.14 Assessment of the embodiment design stage

The current design has been assessed according to the method recommended by Hales and Gooch (Hales & Gooch, 2004). Figure E.4 presents the confidence in meeting each category of the design requirement specifications in a general sense. The worksheet indicates that confidence has increased for some manufacturing requirements, such as production and assembly. It has been shown that the sculpture mechanism to drive the blade material can be manufactured using standard components and materials. However, other manufacturing requirements such as purchasing and transport require some

attention for solutions. Operational and maintenance requirements have been assessed in selecting components in the embodiment design phase which increases confidence in these areas and timing requirements have improved with a suitable supplier for the blade material identified.

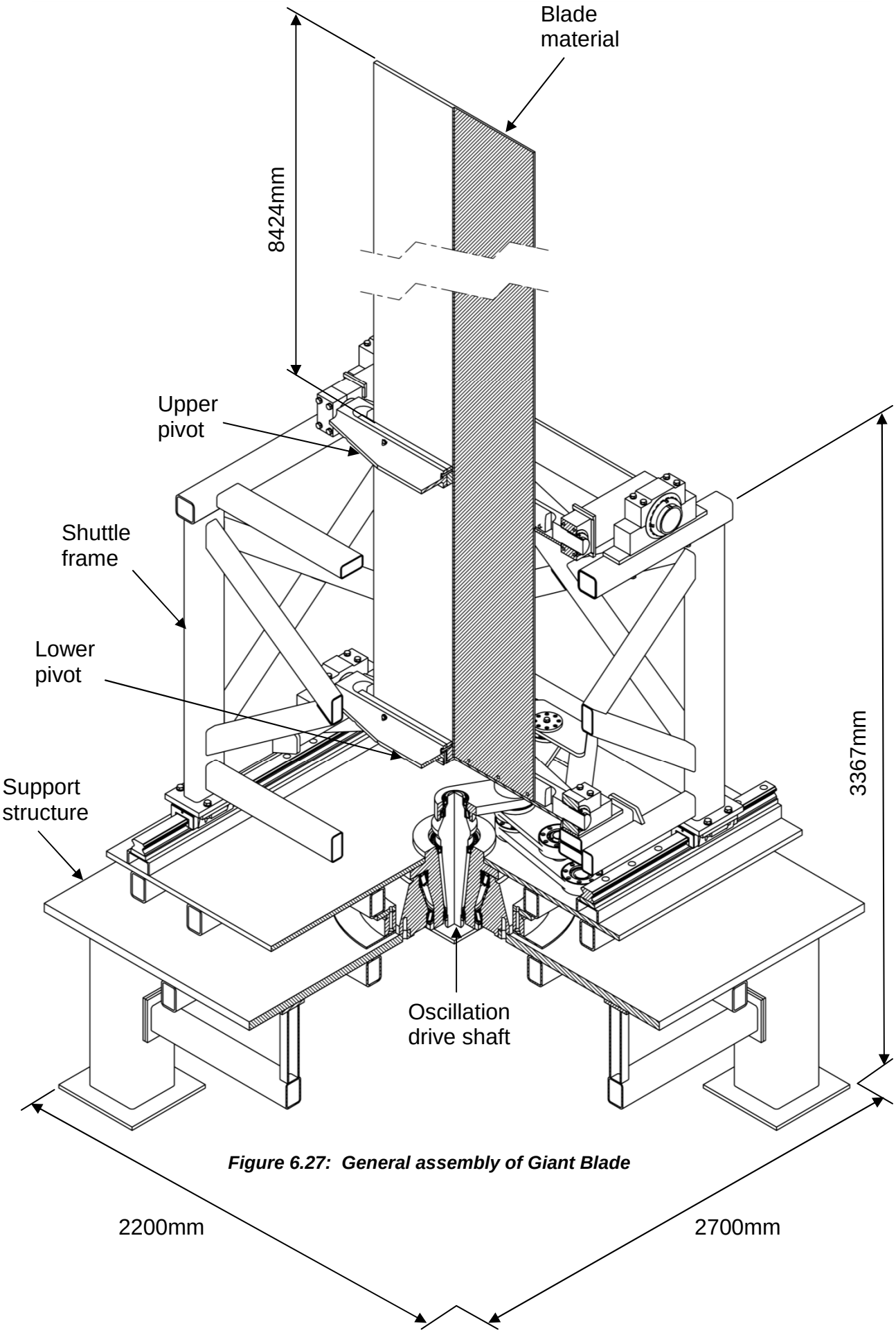

Figure 6.27: General assembly of Giant Blade

6.7 Conclusions

This chapter has presented a partial embodiment design for the drive mechanism of *Giant Blade.* The embodiment eliminates some of the design issues highlighted in the *Big Blade* mechanism. Linear guides from manufacturer THK have been chosen to eliminate the ball bearing rattle that exists in the circular linear bearings in *Big Blade*. A pressurised grease system with low profile guide seals will eliminate the need for bellows to protect the linear guides from environmental damage. A solution to the gearbox noise has been more difficult to achieve due to the large drive forces required to excite the blade material. A gearbox with bevel helical gears has been recommended to withstand the required loading conditions but it is envisaged that a better solution to the gearbox/drive motor noise pollution problem would be to develop an enclosure for the sculpture mechanism with active noise reduction. This could be an all encompassing solution to all noise pollution issues in the scaled sculpture mechanism. Technology in active noise control has improved over the past decade and the University of Canterbury Mechanical Engineering Department has a specific research group dedicated to acoustic study.

A new partial embodiment of the drive mechanism for the blade material in the kinetic sculpture Giant Blade has been completed using standard components at the scale determined in Chapter 3. This design is predicted to eliminate noise issues that exist currently in Big Blade. In the process of designing the new sculpture it has become apparent that an enclosure that employs

active noise control would provide an elegant solution to the noise pollution issues in Blade sculptures.

7 Future work and recommendations

7.1 Introduction

The purpose of this chapter is to provide a possible blueprint for realising Giant Blade at the maximum economic scale.

Due to project timelines, the manufacture of the scaled sculpture will not be completed during the course of this Masters project. The search for an appropriate blade material has consumed significantly more time than originally predicted. In an effort to minimise the disruption to the project as it progresses toward the manufacture stage, this chapter will provide a comprehensive list of the known remaining tasks as well as recommendations from the author regarding how these tasks could be executed. It is intended simply as a suggested course of work rather than a dictation of how work should progress.

7.2 Future work

7.2.1 Ball and wand mechanism

The Design Requirement Specification of Section 6.3 states the ball and wand should be free to move outwards and inwards as well as up and down relative to the blade material. This mechanism has not been designed in the embodiment presented in Chapter 6. Further work should be completed to implement a suitable design for the ball and wand mechanism on the current embodiment design for the scaled sculpture. Currently, there exists various types

of X-Y actuators (Figure 7.1) that could perform the basic function required by the ball and wand sub-system should the predicted loading conditions be met or exceeded by this type of actuator.

Figure 7.1: X-Y actuator of the type that could be utilised for the ball/wand control mechanism. [Retrieved from http://www.intellidrives.com/XY-Tables/XY-Table-BSMA-080-080-600x300]

7.2.2 Blade material

At the time of writing, the blade material has been sourced from Baoti Titanium in China. The dimensions are 10024mm x 1080mm x 22mm corresponding to a *Blade* scale ratio of 5.17 as calculated in Chapter 3. The price of the blade material has been quoted to be $55USD/kg with the cost of insurance and freight being met by Baoti to the Auckland seaport. The lead time is 110 days from the date of order. Mace Engineering in Christchurch has offered the use of their floor borer to provide the desired surface finish. This aspect of the artistic requirements (Table E.1) has proved to be the most time consuming part of the project. The size of the blade material restricts the options available for surface treatment. Many titanium suppliers suggest that the blade material be sanded by hand and while this produced acceptable results on small samples,

this would not be acceptable on the final piece. The aesthetics of the blade material are an integral part of the final experience of the kinetic sculpture and a hand applied sanded finish would result in inconsistencies. A floor borer would provide a sanded grain that can be exactly parallel to the long edge of the blade. Further study into a possible sanding attachment for this floor borer should be carried out. The floor borer spindle has various options for attachment that can be utilised as in Figure 7.2.

Figure 7.2: Floor borer spindle at Mace Engineering. Note the threaded holes for attachment as well as the standard tooling attachment.

7.2.3 Component selection and implementation

The embodiment design of the *Giant Blade* drive mechanism is partially complete. The shuttle to support the blade material has been designed to a point

where detail design is now possible and manufacturing drawings can be completed. The cranks of the variable stroke mechanism should be developed to ensure an optimum strength to weight ratio for each. The machined components of the shuttle drive mechanism and the base rotation mechanism are also ready for detailed design and manufacturing drawings. The support structure has been partially designed and should be checked for strength.

Component selection has been completed for the sculpture mechanism and now requires implementation to the CAD model. Loading conditions (Table 7.1) were provided to suppliers in Christchurch and the components in the quotation provided (storage media) were suggested based on the information provided.

Table 7.1: Loading conditions specified for component selection in Giant Blade design

Loading condition	Value	Reference
Maximum oscillation drive motor torque	1094Nm	Solidworks Simulation results Chapter 5
Maximum oscillation drive speed	243RPM	Section 2.1 Appendix D
Minimum oscillation drive speed	79RPM	Section 2.1 Appendix D
Variable stroke mechanism actuator maximum load	75kN	Solidworks Simulation results Chapter 5
Torque feedback from blade material	1152Nm	Section 18.0 Appendix D

7.2.4 Predicted Noise Issues

There will undoubtedly be some noise pollution from the mechanism in its final state due to the continuous trade-off between strength and noise of components and also the sheer size of the parts interacting with each other. The THK linear guides emit some noise depending on the relative speed of the guide and the rail. This information is readily available from the THK factory through contacts at SAECOWilson Bearings. An example of this sound level testing has been provided in the attached storage media along with the appropriate contact at SAECOWilson.

The gearboxes are also an inevitable source of noise pollution during performances. The load reversals due to the nature of the rotational/oscillatory motion conversion in the drive mechanism will accentuate the effects of backlash and result in noise. As a solution to the noise issues predicted in *Giant Blade* it is suggested that a parallel avenue of research be initiated in the acoustic design of an enclosure for the mechanism. This enclosure could utilise Active Noise Control (ANC) technology to minimise noise pollution during *Blade* performances. The project could begin either as soon as possible using information from manufacturers regarding component noise, or once the sculpture mechanism has been built when the noise pollution can be accurately measured.

7.3 Recommendations

Of interest to the successor to this project, the following is a summary of the anticipated scope of works that remain in order to complete the project. The list is presented in order of perceived importance.

- Optimise the crank design in the variable stroke mechanism. Strength to weight ratio should be a high priority to reduce unnecessary inertial effects.
- The support structure should be checked for strength.
- The components in the attached quotation (storage media) should be implemented into the current CAD model.
- A disc brake for the base rotation mechanism should be sized and implemented into the current CAD model.
- A mechanism to support and control the position of the ball/wand should be designed and implemented into the current CAD model.
- THK should be contacted regarding the continuously pressurised grease system. The appropriate contact at SAECOWilson bearings in Auckland has been provided in the attached storage media.
- Radial seals should be selected and implemented in the CAD model for the base rotation mechanism and oscillation drive bearings.
- An order needs to be placed for the blade material titanium plate. The details regarding the status of this part of the project are given in Section 7.2.2.
- Design an attachment capable of driving a sanding belt that can be attached to the Mace Engineering floor borer. More information can be found in Section 7.2.2.
- Liaise with Mace Engineering in regards to forming a project plan for manufacturing the sculpture mechanism and treating the blade material.

- Discuss the possibility of an active noise control enclosure with the acoustics research group.
- Begin purchasing components while developing an overall costing for the scaled sculpture.

References

ASM Handbook. (1990a). Fatigue and Fracture *ASM Handbook* (10th ed., Vol. 19).

ASM Handbook. (1990b). Heat Treating *ASM Handbook* (10th ed., Vol. 4).

ASM Handbook. (1990c). Properties and Selection: Non Ferrous Alloys and Special Purpose Materials *ASM Handbook* (10th ed., Vol. 2).

ASTM International. (2011). ASTM Standard E1049-85 *"Cycle Counting in Fatigue Analysis"* (2011e1 ed.). West Conshohocken, PA.

ASTM International. (2013). ASTM Standard B265-13a *"Titanium and Titanium Alloy Strip, Sheet, and Plate"*. West Conshohocken, PA.

Autocar Technical Staff. (1919). *The Autocar handbook : for the motorist* (9th ed.). London: Iliffe & Sons.

Baek, S., Cho, S., & Joo, W. (2008). Fatigue life prediction based on the rain-flow cycle counting method for the end beam of a freight car bogie. *International Journal of Automotive Technology, 9*(1), 95-101.

Boyer, R., & Collings, E. (1993). *Materials Properties Handbook: Titanium Alloys*: ASM International.

BS, B. (1982). Part10, Code of Practice for Fatigue: British Standards Institution.

Den Hartog, J. (1956). Mechanical Vibrations: McGraw-Hill, New York.

Deutschman, A. D., Michels, W. J., & Wilson, C. E. (1975). *Machine Design Theory and Practice*. New York: Macmillan Publishing Co.

Dowling, N. E. (1993). *Mechanical Behavior of Materials: Engineering Methods for Deformation, Fracture, and Fatigue*. New Jersey: Prentice Hall.

Dowling, N. E. (2004). *Mean stress effects in stress-life and strain-life fatigue.* Paper presented at the SAE Brasil International Conference on Fatigue, São Paulo.

Downing, S. D., & Socie, D. (1982). Simple rain-flow counting algorithms. *International Journal of Fatigue, 4*(1), 31-40.

Frisch-Fay, R. (1961). A new approach to the analysis of the deflection of thin cantilevers. *Journal of Applied Mechanics, 28*(1), 87-90.

Gallagher, J., van Stone, R., deLaneuville, R., Gravett, P., & Bellows, R. (2001). Improved high-cycle fatigue (HCF) life prediction. *NASA STI/Recon Technical Report N, 3*, 05515.

Gooch, S., & Raine, J. (2000). The dynamics and limits on the scaling of a flexible kinetic sculpture. *Proceedings of the Institution of Mechanical Engineers, Part C: Journal of Mechanical Engineering Science, 214*(4), 537-548.

Gooch, S. D. (2001). *Design and Mathematical Modelling of the Kinetic Sculpture Blade.* (Doctor of Philosophy in Mechanical Engineering), University of Canterbury, Christchurch, New Zealand.

Hales, C., & Gooch, S. (2004). *Managing Engineering Design*. London: Springer.

Hempel, M., & Hillnhagen, E. (1969). *The fatigue strength of commercial titanium alloys*. Farmborough Ministry of Technology, Royal Aircraft Establishment, Library Transaction No. 1353.

Horrocks, R. (2001). *Len Lye - A Biography*. Auckland, New Zealand: Auckland University Press.

Horrocks, R. (2009). *Art that Moves - The Work of Len Lye*. Auckland, New Zealand: Auckland University Press.

Hosseini, S. (2012). Fatigue of Ti-6Al-4V. In R. Hudak, M. Penhaker & J. Majernik (Eds.), *Biomedical Engineering - Technical Applications in Medicine* (pp. 75-92): InTech.

Jones, F. D., Oberg, E., & Horton, H. L. (2004). *Machinery's Handbook* (27th ed.): Industrial Press, Incorporated.

Kang, D.-H., Jang, C., Park, Y.-S., Han, S.-Y., & Kim, J. H. (2012). Fatigue Reliability Assessment of Steel Member Using Probabilistic Stress-Life Method. *Advances in Mechanical Engineering, 2012*, 1-10.

Manson, S. S., Nachtigall, A. J., Ensign, C. R., & Freche, J. C. (1965). Further Investigation of a Relation for Cumulative Fatigue Damage in Bending. *Journal of Engineering for Industry, 87*(1), 25-35. doi: 10.1115/1.3670753

Matsuishi, M., & Endo, T. (1968). Fatigue of metals subjected to varying stress. *Japan Society of Mechanical Engineers, Fukuoka, Japan*, 37-40.

McCallion, H. (1973). *Vibration of linear mechanical systems*: Longman London.

Nayfeh, A., & Mook, D. (1995). Energy transfer from high-frequency to low-frequency modes in structures. *Journal of Vibration and Acoustics, 117*(B), 186-195.

Pahl, G., & Beitz, W. (1996). Engineering Design: A Systematic Approach (3rd ed.). London: Springer-Verlag.

Palm, W. J. (2007). *Mechanical Vibration*. USA: John Wiley & Sons.

Raine, J., & Gooch, S. (1998). Dynamic Analysis and Engineering Design of Flexible Kinetic Sculptures. *Transactions of the Institution of Professional Engineers New Zealand: General Section, 25*(1), 29.

Shigley, J. E., Mischke, C. R., Budynas, R. G., Liu, X., & Gao, Z. (1989). *Mechanical engineering design* (6th Metric ed.): McGraw-Hill New York.

Wang, C. (1986). A critical review of the heavy elastica. *International Journal of Mechanical Sciences, 28*(8), 549-559.

Webb, E. A. (Feb. 2012 - Feb 2014.). *Project meetings with S.D. Gooch and T.D. Spencer*. University of Canterbury.

A. Test Equipment Manufacturing Drawings

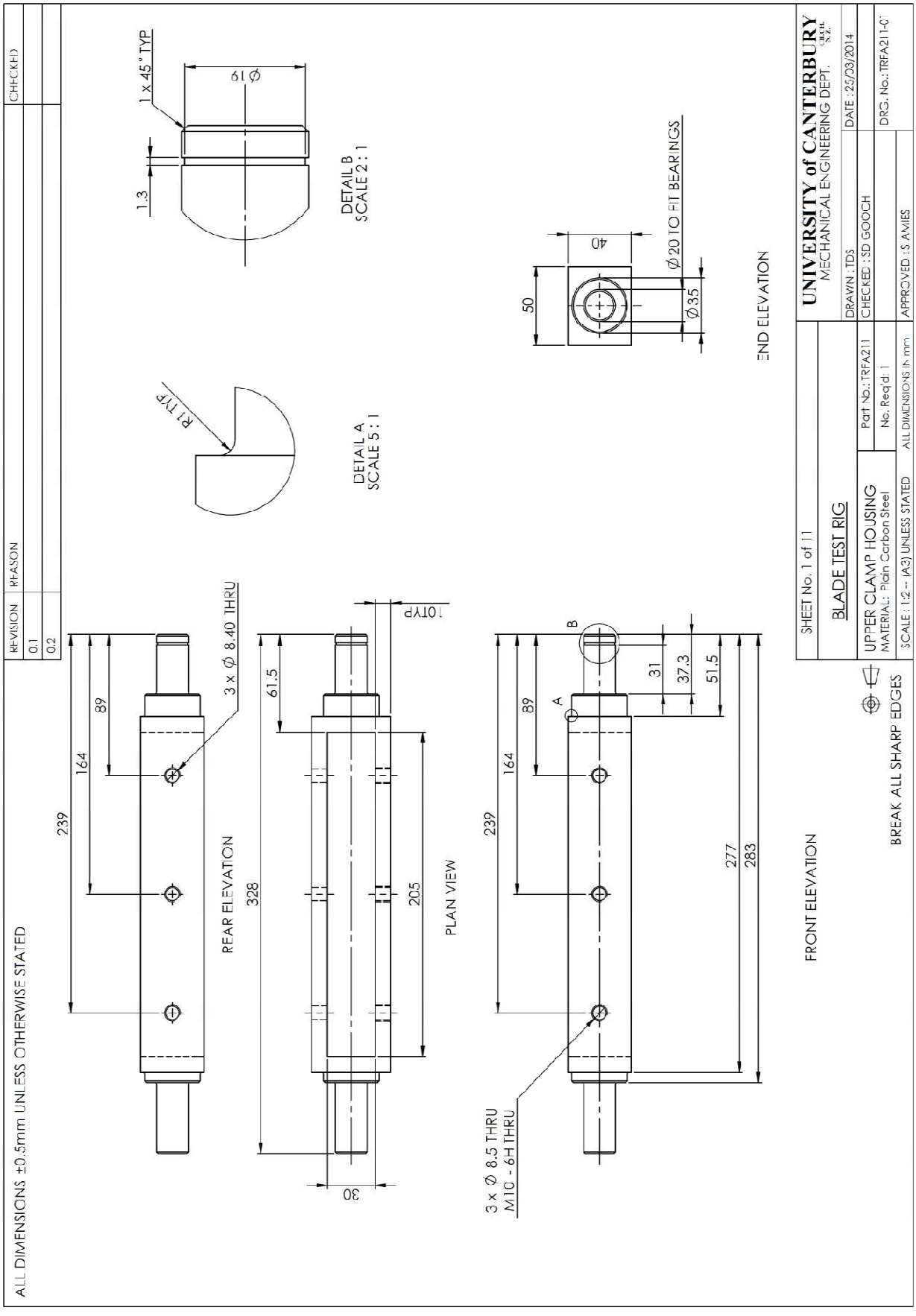

Figure A.1: Manufacturing drawing of the upper clamp housing in fatigue test rig. Drawing no. TRFA211-01

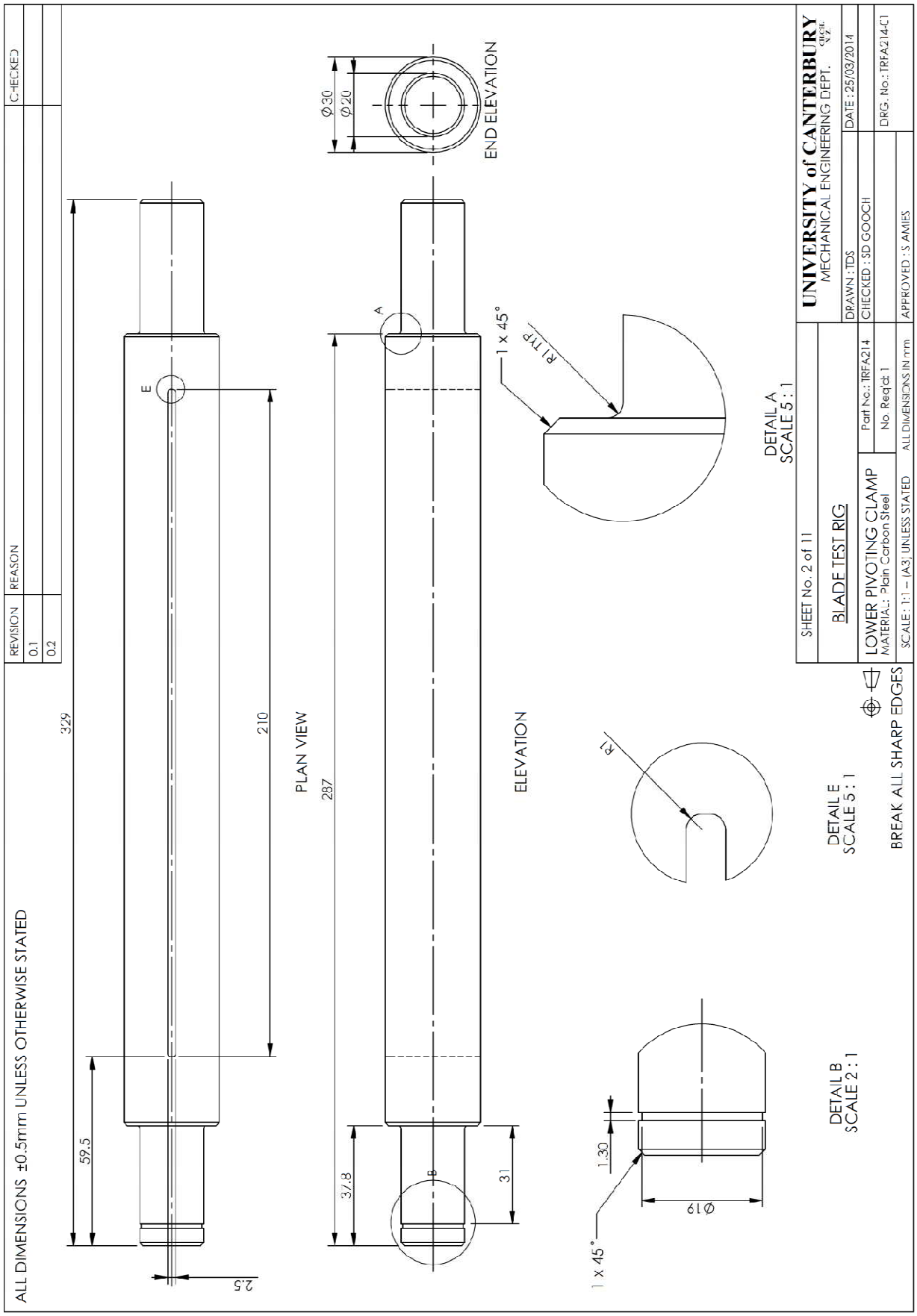

Figure A.2: Manufacturing drawing of lower pivoting clamp in fatigue test rig. Drawing no. TRFA214-01

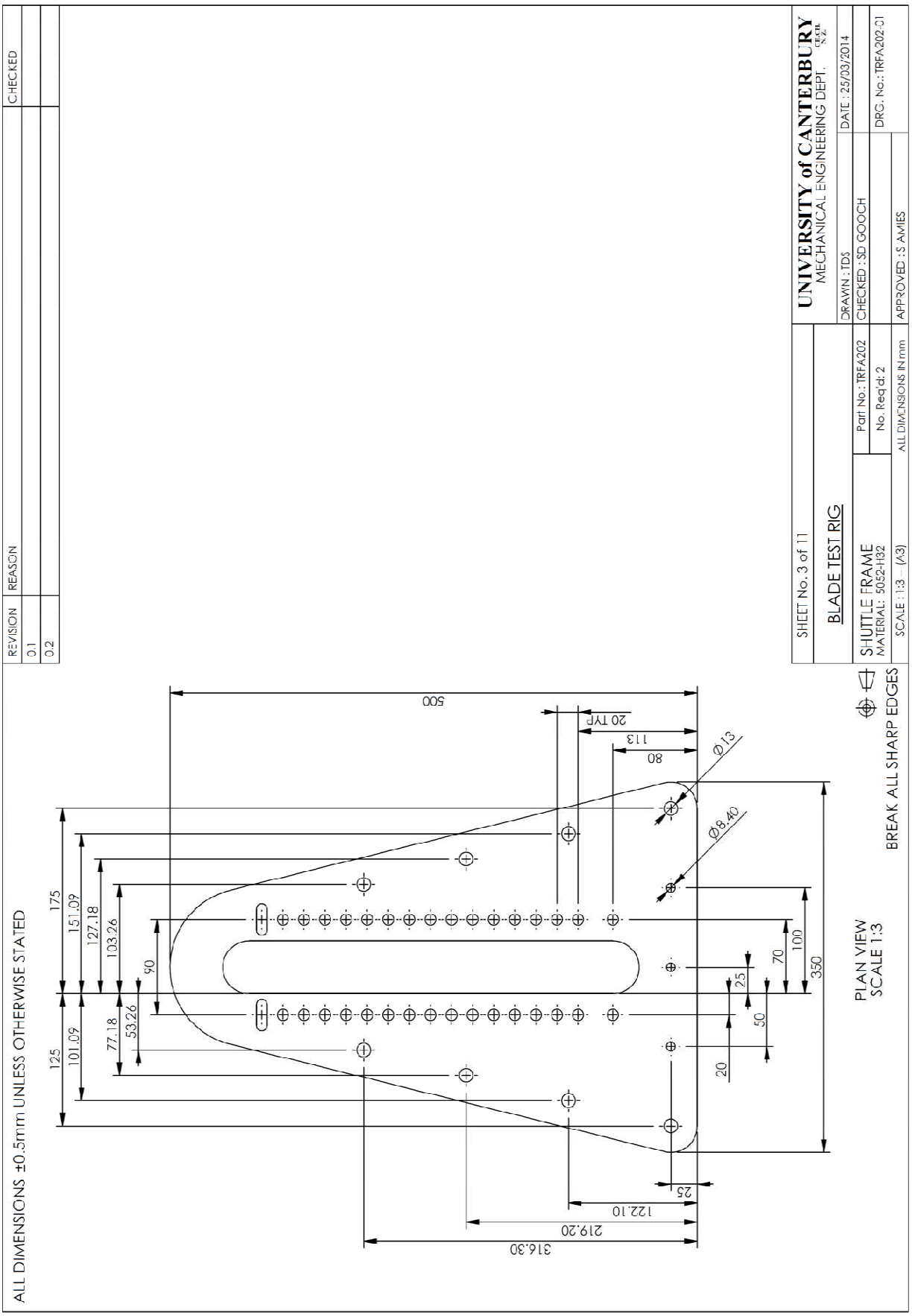

Figure A.3: Manufacturing drawing of shuttle frame in fatigue test rig.

Drawing no. TRFA202-01

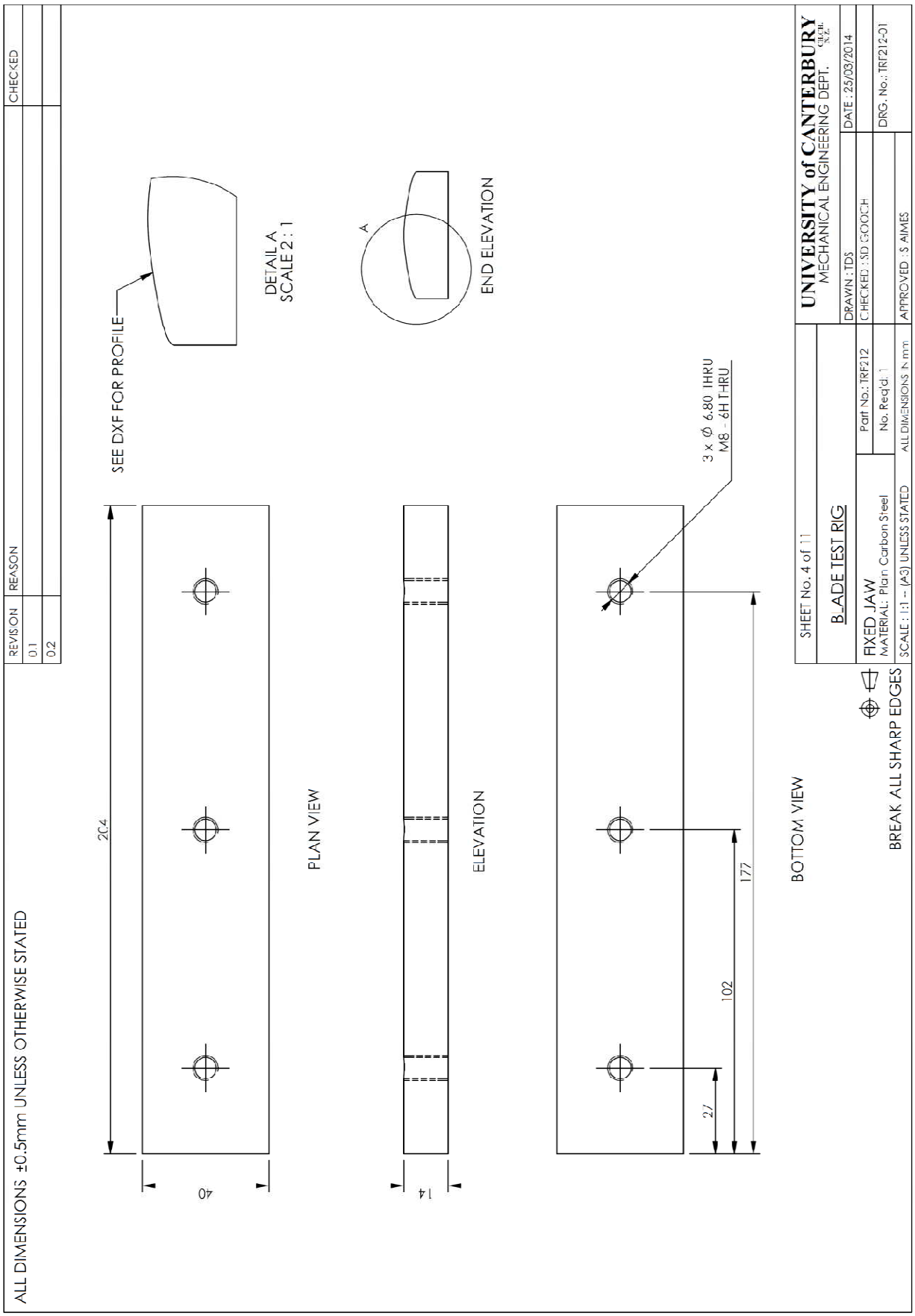

Figure A.4: Manufacturing drawing of the fixed jaw in upper pivot of the fatigue testing rig. Drawing TRF212-01

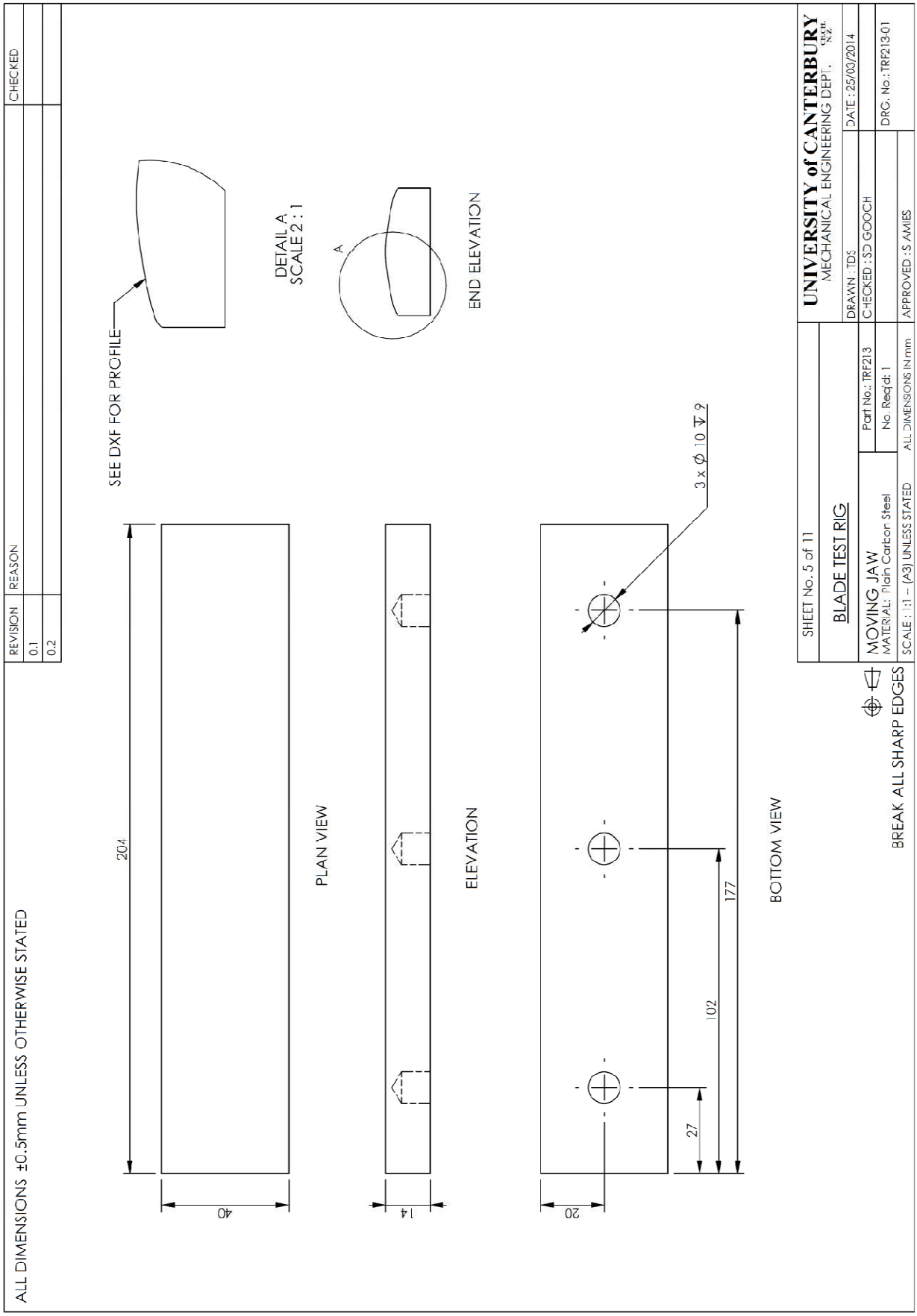

Figure A.5: Manufacturing drawing of the floating jaw in upper pivot of the fatigue testing rig. Drawing no, TRF213-01

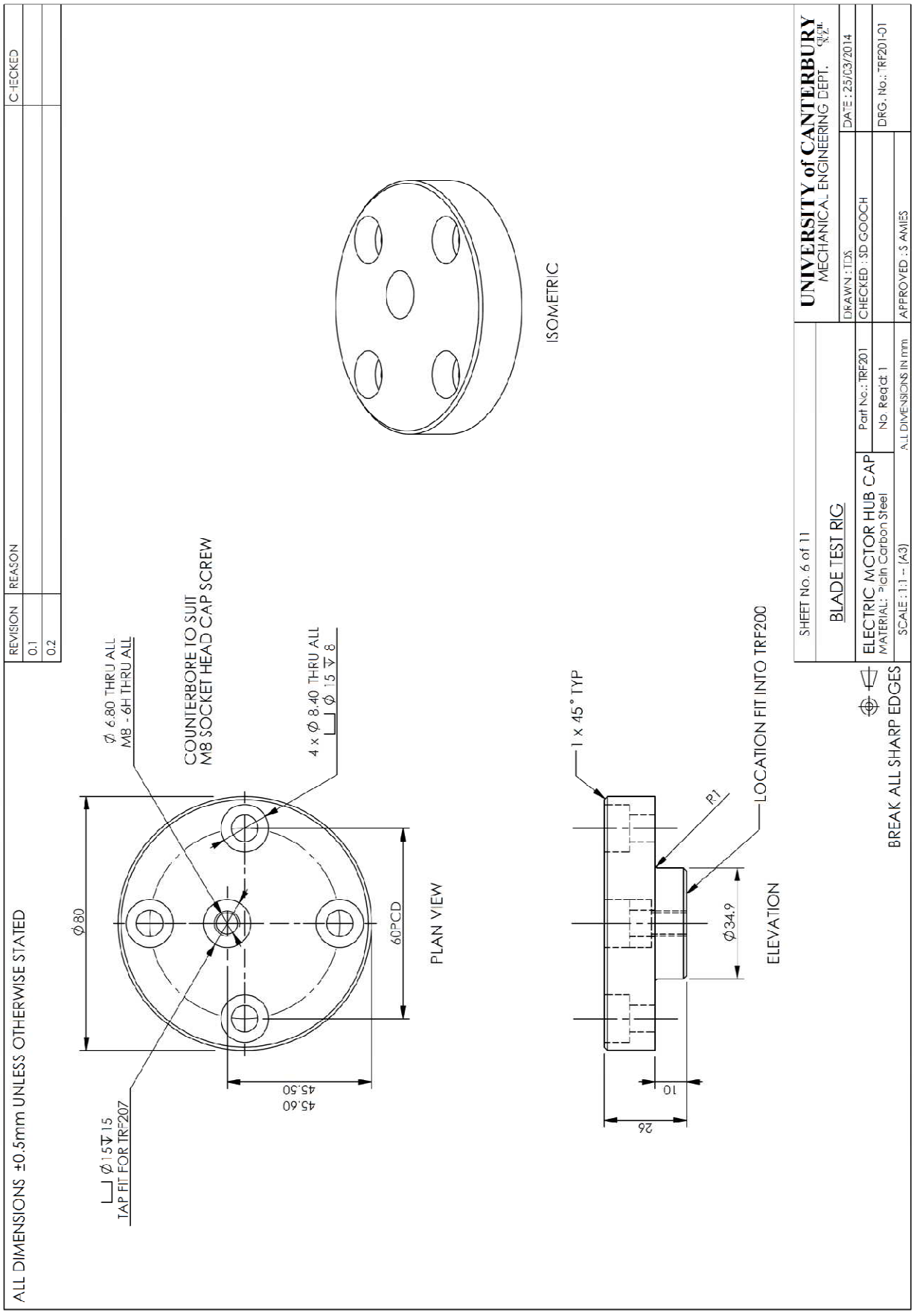

Figure A.6: Manufacturing drawing of electric motor drive hub cap in fatigue test rig. Drawing no. TRF201-01

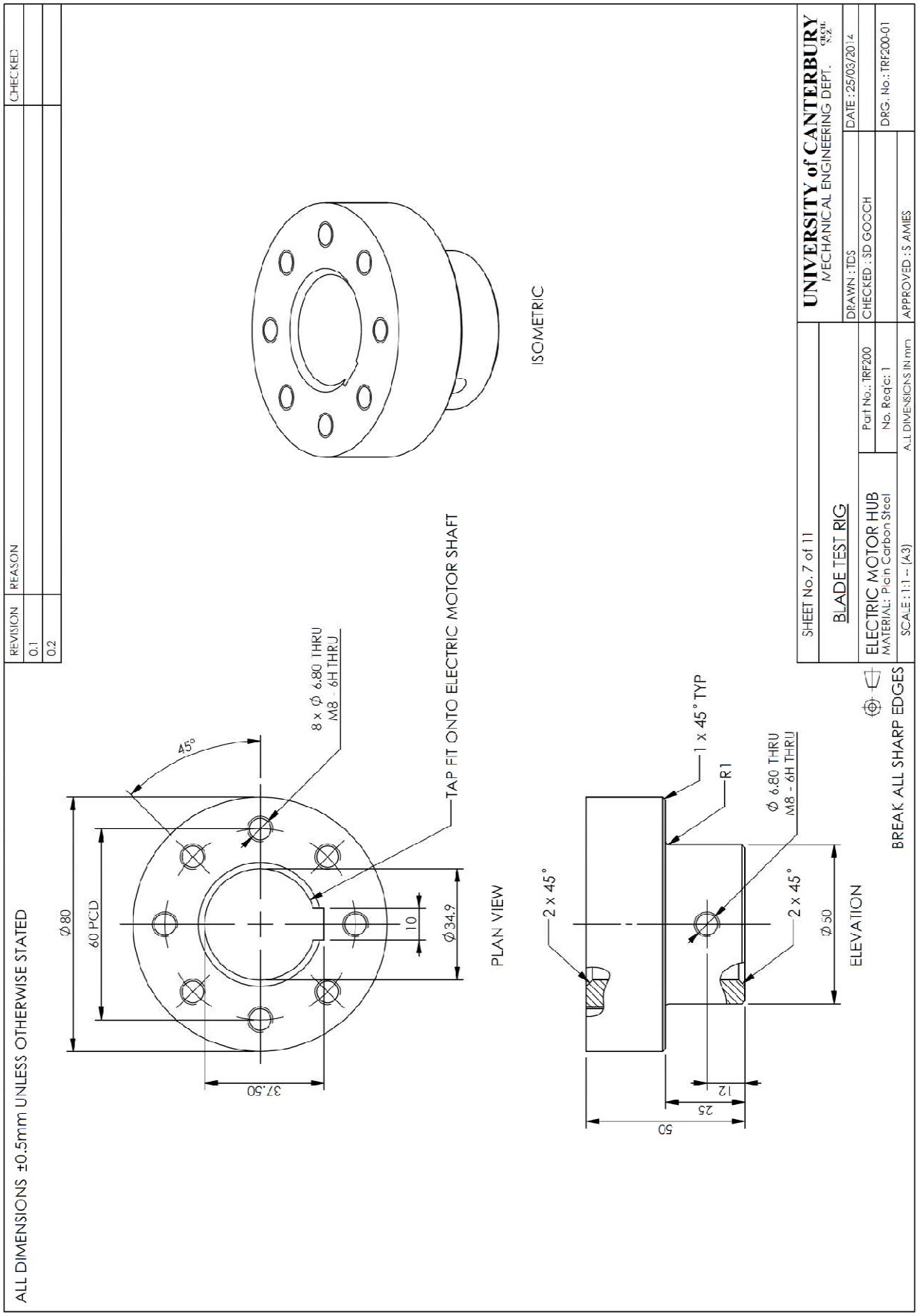

Figure A.7: Manufacturing drawing of electric motor drive hub in fatigue test rig. Drawing no. TRF200-01

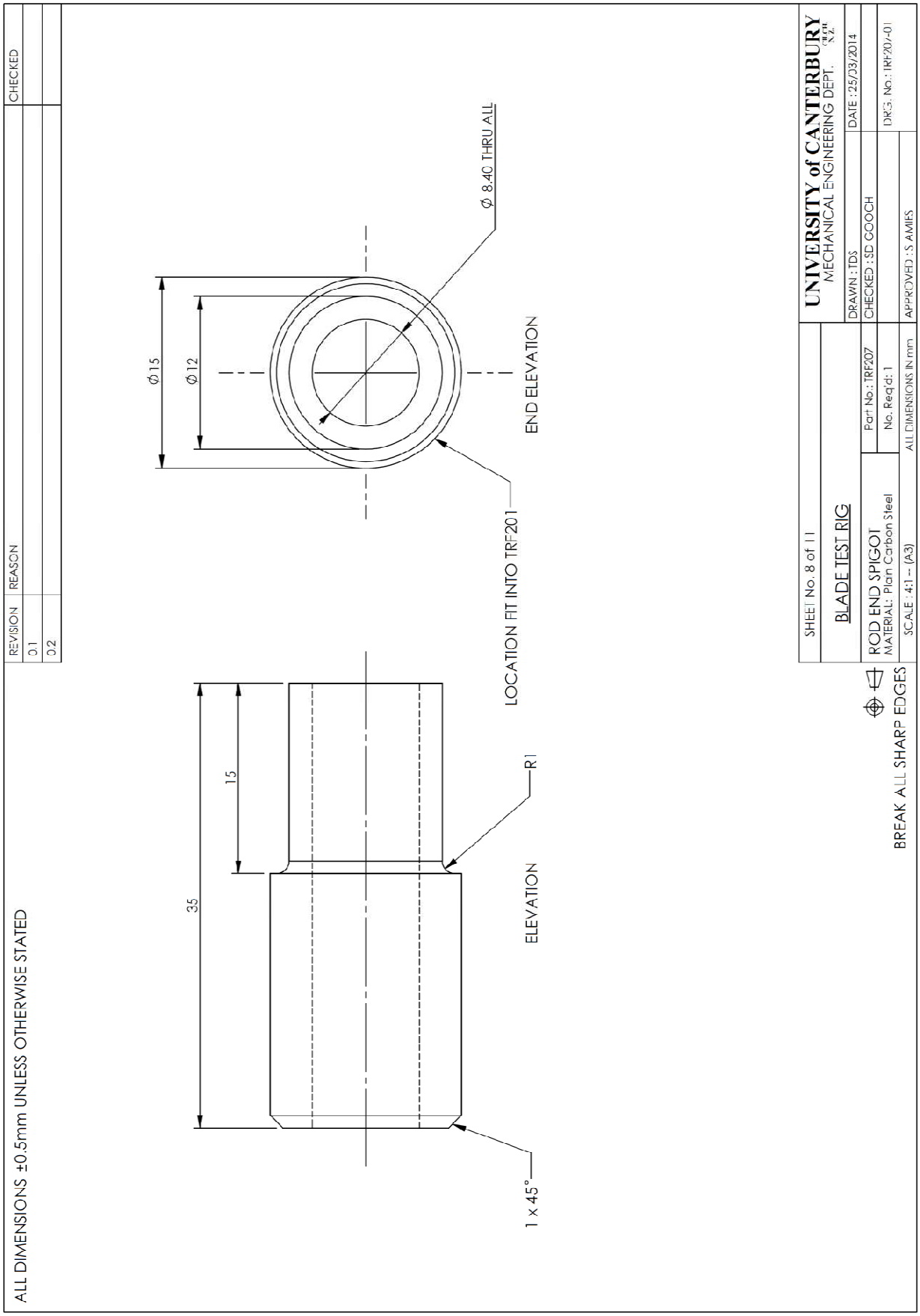

Figure A.8: Manufacturing drawing of rod end spigot in fatigue test rig. Drawing no. TRF207-01

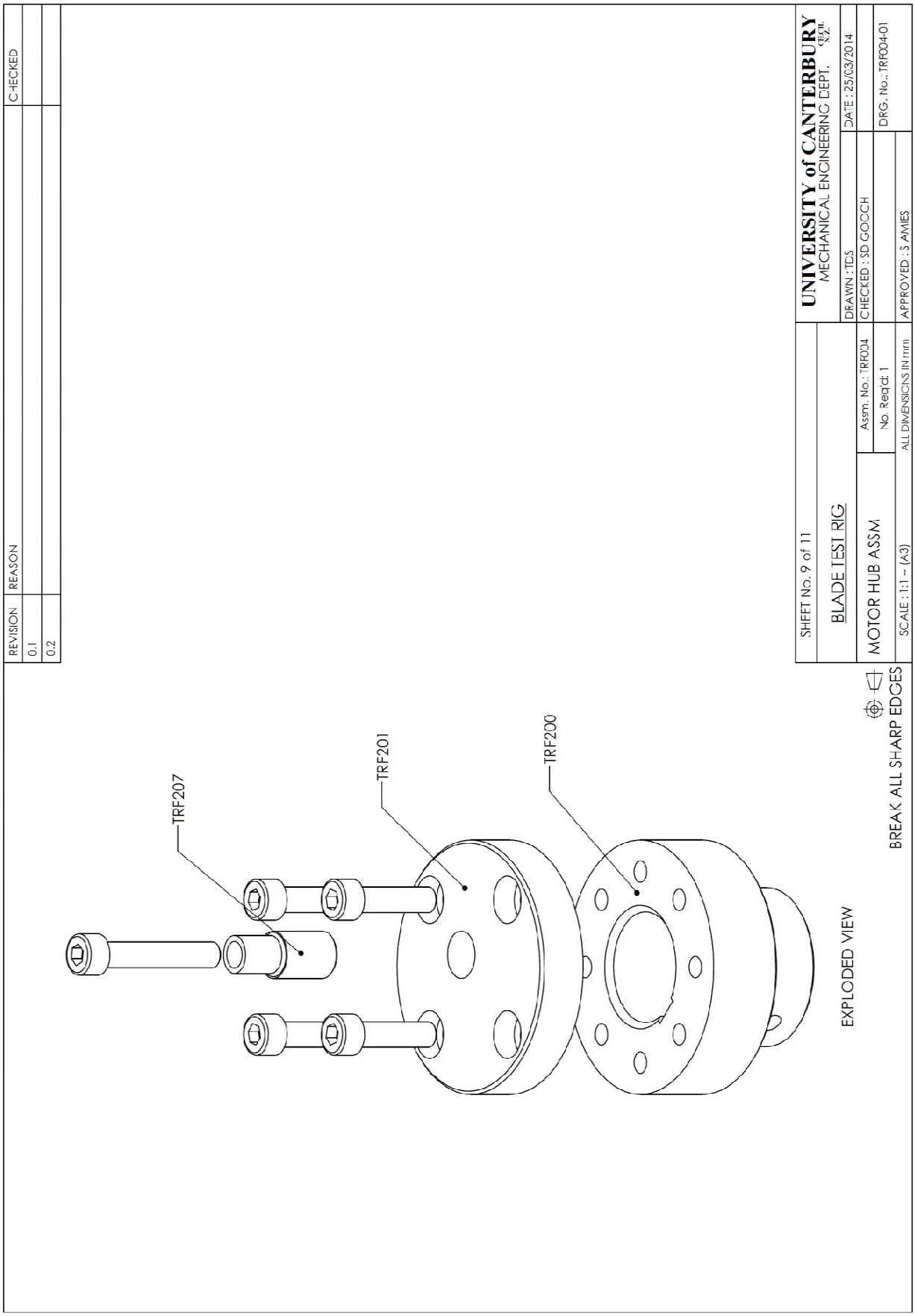

Figure A.9: Exploded view of drive hub assembly in fatigue test rig.

Drawing no. TRF004-01

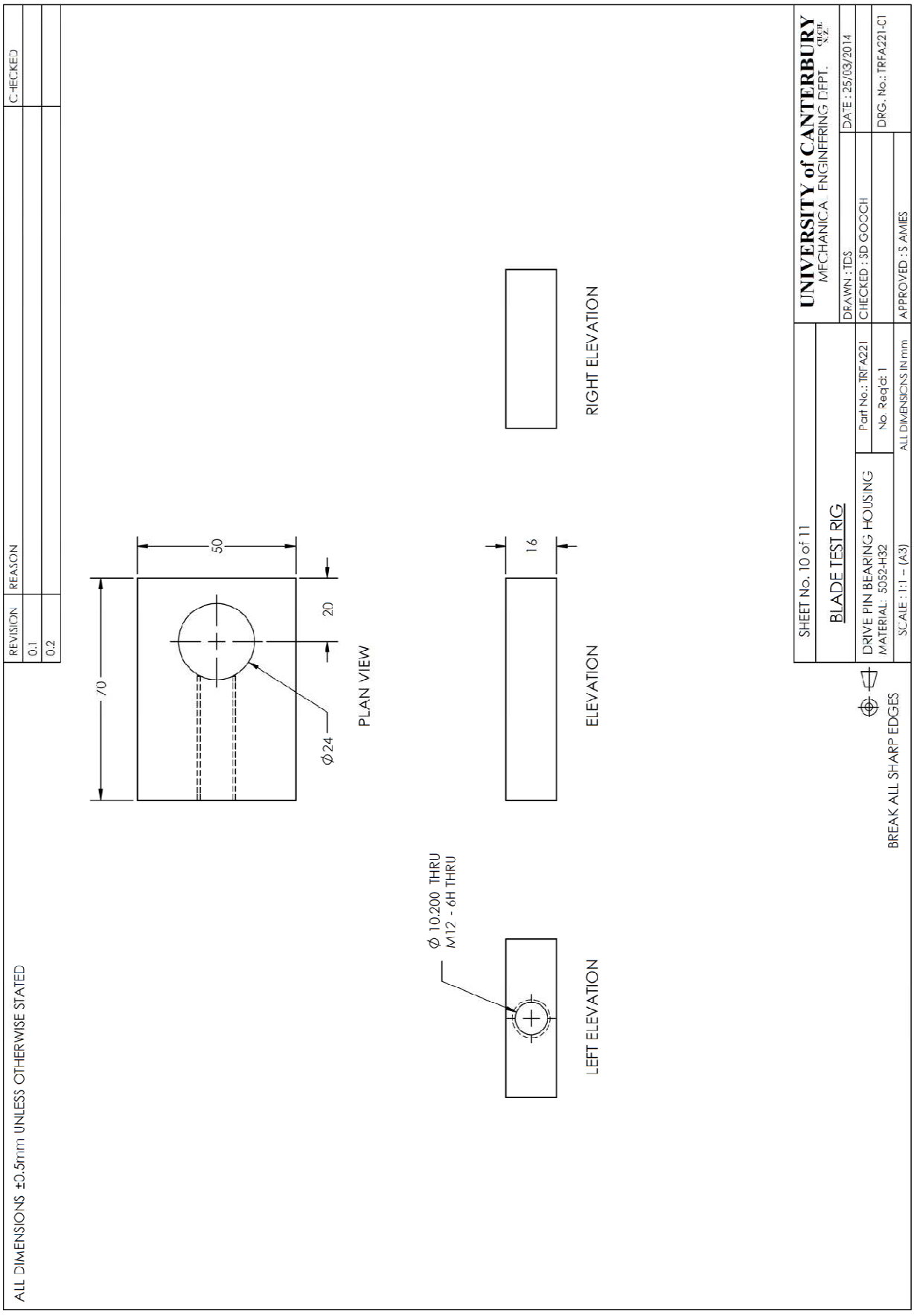

Figure A.10: Manufacturing drawing of drive pin bearing housing in fatigue test rig. Drawing no. TRFA221-01

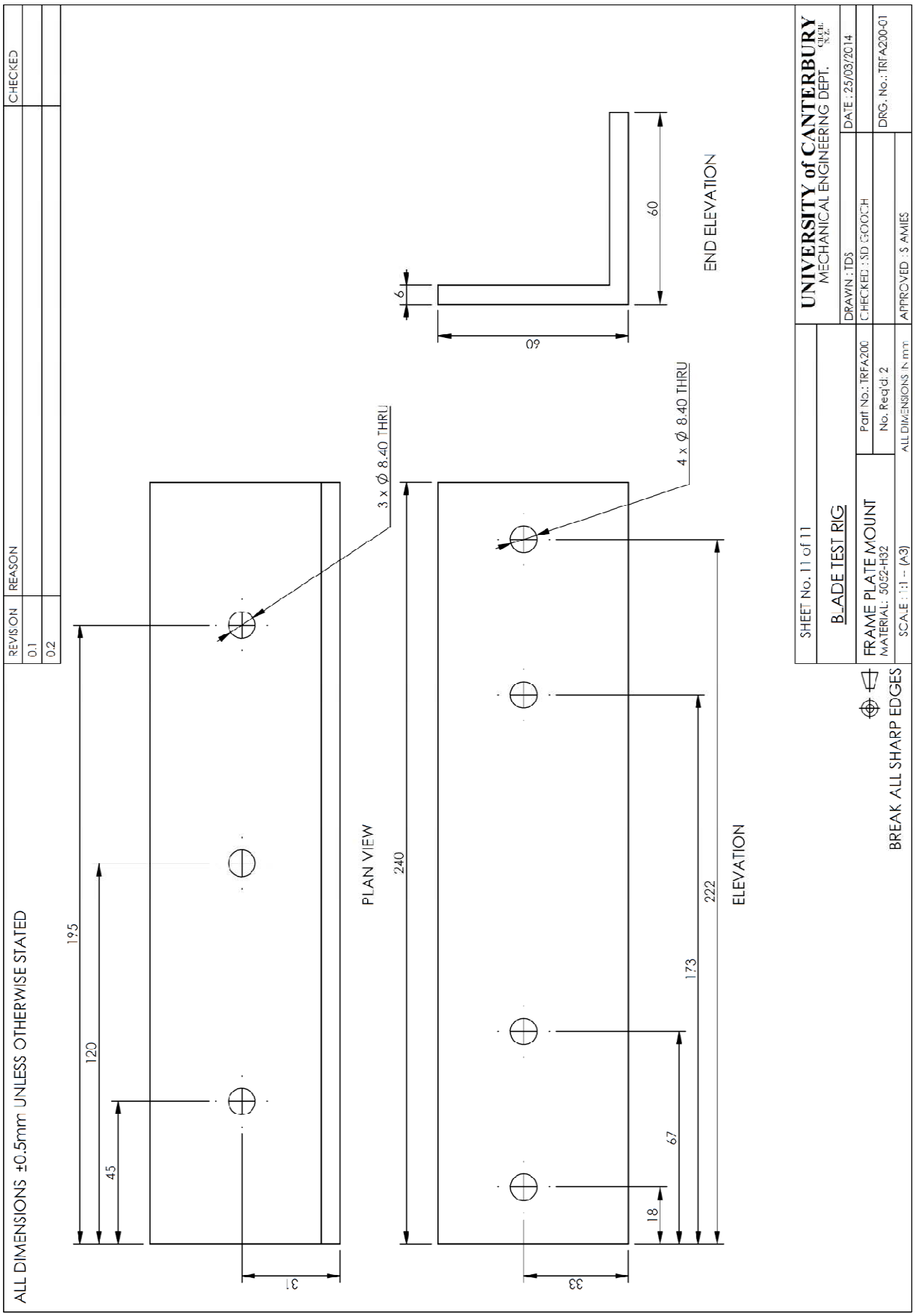

Figure A.11: Manufacturing drawing of frame plate mounts in fatigue test rig. Drawing no. TRFA200-01

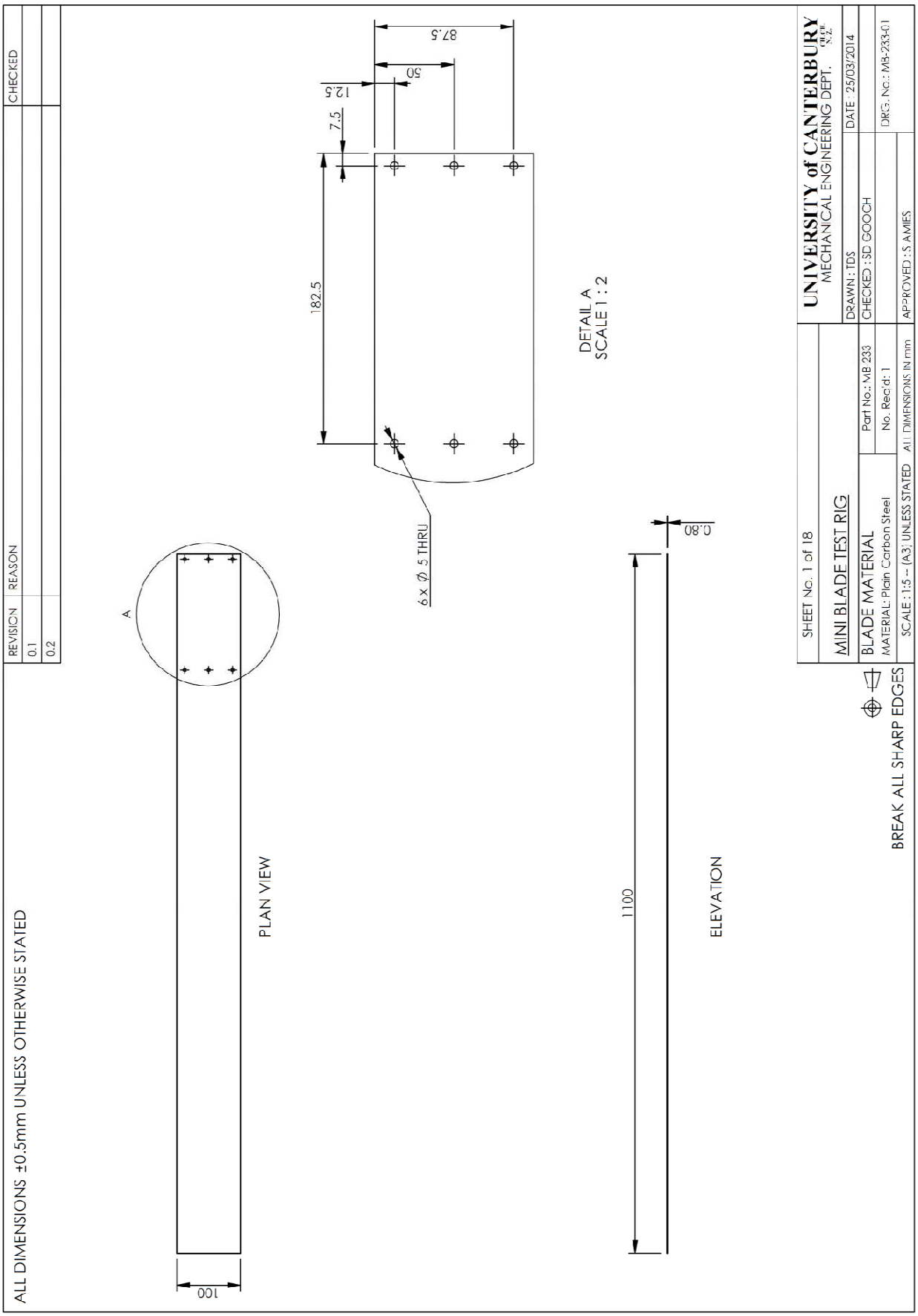

Figure A.12: Manufacturing drawing for the blade material in variable stroke mechanism test rig. Drawing no. MB-233-01

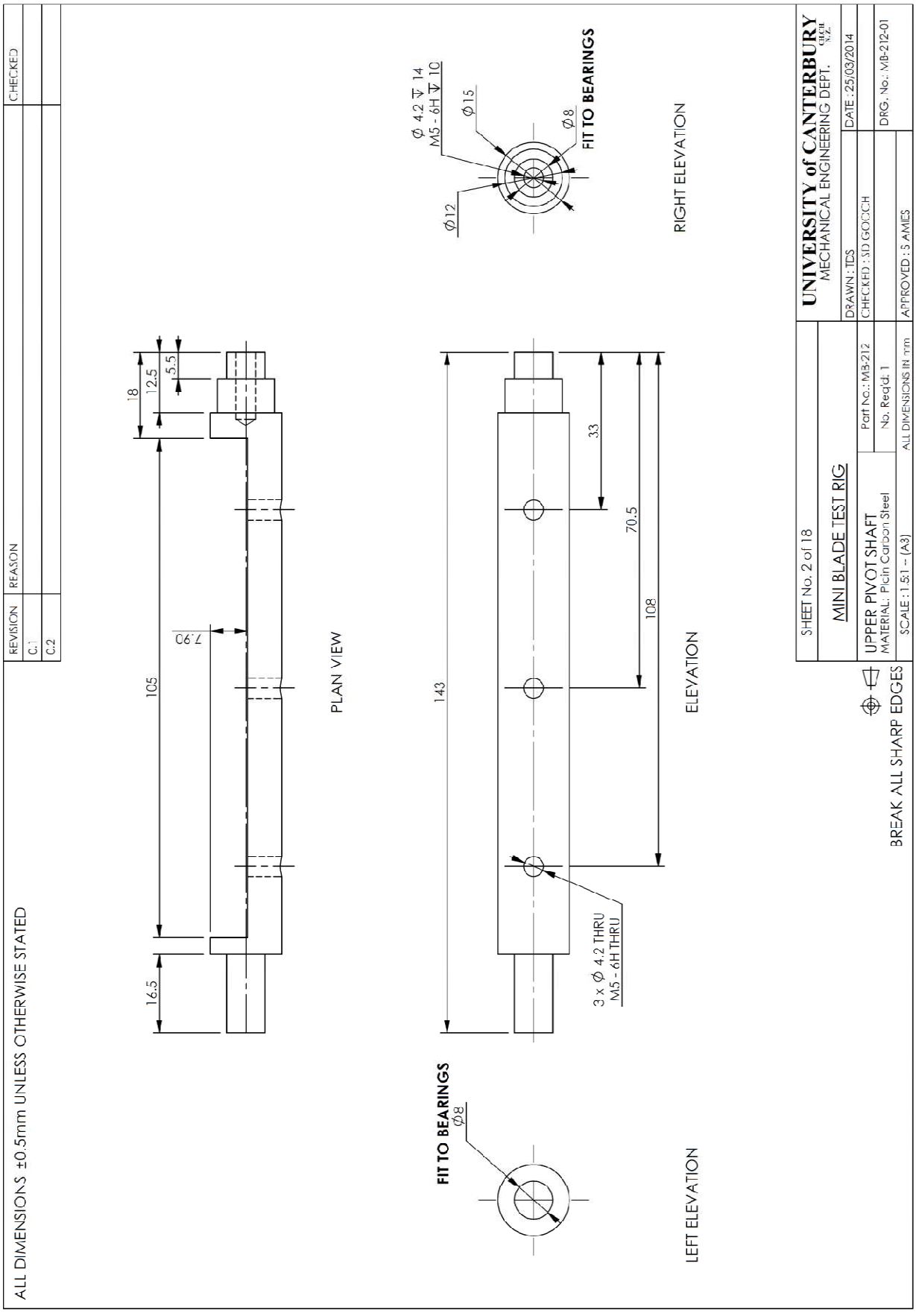

Figure A.13: Manufacturing drawing for the upper pivot shaft in variable stroke mechanism test rig. Drawing no. MB212-01

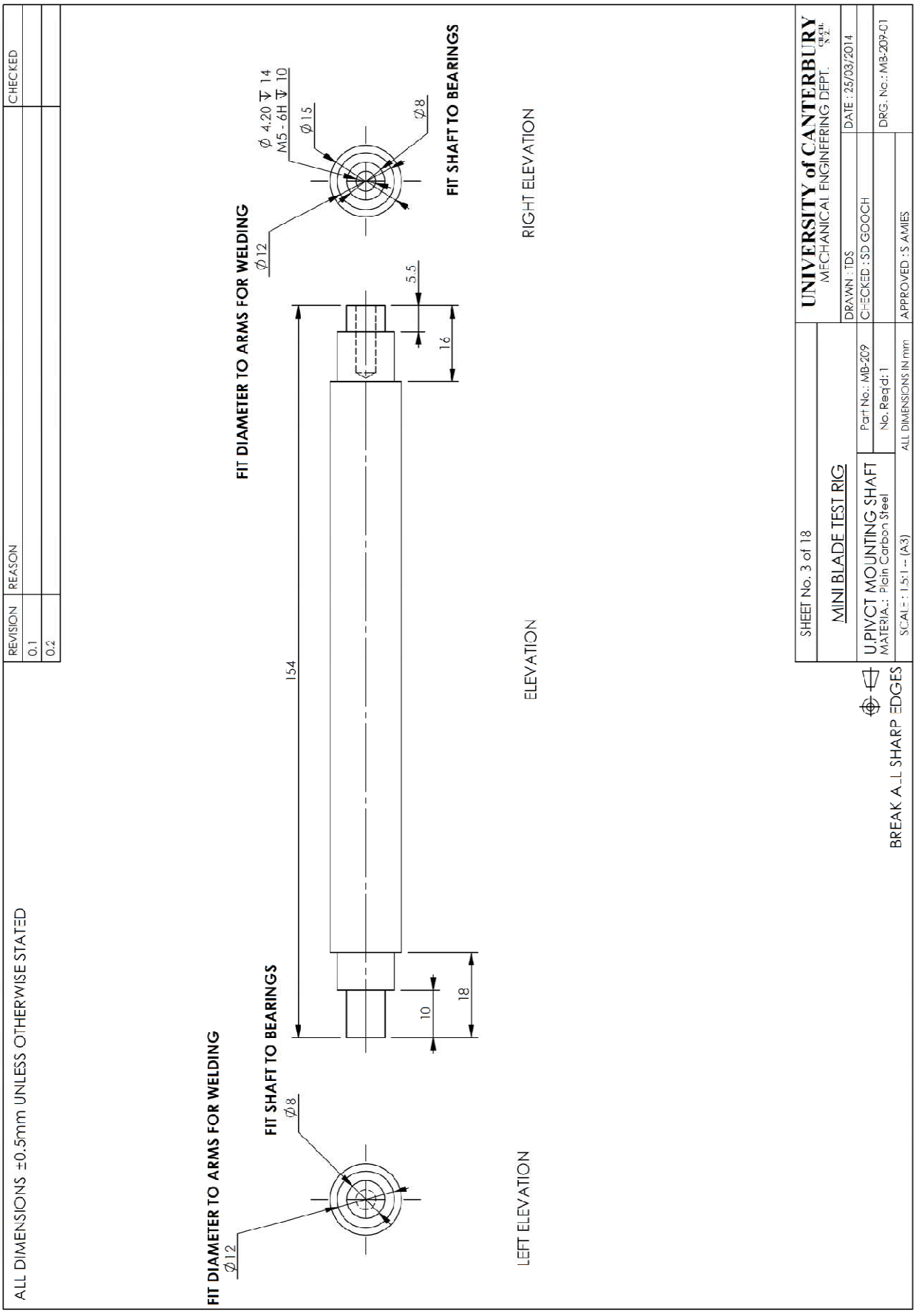

Figure A.14: Manufacturing drawing for upper pivot mounting shaft in variable stroke test rig. Drawing no. MB-209-01

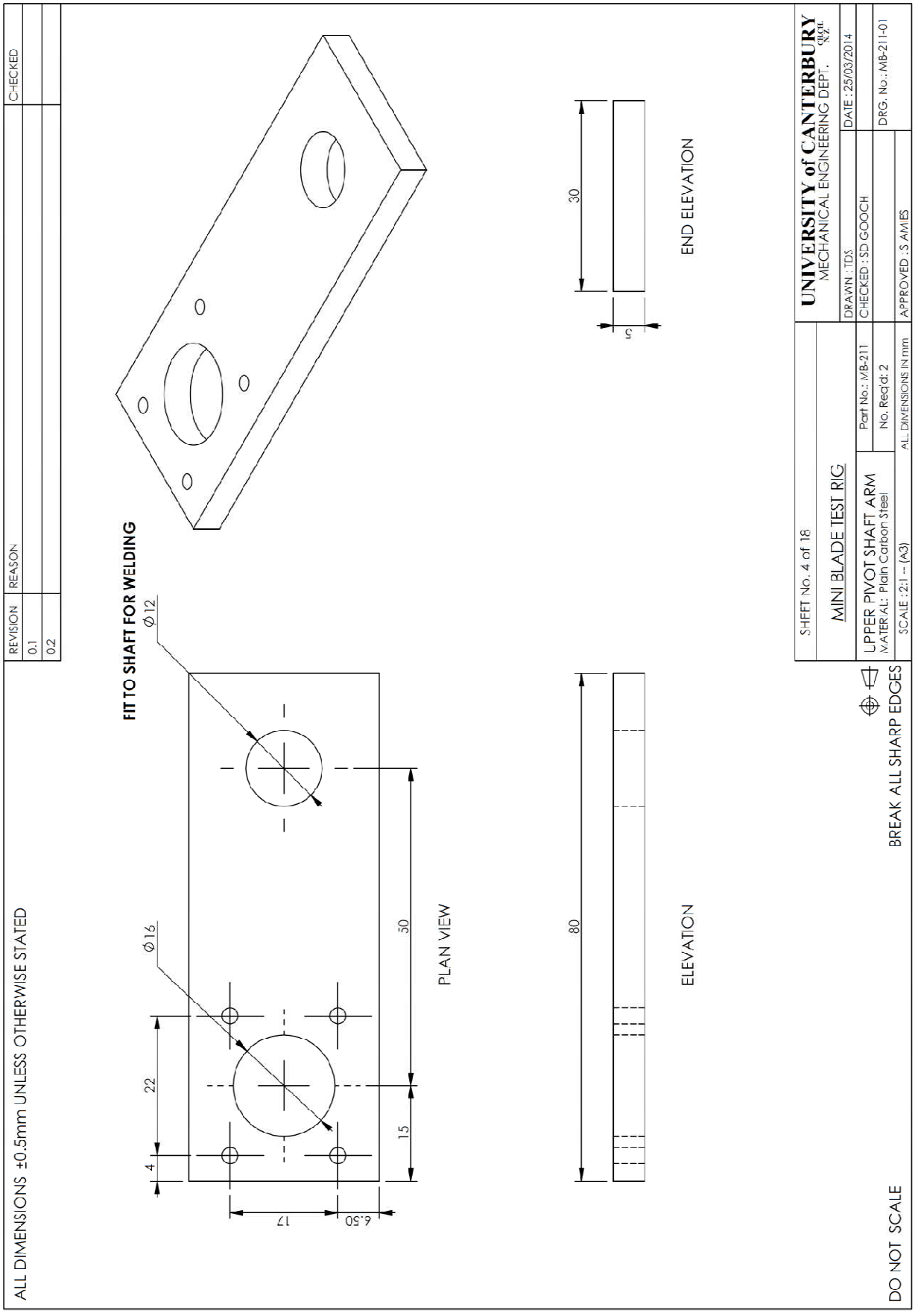

Figure A.15: Manufacturing drawing for the upper pivot shaft arm in variable stroke test rig. Drawing no. MB-211-01

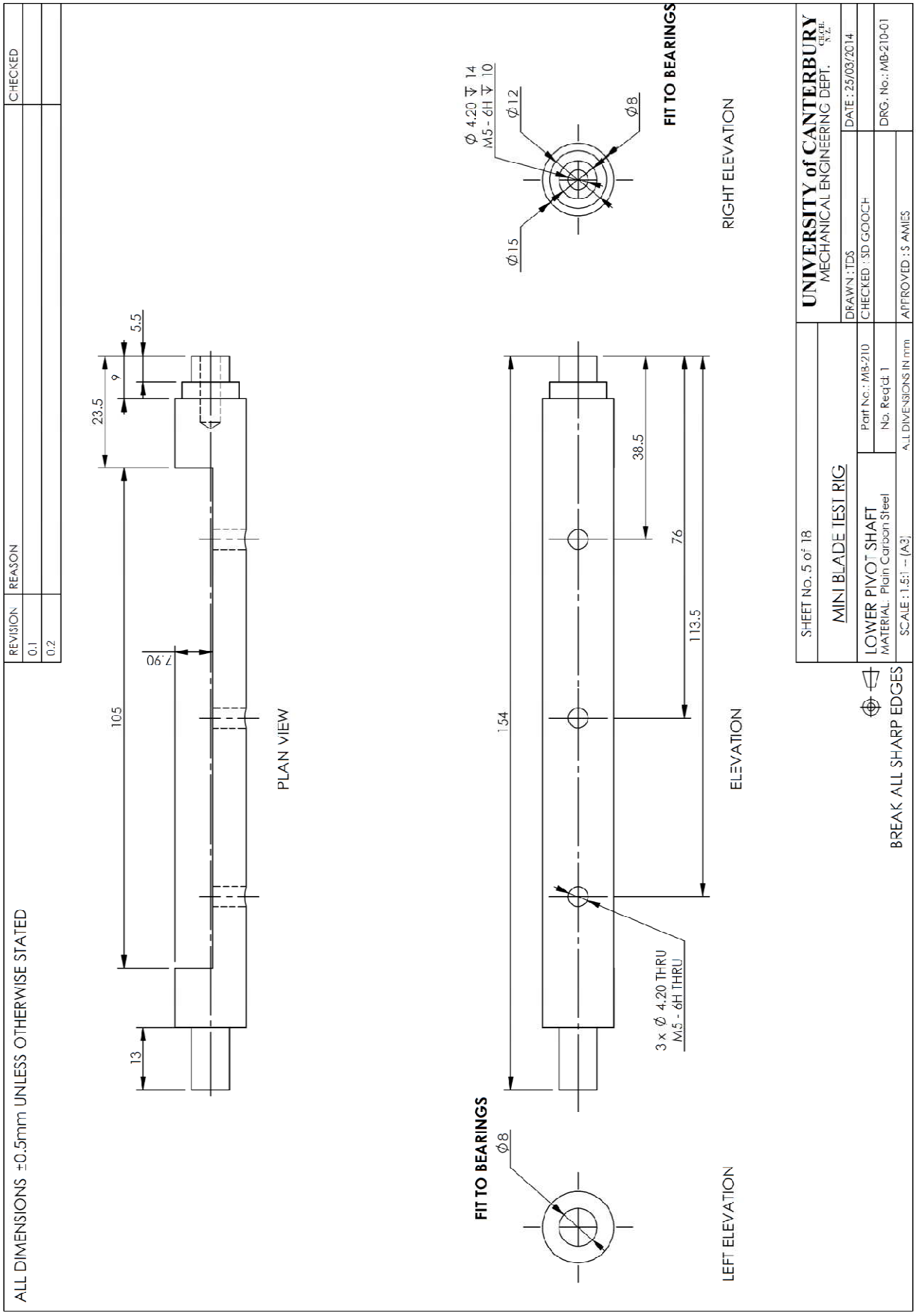

Figure A.16: Manufacturing drawing for the lower pivot shaft in variable stroke test rig. Drawing no. MB-210-01

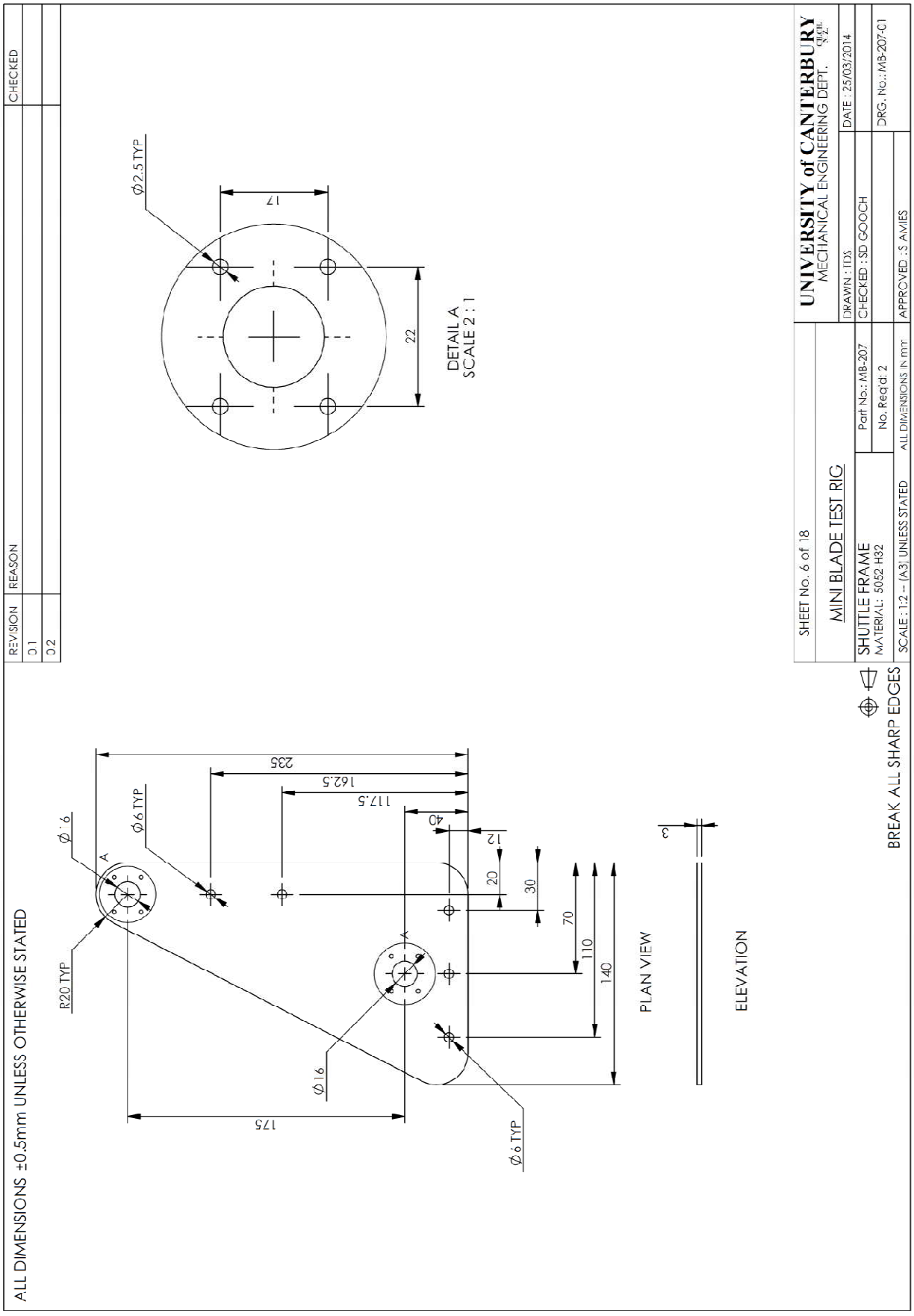

Figure A.17: Manufacturing drawing for the shuttle frame in variable stroke test rig. Drawing no. MB-207-01

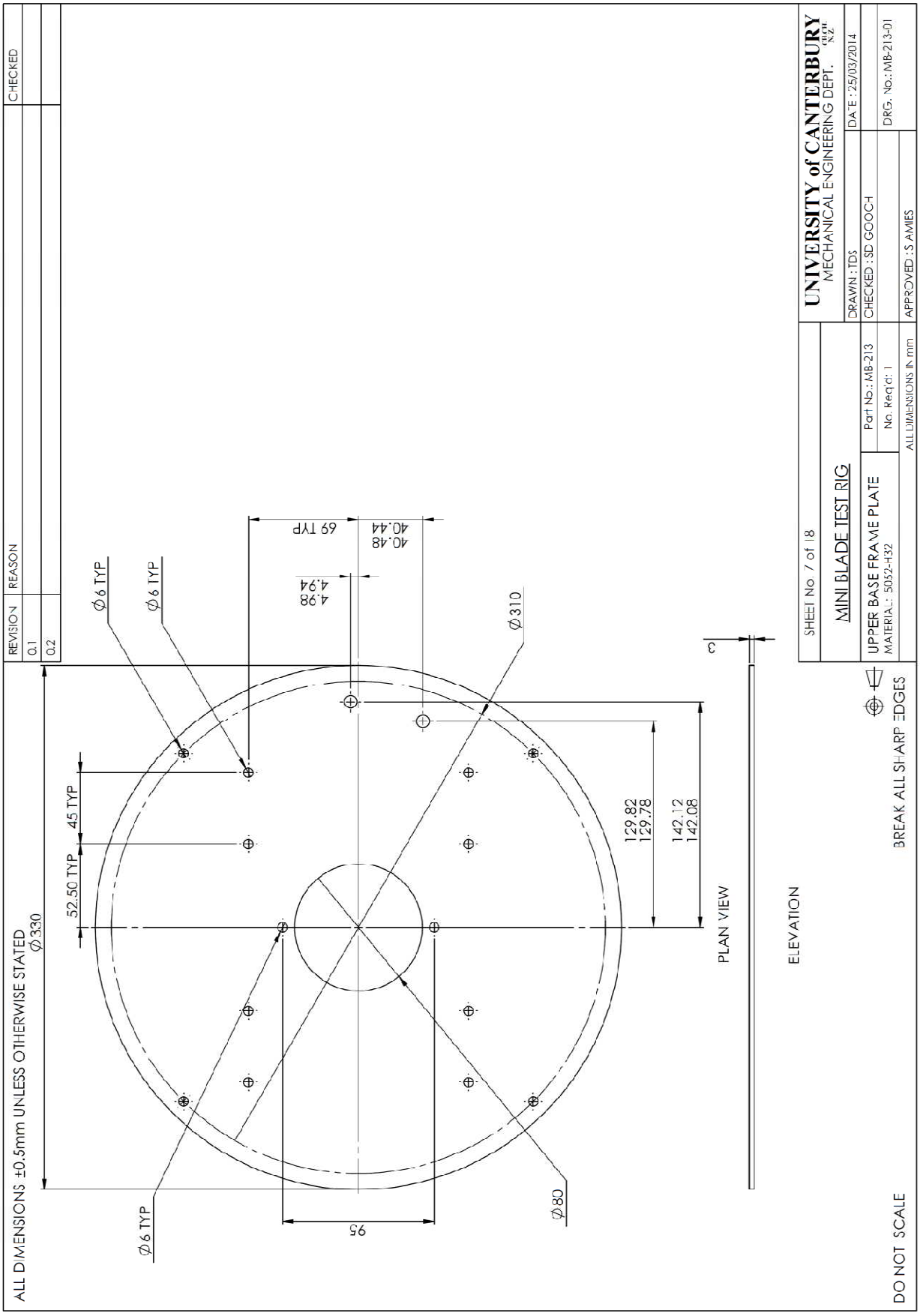

Figure A.18: Manufacturing drawing for the upper base frame plate in the variable stroke test rig. Drawing no. MB-213-01

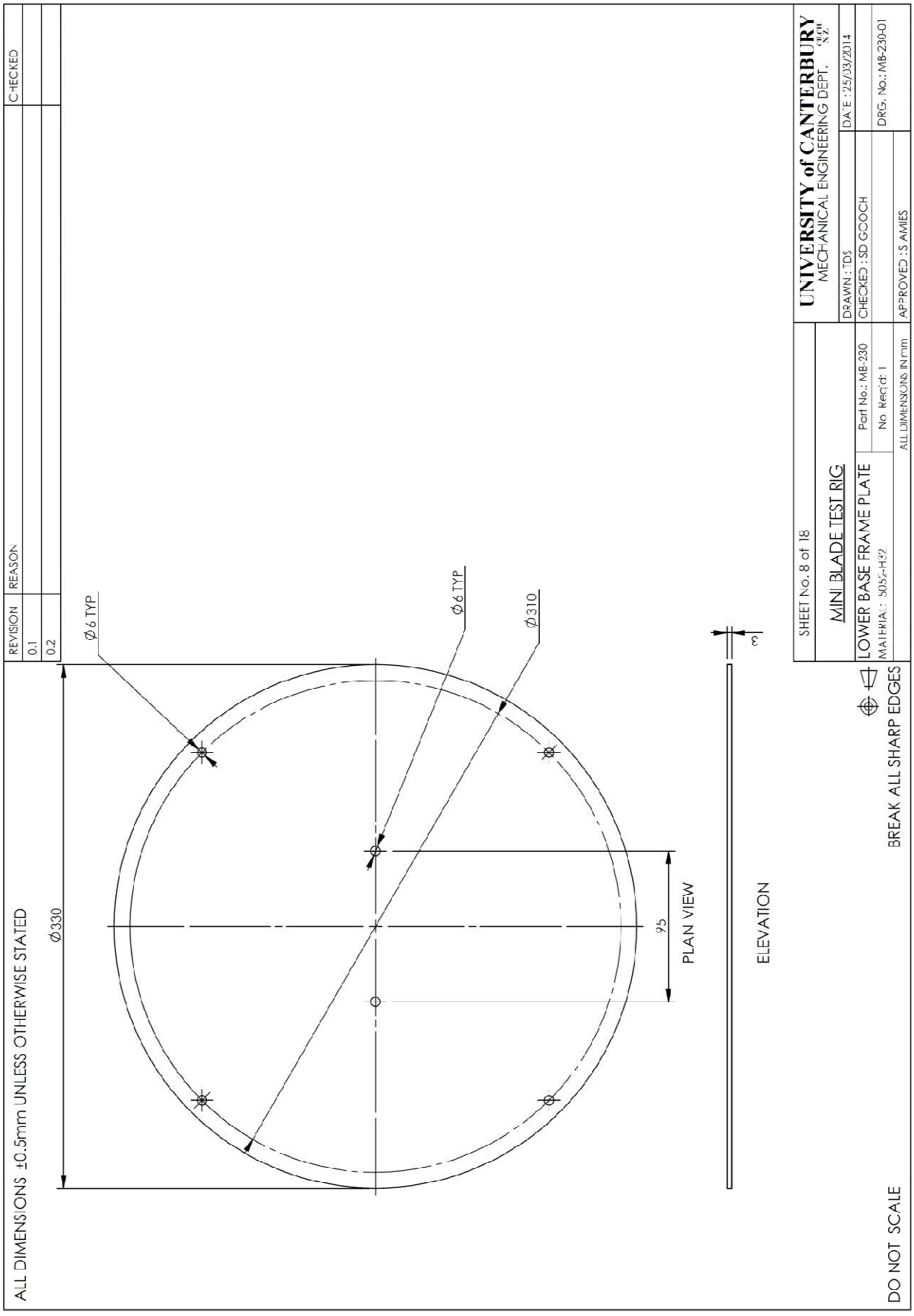

Figure A.19: Manufacturing drawing for the lower base frame place in the variable stroke test rig. Drawing no. MB-230-01

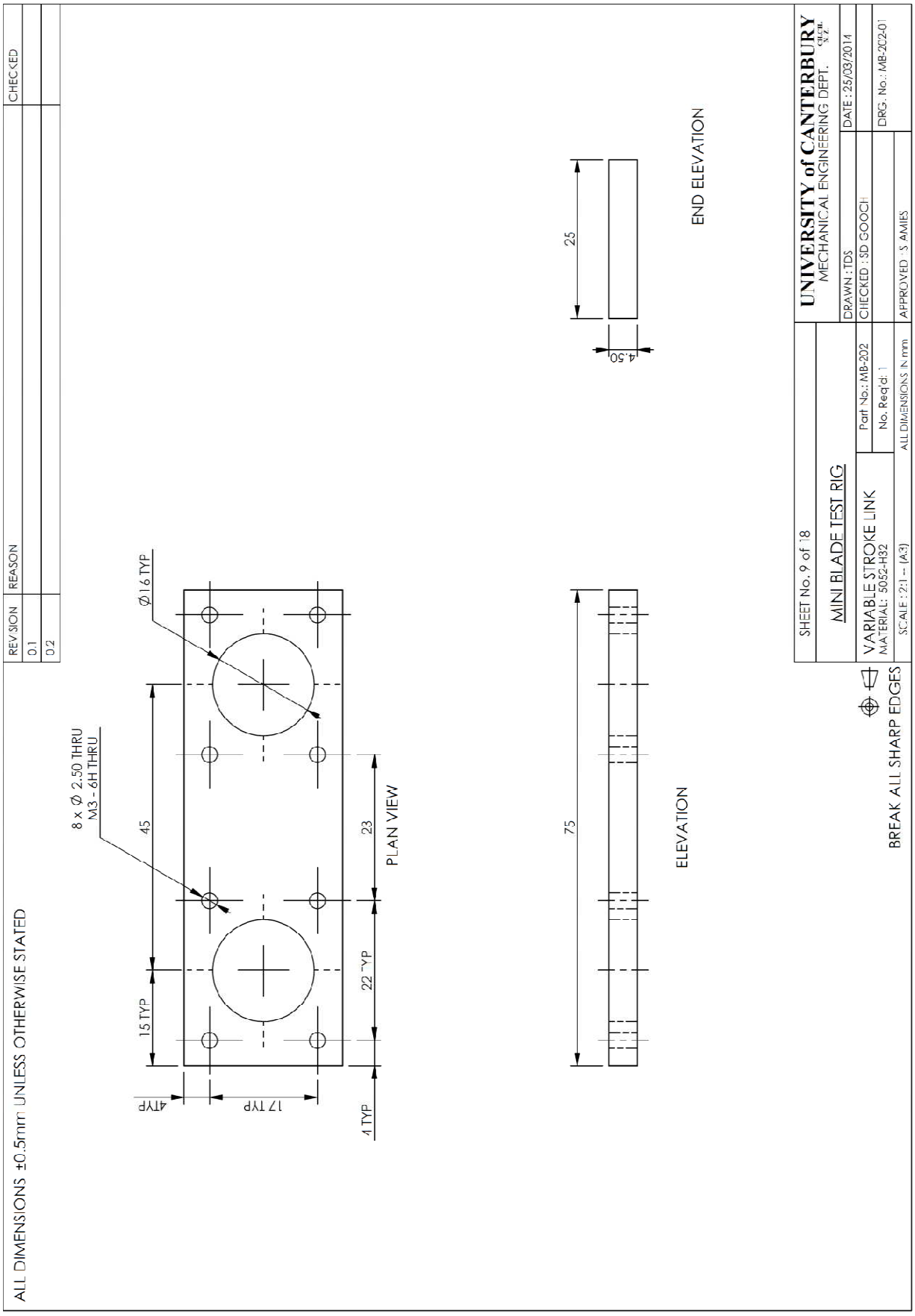

Figure A.20: Manufacturing drawing for link 2 of the variable stroke test rig.

Drawing no. MB-202-01

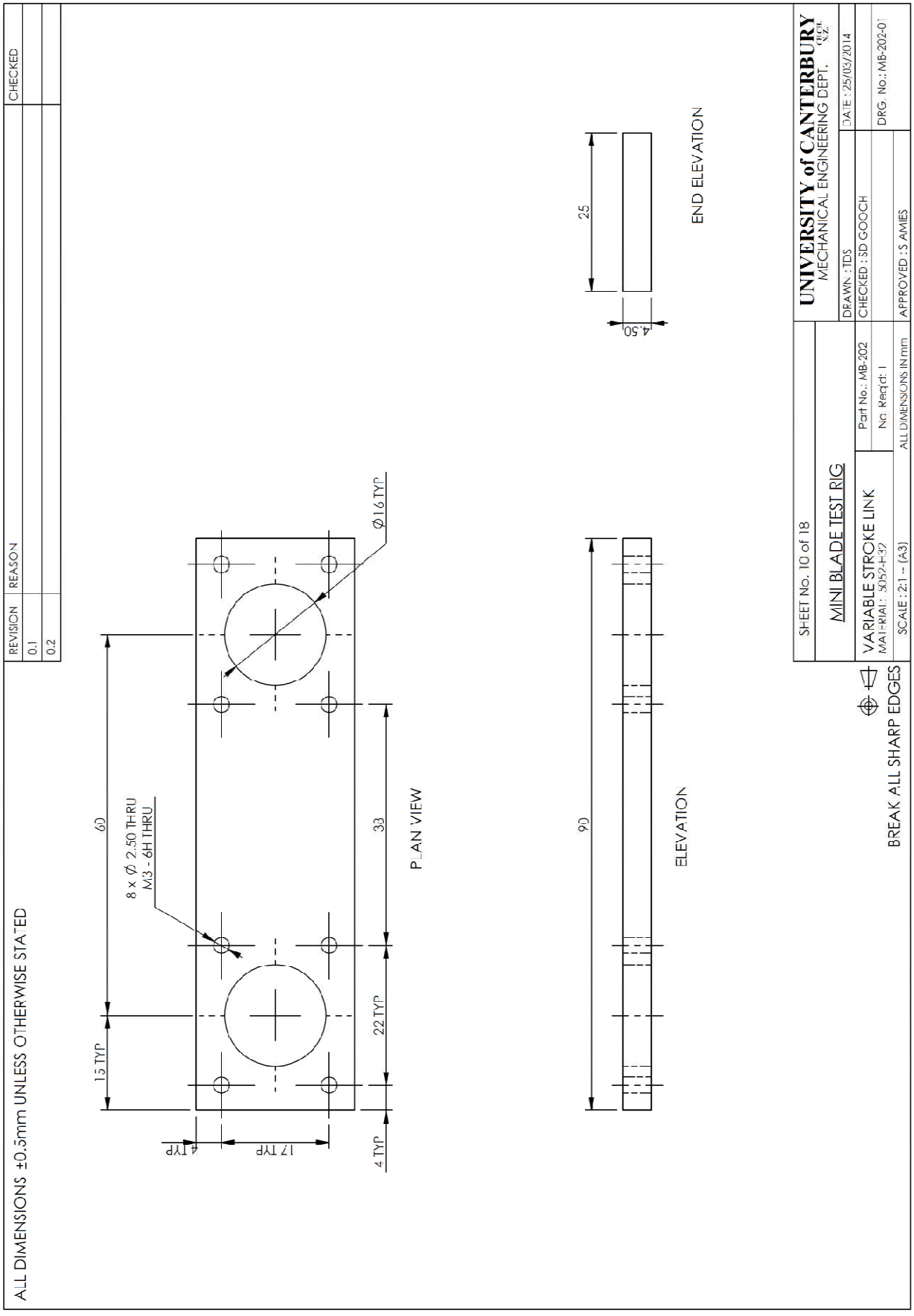

Figure A.21: Manufacturing drawing for link 1 of the variable stroke test rig.

Drawing no. MB-202-01

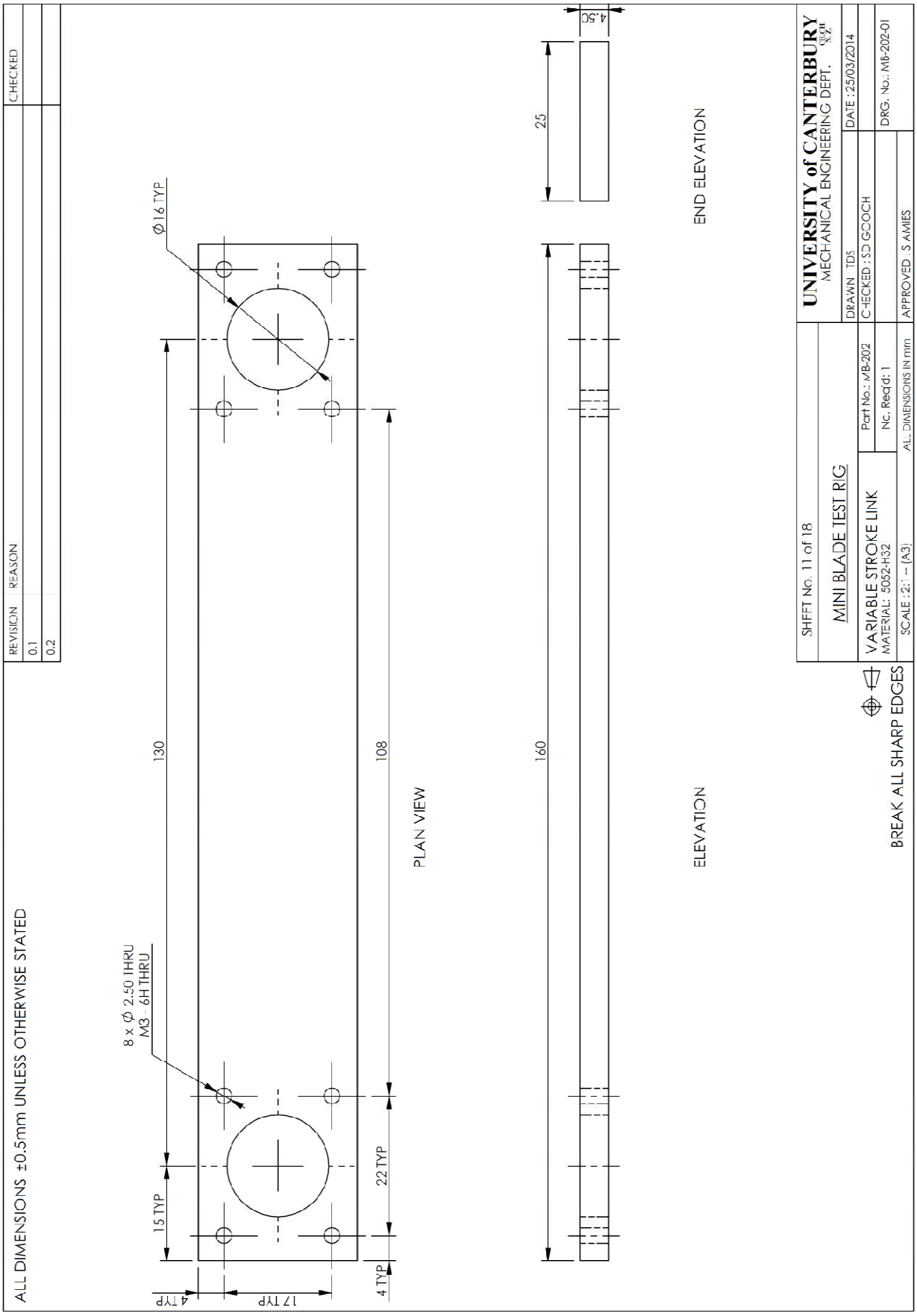

Figure A.22: Manufacturing drawing for link 3 of the variable stroke test rig. Drawing no. MB-202-01

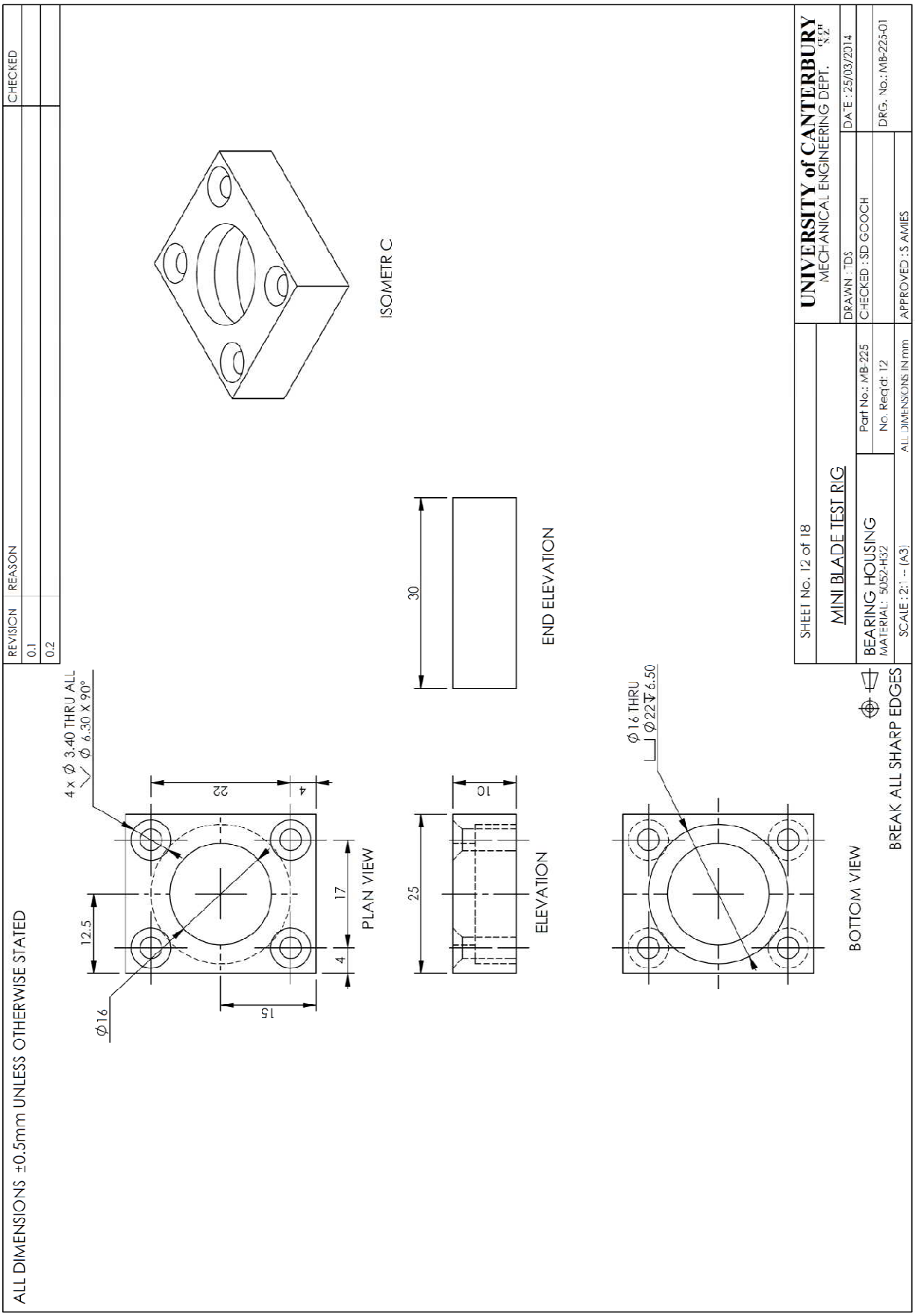

Figure A.23: Manufacturing drawing for the generic bearing housing in variable stroke test rig. Drawing no. MB-225-01

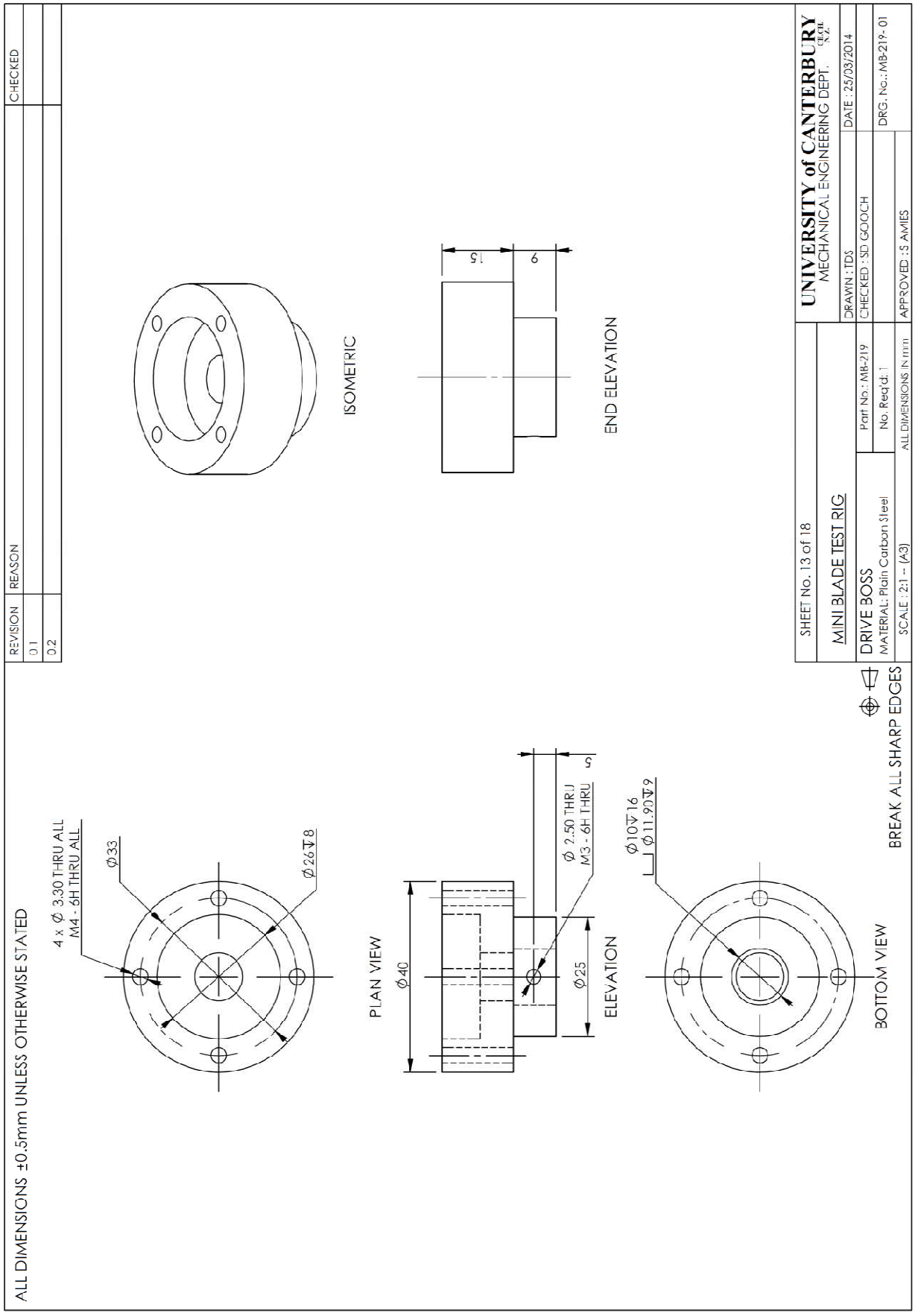

Figure A.24: Manufacturing drawing for the drive boss in variable stroke test rig. Drawing no. MB-219-01

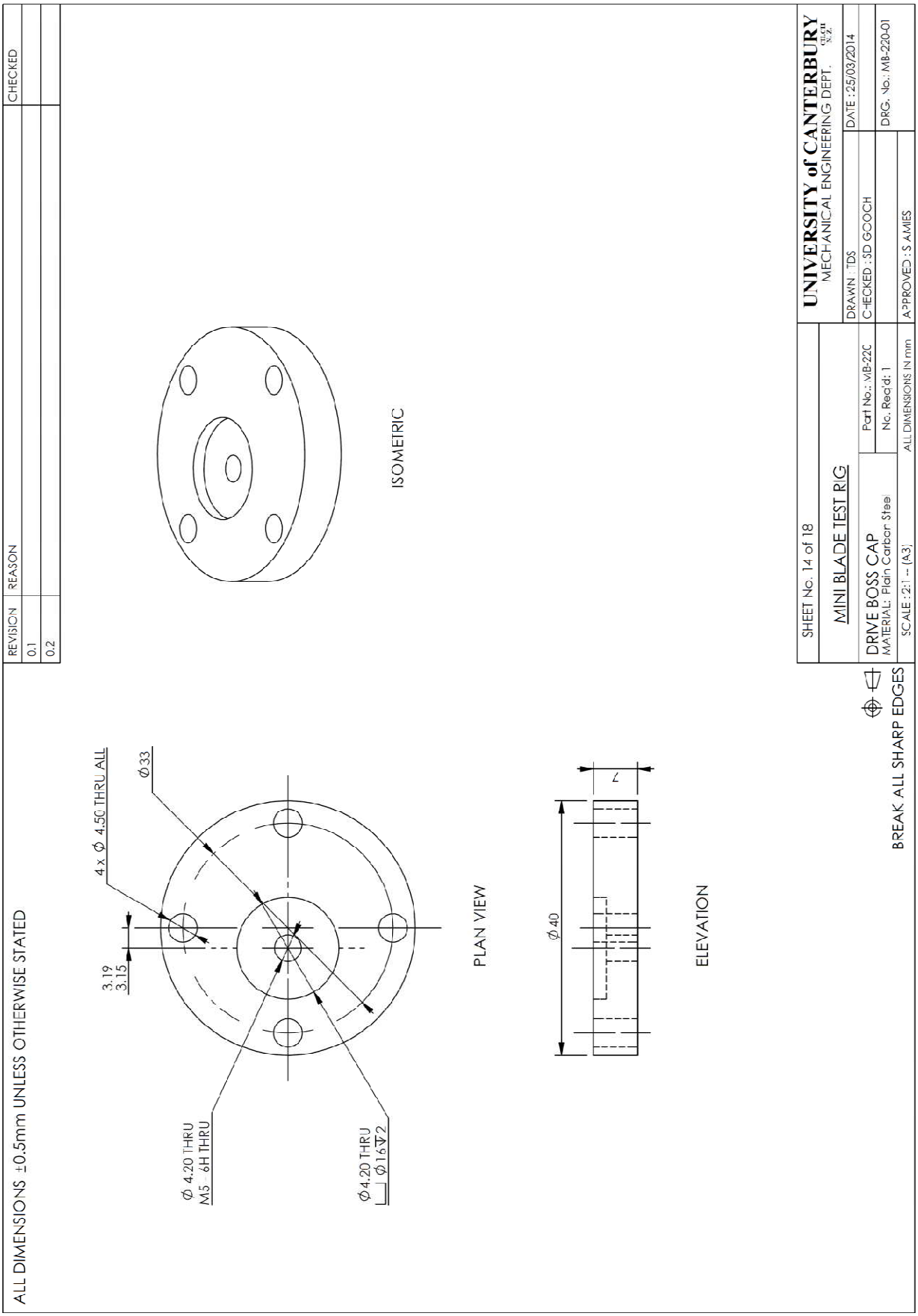

Figure A.25: Manufacturing drawing for the drive boss cap in the variable stroke test rig. Drawing no. MB-22-01

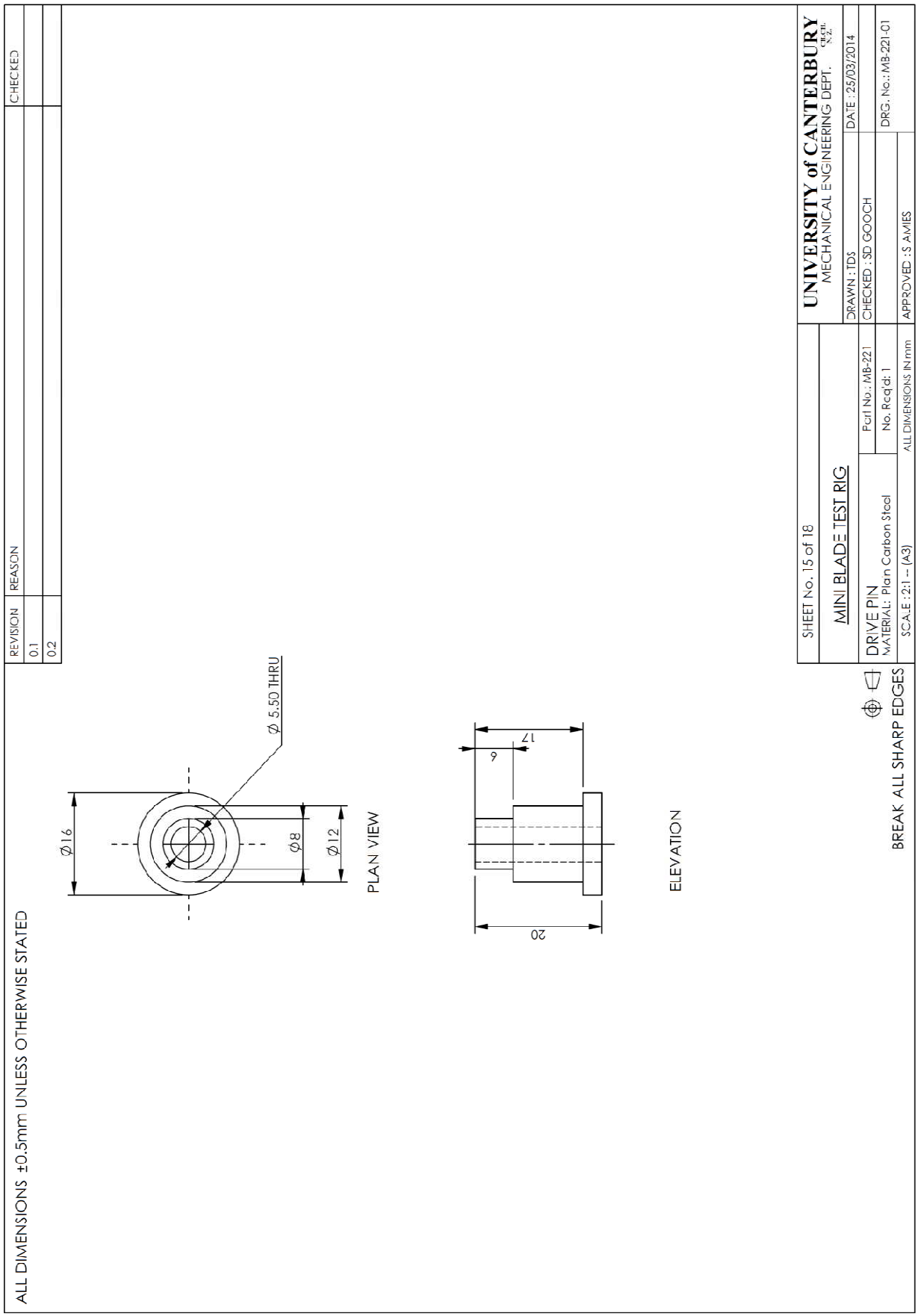

Figure A.26: Manufacturing drawing of the drive pin in variable stroke test rig. Drawing no. MB-221-01

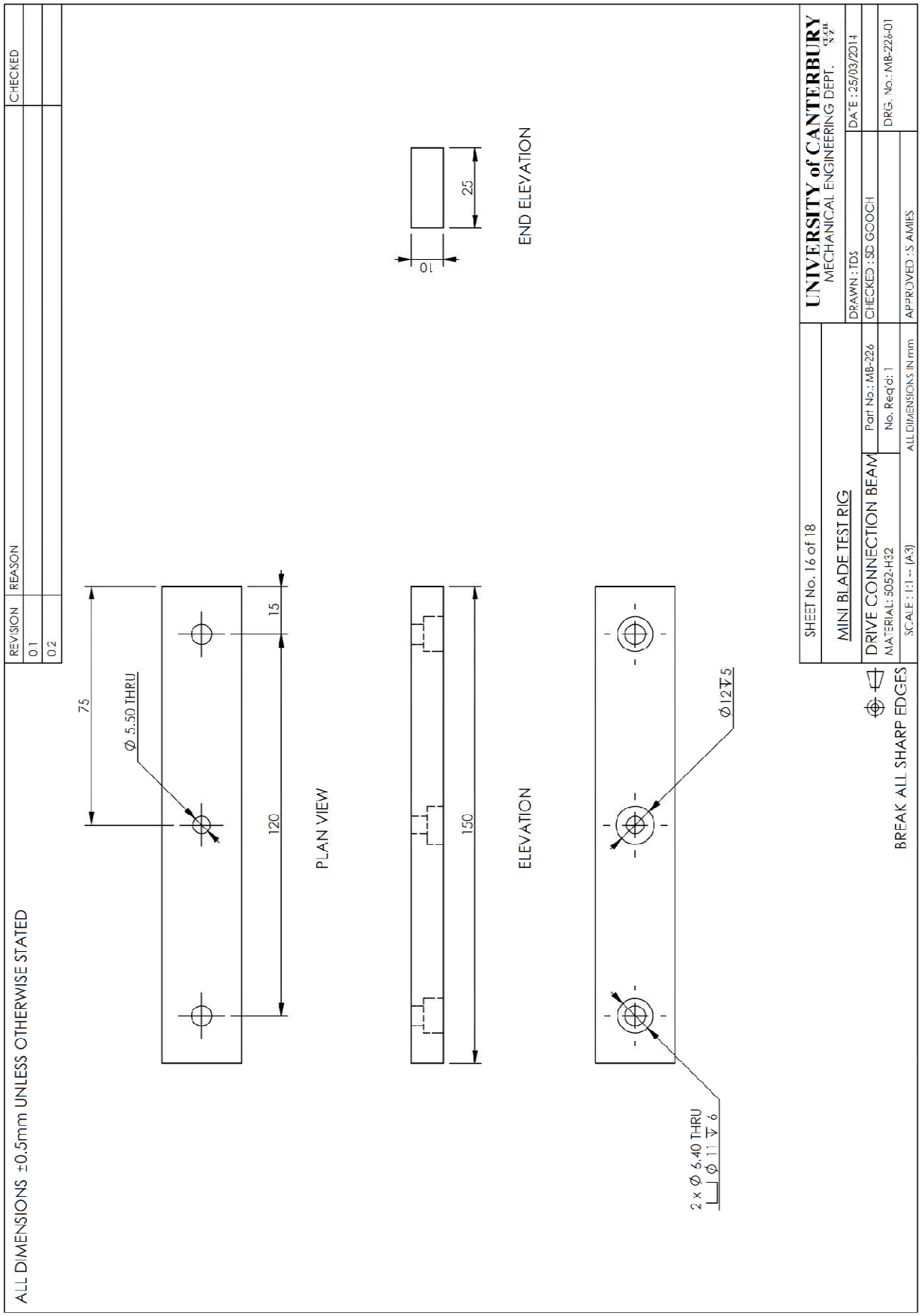

Figure A.27: Manufacturing drawing of the drive connection beam in variable stroke test rig. Drawing no. MB-226-01

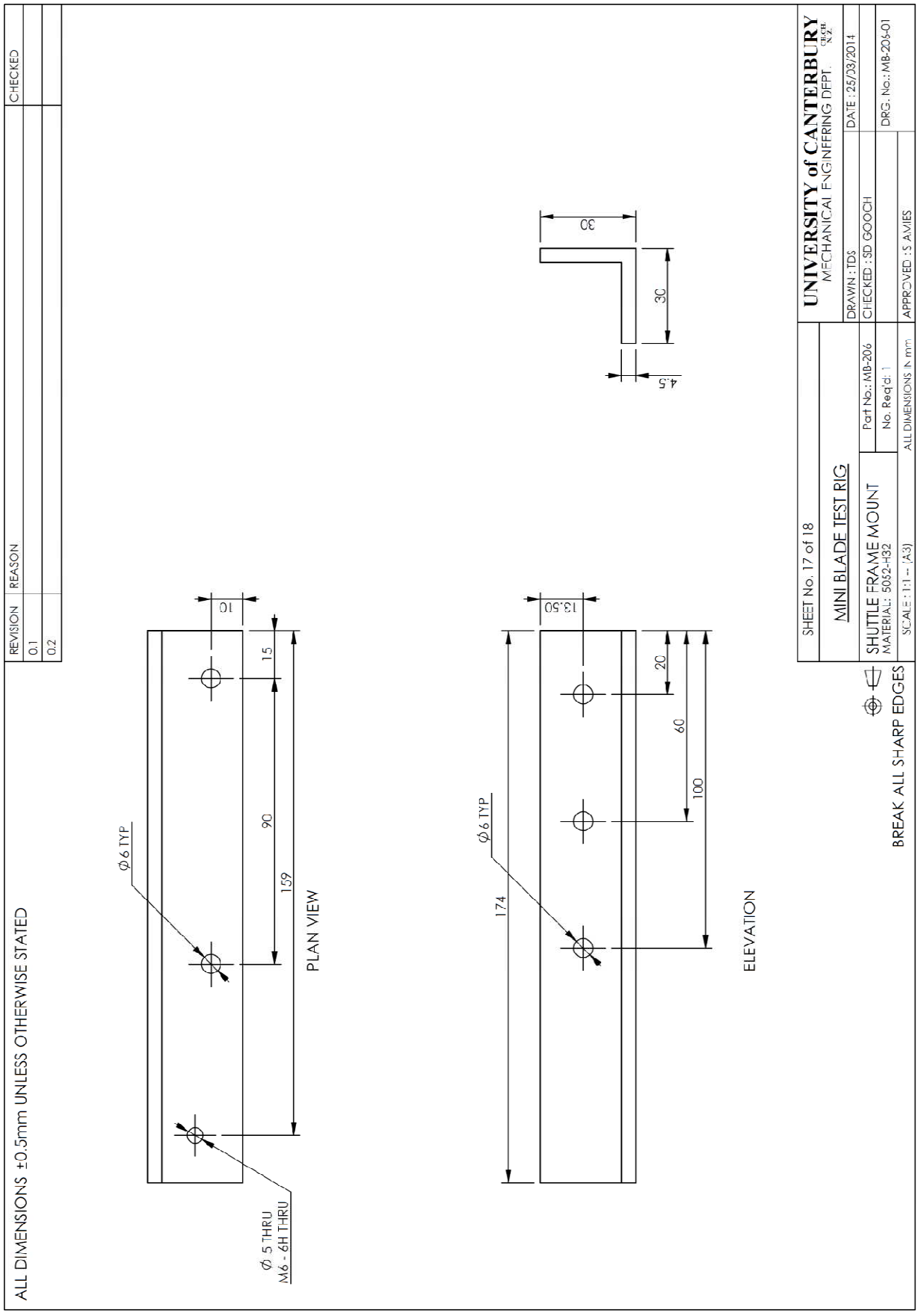

Figure A.28: Manufacturing drawing of LH shuttle frame mount in the variable stroke test rig. Drawing no. MB-206-01

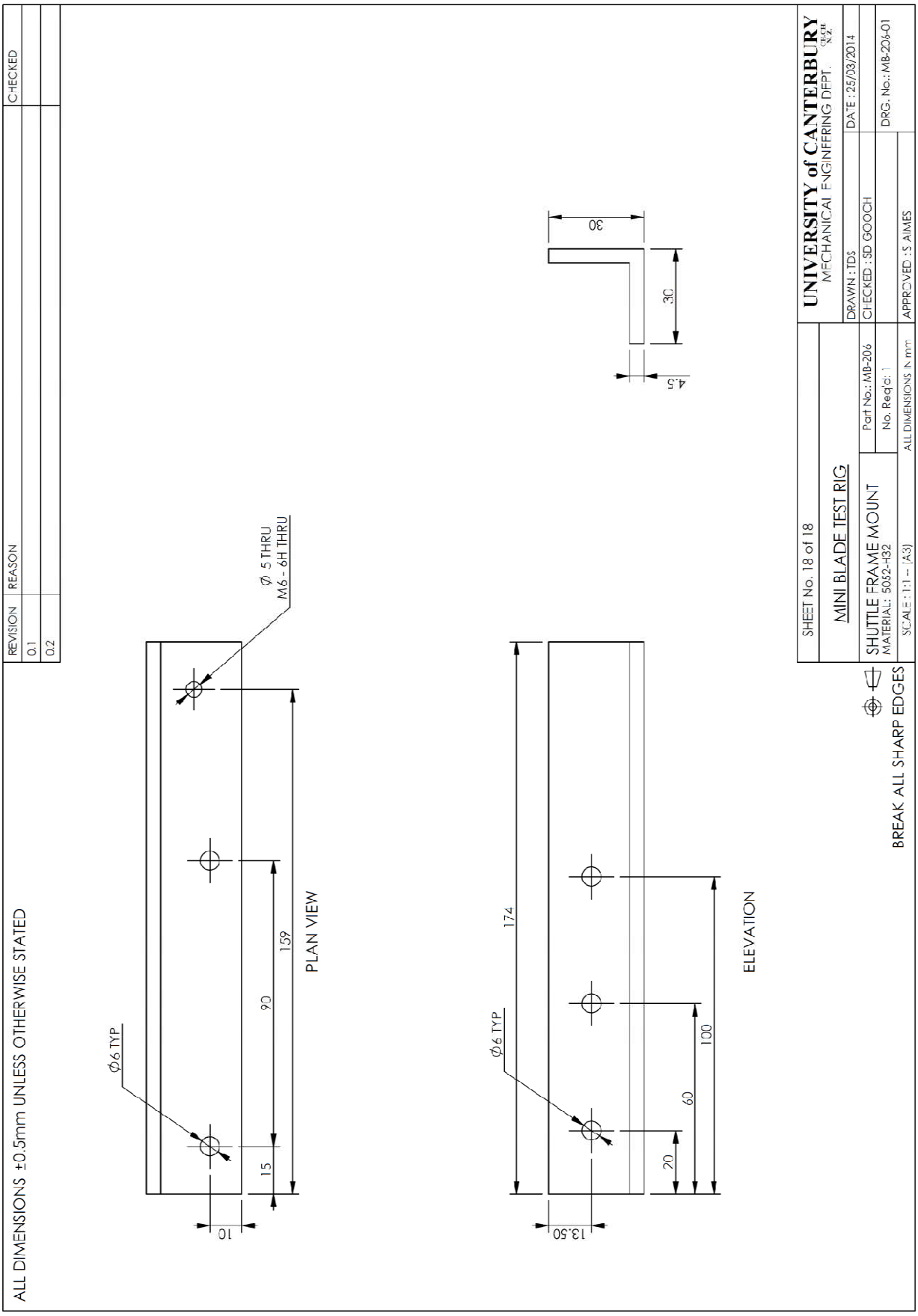

Figure A.29: Manufacturing drawing of RH shuttle frame mount in the variable stroke test rig. Drawing no. MB-206-01

B. Computational Procedures

B1 Tipdeflection.m

```
% Calculating the shape of a horizontal cantilever with varying initial
% angle

clear all
clc

%% Strip Properties

h = 0.0018;          % h = thickness of the strip
b = 0.2;             % b = width of the strip
p = 7789;            % p = the density of the strip (kg/m^3)
g = 9.81;            % g = gravity (m/s^2)
w = b*h*1*p*g;       % w = wieght per unit lenght of the metal strip
(N/m)
Ig = (b*(h^3))/12;   % The geometric second moment of the strip
Ev = 210e9;          % The calculated E of the strip
poison=0.295;
E = Ev*(1-poison^2);
B=E*Ig;
lg = ((B)/(p*g*h*b))^(1/3); %natural bending length


% Given:
% L is 1.93 x bending length for proper tip angle
l = 1.599;           % Length of the strip
global L
L = l/lg;            % Non-dimensional length

global Fy
fy = w*l;
Fy = fy*lg^2/B


alph = 0;            % Initial Angle
v =[-2];             % Set inital guess for shooting parameter

for jj = 1:100;      % Loop to drive fv to its desired value
    m0 = v(1);

    sr = [0 L];      % Integration range

    for hh = 1:1;
        u10 = alph; % Set up initial conditions
        u20 = v(1);
        u30 = 0;
        u40 = [0 0];
```

```
        u50 = [1 0];
        u60 = [0 0];

        u0 = [u10; u20; u30; u40(hh); u50(hh); u60(hh)];%Initial
conditions

        [s,u]=ode45(@horicant, sr, u0);  %Function that outputs the
results

        n = length(s);

        Df(1,hh) = u(n,5);      %Constructing the Jacobian matrix
    end

    fv = [u(n,2)];        %The function fv is driven to zero

    error(:,jj) = fv;
    ch = fv/Df;

    iteration(jj) = jj;

      if abs(fv)<0.0005
          fv*B/lg;
          jj
          break
      end
      v = v - 0.1*ch';

end
baseangle = u(1,1)*(360/(2*pi));
tipangle = u(end,1)*(360/(2*pi));
Nondbasemoment = u(1,2);
result = [baseangle tipangle Nondbasemoment];

X(1) = 0;       % Initialising with boundary conditions
Y(1) = 0;

for ii = 1:n-1;
    X(ii+1) = X(ii) + (s(ii+1)-s(ii))*cos(u(ii,1));
    Y(ii+1) = Y(ii) + (s(ii+1)-s(ii))*sin(u(ii,1));
end

figure(1)
plot(lg*X,Y*lg)
s*lg
moment = u(:,2)*B/lg
stress = (h/(2*Ig))*moment
figure(2)
plot(s*lg,stress)
```

B2 Compare.m

```
function [avgfreq, stress_max, rms, tavg] = compare(text)
%% Strain signal averaging script for clamp separation comparison
% Input is [A,B,C,D,E]=compare(180cs3c.txt)
% '180cs' 180mm clamp separation
% '3' Third mode
% 'c' Cantilever clamp arrangement
raw = dlmread(text, '\t', 23,0);

time = raw(:,1);
strain = raw(:,2);
disp = raw(:,3);
freq = raw(:,4);

rmsvec = zeros(length(strain),1);
tavgvec = zeros(length(strain),1);

%% Time-average of strain signal
for ii = 1:length(tavgvec)
    tavgvec(ii) = abs(strain(ii));
end

tavg = mean(tavgvec);

%% RMS average of strain signal
for jj = 1:length(rmsvec)
    rmsvec(ii) = strain(ii)^2;
end

vecsum = sum(rmsvec);

rms = sqrt(vecsum/length(vecsum));

%% Average frequency for the current data
for kk = 1:length(freq)
    if freq(kk) > 12
        freq(kk) = 0;
    end
end

freq = freq(freq~=0);

avgfreq = mean(freq);

%% Max/min stress for the current data
stress_max = max(tavgvec)*1e-6*210e9;

end
```

B3 Strainconv.m

```
function [stress_max0, stress_min0, stress_maxs, stress_mins,
scaledstress]...
    = strainconv(text, ls)
%% INITIAL CONDITIONS

SF = 1;  %Safety factor on scaled stresses

%% MODEL MATERIAL PROPERTIES

format short

rho0 = 7800;
E0 = 210e9;
l0 = 1.599;
sigy0 = 900;
sigu0 = 1400;

%% SCALED MATERIAL PROPERTIES

rhos = 4429;
Es = 114e9;
%ls = 4.98;
sigys = 931; %Ensure in mPa
sigus = 985;

%% STRAIN DATA FROM STEEL BLADE TEST RIG TO SCALED TITANIUM STRESS

raw = dlmread(text, '\t', 23,0);

time = raw(:,1);
strain = raw(:,2);
disp = raw(:,3);
freq = raw(:,4);

%Model stress conversion
modelstress = (strain.*(1e-6)).*E0;

%Maximum and minimum stresses seen by model
stress_max0 = max(modelstress)/1e6;
stress_min0 = min(modelstress)/1e6;

fprintf(['The maximum model stress is: ' num2str(stress_max0) ' mPa']);
fprintf('\n')
fprintf(['The minimum model stress is: ' num2str(stress_min0) ' mPa']);
fprintf('\n')

%Material factor based on equation 2.20 in thesis
matfac = sqrt((rhos*Es*ls)/(rho0*E0*l0));
scaledstress = modelstress.*matfac*SF;

%Maximum and minimum stresses seen by scaled sculpture
stress_maxs = max(scaledstress)/1e6;
stress_mins = min(scaledstress)/1e6;

fprintf(['The maximum scaled stress is: ' num2str(stress_maxs) ' mPa']);
```

```
fprintf('\n')
fprintf(['The minimum scaled stress is: ' num2str(stress_mins) ' mPa']);
fprintf('\n')
%% CHECK MODEL STRESSES

if abs(stress_max0) && abs(stress_min0) >= sigy0
    fprintf('The model is yielding')
elseif abs(stress_max0) >= sigy0
    fprintf('The model is yielding')
elseif abs(stress_min0) >= sigy0
    fprintf('The model is yielding')
else
    fprintf('The model is NOT yielding')
end

%% CHECK SCALED STRESSES

fprintf('\n')

if abs(stress_maxs) && abs(stress_mins) >= sigys
    fprintf('The scaled Blade will yield')
elseif abs(stress_maxs) >= sigys
    fprintf('The scaled Blade will yield')
elseif abs(stress_mins) >= sigys
    fprintf('The scaled Blade will yield')
else
    fprintf('The scaled Blade will NOT yield, consider fatigue')
end
fprintf('\n')
end
```

B4 Bladefatiguefinalv3.m

```
%% FATIGUE LIFE CALCULATION OF BLADE MATERIAL AT VARIOUS SIZES
% REVISION 3 - USES MANSONS METHOD AND THE MODIFIED MINERS RULE TO
ACCOUNT
%               FOR DAMAGE

clear
clc

T_0 = 370;      %130 seconds for 2nd mode, 220 seconds 3rd mode - Shayne
                %thesis, 20 seconds changing speeds
numtxt = 10;    %Number of text files
results = zeros(numtxt, 1);
                %List of possible blade sizes for life calculations
blades = [4.980; 5.307; 5.624; 5.932; 6.232; 6.526; 6.813; 7.094; 7.369;
...
    7.640; 7.905; 8.167; 8.424];
%ls=8.424;      %Use this if you only want to calculated lives for the
                %largest blade size (turn off the loop as well)

for vv = 1:length(blades)
    ls = blades(vv);
for zz = 1:numtxt
sigmae = 10e6;  %This is the value used to determine if it is a peak or
not
                %(Use endurance limit for miners rule but for mansons
use
                %10e6)

resolution = sigmae*2;  %Preceding stress value difference to determine
a
                        %relative max/min - USE 2x MODIFIED ENDURANCE
LIMIT

[stress_max0, stress_min0, stress_maxs, stress_mins, scaledstress] = ...
    strainconv(['P', num2str(zz), 'W1230813.txt'], ls);

[maxtab, mintab]=peakdet(scaledstress,resolution);

time = 0:T_0/(length(scaledstress)-1):T_0;

%hold on;
%plot(time,scaledstress)
%plot(mintab(:,1), mintab(:,2), 'g*');
%plot(maxtab(:,1), maxtab(:,2), 'r*');
%hold off;


%% Separate out peaks and valleys  - first column is x value indices

xvalleys = mintab(:,1);
xpeaks = maxtab(:,1);
yvalleys = mintab(:,2);
ypeaks = maxtab(:,2);

%Defining new vector EXTREMA with minima and maxima in order as they
appear
```

```
%in printed Figure 1.  ASSUMPTION:  Signal will always start and end in
%whichever extrema has themost occurences in the data - unless equal
%occurences are present

gg = length(yvalleys);
ff = length(ypeaks);

if gg>ff
    limit = gg;
else
    limit = ff;
end

extrema = zeros(gg+ff,1);
lext = length(extrema);  %---REVISION 1 CHANGE---%

if gg>ff  %(More valleys than peaks in the signal)
    extrema(1:2:lext) = yvalleys;
    extrema(2:2:lext-1) = ypeaks;
elseif ff>gg  %(More peaks than valleys in the signal)
    extrema(1:2:lext) = ypeaks;
    extrema(2:2:lext-1) = yvalleys;
else
    if maxtab(1,1)<mintab(1,1)  %(Equal peaks and valleys, with a peak
in
                                %the signal first)
        extrema(1:2:lext-1) = ypeaks;
        extrema(2:2:lext) = yvalleys;
    else  %(Equal peaks and valleys, with a valley in the signal first)
        extrema(1:2:lext-1) = yvalleys;
        extrema(2:2:lext) = ypeaks;
    end
end

%% RAINFLOW COUNTING CYCLE

cycles = zeros(length(extrema),3);      %Version 2
count = 0;
points = zeros(3,1);
location = zeros(3,1);

for ii = 1:lext %---REVISION 1 CHANGE---%

    %Define the first 3 non-zero points in the 'extrema' array and store
    %them in a temporary vector 'points'.  Also record the location in
the
    %'extrema' vector of these points for use when discarding
peaks/valleys.

        for jj = 1:lext
            if extrema(jj)~=0
                points(1)=extrema(jj);
                location(1)=jj;
                for kk=jj+1:lext
                    if extrema(kk)~=0
                        points(2)=extrema(kk);
                        location(2)=kk;
                        for ll=kk+1:lext
                            if extrema(ll)~=0
```

```
                            points(3)=extrema(ll);
                            location(3)=ll;
                            break
                        else
                        end
                    end
                    break
                else
                end
            end
            break
        else
        end
    end


    %Analyse the nature of the 3 points based on S, X and Y as in
ASTM
    %E1049-85
    A = points(1);
    B = points(2);
    C = points(3);
    Y = abs(A-B);
    X = abs(B-C);
    mean = (A+B)/2;
    S = A;

    if X>=Y

        cycles(ii,:) = [Y 0.5 mean]; %Count the half cycle
        extrema(location(1)) = 0; %Discard S in 'extrema' vector

    elseif X<Y

        %Check if there is enough data to step onwards, if not break
        %and go to residual half cycle analysis
        if lext-location(2)<3
            break
        end

        %Step the starting point forward by one (using 'offset' as
        %the last location(1) value to the next S value
        for tt = 1:lext-location(1)
            offset = location(1);
            for jj = offset+1:lext
                if extrema(jj)~=0
                    points(1)=extrema(jj);
                    location(1)=jj;
                    for kk=jj+1:lext
                        if extrema(kk)~=0
                            points(2)=extrema(kk);
                            location(2)=kk;
                            for ll=kk+1:lext
                                if extrema(ll)~=0
                                    points(3)=extrema(ll);
                                    location(3)=ll;
                                    break
                                else
                                end
                            end
```

```
                                break
                            else
                            end
                        end
                        break
                    else
                    end
                end

                %Analyse points again to determine nature
                A = points(1);
                B = points(2);
                C = points(3);
                Y = abs(A-B);
                X = abs(B-C);
                mean = (A+B)/2;
                S = A;


            %If the new points give the condition for a count then record
Y
            %as one cycle and discard the first 2 points of the 3
            %points.  Break the loop and go back to beginning of main
loop.
                if X>=Y
                    cycles(ii,:) = [Y 1 mean];
                    extrema(location(1)) = 0; %Discard first range from
                                              %'extrema' vector
                    extrema(location(2)) = 0;
                else  %Otherwise continue on to next starting point S.
                break
                end
             end


        end
end

%% FORMATION OF STRESS/CYCLE HISTORGRAM

extrema = extrema(extrema~=0);
residual = zeros(length(extrema)-1,2);

for hh = 1:length(residual)
    residual(hh,1) = abs(extrema(hh)-extrema(hh+1));
    residual(hh,2) = 0.5;
    residual(hh,3) = (extrema(hh)+extrema(hh+1))/2;
end

if cycles~=0  %Version 2
    cycles = cycles(any(cycles,2),:);
    totalcycles = [cycles; residual];
else
    totalcycles = residual;
end

c1 = totalcycles(:,1); %Array of cycle ranges
c2 = totalcycles(:,2); %Array of cycle counts
c3 = totalcycles(:,3); %Array of cycle mean values
```

```
maxc1 = max(c1);
minc1 = min(c1);

%Produce Histogram of half cycle stresses
X = [c3,c1];
Number=hist3(X);
figure(2)
hist3(X)
xlabel('Mean, Pa'); ylabel('Range, Pa');
set(gcf,'renderer','opengl');
set(get(gca,'child'),'FaceColor','interp','CDataMode',...
'auto')

edges = 0:10e6:400e6;

bincount = zeros(1, length(edges)-1);
binvalue = zeros(1, length(edges)-1);
binrange = zeros(1, length(edges)-1);

for nn = 1:length(c1)
    for mm = 1:length(edges)-1
        value = c1(nn);
        if value>=edges(mm) && value<edges(mm+1)
            binrange(mm) = value;
            bincount(mm) = bincount(mm)+1;
            binvalue(mm) = binvalue(mm)+c2(nn);
            break
        elseif value == edges(mm+1)
            binrange(mm) = value;
            bincount(mm) = bincount(mm)+1;
            binvalue(mm) = binvalue(mm)+c2(nn);
        end
    end
end

%% LIFE CALCULATION USING SWT FOR EQUIVALENT ZERO-MEAN AMPLITUDES,
% TRUE FRACTURE STRENGTH, ENDURANCE LIMIT
%Refer to Excel file 'Ti 6Al 4V S-N Curve Thesis' for values, references
%and equation of curve
a = 1188.6e6;        %All values obtained from virgin SN curve in excel
                     %file from DOWLING USAF data S=aN^b
b = -0.144;
N0 = 1000;
Ne = 1e6;
itcpt=a*(N0)^b;      %Common y intercept at 1000 cycles for all S-N
curves
                     %following the virgin curve
sigmae=a*(Ne)^b;

ar = zeros(length(c1),1);
%Form the array of equivalent zero-mean amplitudes using equation 5c
%Dowling 2008

for yy = 1:length(c1)
    stress1=abs(c3(yy)+c1(yy)/2);
    stress2=abs(c3(yy)-c1(yy)/2);
    if stress1>=stress2
        sigmax = stress1;
        sigmin = stress2;
```

```
    else
        sigmax = stress2;
        sigmin = stress1;
    end

    ar(yy) = sqrt((c1(yy)/2)*(sigmax));  %Equation 5a in DOWLING PAPER
                                         %(SWT) zero-mean adjusted
                                         %amplitudes

end

%Damage accumulation in material for a single performance of T0 seconds
damage = [ar c2];

if sum(damage(:,1))>0
    damage = damage(any(damage,2),:);

    Dam = zeros(length(ar),1);

    for ss=1:length(ar)  %THIS IS MANSONS METHOD PAGE 420 SHIGLEY AS
                         %RECOMMENDED OVER MINER'S

            n = damage(ss,2);  %Number of cycles of cycle in question
            S1 = damage(ss,1);  %Stress amplitude of cycle in question

            if S1<sigmae
                %Number of cycles to failure of cycle in question
                N(ss) = N0*(10^((log10(S1)-log10(itcpt))/b));
                %Damage to material for cycle in question
                Dam(ss) = n/N(ss);
                %New x intercept at the stress level for cycle in
question
                deltaN = N(ss)-n;
                %New slope to SN curve since stress is above endurance
                b = (log(S1)-log(itcpt))/(log(deltaN)-log(N0));
                D = sum(Dam);
                if D>1
                    break
                else
                end
                %New endurance limit since material is damaged
                sigmae = itcpt*(10^((log10(Ne)-log10(N0))*b));
            else
                %Number of cycles to failure of cycle in question
                N(ss) = N0*(10^((log10(S1)-log10(itcpt))/b));
                %Damage to material for cycle in question
                Dam(ss) = n/N(ss);
                D = sum(Dam);
                if D>1
                    break
                else
                end
            end
    end

    %Expected time to failure in seconds;
    if D>=1
        disp('Scaled Blade will fail by fatigue after 1 performance')
    elseif D<1 && D>0
```

```
        T = T_0/D;

        disp(['Calculated fatigue life in performances: ' num2str...
            (ceil(T/T_0))])
    end

else
    disp('Infinite fatigue life')
end

results(zz,vv) = ceil(T/T_0);

end
end
```

B5 Peakdet.m

```
function [maxtab, mintab]=peakdet(v, delta, x)
%PEAKDET Detect peaks in a vector
%        [MAXTAB, MINTAB] = PEAKDET(V, DELTA) finds the local
%        maxima and minima ("peaks") in the vector V.
%        MAXTAB and MINTAB consists of two columns. Column 1
%        contains indices in V, and column 2 the found values.
%
%        With [MAXTAB, MINTAB] = PEAKDET(V, DELTA, X) the indices
%        in MAXTAB and MINTAB are replaced with the corresponding
%        X-values.
%
%        A point is considered a maximum peak if it has the maximal
%        value, and was preceded (to the left) by a value lower by
%        DELTA.


maxtab = [];
mintab = [];

v = v(:); % Just in case this wasn't a proper vector

if nargin < 3
  x = (1:length(v))';
else
  x = x(:);
  if length(v)~= length(x)
    error('Input vectors v and x must have same length');
  end
end

if (length(delta(:)))>1
  error('Input argument DELTA must be a scalar');
end

if delta <= 0
  error('Input argument DELTA must be positive');
end

mn = Inf; mx = -Inf;
mnpos = NaN; mxpos = NaN;

lookformax = 1;

for i=1:length(v)
  this = v(i);
  if this > mx, mx = this; mxpos = x(i); end
  if this < mn, mn = this; mnpos = x(i); end

  if lookformax
    if this < mx-delta
      maxtab = [maxtab ; mxpos mx];
      mn = this; mnpos = x(i);
      lookformax = 0;
    end
  else
    if this > mn+delta
```

```
      mintab = [mintab ; mnpos mn];
      mx = this; mxpos = x(i);
      lookformax = 1;
    end
  end
end
```

B6 Natural Frequency Calculations (wxMaxima)

```
(%i64) kill(all);

 (%o0) done

(%i1) reset(all);

 (%o1) []

(%i2) l:1.934;

 (%o2) 1.934

(%i3) lc:0.3;

 (%o3) 0.3
```

Normal function for region 1 of beam

```
(%i4) W1(x) := A1*cosh(B*x) + A2*sinh(B*x) + A3*cos(B*x) + A4*sin(B*x);

 (%o4) W1(x):=A1 cosh(B x)+A2 sinh(B x)+A3 cos(B x)+A4 sin(B x)

(%i5) sol : divide("diff(W1(x),x,1),B)$
      a : sol[1]$
      W1_1(x) := "a;

 (%o7) W1_1(x):=A1 sinh(x B)-A3 sin(x B)+A2 cosh(x B)+A4 cos(x B)

(%i8) sol : divide("diff(W1(x),x,2),B^2)$
      a : sol[1]$
      W1_2(x) := "a;

(%o10) W1_2(x):=A2 sinh(x B)-A4 sin(x B)+A1 cosh(x B)-A3 cos(x B)

(%i11) sol : divide("diff(W1(x),x,3),B^3)$
       a : sol[1]$
       W1_3(x) := "a;

(%o13) W1_3(x):=A1 sinh(x B)+A3 sin(x B)+A2 cosh(x B)-A4 cos(x B)
```

Normal function for region 2 of beam

```
(%i14) W2(x) := C1*cosh(B*x) + C2*sinh(B*x) + C3*cos(B*x) + C4*sin(B*x);

(%o14) W2(x):=C1 cosh(B x)+C2 sinh(B x)+C3 cos(B x)+C4 sin(B x)

(%i15) sol : divide("diff(W2(x),x,1),B)$
       a : sol[1]$
       W2_1(x) := "a;

(%o17) W2_1(x):=cos(x B) C4-sin(x B) C3+cosh(x B) C2+sinh(x B) C1

(%i18) sol : divide("diff(W2(x),x,2),B^2)$
       a : sol[1]$
```

```
W2_2(x) := "a;
```

```
(%o20)  W2_2(x):=-sin(x B) C4-cos(x B) C3+sinh(x B) C2+cosh(x B) C1
```

```
(%i21)  sol : divide("diff(W2(x),x,3),B^3)$
        a : sol[1]$
        W2_3(x) := "a;
```

```
(%o23)  W2_3(x):=-cos(x B) C4+sin(x B) C3+cosh(x B) C2+sinh(x B) C1
```

Boundary conditions region 1
BC1 : Deflection at the lower clamp is zero
BC2 : Bending moment at the lower clamp is zero

```
(%i24)  BC1 : W1(0)=0;
```

```
(%o24)  A3+A1=0
```

```
(%i25)  BC2 : W1_2(0)=0;
```

```
(%o25)  A1-A3=0
```

Boundary conditions region 2
BC3 : Deflection at the upper clamp is zero
BC4 : Bending moment at the upper clamp is zero
BC5 : Shear force at the free end of the blade is zero

```
(%i26)  BC3 : W2(lc)=0;
```

```
(%o26)  sin(0.3 B) C4+cos(0.3 B) C3+sinh(0.3 B) C2+cosh(0.3 B) C1=0
```

```
(%i27)  BC4 : W2_2(l)=0;
```

```
(%o27)  -sin(1.934 B) C4-cos(1.934 B) C3+sinh(1.934 B) C2+cosh(1.934 B) C1=0
```

```
(%i28)  BC5 : W2_3(l)=0;
```

```
(%o28)  -cos(1.934 B) C4+sin(1.934 B) C3+cosh(1.934 B) C2+sinh(1.934 B) C1=0
```

Continuity conditions
CC1 : The slopes in the blade at the upper clamp are equal and opposite
CC2 : The bending moments in the blade at the upper clamp are equal and opposite
CC3 : Deflection at the upper clamp is equal

```
(%i29)  CC1 : W1_1(lc)=W2_1(lc);
```

```
(%o29)  A1 sinh(0.3 B)-A3 sin(0.3 B)+A2 cosh(0.3 B)+A4 cos(0.3 B)=cos(0.3 B) C4-
sin(0.3 B) C3+cosh(0.3 B) C2+sinh(0.3 B) C1
```

```
(%i30)  CC2 : W2_2(lc)=W1_2(lc);
```

```
(%o30)  -sin(0.3 B) C4-cos(0.3 B) C3+sinh(0.3 B) C2+cosh(0.3 B) C1=A2 sinh(0.3 B)-A4
sin(0.3 B)+A1 cosh(0.3 B)-A3 cos(0.3 B)
```

(%i31) CC3 : W1(lc)+W2(lc)=0;

(%o31) $\sin(0.3\,B)\,C4+\cos(0.3\,B)\,C3+\sinh(0.3\,B)\,C2+\cosh(0.3\,B)\,C1+A2\sinh(0.3\,B)+A4\sin(0.3\,B)+A1\cosh(0.3\,B)+A3\cos(0.3\,B)=0$

Coefficient matrix of boundary condition normal functions

(%i32) A : coefmatrix([BC1,BC2,BC3,BC4,BC5,CC1,CC2,CC3],[A1,A2,A3,A4,C1,C2,C3,C4]);

(%o32)

$$\begin{bmatrix}
1 & 0 & 1 & 0 & 0 & 0 & 0 & 0 \\
1 & 0 & -1 & 0 & 0 & 0 & 0 & 0 \\
0 & 0 & 0 & 0 & \cosh(0.3\,B) & \sinh(0.3\,B) & \cos(0.3\,B) & \sin(0.3\,B) \\
0 & 0 & 0 & 0 & \cosh(1.934\,B) & \sinh(1.934\,B) & -\cos(1.934\,B) & -\sin(1.934\,B) \\
0 & 0 & 0 & 0 & \sinh(1.934\,B) & \cosh(1.934\,B) & \sin(1.934\,B) & -\cos(1.934\,B) \\
\sinh(0.3\,B) & \cosh(0.3\,B) & -\sin(0.3\,B) & \cos(0.3\,B) & -\sinh(0.3\,B) & -\cosh(0.3\,B) & \sin(0.3\,B) & -\cos(0.3\,B) \\
-\cosh(0.3\,B) & -\sinh(0.3\,B) & \cos(0.3\,B) & \sin(0.3\,B) & \cosh(0.3\,B) & \sinh(0.3\,B) & -\cos(0.3\,B) & -\sin(0.3\,B) \\
\cosh(0.3\,B) & \sinh(0.3\,B) & \cos(0.3\,B) & \sin(0.3\,B) & \cosh(0.3\,B) & \sinh(0.3\,B) & \cos(0.3\,B) & \sin(0.3\,B)
\end{bmatrix}$$

(%i33) CHAR : determinant(A)$

(%i34) CHAR : trigsimp(%);

```
rat: replaced 1.934 by 967/500 = 1.934
rat: replaced 1.934 by 967/500 = 1.934
rat: replaced 1.934 by 967/500 = 1.934
rat: replaced 0.3 by 3/10 = 0.3
rat: replaced 0.3 by 3/10 = 0.3
rat: replaced 0.3 by 3/10 = 0.3
rat: replaced 1.934 by 967/500 = 1.934
rat: replaced 0.3 by 3/10 = 0.3
```

(%o34)

$$\left(\left(-4\cosh\left(\frac{3B}{10}\right)^2-4\cos\left(\frac{3B}{10}\right)^2+8\right)\sin\left(\frac{967B}{500}\right)+\left(4\cos\left(\frac{3B}{10}\right)\sin\left(\frac{3B}{10}\right)-4\cosh\left(\frac{3B}{10}\right)\sinh\left(\frac{3B}{10}\right)\right)\cos\left(\frac{967B}{500}\right)\right)$$
$$\sinh\left(\frac{967B}{500}\right)+\left(4\cosh\left(\frac{3B}{10}\right)\sinh\left(\frac{3B}{10}\right)-4\cos\left(\frac{3B}{10}\right)\sin\left(\frac{3B}{10}\right)\right)\cosh\left(\frac{967B}{500}\right)\sin\left(\frac{967B}{500}\right)+$$
$$\left(4\cosh\left(\frac{3B}{10}\right)^2-4\cos\left(\frac{3B}{10}\right)^2\right)\cos\left(\frac{967B}{500}\right)\cosh\left(\frac{967B}{500}\right)+8\sin\left(\frac{3B}{10}\right)\sinh\left(\frac{3B}{10}\right)$$

(%i35) wxplot2d([CHAR], [B,0,20], [y,-100000,100000])$

```
plot2d: some values were clipped.
```

(%t35)

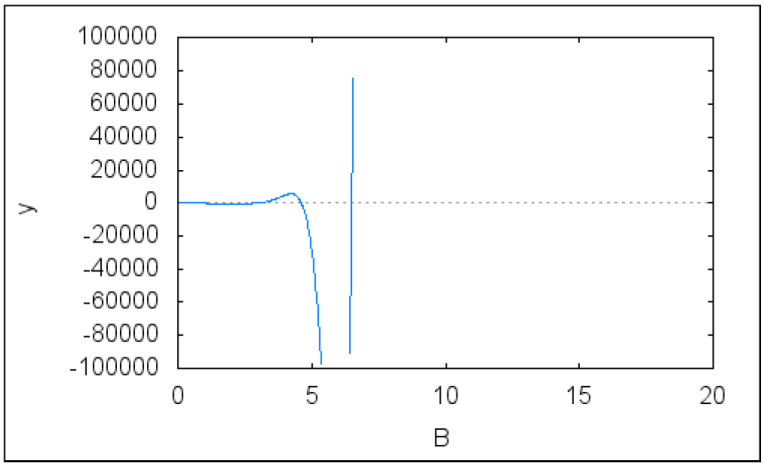

(%i36) B1 : find_root("(CHAR), B, 1, 2);

(%o36) 1.086094066174411

(%i37) B2 : find_root("(CHAR), B, 2, 4);

(%o37) 2.743290330718107

(%i38) B3 : find_root("(CHAR), B, 4, 5);

(%o38) 4.616889584233593

(%i39) COEF : linsolve([BC1, BC2, BC3, BC4, BC5, CC1, CC2], [A1,A2,A3,A4,C1,C2,C3,C4])$

(%i40) EIGFUN1 : subst(rhs(COEF[1]), A1, W1(x))$

(%i41) EIGFUN1 : subst(rhs(COEF[2]), A2, EIGFUN1)$

(%i42) EIGFUN1 : subst(rhs(COEF[3]), A3, EIGFUN1)$

(%i43) EIGFUN1 : subst(rhs(COEF[4]), A4, EIGFUN1)$

CHANGE THE REAL NUMBER VARIABLE FOR EACH RUN

(%i44) EIGFUN1 : subst(1, %r4, EIGFUN1)$

(%i45) EIGFUN1 : trigsimp(EIGFUN1);

```
rat: replaced 0.3 by 3/10 = 0.3
rat: replaced 0.3 by 3/10 = 0.3
rat: replaced 1.934 by 967/500 = 1.934
rat: replaced 1.934 by 967/500 = 1.934
rat: replaced 1.934 by 967/500 = 1.934
rat: replaced 1.934 by 967/500 = 1.934
rat: replaced 0.3 by 3/10 = 0.3
rat: replaced 0.3 by 3/10 = 0.3
```

(%o45)

$$-((\left(2\sinh\left(\frac{3B}{10}\right)+2\cos\left(\frac{3B}{10}\right)\cosh\left(\frac{3B}{10}\right)\sin\left(\frac{3B}{10}\right)\right)\sin\left(\frac{967B}{500}\right)+2\cos\left(\frac{3B}{10}\right)^2\cosh\left(\frac{3B}{10}\right)\cos\left(\frac{96}{5}\right.$$
$$\sinh\left(\frac{967B}{500}\right)+\left(-2\cos\left(\frac{3B}{10}\right)\sin\left(\frac{3B}{10}\right)\sinh\left(\frac{3B}{10}\right)-2\cosh\left(\frac{3B}{10}\right)\right)\cosh\left(\frac{967B}{500}\right)\sin\left(\frac{967B}{500}\right)-2\cos\left(\frac{3B}{10}\right)^2$$
$$\sinh\left(\frac{3B}{10}\right)\cos\left(\frac{967B}{500}\right)\cosh\left(\frac{967B}{500}\right)-2\sin\left(\frac{3B}{10}\right))\sinh(xB)+((\left(-2\cos\left(\frac{3B}{10}\right)\cosh\left(\frac{3B}{10}\right)\sinh\left(\frac{3B}{10}\right)-2\right.$$
$$\left(2\cosh\left(\frac{3B}{10}\right)\sin\left(\frac{3B}{10}\right)\sinh\left(\frac{3B}{10}\right)-2\cos\left(\frac{3B}{10}\right)\right)\cos\left(\frac{967B}{500}\right))\sinh\left(\frac{967B}{500}\right)+2\cos\left(\frac{3B}{10}\right)\cosh\left(\frac{3B}{10}\right)^2$$
$$\cosh\left(\frac{967B}{500}\right)\sin\left(\frac{967B}{500}\right)-2\cosh\left(\frac{3B}{10}\right)^2\sin\left(\frac{3B}{10}\right)\cos\left(\frac{967B}{500}\right)\cosh\left(\frac{967B}{500}\right)-2\sinh\left(\frac{3B}{10}\right))\sin(xB))/((($$
$$\left(-\cos\left(\frac{3B}{10}\right)\sinh\left(\frac{3B}{10}\right)^2-\cosh\left(\frac{3B}{10}\right)\sin\left(\frac{3B}{10}\right)\sinh\left(\frac{3B}{10}\right)\right)\cos\left(\frac{967B}{500}\right))\sinh\left(\frac{967B}{500}\right)+$$
$$\left(-\cos\left(\frac{3B}{10}\right)\sinh\left(\frac{3B}{10}\right)^2-\cosh\left(\frac{3B}{10}\right)\sin\left(\frac{3B}{10}\right)\sinh\left(\frac{3B}{10}\right)\right)\cosh\left(\frac{967B}{500}\right)\sin\left(\frac{967B}{500}\right)+$$
$$\left(\cos\left(\frac{3B}{10}\right)\cosh\left(\frac{3B}{10}\right)\sinh\left(\frac{3B}{10}\right)+\cosh\left(\frac{3B}{10}\right)^2\sin\left(\frac{3B}{10}\right)\right)\cos\left(\frac{967B}{500}\right)\cosh\left(\frac{967B}{500}\right)+\cos\left(\frac{3B}{10}\right)^2\sinh\left(\frac{3B}{10}\right)+$$
$$\cos\left(\frac{3B}{10}\right)\cosh\left(\frac{3B}{10}\right)\sin\left(\frac{3B}{10}\right))$$

(%i46) MODE1_1 : subst(B1, B, EIGFUN1);

(%o46) -0.8138551878135 (7.226692679522595 sin(1.086094066174411 x)-
6.975420646683228 sinh(1.086094066174411 x))

(%i47) MODE1_1 : wxplot2d([MODE1_1], [x,0,0.3], [y,-1,1])$

(%t47)

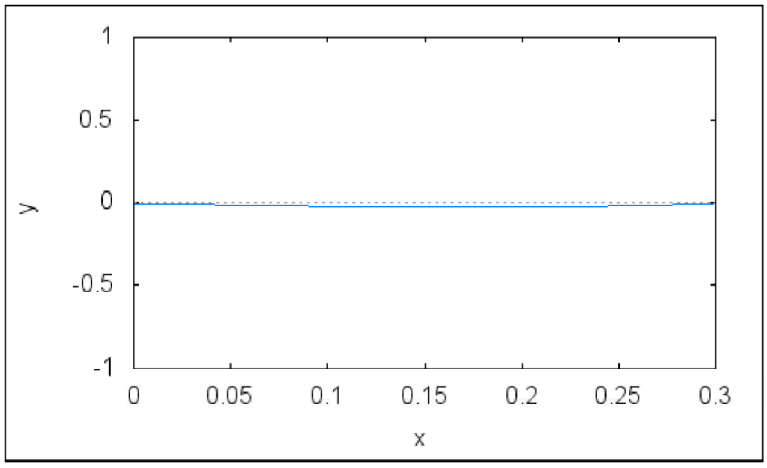

(%i48) MODE1_2 : subst(B2, B, EIGFUN1);

(%o48) 0.054772716561595 (58.18876865202984 sinh(2.743290330718107 x)-
72.94322665525908 sin(2.743290330718107 x))

(%i49) MODE1_2 : wxplot2d([MODE1_2], [x,0,0.3], [y,-1,1])$

(%t49)

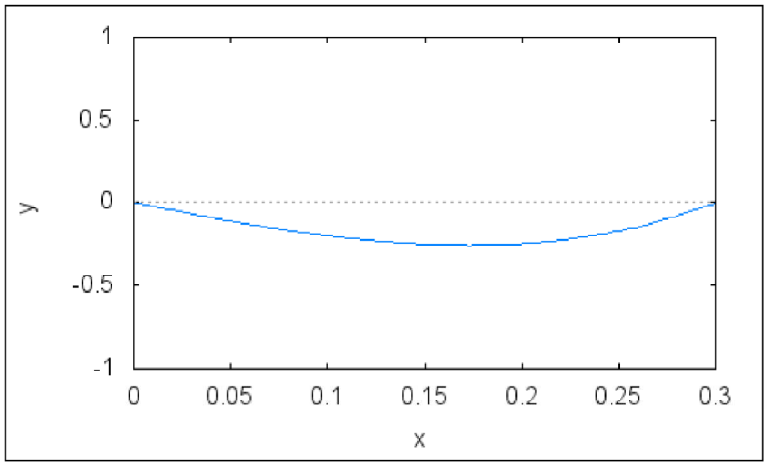

(%i50) MODE1_3 : subst(B3, B, EIGFUN1);

(%o50) 0.001077998747465 (1513.13886108802 sin(4.616889584233593 x)-
794.232624496356 sinh(4.616889584233593 x))

(%i51) MODE1_3 : wxplot2d([MODE1_3], [x,0,0.3], [y,-1,1])$

(%t51)

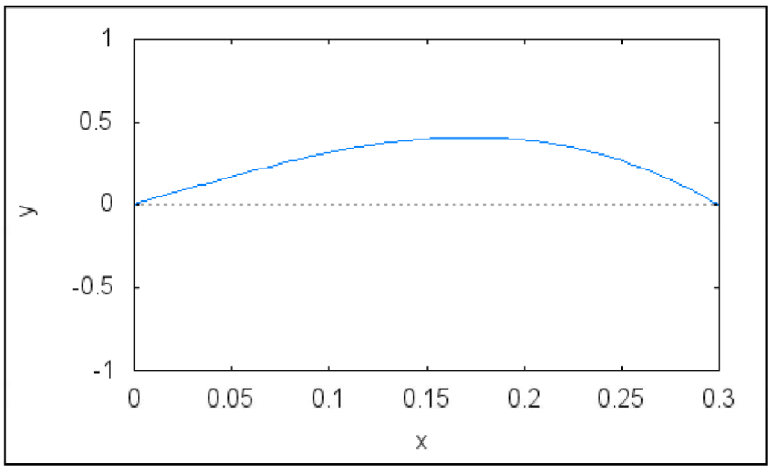

(%i52) EIGFUN2 : subst(rhs(COEF[5]), C1, W2(x))$

(%i53) EIGFUN2 : subst(rhs(COEF[6]), C2, EIGFUN2)$

(%i54) EIGFUN2 : subst(rhs(COEF[7]), C3, EIGFUN2)$

(%i55) EIGFUN2 : subst(rhs(COEF[8]), C4, EIGFUN2)$

CHANGE THE REAL NUMBER VARIABLE FOR EACH RUN

(%i56) EIGFUN2 : subst(1, %r4, EIGFUN2)$

(%i57) EIGFUN2 : trigsimp(EIGFUN2);

```
rat: replaced 0.3 by 3/10 = 0.3
rat: replaced 0.3 by 3/10 = 0.3
rat: replaced 0.3 by 3/10 = 0.3
rat: replaced 1.934 by 967/500 = 1.934
rat: replaced 1.934 by 967/500 = 1.934
rat: replaced 1.934 by 967/500 = 1.934
rat: replaced 1.934 by 967/500 = 1.934
rat: replaced 0.3 by 3/10 = 0.3
```

(%o57)
$$-((\left(\cos\left(\frac{3B}{10}\right)\sin\left(\frac{967B}{500}\right)-\sin\left(\frac{3B}{10}\right)\cos\left(\frac{967B}{500}\right)\right)\sinh\left(\frac{967B}{500}\right)-\sin\left(\frac{3B}{10}\right)\cosh\left(\frac{967B}{500}\right)$$
$$\sin\left(\frac{967B}{500}\right)-\cos\left(\frac{3B}{10}\right)\cos\left(\frac{967B}{500}\right)\cosh\left(\frac{967B}{500}\right)-\cosh\left(\frac{3B}{10}\right))\sinh(xB)+(\left(\sinh\left(\frac{3B}{10}\right)\cos\left(\frac{967B}{500}\right)-\cosh($$
$$\cosh\left(\frac{3B}{10}\right)\cos\left(\frac{967B}{500}\right)\cosh\left(\frac{967B}{500}\right)-\cos\left(\frac{3B}{10}\right))\sin(xB)+(\left(\sin\left(\frac{3B}{10}\right)\sin\left(\frac{967B}{500}\right)+\cos\left(\frac{3B}{10}\right)\cos\left(\frac{967B}{500}\right)\right)$$
$$\sinh\left(\frac{967B}{500}\right)-\cos\left(\frac{3B}{10}\right)\cosh\left(\frac{967B}{500}\right)\sin\left(\frac{967B}{500}\right)+\sin\left(\frac{3B}{10}\right)\cos\left(\frac{967B}{500}\right)\cosh\left(\frac{967B}{500}\right)+\sinh\left(\frac{3B}{10}\right))$$
$$\cosh(xB)+(\left(-\sinh\left(\frac{3B}{10}\right)\sin\left(\frac{967B}{500}\right)-\cosh\left(\frac{3B}{10}\right)\cos\left(\frac{967B}{500}\right)\right)\sinh\left(\frac{967B}{500}\right)+\cosh\left(\frac{3B}{10}\right)\cosh\left(\frac{967B}{500}\right)$$
$$\sin\left(\frac{967B}{500}\right)+\sinh\left(\frac{3B}{10}\right)\cos\left(\frac{967B}{500}\right)\cosh\left(\frac{967B}{500}\right)+\sin\left(\frac{3B}{10}\right))\cos(xB))/(\left(\cosh\left(\frac{3B}{10}\right)\sin\left(\frac{967B}{500}\right)-\sinh($$
$$\cosh\left(\frac{3B}{10}\right)\cos\left(\frac{967B}{500}\right)\cosh\left(\frac{967B}{500}\right)+\cos\left(\frac{3B}{10}\right))$$

(%i58) MODE2_1 : subst(B1, B, EIGFUN2);

(%o58) $-0.53015472662575\ (3.726575654503795\sinh(1.086094066174411\,x)-1.886241789004961\sin(1.086094066174411\,x)-4.543582873810481\cosh(1.086094066174411\,x)+4.38560254232198\cos(1.086094066174411\,x))$

(%i59) MODE2_1 : wxplot2d([MODE2_1], [x,0.3,1.934], [y,-10,10])$

(%t59)

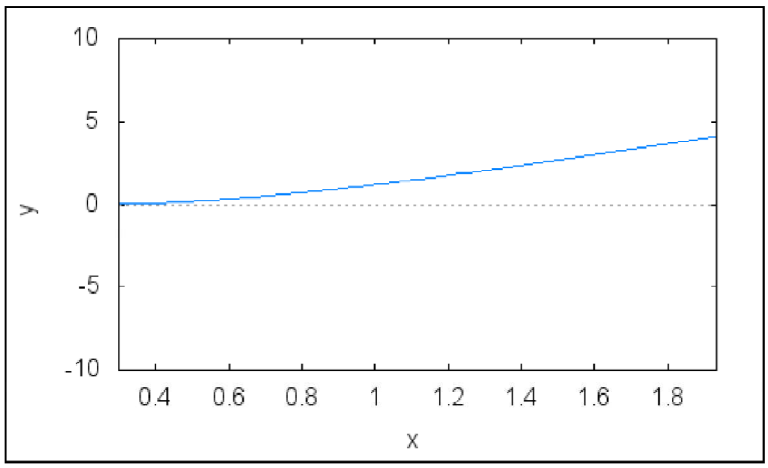

(%i60) MODE2_2 : subst(B2, B, EIGFUN2);

(%o60) 0.088776715056627 (−76.4812460115987 sinh(2.743290330718107 x)+
11.2642149392681 sin(2.743290330718107 x)+76.0480925405858
cosh(2.743290330718107 x)−60.66560345878624 cos(2.743290330718107 x))

(%i61) MODE2_2 : wxplot2d([MODE2_2], [x,0.3,1.934], [y,-10,10])$

(%t61)

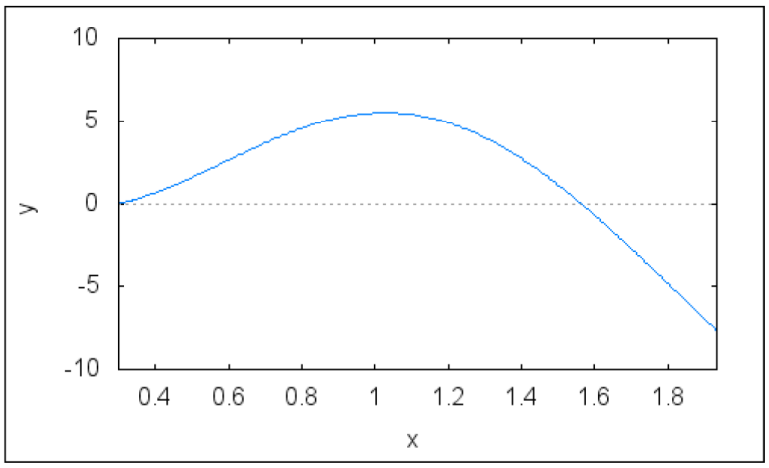

(%i62) MODE2_3 : subst(B3, B, EIGFUN2);

(%o62) 0.0026216456168186 (2440.83334661839 sinh(4.616889584233593 x)+
381.4398077240894 sin(4.616889584233593 x)−2441.083820258623
cosh(4.616889584233593 x)+1281.302370217047 cos(4.616889584233593 x))

(%i63) MODE2_3 : wxplot2d([MODE2_3], [x,0.3,1.934], [y,-10,10])$

(%t63)

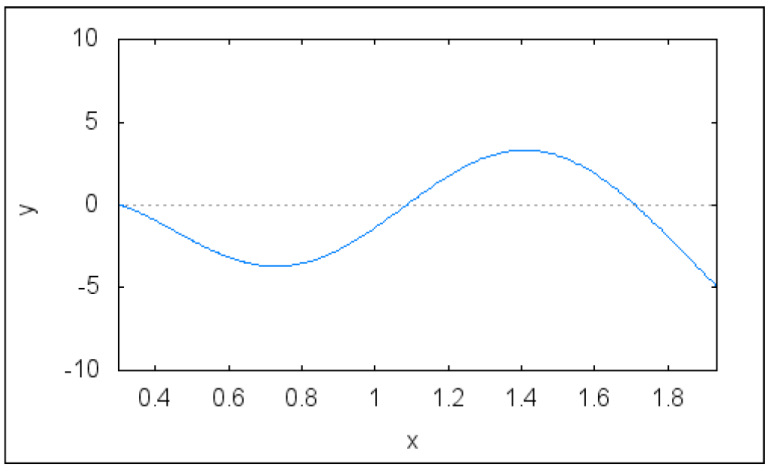

C. Variable Stroke Mechanisms

Study of a Variable Compression Ratio System

by Shunichi Aoyama, Nissan

Recent research at Nissan on a variable compression ratio (VCR) mechanism that uses multiple links to form a new piston/crank system has revealed new potentialities for the multiple-link mechanism in addition to its intended VCR capability.

Configuration of the VCR System

The selection of a suitable link pattern and geometry proved to optimally resolve various associated issues, such as the increase in engine size, cylinder block vibration and engine friction. The Nissan VCR system design concept and some of the results obtained are described in Figure 1. Figure 2 shows the configuration of the multiple-link mechanism incorporated in a VCR prototype engine. In place of conventional connecting rods, the pistons are driven by three types of links fitted to the crankshaft: an upper link (U-link), a lower link (L-link) and a control link (C-link). The C-link pivots around the centre control point of the eccentric bearing of the control shaft positioned parallel to the crankshaft. The angular position of the control shaft can be freely adjusted within a specified range of angles by an actuator, thereby changing the control point and making it possible to vary the compression ratio continuously.

The key point for achieving a compact design is to select a suitable lever ratio for the multiple-link mechanism. A suitable lever ratio makes it possible to obtain the same piston stroke as that of the baseline engine with shorter crank throws. As a result, the stiffness of the crankshaft increases, and the crankpins of the VCR engine crankshaft can be designed with a smaller diameter and a larger width, while maintaining the same level of overall stiffness. A smaller crankpin diameter allows the size of the L-link itself to be reduced. A longer crankpin is also necessary to ensure a sufficient width for the L-link bearing in order to handle the greater load applied to the crankpins on account of the in-

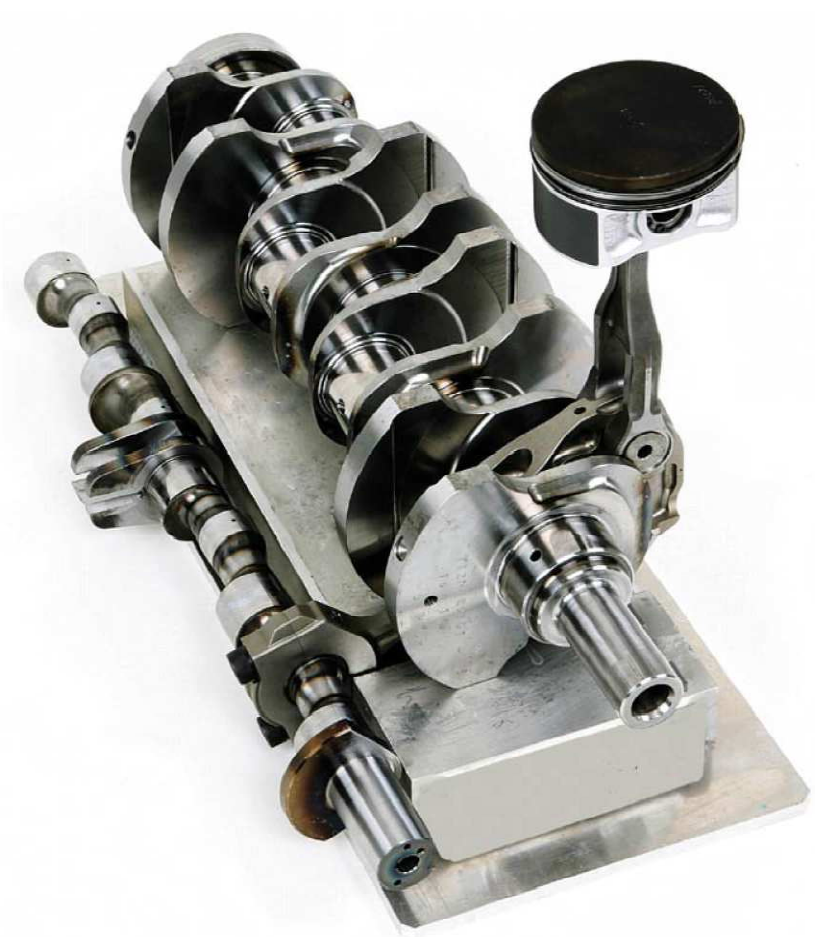

Nissan has developed a new engine mechanism that enables both high power of turbo engine and low fuel consumption of non-turbo engine.

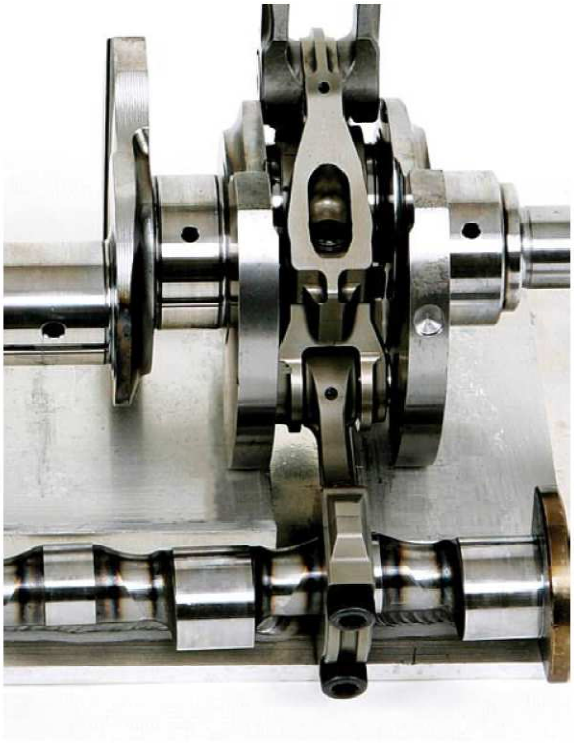

creased piston stroke and lever ratio. In addition, this measure ensures a sufficient width for the bearings of the connecting pins that serve as joints for the multiple-link mechanism.

Vibration Reduction

In a conventional piston/crank system (baseline), the piston acceleration near top dead centre (TDC) is approximately double the acceleration near bottom dead centre (BDC). That is why a balancer shaft is installed to reduce vertical vibration. The link geometry for the Nissan VCR engine was selected on the basis of many trial calculations in order to achieve a piston stroke close to simple harmonic motion and to obtain symmetrical piston acceleration between the TDC and BDC sides. The aim here is to achieve a greater reduction in second-order inertial vibration in a 4-cylinder engine than is possible with a balancer shaft system. The second-order

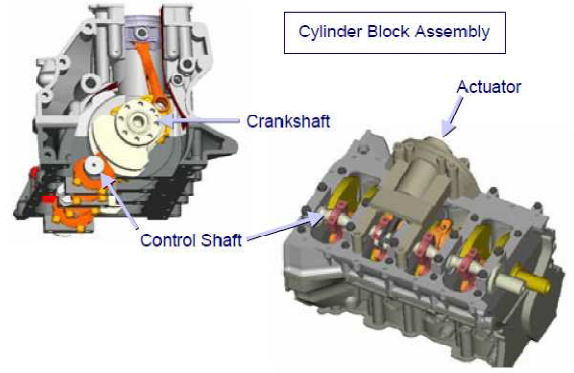

Figure 1: VCR engine with the multiple-link mechanism.

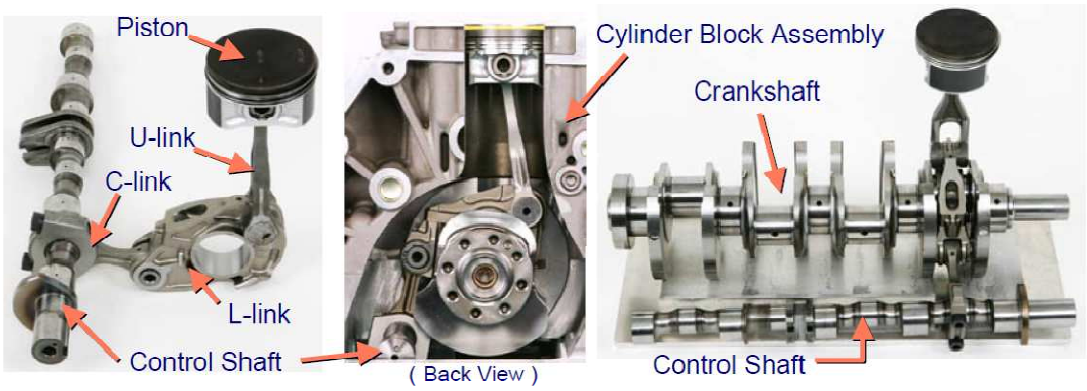

Figure 2: Configuration of the multiple-link mechanism of the Nissan VCR engine.

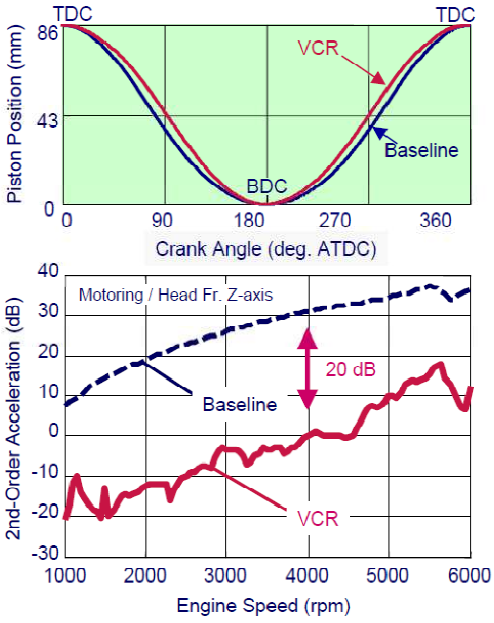

Figure 3: Effect of the modified piston stroke on reducing second-order inertial vibration.

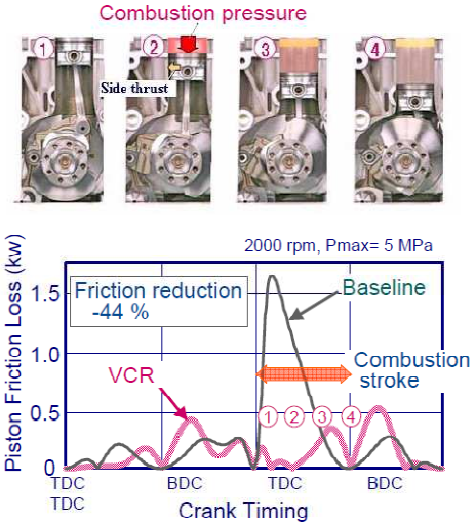

Figure 4: Reduction in piston friction.

inertial vibration level measured for the VCR prototype engine is compared with that of the baseline engine in Figure 3. The piston stroke characteristics resembling simple harmonic motion have a substantial effect on reducing second-order inertial vibration. A slower piston speed in the vicinity of the peak in-cylinder gas pressure also has the effect of reducing the amplitude of the torque generated by the gas pressure. This is another benefit of a piston stroke resembling simple harmonic motion.

Friction

One point that was given special attention in designing the multiple-link mechanism is the piston side thrust characteristic. Figure 4 shows the results of an analysis of the friction characteristics at the piston skirt during the combustion (expansion) stroke. The numbers 1 to 4 in the graph correspond to the positions of the piston in this stroke. In the interval from 1 to 2 after TDC, the combustion gas pressure on the piston reaches its maximum level. Consequently, the baseline SR20 engine shows a sudden increase in side thrust, resulting in a large frictional force peak. By contrast, the VCR prototype engine shows virtually no generation of frictional force due to side thrust. That is because the multiple-link mechanism is designed in such a way that the U-link maintains a more upright orientation as it descends during this interval. Although friction tends to increase near BDC because of the inclination of the U-link, the friction level for the combustion stroke as a whole is reduced by approximately 40 %.

In order to achieve such a reduction in friction in addition to the second-order inertial vibration reduction, the geometry of the multiple-link mechanism had to be investigated to find a solution for both effects. Owing largely to the reduction in the piston side thrust as described here, the measured friction level of the VCR prototype engine is lower in the low-speed region, despite the multiple-link mechanism, although it tends to increase in the high-speed region, due mainly to the higher crank bearing.

Effect of VCR Control

Figure 5 shows a heat balance comparison based on the experimental engine performance results. With the multiple-link mechanism, the cooling loss and blow-by gas loss increase on account of the piston stroke characteristics that resemble simple harmonic motion, but the friction loss and time loss are reduced, as was explained above. The heat balance comparison shows that these effects cancel each other out at an identical compression ratio of 8.6:1, giving the VCR engine an equivalent fuel economy potential.

When the compression ratio is set higher at 14.3:1, the expansion ratio increases, which substantially reduces the exhaust loss, but the cooling loss increases owing to the higher combustion temperature and the flatter combustion chamber of the VCR prototype engine. The application of

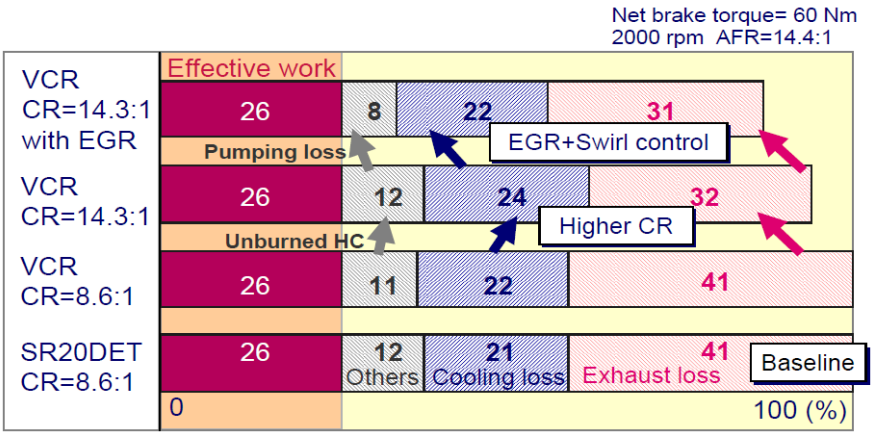

Figure 5: Effect of the higher compression ratio on the engine heat balance.

exhaust gas recirculation (EGR) is effective in eliminating this increased cooling loss trade-off, besides its effect on reducing the pumping loss. The higher compression ratio increases the EGR limit, because combustion is also improved as a result of raising the compression ratio.

As for maximum power, VCR control allows the boost pressure to be raised further, resulting in a measured improvement in power output of approximately 10 %.

Compression Ratio Control Map

Figure 6 shows one example of a compression ratio control map when the multiple-link mechanism is applied to a turbocharged petrol engine. The compression ratio control targets set for this VCR engine are set out in the following.

In the low-speed, low-load region where an engine often operates in everyday driving, the compression ratio is set at a high level of 14:1, which is higher than that of ordinary non-turbocharged engines. In the turbocharging region, the compression ratio is set at 8:1, lower than that of conventional turbocharged engines.

If the driver depresses the accelerator pedal, the compression ratio must be lowered quickly as the combustion pressure in the cylinder rises in order to avoid knocking. The link-geometry is designed in such a way that the cylinder gas pressure assists the control shaft rotation towards the lower compression ratio.

Summary

At the stage of selecting the fundamental link arrangement of the multiple-link mechanism for achieving a variable compression ratio (VCR), priority was placed on finding a link geometry for optimally resolving various attendant issues, including a compact system design and reduction of second-order inertial vibration and friction. A piston stroke resembling simple harmonic motion proved to be effective for reducing both the second-order inertial vibration and the amplitude of the torque generated by the cylinder gas pressure.

The increase in friction due to the multiple links can be cancelled out by selecting an optimised link geometry that reduces the piston side thrust load. As a result of applying the multiple-link mechanism to a Nissan turbocharged petrol engine, it was confirmed that, at an identical compression ratio of 8.6:1, the VCR prototype engine has an equivalent fuel economy potential. By controlling the compression ratio, both fuel economy and power output were improved by 10 %.

[1] K, Moteki, S. Aoyama, K. Ushijima, R. Hiyoshi, S. Takemura, H. Fujimoto, T. Arai, :"A Study of Variable Compression Ratio System with a Multi-Link", SAE Paper No. 2003-01-0921, SAE Transactions (2004).

[2] N. Takahashi, S. Aoyama, K. Moteki, R. Hiyoshi: "A Study Concerning the Noise and Vibration Characteristics of an Engine with Multiple-Link Variable Compression Ratio", SAE Paper No. 2005-01-1134.

[3] R. Hiyoshi, S. Aoyama, S. Takemura, K. Ushijima, T. Sugiyama: "A Study of a Multiple-link Variable Compression Ratio System for Improving Engine Performance", SAE Paper No. 2006-01-0616.

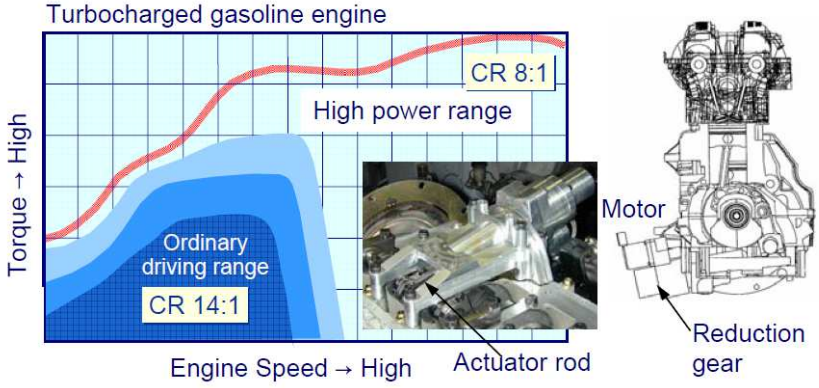

Figure 6: Example of a VCR control map.

Feb. 1, 1966 LOUIS-MARIE OUELLET 3,232,828

VARIABLE STROKE SHAKER MECHANISM FOR PAPER MAKING MACHINES

Filed July 15, 1963 3 Sheets-Sheet 1

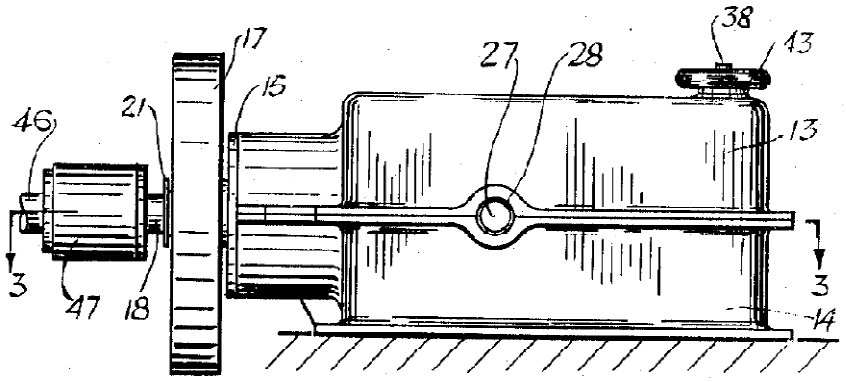

FIG. 1

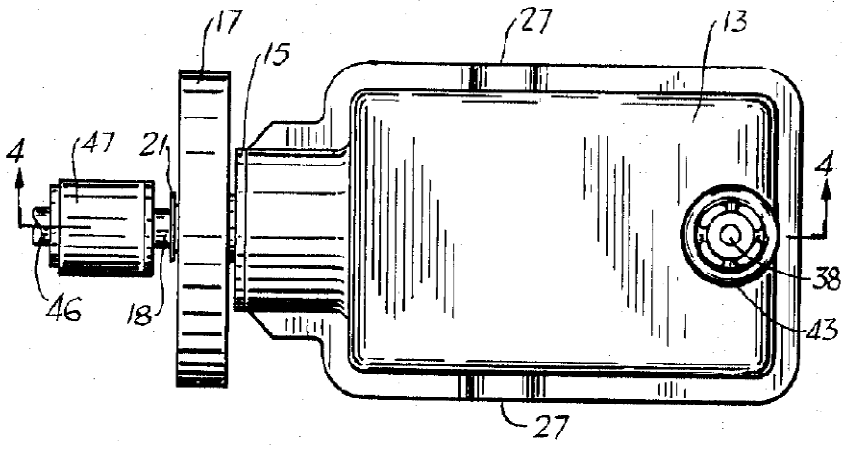

FIG. 2

INVENTOR
L-M. OUELLET
Fetherstonhaugh & Co.
ATTORNEYS

Feb. 1, 1966 LOUIS-MARIE OUELLET 3,232,828

VARIABLE STROKE SHAKER MECHANISM FOR PAPER MAKING MACHINES

Filed July 15, 1963 3 Sheets-Sheet 2

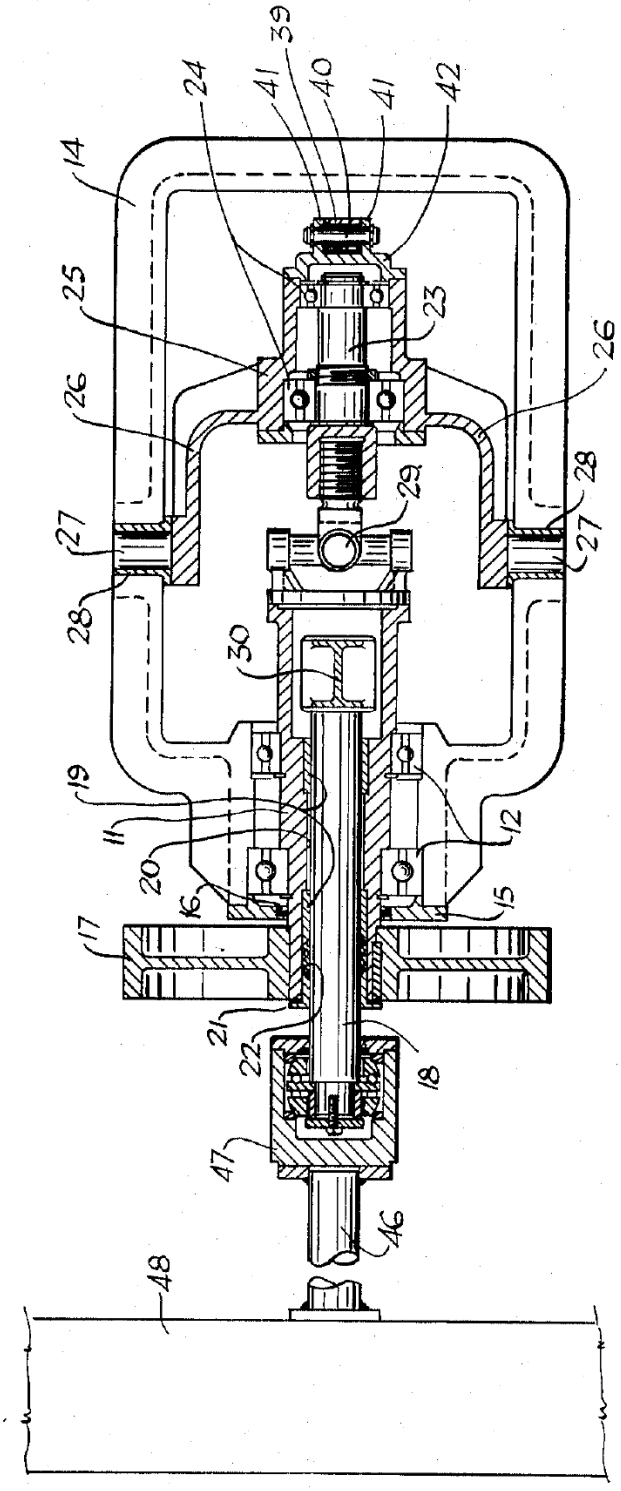

FIG. 3

INVENTOR
L-M. OUELLET
Fetherstonhaugh & Co.
ATTORNEYS

Feb. 1, 1966 LOUIS-MARIE OUELLET 3,232,828

VARIABLE STROKE SHAKER MECHANISM FOR PAPER MAKING MACHINES

Filed July 15, 1963 3 Sheets-Sheet 3

FIG. 5

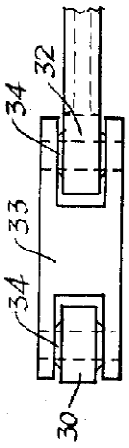

FIG. 4

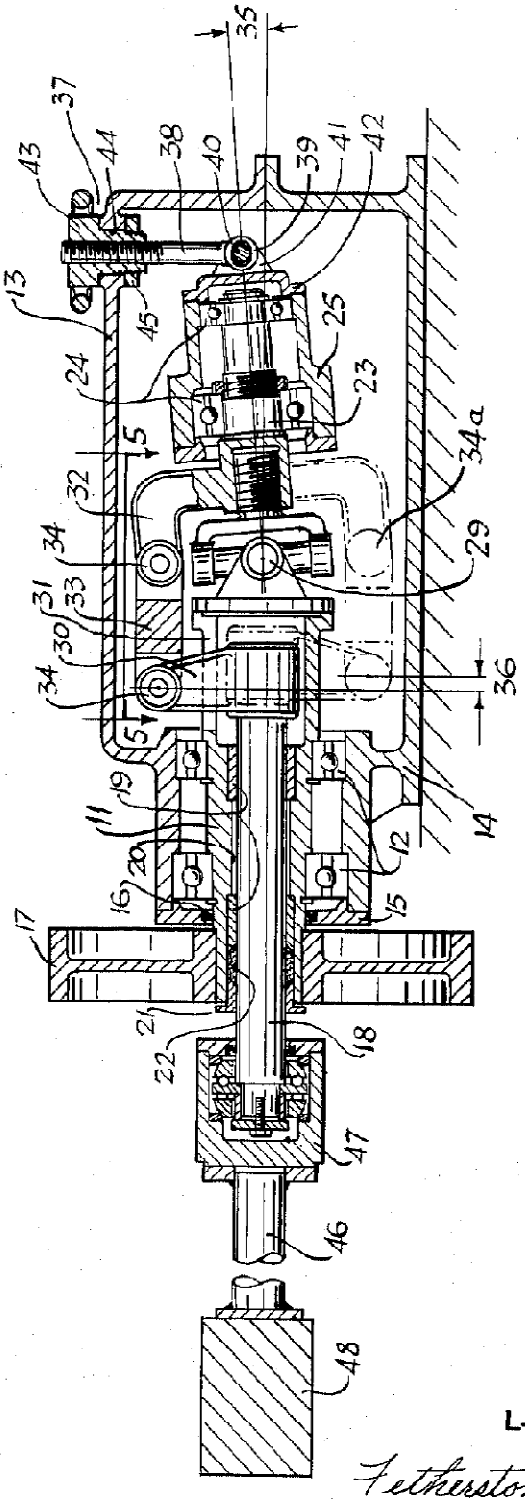

INVENTOR
L-M. OUELLET

Fetherstonhaugh & Co.

ATTORNEYS

United States Patent Office

3,232,828

Patented Feb. 1, 1966

3,232,828

VARIABLE STROKE SHAKER MECHANISM FOR PAPER MAKING MACHINES

Louis-Marie Ouellet, Chateauguay Centre, Quebec, Canada, assignor to Dominion Engineering Works Limited, Montreal, Quebec, Canada

Filed July 15, 1963, Ser. No. 295,141
Claims priority, application Canada, May 27, 1963, 876,599
8 Claims. (Cl. 162—355)

This invention relates to paper making machine fourdriniers and particularly to an improved mechanism for imparting a shaking motion, of variable stroke amplitude, to the drainage screen of a fourdrinier.

It will also be understood that the principle of this invention can be applied to any situation where it is required to convert a rotary input into a reciprocating output.

In the manufacture of certain grades of paper the fourdrinier table, around which the fourdrinier drainage screen is draped, must be shaken in the plane of the screen at right angles to its direction of travel.

In fourdriniers of this type, the fourdrinier table is pivotally mounted to permit oscillation or shaking motion at right angles to the direction of travel of the screen and is normally centered by spring means such that the bias towards null position is proportional to the displacement. Therefore, the table tends to oscillate with simple harmonic motion.

Thus, any mechanism which is used to impart a shaking motion to a fourdrinier table should, for minimum stress and wear, have the characteristic of simple harmonic motion.

It is also desirable that the shaking mechanism be provided with variable stroke amplitude control and that the output characteristic is simple harmonic over the range of amplitude control from zero to maximum.

A well known mechanism, which is used to impart a shaking motion to fourdrinier tables, employs an eccentric crank of fixed throw which imparts reciprocating motion to the output shaft by way of an adjustable toggle linkage.

One of the disadvantages of this well known mechanism is that at full stroke the deviation from simple harmonic motion is considerable.

Another disadvantage is that it is impossible to run the mechanism at zero stroke.

Still another disadvantage is that when at or near minimum stroke setting the output frequency, for a given input speed, is doubled.

These kinematic defects result in early structural and mechanical failure of the shaking mechanism and/or the fourdrinier table and the service life of the assembly is thus very unsatisfactory.

These inherent kinematic defects cannot be corrected by increasing component strength for, strengthening the shaking mechanism causes the table structure to fail and strengthening the table structure causes the shaking mechanism to fail.

The disadvantages inherent in the aforementioned well known mechanism are overcome in the present invention by the provision of an improved mechanism which converts uniform rotary motion into simple harmonic reciprocating motion of controllable stroke amplitude. This is achieved by the provision of a hollow input shaft rotatably journalled in the shaker casing and an output shaft coaxially mounted to reciprocate in said hollow input shaft. Stroke regulating means interconnects the input and output shafts such that rotation of the input shaft imparts reciprocating motion to said output shaft.

The stroke regulating means includes a secondary shaft rotatably journalled in a secondary housing which is pivotally mounted in the shaker casing to adjustably position the secondary shaft in positions of angular misalignment with the input shaft. The secondary shaft is coupled to the input shaft by means of a universal joint, the transverse centre line of which lies on a line through the pivotal axes of the secondary housing, thus the shafts will rotate together when they are axially aligned and also when their axes are angularly misaligned. An arm extending laterally from the output shaft through a slot in the input shaft is operatively connected to the secondary shaft through a ball joint linkage.

Thus, rotation of the input shaft when the input and secondary shafts are angularly misaligned, will result in reciprocation of the output shaft, from zero stroke when the input and secondary shafts are axially aligned to finite stroke when the input and secondary shafts are angularly misaligned. The operaing principle of this invention can be considered as analogous to the basic principle of the adjustable angle swash-plate mechanism by substituting for the swash-plate two shafts coupled together by a universal joint.

It is, therefore, the main object of this invention to provide a mechanism which will impart simple harmonic reciprocating motion to a fourdrinier table.

Another object of this invention is to provide a mechanism which will impart simple harmonic reciprocating motion, with variable stroke amplitude control, to a fourdrinier table.

Another object of this invention is to provide a shaking mechanism, the output characteristic of which is simple harmonic, over the range of stroke amplitude control from zero amplitude to maximum amplitude.

Another object of this invention is to provide a fourdrinier table shaking mechanism in which wear and stress is kept to a minimum.

Another object of this invention is to provide a mechanism, for imparting shaking motion to a fourdrinier table, in which the stroke amplitude can be varied during operation.

A further object of this invention is to provide a fourdrinier table shaking mechanism which is of simple yet robust construction, is of compact design and is relatively inexpensive, as compared with shaking mechanisms of the well known type.

These and other objects of this invention will be apparent by reference to the following detailed specification and figures in which:

FIG. 1 is a side view of a shaking mechanism embodying the features of this invention.

FIG. 2 is a plan view of a shaking mechanism embodying the features of this invention.

FIG. 3 is a sectional view, to an enlarged scale, taken on 3—3 in FIG. 1 and showing details of the invention.

FIG. 4 is a sectional view, to an enlarged scale, taken on 4—4 in FIG. 2 and showing further details of this invention.

FIG. 5 is a view to a further enlarged scale, taken on 5—5 in FIG. 4.

To obtain simple harmonic motion from the reciprocating output of the improved mechanism of the present invention, the universal joint used must be of the constant velocity type. However, when this improved mechanism is applied to shake a paper making machine fourdrinier table the range of shaft angular misalignment required to provide the required shake stroke amplitudes is small and permits the use of the simpler and less expensive Hooke's joint type universal joint, where the error thus introduced due to the small shaft angular misalignment is considered negligible. In the follow-

ing description of the preferred execution of this invention a Hooke's joint type universal joint is shown incorporated into the mechanism for simplicity.

With reference now to the figures, input shaft **11** is rotatably journalled in bearings **12** located in upper half casing **13** and lower half casing **14**. End cap **15** closes the open ends of upper and lower half casings **13** and **14** respectively and seal **16** seals the bore in end cap **15** through which input shaft **11** passes. Input pulley **17** is attached to the outer end of input shaft **11** and is driven by a driving motor (not shown) to provide the required input rotation. Output shaft **18** is coaxially mounted to reciprocate in bearings **19** positioned in bore **20** in input shaft **11**. Packing gland **21** retains shaft packing **22** to effectively seal bore **20**.

Secondary shaft **23** is rotatably journalled in bearings **24** in secondary housing **25**. Pivot arms **26** extend outwardly from secondary housing **25** with trunnions **27** extending outwardly from pivot arms **26** and transverse to secondary shaft **23**. Trunnions **27** are pivotally mounted in bearings **28**, positioned in upper and lower half casings **13** and **14** respectively.

The inner end of input shaft **11** is coupled to secondary shaft **23** by universal joint **29**, the transverse centre line of which is arranged to lie on a line through the pivotal axes of trunnions **27**. Thus, input and secondary shafts **11** and **23** respectively will rotate together when they are axially aligned and also when their axes are angularly misaligned, as shown in FIG. 4.

Output arm **30** extends laterally from the inner end of output shaft **18**, through a slot **31** in input shaft **11** and secondary arm **32** extends laterally from the inner end of secondary shaft **23**. Slot **31** in input shaft **11** is dimensioned to locate output arm **30** such that output arm **30** can move axially in slot **31** but with output shaft **18** prevented from rotating relative to input shaft **11**.

Output and secondary arms **30** and **32** respectively are operatively connected by link **33** and ball joints **34**. Reference again to FIG. 4 shows secondary shaft **23** angularly misaligned with input shaft **11** by an angle **35**. It will therefore be seen that rotation of input shaft **11** produces a corresponding rotation of angularly misaligned secondary shaft **23**, ball joint **34**, of secondary arm **32**, being axially displaced when input shaft **11** is rotated 180° to the lower vertical position shown in broken line at **34***a*. This axial displacement is transferred, through link **33**, to output arm **30**, as shown at **36**.

Thus, when the axes of input and secondary shafts **11** and **23** respectively are angularly misaligned, as at **35**, rotation of input shaft **11** will result in reciprocation of output shaft **18** by the amount shown at **36**.

The axial displacement, or stroke, **36** will vary from a predetermined maximum amplitude, corresponding with the predetermined maximum angle of misalignment **35** between shafts **11** and **23**, to zero stroke, when shafts **11** and **23** are axially aligned.

Adjustment of angle **35**, corresponding to adjustment of stroke amplitude, is accomplished by means of the adjusting mechanism shown generally at **37**.

Adjusting mechanism **37** includes an adjusting screw **38** having a head end **39** which is slotted to receive pivot pin **40**. Pivot pin **40** is positioned through lugs **41** on secondary housing end cap **42**. The other end of adjusting screw **38** is threaded to engage in adjusting nut **43**. Adjusting nut **43** has a reduced diameter plain portion which is rotatably positioned in bore **44** in upper half casing **13** and a further reduced diameter threaded portion which engages in lock nut **45**. Lock nut **45** is adjusted to provide free rotation of adjusting nut **43** in bore **44**. Thus, rotation of adjusting nut **43** will result in the raising or lowering of the outer end of secondary housing **25**, thus respectively increasing or decreasing angle **35** according to the direction of rotation.

The outer end of output shaft **18** is connected to shaker shaft **46** by means of a two-way thrust bearing **47**, whereby reciprocation may be transmitted to shaker shaft **46** from reciprocating and rotating output shaft **18**, without rotation of shaker shaft **46**.

Shaker shaft **46** is directly connected to the fourdrinier shake rail **48**.

In the operation of this invention, input rotation provided through input pulley **17** will result in non-rotating reciprocation of shaker shaft **46**, of amplitude predetermined by the angular positioning of secondary shaft **23** by means of the adjusting mechanism **37**.

Shaking mechanisms according to this invention can be operated in pairs by means of a simple worm and screw interconnection between each adjusting mechanism **37**, with each shaking mechanism being positively driven. Differential stroke amplitudes can be obtained by use of suitable worm and screw ratios and corresponding drive ratios.

This invention, therefore, provides a shaking mechanism in which modulated stroke amplitude control is obtained from zero stroke, to maximum stroke, with no double frequency output in any part of the range of stroke adjustment. When a constant velocity type universal joint is used in the mechanism, true simple harmonic motion output is obtained throughout the range of stroke adjustment, but where a small deviation from mathematically exact simple harmonic motion can be tolerated, then a less costly Hooke's joint type universal joint can be substituted for the constant velocity type universal joint.

What I claim is:

1. A shaker mechanism for fourdrinier paper making machines including a shake rail mounted to swing laterally to either side of a central position, a rotary hollow input shaft mounted to rotate about a fixed longitudinal axis, an output shaft mounted to reciprocate within said input shaft and to rotate therewith, said output shaft having an output arm extending laterally therefrom and projecting through slot means in said hollow input shaft, adjustable motion transmitting means interconnecting said input shaft and said output arm for imparting a rotating and reciprocating motion of adjustable stroke to said output shaft in response to rotation of said input shaft, and means connecting said output shaft to said shake rail to impart swinging motion to said shake rail on either side of said central position in accordance with the reciprocating stroke of said output shaft.

2. A shaker mechanism for fourdrinier paper making machines including a shake rail mounted to swing laterally to either side of a central position, rotary input shaft means, an output shaft mounted for rotary and reciprocating movement, motion transmitting means interconnecting said input shaft means and said output shaft for imparting a rotating and reciprocating motion to said output shaft in response to rotation of said input shaft means, said motion transmitting means including a secondary shaft operatively connected to said input shaft means to rotate therewith and operatively connected to said output shaft to impart said rotating and reciprocating motion thereto, and means connecting said output shaft to said shake rail to impart swinging motion to said shake rail on either side of said central position in accordance with the reciprocating stroke of said output shaft.

3. A shaker mechanism for fourdrinier paper making machines including a shake rail mounted to swing laterally to either side of a central position, a rotary input shaft, an output shaft mounted for rotary and reciprocating motion, said output shaft having an output arm extending laterally therefrom, adjustable motion transmitting means interconnecting said input shaft and said output arm for imparting a rotating and reciprocating motion of adjustable stroke to said output shaft in response to rotation of said input shaft, said motion transmitting means including a secondary shaft operatively connected to said input shaft and mounted to rotate therewith, a secondary

arm extending laterally from said secondary shaft, and link means operatively connecting said output and secondary arms, said secondary shaft adapted to rotate about an axis adjustable from a position of axial alignment with said output shaft to a position of angular misalignment with said output shaft to provide said adjustable stroke of said output shaft, and means connecting said output shaft to said shake rail to impart swinging motion to said shake rail on either side of said central position in accordance with the reciprocating stroke of said output shaft.

4. A shaker mechanism for fourdrinier paper making machines including a shake rail mounted to swing laterally to either side of a central position, a rotary hollow input shaft mounted to rotate about a fixed longitudinal axis, an output shaft mounted to reciprocate within said input shaft and to rotate therewith, motion transmitting means interconnecting said input shaft and said output shaft for imparting a rotating and reciprocating motion to said output shaft in response to rotation of said input shaft, said motion transmitting means including a secondary shaft operatively connected to said input shaft to rotate therewith and operatively connected to said output shaft to impart said rotating and reciprocating motion thereto, and means connecting said output shaft to said shake rail to impart swinging motion to said shake rail on either side of said central position in accordance with the reciprocating stroke of said output shaft.

5. A shaker mechanism for fourdrinier paper making machines including a shake rail mounted to swing laterally to either side of a central position, a rotary hollow input shaft mounted to rotate about a fixed longitudinal axis, an output shaft mounted to reciprocate within said input shaft and to rotate therewith, said output shaft having an output arm extending laterally therefrom and projecting through slot means in said hollow input shaft, adjustable motion transmitting means interconnecting said input shaft and said output arm for imparting a rotating and reciprocating motion of adjustable stroke to said output shaft in response to rotation of said input shaft, said motion transmitting means including a secondary shaft operatively connected to said input shaft and mounted to rotate therewith, a secondary arm extending laterally from said secondary shaft, and link means operatively connecting said output and secondary arms, said secondary shaft adapted to rotate about an axis adjustable from a position of axial alignment with said output shaft to a position of angular misalignment with said output shaft to provide said adjustable stroke of said output shaft, and means connecting said output shaft to said shake rail to impart swinging motion to said shake rail on either side of said central position in accordance with the reciprocating stroke of said output shaft.

6. A shaker mechanism for fourdrinier paper making machines including a shake rail mounted to swing laterally to either side of a central position, a casing for said shaker mechanism, a rotary hollow input shaft mounted in said casing to rotate about a fixed longitudinal axis, an output shaft coaxially mounted to reciprocate within said input shaft and to rotate therewith, said output shaft having an output arm extending laterally therefrom and projecting through slot means in said hollow input shaft, adjustable motion transmitting means interconnecting said input shaft and said output arm for imparting a rotating and reciprocating motion of adjustable stroke to said output shaft in response to rotation of said input shaft, said motion transmitting means including a secondary shaft operatively connected to said input shaft and mounted to rotate therewith, a secondary arm extending laterally from said secondary shaft, link means operatively connecting said output and secondary arms, said secondary shaft rotatably mounted in secondary housing means, said secondary housing means pivotally mounted in said casing for adjustment of said secondary shaft from a position axially aligned with said output shaft to a position of angular misalignment with said output shaft to provide said adjustable stroke of said output shaft, said secondary housing means including a body portion having two arm members extending outwardly therefrom, said secondary shaft being rotatably journalled in said body portion, said secondary housing means being pivotally mounted on trunnion portions at the outer ends of said arm members and journalled in said casing, the axes of said trunnion portions adapted to lie on the transverse centre line of the operative connection between said input and secondary shafts, and thrust bearing means connecting said output shaft to said shake rail to impart swinging motion to said shake rail on either side of said central position in accordance with the reciprocating stroke of said output shaft.

7. A shaker mechanism as set forth in claim 6 in which the operative connection between said input and secondary shafts comprises a universal joint.

8. A shaker mechanism as set forth in claim 6 including adjusting screw and nut means connected between said secondary housing means and said casing for adjusting the pivotal position of said secondary housing within said casing and thus the angular position of said secondary shaft relative to said output shaft.

References Cited by the Examiner

UNITED STATES PATENTS

1,694,834	12/1928	Sinclair	74—22
1,917,287	1/1933	Aldrich et al.	162—355
2,436,492	2/1948	Shepard	74—22 X
2,892,352	6/1959	Saalfrank	74—22 X

DONALL H. SYLVESTER, *Primary Examiner.*

BROUGHTON G. DURHAM, *Examiner.*

JOHN H. NEWSOME, *Assistant Examiner.*

through the part and a keyway is provided to fit the driving shaft. A female dovetail is milled in the rectangular section at the opposite end. From a square piece of stock, a male dovetail slide *B* is then machined to fit the adapter. One end of this member is turned to fit a connecting-link arm *C*. Two side-plates *D*, made from flat stock, are bolted to the sides of the adapter with socket-head cap-screws, as shown. Each plate also has a hole tapped to receive headless set-screws *E*, which are used for adjusting the amount of eccentricity and for locking the slide *B* securely in place during operation of the connected drive.

The slide and adapter may be scribed with gage lines, if desired, in case minute adjustment is needed.

Eccentric Driving Mechanism Permits Stroke Adjustment During Operation

Small variations in the stroke length of a reciprocating slide can be made while it is operating, by means of the mechanism shown in Fig. 4. Driving disc *A* has an integral shank revolving in fixed bearing *B*, where it is retained by bearing cap *C*. Driving gear *D*, keyed to the shank, revolves continuously.

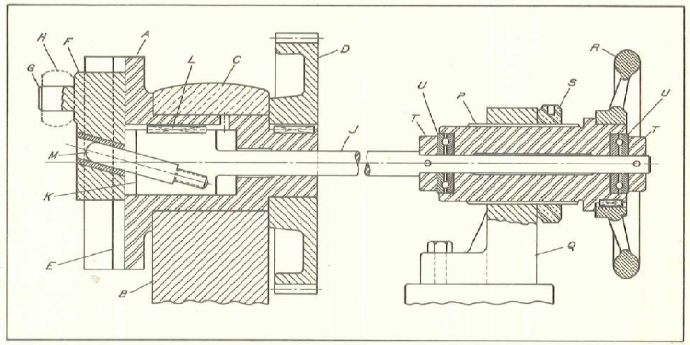

FIG. 4. By revolving handwheel *R*, the throw of crank pin *G* can be varied without stopping the slide.

The disc face contains a dovetail *E* milled across its diameter. Crankpin block *F*, fitting the dovetail, has an integral crankpin *G*, over which is fitted one end of a connecting-rod *H*. At its other end, the rod is attached to the reciprocating slide (not shown).

Rod *J*, by which the device is adjusted, has a shouldered section *K* fitting the bore of disc *A*. Key *L* causes the rod to revolve with the disc yet permits a short axial movement of the rod along the bore. A hard pin *M* is pressed at an angle into the end of section *K*. This pin engages a hole that is drilled in the crankpin block.

Rod *J* extends from any convenient distance to a control point. At its right end, the rod is reduced in diameter and can rotate in sleeve *P*. An external thread on the sleeve engages a threaded hole in angle-bracket *Q*. By revolving handwheel *R*, keyed to the sleeve, the sleeve can be adjusted axially. Threaded ring *S* locks the sleeve, once it has been adjusted. Rod *J* moves axially in unison with the sleeve, by means of the stop collars *T* and thrust bearings *U*.

If the stroke of the slide has to be lengthened, ring *S* is released, and the handwheel revolved counterclockwise. This movement is transmitted to the rod, and pin *M* is retracted a corresponding amount from the crankpin block, causing the block to move radially outward in disc *A*. Thus, crankpin *G* has a greater throw. By revolving the handwheel clockwise, the throw of the crankpin is similarly decreased.

Mechanism for Effecting a Varying Reciprocating Motion

On a wire-forming machine, a reciprocating slide was required to move at a uniform rate of speed during part of the cycle and, at a predetermined point, to increase in speed for the remainder of the cycle. The motive power for operating this slide was taken from a uniformly reciprocating slide and then transformed into varying reciprocating motion by the mechanism here shown.

D. Hand Calculations

1.0 ENGINEERING DATA

$\sigma_{ySt} := 248 \cdot 10^6$	Mild steel wikipedia.org
$\sigma_{yTi} := 931 \cdot 10^6$	Titanium 6Al-4V Gooch Thesis Page 59
$\sigma_{y4140} := 700 \cdot 10^6$	4140 shaft steel Fletcher steel catalogue [1]
$\sigma_{uts4140} := 850 \cdot 10^6$	4140 shaft steel Fletcher steel catalogue [1]
$\sigma_{y7068} := 680 \cdot 10^6$	AL 7068 wikipedia.org (Note: Aluminium does not have an endurance limit)
$\sigma_{y1040} := 450 \cdot 10^6$	Fletchers Special Steel Catalogue [1] 1040 Shaft Steel (WCS)
$\sigma_{uts1040} := 600 \cdot 10^6$	Fletchers Special Steel Catalogue [1] 1040 Shaft Steel (WCS)
$\sigma_{yBi80} := 690 \cdot 10^6$	Fletchers Special Steel Catalogue [1] Bisalloy 80
$\sigma_{utsBi80} := 790 \cdot 10^6$	Fletchers Special Steel Catalogue [1] Bisalloy 80
$E_{st} := 207 \cdot 10^9$	Elastic modulus of steel
$\sigma_{y12.9} := 1100 \cdot 10^6$	Engineering grade 12.9 bolt yield Keith's 311 bolt notes
$\sigma_{uts12.9} := 1220 \cdot 10^6$	Engineering grade 12.9 bolt UTS Keith's 311 bolt notes
$\sigma_{p12.9} := 970 \cdot 10^6$	Engineering grade 12.9 bolt proof Keith's 311 bolt notes
$S_{e12.9} := 190 \cdot 10^6$	Fully corrected endurance limit 12.9 Grade bolt
$\sigma_{yHA250} := 250 \cdot 10^6$	HA250 Plate from Steel and Tube Page 6/7 AS/NZS HA250 [2]
$\sigma_{yC350} := 350 \cdot 10^6$	C350 RHS specs from Steel and Tube page 9 and AS1163 specs [2]
$\sigma_{utsC350} := 430 \cdot 10^6$	
$\sigma_{yLP} := 240 \cdot 10^6$	Linepipe specs for pipe on page 14 Steel and Tube, specs in ASTM 106b [2]
$\sigma_{utsLP} := 413 \cdot 10^6$	

Look in titanium handbook TA480.T54 on page 522 for Titanium design strengths

1.0 PARAMETERS AND KNOWN VARIABLES

	Test Rig Blade	Big Blade	Giant Blade	
Mass (kg)	$M_{tr} := 5.43$	$M_b := 36.39$	$M_g := 1108$	$g := 9.807$
Thickness (m)	$d_{tr} := 0.0018$	$d_b := 0.00553$	$d_g := 0.022$	
Width (m)	$b_{tr} := 0.2$	$b_b := 0.430$	$b_g := 1.080$	
Length (m)	$L_{tr} := 1.599$	$L_b := 3.355$	$L_g := 8.424$	
Density (kg/m^3)	$\rho_{tr} := 7800$	$\rho_b := 4429$	$\rho_g := 4429$	
Elastic Modulus (Pa)	$E_{tr} := 210 \cdot 10^9$	$E_b := 114 \cdot 10^9$	$E_g := 114 \cdot 10^9$	
	$G_{tr} := 80 \cdot 10^9$		$G_g := 44 \cdot 10^9$	

$r_{cl} := \frac{0.3}{1.599} = 0.188$ Ratio of clamped blade to unclamped in 300mm pivoting

Scale Factor

$s_b := \frac{L_b}{L_{tr}}$ $s_g := \frac{L_g}{L_{tr}}$

$s_b = 2.098$

$s_g = 5.268$

Distance to Centroid (m)

$Y_{tr} := \frac{d_{tr}}{2}$ $Y_b := \frac{d_b}{2}$ $Y_g := \frac{d_g}{2}$

$Y_{tr} = 9 \times 10^{-4}$

$Y_b = 2.765 \times 10^{-3}$

$Y_g = 0.011$

Cross Sectional Area (m^2)

$A_{tr} := b_{tr} \cdot d_{tr}$ $A_b := b_b \cdot d_b$ $A_g := b_g \cdot d_g$

$A_{tr} = 3.6 \times 10^{-4}$

$A_b = 2.378 \times 10^{-3}$

$A_g = 0.024$

Second Moment of Area (m^4)

$I_{tr} := \frac{b_{tr} \cdot (d_{tr})^3}{12}$ $I_b := \frac{b_b \cdot (d_b)^3}{12}$ $I_g := \frac{b_g \cdot (d_g)^3}{12}$

$I_{tr} = 9.72 \times 10^{-11}$

$I_b = 6.06 \times 10^{-9}$

$I_g = 9.583 \times 10^{-7}$

Polar Second Moment of Area (m^4)

$$J_{tr} := \frac{b_{tr} \cdot d_{tr} \cdot \left[(b_{tr})^2 + (d_{tr})^2 \right]}{12} \qquad J_b := \frac{b_b \cdot d_b \cdot \left[(b_b)^2 + (d_b)^2 \right]}{12} \qquad J_g := \frac{b_g \cdot d_g \cdot \left[(b_g)^2 + (d_g)^2 \right]}{12}$$

$$J_{tr} = 1.2 \times 10^{-6}$$

$$J_b = 3.665 \times 10^{-5}$$

$$J_g = 2.31 \times 10^{-3}$$

Mass Per Unit Length (kg/m)

$$m_{tr} := \rho_{tr} \cdot A_{tr} \qquad m_b := \rho_b \cdot A_b \qquad m_g := \rho_g \cdot A_g$$

$$m_{tr} = 2.808$$

$$m_b = 10.532$$

$$m_g = 105.233$$

2.0 BLADE DYNAMICS

$n := 1, 2.. 4$

2.1 Shuttle Motor Speeds for Test Rig (RPM)

Third Mode | Shimmering | Second Mode | Kissing | Values measured from fatigue testing August 2013 [3]

$N_{tr_1} := 565.8$ $N_{tr_2} := 525$ $N_{tr_3} := 198$ $N_{tr_4} := 184$

$\omega_{tr_n} := \left(\frac{1}{60}\right) \cdot N_{tr_n}$ Shuttle Motor Speeds for Test Rig (Hz)

$$\omega_{tr_n} = \begin{pmatrix} 9.43 \\ 8.75 \\ 3.3 \\ 3.067 \end{pmatrix}$$

$$\omega_{g_n} := \frac{\omega_{tr_n}}{\sqrt{\frac{E_{tr} \cdot d_{tr}^{\,2} \cdot L_g^{\,4} \cdot \rho_g}{E_g \cdot d_g^{\,2} \cdot L_{tr}^{\,4} \cdot \rho_{tr}}}}$$

Shuttle Motor Speeds for Giant Blade (Hz)

$$\omega_{g_n} = \begin{pmatrix} 4.06 \\ 3.768 \\ 1.421 \\ 1.32 \end{pmatrix}$$

$N_{g_n} := 60 \cdot \omega_{g_n}$

Shuttle Motor Speeds for Giant Blade (RPM)

$$N_{g_n} = \begin{pmatrix} 243.619 \\ 226.051 \\ 85.254 \\ 79.226 \end{pmatrix}$$

$t_{perf_1} := 160$ $t_{perf_2} := 60$ $t_{perf_3} := 60$ $t_{perf_4} := 120$

2.2 Maximum Clamp Acceleration

$r_{tr} := 0.005$ Crank offset for test rig (m)

Crank offset for Giant Blade (m)

$r_g := r_{tr} \cdot s_g$

$a_{g_n} := \left(\omega_{g_n} \cdot 2 \cdot \pi\right)^2 \cdot r_g$ Maximum Clamp Acceleration (m/s^2)

$$a_{g_n} = \begin{pmatrix} 19.887 \\ 17.123 \\ 2.435 \\ 2.103 \end{pmatrix}$$

$v_{g_n} := -\omega_{g_n} \cdot 2 \cdot \pi \cdot r_g$ Maximum clamp velocity (m/s)

$$v_{g_n} = \begin{pmatrix} -0.78 \\ -0.723 \\ -0.273 \\ -0.254 \end{pmatrix}$$

3.0 SHEAR AND BENDING STRESSES IN BLADE

Shear force was not measured directly using the test rig.

As a conservative estimate of the shear force in Giant Blade using a pivoting clamp system, the shear force calculated for Big Blade in compile.mcd [4] will be scaled. The shear force in Giant Blade will be smaller than this in reality.

In the calculations for Big Blade, it was found that the shear force has a minimal effect on principal stress results.

$Q_{b_1} := 2.968\,10^3$ $Q_{b_2} := 807.39$ $Q_{b_3} := 1.821 \cdot 10^3$ $Q_{b_4} := 1.458\,10^3$

Shear force at clamp exit in Big Blade (N)

$$Q_{b_n} = \begin{pmatrix} 2.968\times 10^3 \\ 807.393 \\ 1.821\times 10^3 \\ 1.458\times 10^3 \end{pmatrix}$$

$$Q_{g_n} := \frac{Q_{b_n}}{\left(\frac{L_b}{L_g}\right)^{\left(\frac{7}{2}\right)}}$$ Page 21 Gooch Thesis

$$Q_{g_n} = \begin{pmatrix} 7.445\times 10^4 \\ 2.025\times 10^4 \\ 4.568\times 10^4 \\ 3.657\times 10^4 \end{pmatrix}$$

3.1 Shear stresses at clamp exit

$$\tau_{g_n} := \frac{Q_{g_n}}{A_g}$$ Shear stress at the clamp exit (Pa)

$$\tau_{g_n} = \begin{pmatrix} 3.133\times 10^6 \\ 8.524\times 10^5 \\ 1.922\times 10^6 \\ 1.539\times 10^6 \end{pmatrix}$$

3.2 Bending stress at the clamp exit

$\sigma_{1g_{10}} := 331\times 10^6$ This is the maximum stress recorded for 8.424m blade during 230813 fatigue testing [3] - run bladefatiguefinalv3.m

3.3 More accurate estimate of shear force at clamp exit (Stress formula Shigley page 122)

$Q_{g_1} := M_g \cdot a_{g_1} = 2.204\times 10^4$ Mass of blade above clamp multiplied by maximum shuttle acceleration (N)

$$\tau_{g_1} := \frac{3\cdot Q_{g_1}}{2A_g} = 1.391\times 10^6$$

4.0 UPPER PIVOT SHAFT CALCULATIONS

4.1 Shaft geometry (see Sketches Fig D1 and Fig D2)

$\sigma_{yield} := \sigma_{yBi8($

$\tau_{yield} := 0.58 \cdot \sigma_{yield}$

$\sigma_{uts} := \sigma_{utsBi8($

$S'_e := 0.5 \cdot \sigma_{uts}$

Page 369 Shigley

$D_1 := 90 \cdot 10^{-3}$ Diameter of shaft bearing interfaces (m)

$D_2 := 90 \cdot 10^{-3}$ Diameter of bearing shoulder (m)

$r_1 := 5 \cdot 10^{-3}$ Fillet radius of d1 (m)

$r_2 := 5 \cdot 10^{-3}$ Fillet radius of d2 (m)

Assume that strengthening rib is a uniform T-section

$w_f := 100 \cdot 10^{-3}$ Width of T flange (m)

$L_w := 150 \cdot 10^{-3}$ Length of T web (m)

$t_f := 24 \cdot 10^{-3}$ Thickness of T flange (m)

$t_w := 20 \cdot 10^{-3}$ Thickness of T web (m)

$w_{cl} := 150 \cdot 10^{-3}$ Width of clamp (m)

$h_{cl} := 100 \cdot 10^{-3}$ Height of the clamp (m)

$I_{D1} := \pi \cdot \frac{D_1^4}{64}$ Moment of inertia for Section 1 (m^4)

$I_{D2} := \pi \cdot \frac{D_2^4}{64}$ Moment of inertia for Section 2 (m^4)

$A_{D1} := \pi \cdot \left(\frac{D_1}{2}\right)^2$ Cross sectional area Section 1 (m^2)

$A_{D2} := \pi \left(\frac{D_2}{2}\right)^2$ Cross sectional area Section 1 (m^2)

4.2 Centroid calculation

$A_1 := t_f \cdot w_f = 2.4 \times 10^{-3}$ Area of flange (m^2)

$A_2 := t_w \cdot L_w = 3 \times 10^{-3}$ Area of web (m^2)

$y_1 := \frac{L_w}{2}$ $y_2 := L_w + \frac{t_f}{2}$ Distance to centroid of each rectangle from x axis (m)

$y := \frac{A_1 \cdot y_1 + A_2 \cdot y_2}{A_1 + A_2}$ Location of neutral axis w.r.t x axis (mm)

$y = 0.123$

4.3 Moment of inerita by parallel axis theorem

$I_1 := \frac{w_f \cdot t_f^{\,3}}{12}$ $I_2 := \frac{t_w \cdot L_w^{\,3}}{12}$ Moment of inertia for each rectangle (m)

$d_1 := y - \frac{L_w}{2}$

Distance to centroid of each axis from neutral axis (m)

$d_2 := \left(L_w + \frac{t_f}{2}\right) - y$

$I_T := I_1 + I_2 + A_1 \cdot d_1^{\,2} + A_2 \cdot d_2^{\,2}$ Moment of inertia about neutral axis T section (m^4)

$I_T = 1.583 \times 10^{-5}$

4.4 Bending stress in T section

Table E-9 Shigley number 16 Fixed Fixed beam Page 1178

$V := Q_{g_1}$ Shear force at the clamp exit (N)

$w := \frac{V}{b_g}$ Distributed force on clamp jaw (N/m)

$w = 2.04 \times 10^{4}$

$x := \frac{b_g}{2}$ Location of maximum bending stress (m)

$M := \left(\frac{w}{12}\right) \cdot \left(6 b_g \cdot x - 6x^2 - b_g^{\,2}\right)$ Maximum bending moment in T section (Nm)

$M = 991.582$

$y = 0.123$

$\sigma_x := \frac{M \cdot y}{I_T}$ Pure bending stress in the surface of strengthening T section (Pa)

$\sigma_x = 7724453$

4.5 Shear stress due to bending in T section page 122 Shigley

$A_T := A_1 + A_2 = 5.4 \times 10^{-3}$

$\tau_{xy} := \frac{V}{A_T}$ Shear stress due to bending (Pa)

$\tau_{xy} = 4080583$

4.6 Principal Stresses due to Bending page 97 Shigley

$\sigma_y := 0$

$$\sigma_1 := \left(\frac{\sigma_x + \sigma_y}{2}\right) + \left[\left(\frac{\sigma_x - \sigma_y}{2}\right)^2 + \tau_{xy}^{\ 2}\right]^{0.5}$$

$\sigma_1 = 9480763$

$$\sigma_2 := \frac{\sigma_x + \sigma_y}{2} - \left[\left(\frac{\sigma_x - \sigma_y}{2}\right)^2 + \tau_{xy}^{\ 2}\right]^{0.5}$$

$\sigma_2 = -1756310$

4.7 Distortion Energy Theory eq 6-9 page 328 Shigley

$$\sigma_{de} := \left(\sigma_1^{\ 2} - \sigma_1 \cdot \sigma_2 + \sigma_2^{\ 2}\right)^{0.5}$$

$\sigma_{de} = 10469988$

4.8 Factors of safety on bending stresses

$$FOS := \frac{\sigma_{yield}}{\sigma_{de}}$$

$FOS = 65.903$

4.9 Shear stress due to blade edges

$$\tau := \frac{\left(\frac{V}{2}\right)}{A_T}$$

Shear stress in the clamp walls at edges of blade (Pa)

$\tau = 2040292$

4.10 Factors of safety on shear stresses

$$FOS := \frac{\tau_{yield}}{\tau}$$

$FOS = 196.148$

4.11 Deflection of T section part of clamp page 1174 figure 7

$$y_{max} := \frac{-w \cdot b_g^{\ 4}}{384 \cdot E_{st} \cdot I_T}$$

Deflection of clamped T section at mid span

$y_{max} = -2.206 \times 10^{-5}$

4.12 Deflection and stresses at the shoulders

3 sections of stub axle
Section c is approximated as a rectangle with two ribs (Sketches Fig D3)
Section b is circular
Section a is circular (third section in case of step down for lock nut thread)

4.13 Moment of inertia Section 3

$$I_3 := \frac{h_{cl} \cdot w_{cl}^{3}}{12} \qquad I_3 = 2.813 \times 10^{-5}$$

$$d := \left(\frac{w_{cl}}{2}\right) + \left(\frac{L_w}{2}\right)$$

$I_{rect} := 2 \cdot \left(I_2 + A_2 \cdot d^{2}\right) + I_3$ Moment of inertia for rectangular section (m^4)

$I_{rect} = 1.744 \times 10^{-4}$

$M_1 := \frac{w \cdot b_g^{2}}{12}$ Moment at end of T section (carry over to stub)

$M_1 = 1.983 \times 10^{3}$

$l_a := 10 \cdot 10^{-3}$ Length of Section a (m)

$l_b := 100 \cdot 10^{-3}$ Length of Section b (m)

$l_c := 228 \cdot 10^{-3}$ Length of Section c (m)

$$R_1 := \frac{\left[\frac{V}{2} \cdot \left(l_c\right) + M_1\right]}{l_b}$$ Reaction at DU bush (N)

$R_1 = 44952$

$R_2 := R_1 + \frac{V}{2}$ Reaction at DU bush (N)

$R_2 = 55969$

Use shaft deflection spreadsheet [5] to determine moments and deflections at critical shoulder locations

Shaft deflection calculated from spreadsheet is

$y_{stub} := -4.6 \cdot 10^{-5}$

$y_{total} := y_{stub} + y_{max} = -6.806 \times 10^{-5}$

$M_{s1} := 0$ Moment at shoulder 1 from spreadsheet (Nm)

$M_{s2} := 4405$ Moment at shoulder 2 from spreadsheet (Nm)

$$\sigma_{s1} := \frac{\left[M_{s1} \cdot \left(\frac{D_1}{2}\right)\right]}{I_{D1}} \qquad \sigma_{s2} := \frac{\left[M_{s2} \cdot \left(\frac{D_2}{2}\right)\right]}{I_{D2}}$$

$\sigma_{s1} = 0$

$\sigma_{s2} = 61548644$

$V_{s1} := 0$ Shear force at shoulder 1 (N)

$V_{s2} := 3722$ Shear force at shoulder 2 (N)

Both from shaft deflection spreadsheet

$$\tau_{s1} := \frac{V_{s1}}{A_{D1}}$$ Shear stress in shaft at shoulder 1 (Pa)

$\tau_{s1} = 0$

$$\tau_{s2} := \frac{V_{s2}}{A_{D2}}$$ Shear stress in shaft at shoulder 2 (Pa)

$\tau_{s2} = 5.851 \times 10^{6}$

4.14 Principal stresses shoulder 1

$$\sigma_{1s1} := \left(\frac{\sigma_{s1} + 0}{2}\right) + \left[\left(\frac{\sigma_{s1} - 0}{2}\right)^2 + \tau_{s1}^{\,2}\right]^{0.5}$$

$\sigma_{1s1} = 0$

$$\sigma_{2s1} := \frac{\sigma_{s1} + 0}{2} - \left[\left(\frac{\sigma_{s1} - 0}{2}\right)^2 + \tau_{s1}^{\,2}\right]^{0.5}$$

$\sigma_{2s1} = 0$

$$\sigma_{s1de} := \left(\sigma_{1s1}^{\,2} - \sigma_{1s1} \cdot \sigma_{2s1} + \sigma_{2s1}^{\,2}\right)^{0.5}$$

$\sigma_{s1de} = 0$

4.15 Stress concentration shoulder 1 page 1185 Shigley

$$K_{ts1} := 0.632 + 0.377\left(\frac{D_2}{D_1}\right)^{-4.4} + \left(\frac{r_1}{D_1}\right)^{-0.5} \cdot \left[\frac{-0.14 - 0.363\left(\frac{D_2}{D_1}\right)^2 + 0.503\left(\frac{D_2}{D_1}\right)^4}{1 - 2.39\left(\frac{D_2}{D_1}\right)^2 + 3.368\left(\frac{D_2}{D_1}\right)^4}\right]^{0.5}$$

$K_{ts1} = 1.009$

$\sigma_{s1K} := \sigma_{s1de} \cdot K_{ts1}$ Maximum stress at shoulder 1 (Pa)

$\sigma_{s1K} = 0$

4.16 Principal stress shoulder 2

$$\sigma_{1s2} := \left(\frac{\sigma_{s2} + 0}{2}\right) + \left[\left(\frac{\sigma_{s2} - 0}{2}\right)^2 + \tau_{s2}^2\right]^{0.5}$$

$\sigma_{1s2} = 62099966$

$$\sigma_{2s2} := \frac{\sigma_{s2} + 0}{2} - \left[\left(\frac{\sigma_{s2} - 0}{2}\right)^2 + \tau_{s2}^2\right]^{0.5}$$

$\sigma_{2s2} = -551321$

$$\sigma_{s2de} := \left(\sigma_{1s2}^2 - \sigma_{1s2}\cdot\sigma_{2s2} + \sigma_{2s2}^2\right)^{0.5}$$

$\sigma_{s2de} = 62377454$

4.17 Stress concentration shoulder 1 page 1185 Shigley

$w_{cl} = 0.15$

$$K_{ts2} := 0.632 + 0.377\left(\frac{w_{cl}}{D_2}\right)^{-4.4} + \left(\frac{r_2}{D_2}\right)^{-0.5}\cdot\left[\frac{-0.14 - 0.363\left(\frac{w_{cl}}{D_2}\right)^2 + 0.503\left(\frac{w_{cl}}{D_2}\right)^4}{1 - 2.39\left(\frac{w_{cl}}{D_2}\right)^2 + 3.368\left(\frac{w_{cl}}{D_2}\right)^4}\right]^{0.5}$$

$K_{ts2} = 2.227$

$\sigma_{s2K} := \sigma_{s2de}\cdot K_{ts2}$ Maximum stress at shoulder 1 (Pa)

$\sigma_{s2K} = 138891434$

4.18 Endurance limit modification for first shoulder where highest stress occurs

$a := 4.4$

$b := -0.26$

$S'_e = 3.95\times 10^8$

$$k_a := a\cdot\left(\frac{\sigma_{uts}}{1\cdot 10^6}\right)^b$$ Surface factor Shigley page 375

$k_a = 0.759$

$k_b := 0.859 - 0.000837 D_1$ Size factor Shigley page 376

$k_b = 0.859$

$k_c := 1$ Marin loading factor Shigley page 378

$k_c = 1$

$k_d := 1$ Temperature factor Shigley page 380

$k_d = 1$

$k_e := 0.8$ Miscellaneous effects factor Shigley page 381
0.8 due to outdoor environment

$S_e := k_a \cdot k_b \cdot k_c \cdot k_d \cdot k_e \cdot S'_e$

$S_e = 206125153$

Stresses in FEA and above calculations are below this modified endurance limit - upper clamp shaft is safe in fatigue

$FOS_{fatigue} := \frac{S_e}{\sigma_{s2K}} = 1.484$ **THIS IS THE CRITICAL FOS FOR SIZE ON THE SHAFT**

5.0 DU BUSH SELECTION

5.1 Travel of linear bearings over lifetime of sculpture

$N_{fail} := 384$ Performances to failure, speed times.xls [3]

$str_g := 2 \cdot r_g = 0.061$

$N_{osc} := \left(\omega_{g_1} \cdot t_{perf_1} + \omega_{g_2} \cdot t_{perf_2} + \omega_{g_3} \cdot t_{perf_3} + \omega_{g_4} \cdot t_{perf_4}\right) \cdot N_{fail}$

$N_{osc} = 4.299 \times 10^5$ 2 times str.g because in a whole cycle it covers the stroke twice

$D_{trav} := 2 \cdot str_g \cdot N_{osc} = 5.254 \times 10^4$ Distance travelled (m)

$L_H := \frac{\left[\left(t_{perf_1} + t_{perf_2} + t_{perf_3} + t_{perf_4}\right) N_{fail}\right]}{3600} = 42.667$ Life time in hours of sculpture

Lets assume that the worst case scenario of swinging occurs at the frequency of the first mode of vibration for blade during the third mode. That means that a worst case has the number of cycles as follows

$\omega_{trfirst} := 0.3$ Approximate first mode frequency from Shayne's phd page 79

$\omega_{gfirst} := \frac{\omega_{trfirst}}{\sqrt{\frac{E_{tr} \cdot d_{tr}^2 \cdot L_g^4 \cdot \rho_g}{E_g \cdot d_g^2 \cdot L_{tr}^4 \cdot \rho_{tr}}}}$ $\omega_{gfirst} = 0.129$

$N_{oscwcs} := \omega_{gfirst} \cdot t_{perf_1} \cdot N_{fail} = 7.936 \times 10^3$ Cycles at the worst case loading scenario

$L_{Hwcs} := \left(\frac{N_{oscwcs}}{N_{osc}}\right) \cdot L_H = 0.788$ Time at the worst case scenario (h)

5.2 Bush selection for upper clamp shaft

DU/DUB designers handbook [6]

Select DU bush PTFE/Lead impregnated steel
Maximum static load 250MPa, maximum dynamic load 140MPa page 9

Using worked examples on page 20 as a template

Load details: Dynamic load oscillating
Shaft: Steel
Lubricated at 25degC

$D_i := 90$ Inside diameter (mm)

$F := \frac{\left(Q_{g_1}\right)}{2}$ Bearing load shared between two bearings (N) $F = 1.102 \times 10^4$

$C := N_{g_1}$ Dynamic load oscillation frequency (RPM) Take worst case scenario of third mode $C = 243.619$

$N_{osz} := N_{g_1}$ Oscillation frequency (RPM) $N_{osz} = 243.619$

$p_{lim} := 22$ Dynamic load limit (N/mm2) Table 4 Page 13

This dynamic load limit assumes that the bushes last at least as long as the blade material

$a_T := 1$ Temperature application factor Table 6 Page 14

$a_M := 1$ Material application factor Table 7 Page 15

$a_B := 0.7$ Bearing size factor Fig 13 Page 16

$a_L := 200$ Life correction constant Table 7 Page 15

$\varphi := 30$ Oscillation amplitude (deg)

$N := \frac{4 \cdot \varphi \cdot N_{osz}}{360} = 81.206$ Average speed (RPM) page 18

Preliminary bearing length calculation page 17

Assumes the bushes last as long as blade material, LH from above in travel section

$B := \left[\frac{F \cdot N \cdot \left(L_{Hwcs} + a_L\right)}{1.25\,10^7 \cdot a_T \cdot a_M \cdot a_B}\right] + \frac{F}{p_{lim} \cdot D_i} = 26.095$ Required bush length (mm)

Select 100mm for length of DU bush from catalogue page 37 $B := 100$

$p := \frac{F}{D_i \cdot B}$ Specific load (N/mm2) page 12 should be less than 140 $p = 1.224$

$U := \frac{D_i \cdot \pi \cdot N}{60 \cdot 10^3}$ Sliding speed (m/s) page 13 more than 2.5 leads to overheating $U = 0.383$

$pU := p \cdot U$ pU factor see page 14 for limits can be up to 3.6 for intermittent and 1.8 for continuous $pU = 0.468$

$a_E := \frac{p_{lim} - p}{p}$ High load factor (must be >0), -ve indicates overload Page 18 $a_E = 16.971$

$pU_{mod} := \frac{5.25 \cdot 10^{-5} \cdot F \cdot N}{a_E \cdot B \cdot a_T \cdot a_M \cdot a_B}$ Modified pU factor for life equation page 18

$pU_{mod} = 0.04$

$L_{Hb} := \left(\frac{1230}{pU_{mod}}\right) - a_L$ Bearing life based on rotating load page 19 (h)

$L_{Hb} = 3.091 \times 10^4$

$Z_{T1} := L_{Hb} \cdot N_{osz} \cdot 60 = 4.518 \times 10^8$ Page 19, Check Q cycles page 13 is less for calculated p

Q for 4.65 is 10^8 so bearing is OK

$Z_{T2} := L_{Hb} \cdot C \cdot 60 = 4.518 \times 10^8$ Bearing limited by wear after ZT cycles

$FOS_{time} := \frac{L_{Hb}}{L_H}$ Factor of safety on life of the sculpture in hours

$FOS_{time} = 724.425$

6.0 UPPER CLAMP PILLOW BLOCK CALCULATIONS

$N_{bolts} := 4$

Using figure 16 on page 1178 Shigley to find the moment at each pillow block

Assume the entire shaft has moment of inertia equal to the two T sections plus a central rectangle (see above in Section 4.0 and sketch Fig D3)

$I_{shaft} := I_{rect}$

$L_{shaft} := 1.563$ Separation of centre of bearing force (m)

$w = 2.04 \times 10^4$

$x := \frac{L_{shaft}}{2}$

Page 1178 figure 16

$M_{bolts} := \left(\frac{w}{12}\right) \cdot \left(6 \cdot L_{shaft} \cdot x - 6 \cdot x^2 - L_{shaft}^2\right)$

$M_{bolts} = 2.077 \times 10^3$

$d_{sep} := 70 \cdot 10^{-3}$ Separation of bolts in each pillow block (m)

$F_M := \frac{M_{bolts}}{d_{sep}}$

$F_M = 29669$

$F_{bolt} := \frac{F_M}{2}$ Force per bolt in pillow block (N)

$F_{bolt} = 14834$

$d_{bolt} := 16 \cdot 10^{-3}$ Major diameter for chosen M16 fastener (m)

$t_{wash} := 4 \cdot 10^{-3}$ Washer thickness Shigley page 1211

$t_1 := 96 \cdot 10^{-3}$ From Solidworks model see Table 8-6 page 461 Shigley

$t_2 := 104 \cdot 10^{-3}$ $h := t_1 + t_{wash} = 0.1$

$t_2 > h$ Therefore effective bolt grip is h+d/2

$l := h + \frac{d_{bolt}}{2}$ Effective bolt grip page 461 Shigley (m)

$l = 0.108$

$L_T := 2 \cdot d_{bolt} + 12 \cdot 10^{-3}$ Threaded length of bolt see page 461

$L_T = 0.044$

Length of bolt 130mm must be larger than L below

$L := h + 1.5 \cdot d_{bolt} = 0.124$ $L = 0.124$

$l_d := L - L_T$ Useful unthreaded section page 461 (mm) $l_d = 0.08$

$l_t := l - l_d$ Length of useful threaded section page 461 (mm) $l_t = 0.028$

$A_d := \frac{\pi \cdot d_{bolt}^2}{4}$ Major diameter are of bolt (m^2) $A_d = 2.011 \times 10^{-4}$

$A_t := 157 \cdot 10^{-6}$ Tensile stress are from Table 8-1 Shigley page 448 (m^2) $A_t = 1.57 \times 10^{-4}$

$k_b := \frac{A_d \cdot A_t \cdot E_{st}}{A_d \cdot l_t + A_t \cdot l_d}$ Fastener stiffness by Shigley page 461 $k_b = 3.592 \times 10^8$

$A := 0.7871$ From Table 8-7 Shigley page 464

$B := 0.6287$ From Table 8-7 Shigley page 464

$k_m := E_{st} \cdot d_{bolt} \cdot A \cdot \exp\left(\frac{B \cdot d_{bolt}}{l}\right)$ Member stiffness page 464 Shigley $k_m = 2.862 \times 10^9$

$F_{range} := \left(\frac{k_b}{k_b + k_m}\right) \cdot F_{bolt}$ Alternating force in bolt as in Keith's bolt notes $F_{range} = 1655$

Preload the bolts to the standard 70% proof stress

$F_i := 7000$ Bolt load at close to 70% proof stress for M16 Keith's 311 notes

$F_{mean} := F_i + \frac{F_{range}}{2}$ Mean force in bolts (N) $F_{mean} = 70827$

$F_a := \frac{F_{range}}{2}$ Alternating force in bolts (N) $F_a = 827$

$\sigma_{mean} := \frac{F_{mean}}{A_t}$ Mean stress in bolt Keiths 311 notes (Pa) $\sigma_{mean} = 451129193$

$\sigma_{alt} := \frac{F_a}{A_t}$ Alternating stress in bolt Keiths notes (Pa) $\sigma_{alt} = 5269320$

Grease the bolts and the following equation applies for torque on bolts (Keiths notes)

$T_{bolt} := 0.2 \cdot F_i \cdot d_{bolt}$ Bolt torque (Nm) $T_{bolt} = 224$

6.1 Bearing Stress on Pillow Block

Make pillow block out of 100mm HA250 Plate (GOOD WELDABILITY REQUIRED)

$L_{du} := 100 \cdot 10^{-3}$ Length of DU bush in pillow block (m)

$D_o := 95 \cdot 10^{-3}$ Outer diameter of DU bush (m)

$F_b := \frac{V}{2}$ Reaction force at each DU bush (N)

$A_b := L_{du} \cdot D_o$ Projected bearing stress area onto pillow block (m^2) $A_b = 9.5 \times 10^{-3}$

$\sigma_b := \frac{F_b}{A_b}$ Bearing stress from reaction force on pillow block (Pa) $\sigma_b = 1159745$

$FOS_b := \frac{\sigma_{yHA250}}{\sigma_b}$ Factor of safety on yielding $FOS_b = 215.565$

6.2 Fillet weld at base of pillow block in TENSION

Arc weld pillow blocks to mounting base using 10mm leg length FES 28 electrode page 72 Special Steel Book Fletchers

$L_{leg} := 15 \cdot 10^{-3}$ Weld Leg length (H in notes) $F_{weld} := \frac{V}{2} = 1.102 \times 10^{4}$

Table 9-3 Keith's notes

$b := 106 \cdot 10^{-3}$ Weld dimensions based on pillow block base dimensions

$d := 200 \cdot 10^{-3}$

$A_{weld} := 1.414 L_{leg} \cdot (b + d)$ Tensile are of weld (m^2) $A_{weld} = 6.49 \times 10^{-3}$

$\sigma_{tens} := \frac{F_{weld}}{A_{weld}}$ Stress in the pillow block weld due to tension (Pa) $\sigma_{tens} = 1697555$

$FOS_{tens} := \frac{\sigma_{ySt}}{\sigma_{tens}}$ Factor of safety for tension in welds $FOS_{tens} = 146.092$

6.4 Fillet weld at base of pillow block BENDING

$M_{weld} := M_{bolts} = 2.077 \times 10^{3}$ Transferred from bolts through pillow block to weld

$I_u := \left(\frac{b^3}{6}\right) + \frac{d \cdot b^2}{2} = 1.322 \times 10^{-3}$ Unit moment of inertia for weld on its side (d and b exchanged since moment acts to bend about y axis)

$I_{bend} := 0.7071 L_{leg} \cdot I_u = 1.402 \times 10^{-5}$ Moment of inertia for weld about y axis (m^4) Shigley page 538

$\sigma_{bend} := \frac{M_{weld} \cdot \left(\frac{b}{2}\right)}{I_{bend}}$ Bending stress in weld caused by moment at ends of upper clamp shaft (Pa)

$\sigma_{bend} = 7849420$

$FOS_{bend} := \frac{\sigma_{ySt}}{\sigma_{bend}}$ Factor of safety for welds bending

$FOS_{bend} = 31.595$

6.5 Fatigue of fillet weld BS5400

$N_{oscwcs} = 7.936 \times 10^{3}$

Weld is a W class weld as specified in BS5400

$\sigma_{sr} := 2 \cdot \sigma_{bend}$

$\sigma_{sr} = 1.57 \times 10^{7}$

At the worst case stress range of 53.04MPa, W class welds are safe for 1e6 cycles so welds safe for number of blade lives

$N_{safe} := 1 \cdot 10^{6}$

$N_{lives} := \frac{N_{safe}}{N_{oscwcs}} = 126.003$

7.0 UPPER PIVOT ARM CALCULATIONS

7.1 Deflection of arms at upper clamp shaft

$b := 100 \cdot 10^{-3}$ RHS short dimension C350 RHS material Steel and Tube

$d := 200 \cdot 10^{-3}$ RHS Long dimension

$t := 9 \cdot 10^{-3}$

Dimensions of arm cross section (m)

$b_i := b - 2 \cdot t = 0.082$

$d_i := d - 2 \cdot t = 0.182$

$A_{arm} := b \cdot d - b_i \cdot d_i = 5.076 \times 10^{-3}$ Cross sectional area arm (m^2)

$F_{arm} := F_{weld} = 1.102 \times 10^{4}$ Tension/compression force in arm (N)

$l_{arm} := 416 \cdot 10^{-3}$ Centre to centre distance of arm between shafts

Bending of upper clamp end of arms

$M_{tube} := M_{weld}$ The moment at the tube-arm transition is the same as the moment at the pillow block end of the arms - Shigley page 1172 Figure 4

$I_x := \left(\frac{b \cdot d^3}{12}\right) - \left(\frac{b_i \cdot d_i^3}{12}\right)$ Moment of inertia about x axis

$I_x = 2.547 \times 10^{-5}$

$I_y := \left(\frac{d \cdot b^3}{12}\right) - \left(\frac{d_i \cdot b_i^3}{12}\right)$ Moment of inertia about y axis

$I_y = 8.304 \times 10^{-6}$

Deflection as per Shigley page 1172 figure 4

$$y_{arm} := \frac{M_{weld} \cdot l_{arm}^{2}}{w \cdot E_{st} \cdot I_y}$$ Deflection of arm at the upper clamp shaft end (m)

$$y_{arm} = 1.025 \times 10^{-8}$$

7.2 Bending stress at tube-arm weld

$$\sigma_{bend} := \frac{M_{tube} \cdot \left(\frac{b}{2}\right)}{I_y}$$ Stress due to bending in the weld at the shaft-arm interface (Pa)

$$\sigma_{bend} = 12504561$$

$$FOS_{yield} := \frac{\sigma_{yC350}}{\sigma_{bend}}$$

$$FOS_{yield} = 27.99$$

7.3 Tension stress at tube-arm weld

$$\sigma_{tens} := \frac{F_{arm}}{A_{arm}} = 2170523$$

$$FOS_{tens} := \frac{\sigma_{yC350}}{\sigma_{tens}}$$

$$FOS_{tens} = 161.251$$

7.4 Fatigue of weld by BS5400

$$\sigma_{sr} := 2\left(\sigma_{bend} + \sigma_{tens}\right)$$ Stress range at the tube-arm weld (Pa) (Arm can only bend one way)

$$\sigma_{sr} = 29350169$$

Weld is class W - at stress range of 100MPa, 1e5 cycles allowable

Amount of blade lives that weld is good for

$$N_{safe} := 1 \cdot 10^{5}$$

$$N_{lives} := \frac{N_{safe}}{N_{oscwcs}} = 12.6$$

7.5 Buckling of arms

Design With Steel Catalogue [7] (Steel and tube dimensions and properties)

$r_y := 39.9 \cdot 10^{-3}$ Radius of gyration for C350 RHS 200 x 100

Quite a short column so check both parabolic and Euler buckling

$C := 1.2$ Recommended Table 4-6 Shigley Page 208

$$\sigma_{crE} := \frac{C \cdot \pi^{2} \cdot E_{st}}{\left(\frac{l_{arm}}{r_y}\right)^{2}}$$ Critical Euler buckling stress in arm (Pa) page 208

$$\sigma_{crE} = 22553319223$$

$$\sigma_{crP} := \sigma_{yC350} - \left(\frac{\sigma_{yC350}}{2\cdot\pi}\cdot\frac{1}{r_y}\right)^2\cdot\left(\frac{1}{C\cdot E_{st}}\right)$$ Critical parabolic buckling stress (Pa) page 209

$\sigma_{crP} = 342153446$

$$FOS_{buck} := \frac{\sigma_{crP}}{\sigma_{tens}}$$ Factor of safety on buckling based on force in arm

$FOS_{buck} = 157.636$

8.0 UPPER PIVOT TUBE

$D_o := 150\cdot10^{-3}$ Dimensions of turned tube to fit DU Bush

$D_i := 113.52\cdot10^{-3}$ Use Seamless Linepipe steel and tube ASTM 106B Strength

$$I_{tube} := \frac{\pi\left(D_o^{\,4} - D_i^{\,4}\right)}{61}$$ Moment of inertia of tube (m^4)

$l_{DU\_arm} := 75\cdot10^{-3}$ Distance from DU bush edge to centre of arm (m)
Solidworks model

$M_{DU\_tube} := F_{arm}\cdot l_{DU\_arm} + M_{tube}$

Maximum bending moment in the tube (Nm)
Fig D4 Sketch

$M_{DU\_tube} = 2.903\times 10^{3}$

$$\sigma_{bend\_tube} := \frac{M_{DU\_tube}\cdot\left(\frac{D_o}{2}\right)}{I_{tube}}$$

Maximum bending stress in tube (Pa)

$\sigma_{bend\_tube} = 12427948$

$$A_{tube} := \pi\cdot\left[\left(\frac{D_o}{2}\right)^2 - \left(\frac{D_i}{2}\right)^2\right]$$ Cross sectional area of turned section of tube (m^2)

$A_{tube} = 7.55\times 10^{-3}$

$$\tau_{tube} := \frac{2F_{arm}}{A_{tube}}$$ Shear due to bending Shigley page 122

$\tau_{tube} = 2918487$

8.1 Principal stresses in tube

$$\sigma_{1\_tube} := \left(\frac{\sigma_{bend\_tube} + 0}{2}\right) + \left[\left(\frac{\sigma_{bend\_tube} - 0}{2}\right)^2 + \tau_{tube}{}^2\right]^{0.5}$$

$$\sigma_{1\_tube} = 13079179$$

$$\sigma_{2\_tube} := \frac{\sigma_{bend\_tube} + 0}{2} - \left[\left(\frac{\sigma_{bend\_tube} - 0}{2}\right)^2 + \tau_{tube}{}^2\right]^{0.5}$$

$$\sigma_{2\_tube} = -651231$$

$$FOS_{yield} := \frac{\sigma_{yLP}}{\sigma_{1\_tube}}$$ Factor of safety on yield for upper pivot tube

$$FOS_{yield} = 18.35$$

8.2 Bush selection for upper clamp TUBE

DU/DUB designers handbook [6]

Select DU bush PTFE/Lead impregnated steel
Maximum static load 250MPa, maximum dynamic load 140MPa page 9

Using worked examples on page 20 as a template

Load details: Dynamic load oscillating
Shaft: Steel
Lubricated at 25degC

$D_i := 150$ Inside diameter (mm)

$F := \frac{\left(Q_{g_1}\right)}{2}$ Bearing load shared between two bearings (N) $F = 1.102 \times 10^4$

$C := N_{g_1}$ Dynamic load oscillation frequency (RPM) Take worst case scenario of third mode $C = 243.619$

$N_{osz} := N_{g_1}$ Oscillation frequency (RPM) $N_{osz} = 243.619$

$p_{lim} := 22$ Dynamic load limit (N/mm2) Table 4 Page 13

$a_T := 1$ Temperature application factor Table 6 Page 14

$a_M := 1$ Material application factor Table 7 Page 15

$a_B := 0.7$ Bearing size factor Fig 13 Page 16

$a_L := 200$ Life correction constant Table 7 Page 15

$\varphi := 10$ Oscillation amplitude (deg)

This dynamic load limitassumes that the bushes last at least as long as the blade material

$N := \frac{4 \cdot \varphi \cdot N_{osz}}{360} = 27.069$ Average speed (RPM) page 18

Preliminary bearing length calculation page 17

Assumes the bushes last as long as blade material, LH from above in travel section

$B := \left[\frac{F \cdot N \cdot (L_H + a_L)}{1.25 \cdot 10^7 \cdot a_T \cdot a_M \cdot a_B} \right] + \frac{F}{p_{lim} \cdot D_i} = 11.61$ Required bush length (mm)

Select 100mm for length of DU bush from catalogue page 37 $B := 100$

$p := \frac{F}{D_i \cdot B}$ Specific load (N/mm2) page 12 should be less than 140 $p = 0.735$

$U := \frac{D_i \cdot \pi \cdot N}{60 \cdot 10^3}$ Sliding speed (m/s) page 13 more than 2.5 leads to overheating $U = 0.213$

$pU := p \cdot U$ pU factor see page 14 for limits can be up to 3.6 for intermittent and 1.8 for continuous $pU = 0.156$

$a_E := \frac{p_{lim} - p}{p}$ High load factor (must be >0), -ve indicates overload Page 18 $a_E = 28.952$

$pU_{mod} := \frac{5.25 \cdot 10^{-5} \cdot F \cdot N}{a_E \cdot B \cdot a_T \cdot a_M \cdot a_B}$ Modified pU factor for life equation page 18 $pU_{mod} = 7.726 \times 10^{-3}$

$L_{Hb} := \left(\frac{1230}{pU_{mod}} \right) - a_L$ Bearing life based on rotating load page 19 (h) $L_{Hb} = 1.59 \times 10^5$

$Z_{T1} := L_{Hb} \cdot N_{osz} \cdot 60 = 2.324 \times 10^9$

$Z_{T2} := L_{Hb} \cdot C \cdot 60 = 2.324 \times 10^9$

Page 19, Check Q cycles page 13 is less for calculated p
Q for 2.48 is 10^8 so bearing is OK
Bearing limited by wear after ZT cycles

$FOS_{time} := \frac{L_{Hb}}{L_H}$ Factor of safety on life of the sculpture in hours $FOS_{time} = 3.727 \times 10^3$

9.0 PILLOW BLOCK MOUNTING PAD

9.1 Compressive stress on mounting pad lip (assume bolts provide no friction)

$F_{lip} := F = 1.102 \times 10^4$

$b_{lip} := 110 \cdot 10^{-3}$

$d_{lip} := 10 \cdot 10^{-3}$

Lip dimensions from Solidworks model

$A_{lip} := b_{lip} \cdot d_{lip} = 1.1 \times 10^{-3}$ Stress area of lip

$\sigma_{lip} := \frac{F_{lip}}{A_{lip}}$ Compressive stress in pillow block pad lip

$\sigma_{lip} = 10015978$

$FOS_{yield} := \frac{\sigma_{ySt}}{\sigma_{lip}}$ Mild steel factor of safety

$FOS_{yield} = 24.76$

9.2 Pivoting Clamp Loads

$jj := 1, 2.. 20$

Bending moment caused by stress measured at the top clamp is equal to the moment provided by the full clamp system to stop blade toppling over - see Fig D5 Sketch

$M_{tcl} := \frac{\sigma_{1g_{10}} \cdot I_g}{Y_g}$ Bending moment in the blade at the top clamp (Nm) $M_{tcl} = 28837$

Shear force in the blade at the top clamp (N)

$d_{sep} := L_g \cdot r_{cl}$ Clamp separation based on 300mm test rig separation (m) $d_{sep} = 1.58$

$Q_{bcl} := \left(\frac{M_{tcl}}{d_{sep}}\right)$ Reaction force at the lower clamp (N) $Q_{bcl} = 18245$

$x_{jj} := \left(\frac{jj}{20}\right) \cdot d_{sep}$ Dividing the section of blade between clamp into n divisions

$M_{cl_{jj}} := Q_{bcl} \cdot x_{jj}$ Moment in blade material between clamps (Nm)

9.3 Bush selection for upper clamp TUBE

DU/DUB designers handbook in [6]

Select DU bush PTFE/Lead impregnated steel
Maximum static load 250MPa, maximum dynamic load 140MPa page 9

Using worked examples on page 20 as a template

Load details: Dynamic load oscillating
Shaft: Steel
Lubricated at 25degC

$D_i := 90$ Inside diameter (mm)

$F := \frac{(Q_{bcl})}{2}$ Bearing load shared between two bearings (N) $F = 9.123 \times 10^3$

$C := N_{g_1}$ Dynamic load oscillation frequency (RPM) Take worst case scenario of third mode $C = 243.619$

$N_{osz} := N_{g_1}$ Oscillation frequency (RPM) $N_{osz} = 243.619$

$p_{lim} := 22$ Dynamic load limit (N/mm2) Table 4 Page 13

This dynamic load limitassumes that the bushes last at least as long as the blade material

$a_T := 1$ Temperature application factor Table 6 Page 14

$a_M := 1$ Material application factor Table 7 Page 15

$a_B := 0.7$ Bearing size factor Fig 13 Page 16

$a_L := 200$ Life correction constant Table 7 Page 15

$\varphi := 30$ Oscillation amplitude (deg)

$N := \frac{4 \cdot \varphi \cdot N_{osz}}{360} = 81.206$ Average speed (RPM) page 18

Preliminary bearing length calculation page 17

Assumes the bushes last as long as blade material, LH from above in travel section

$B := \left[\frac{F \cdot N \cdot \left(L_H + a_L \right)}{1.25 10^7 \cdot a_T \cdot a_M \cdot a_B} \right] + \frac{F}{p_{lim} \cdot D_i} = 25.153$ Required bush length (mm)

Select 100mm for length of DU bush from catalogue page 37 $B := 100$

$p := \frac{F}{D_i \cdot B}$ Specific load (N/mm2) page 12 should be less than 140 $p = 1.014$

$U := \frac{D_i \cdot \pi \cdot N}{60 \cdot 10^3}$ Sliding speed (m/s) page 13 more than 2.5 leads to overheating $U = 0.383$

$pU := p \cdot U$ pU factor see page 14 for limits can be up to 3.6 for intermittent and 1.8 for continuous $pU = 0.388$

$a_E := \frac{p_{lim} - p}{p}$ High load factor (must be >0), -ve indicates overload Page 18 $a_E = 20.704$

$pU_{mod} := \frac{5.25 10^{-5} \cdot F \cdot N}{a_E \cdot B \cdot a_T \cdot a_M \cdot a_B}$ Modified pU factor for life equation page 18 $pU_{mod} = 0.027$

$L_{Hb} := \left(\frac{1230}{pU_{mod}} \right) - a_L$ Bearing life based on rotating load page 19 (h) $L_{Hb} = 4.563 \times 10^4$

$Z_{T1} := L_{Hb} \cdot N_{osz} \cdot 60 = 6.67 \times 10^8$

$Z_{T2} := L_{Hb} \cdot C \cdot 60 = 6.67 \times 10^8$

Page 19, Check Q cycles page 13 is less for calculated p
Q for 2.48 is 10^8 so bearing is OK
Bearing limited by wear after ZT cycles

$FOS_{time} := \frac{L_{Hb}}{L_H}$ Factor of safety on life of the sculpture in hours $FOS_{time} = 1.07 \times 10^3$

10.0 FRAME STRENGTH ANALYSIS

Use beam elements when "You can treat these structural members as solids by selecting their icons in the Simulation study tree and select Treat as Solid. For short structural members (ratio of length over largest orthogonal cross-sectional distance from the centroid is less than 3.0), it is recommended to use a solid mesh."

Innova Systems Tutorial - length of the beam should be 10 times larger than the largest dimension of its cross section

FEA MODEL RESULTS

$\sigma_{max} := 50 \cdot 10^{6}$ Maximum stress at critical location in frame according to FEA results [8] (Pa)

$\sigma_{min} := -50 \cdot 10^{6}$ Minimum stress at critical location in frame according to FEA results [8] (Pa)

$$\sigma_r := \sigma_{max} - \sigma_{min} = 1 \times 10^{8}$$

$$\sigma_m := \left(\frac{\sigma_{max} + \sigma_{min}}{2} \right) = 0$$

Weld is class W - at stress range of 100MPa, 1e5 cycles allowable

Amount of blade lives that weld is good for

$$N_{safe} := 1 \cdot 10^{5}$$

$$N_{lives} := \frac{N_{safe}}{N_{oscwcs}} = 12.6$$

11.0 LOWER PIVOT SHAFT CALCULATIONS

11.1 Shaft geometry (see Sketches Fig D1 and Fig D2)

$\sigma_{yield} := \sigma_{yBi8($

$D_1 := 90 \cdot 10^{-3}$ Diameter of shaft bearing interfaces (m)

$\tau_{yield} := 0.58 \sigma_{yield}$

$D_2 := 90 \cdot 10^{-3}$ Diameter of bearing shoulder (m)

$\sigma_{uts} := \sigma_{utsBi8($

$r_1 := 5 \cdot 10^{-3}$ Fillet radius of d1 (m)

$S'_e := 0.5 \cdot \sigma_{uts}$

$r_2 := 5 \cdot 10^{-3}$ Fillet radius of d2 (m)

Page 369 Shigley

Assume that strengthening rib is a uniform T-section

$w_f := 100 \cdot 10^{-3}$ Width of T flange (m)

$L_w := 150 \cdot 10^{-3}$ Length of T web (m)

$t_f := 24 \cdot 10^{-3}$ Thickness of T flange (m)

$t_w := 20 \cdot 10^{-3}$ Thickness of T web (m)

$w_{cl} := 150 \cdot 10^{-3}$ Width of clamp (m)

$h_{cl} := 100 \cdot 10^{-3}$ Height of the clamp (m)

$I_{D1} := \pi \cdot \frac{D_1^4}{64}$ Moment of inertia for Section 1 (m^4)

$I_{D2} := \pi \cdot \frac{D_2^4}{64}$ Moment of inertia for Section 2 (m^4)

$A_{D1} := \pi \cdot \left(\frac{D_1}{2}\right)^2$ Cross sectional area Section 1 (m^2)

$A_{D2} := \pi \left(\frac{D_2}{2}\right)^2$ Cross sectional area Section 1 (m^2)

11.2 Centroid calculation

$A_1 := t_f \cdot w_f = 2.4 \times 10^{-3}$ Area of flange (m^2)

$A_2 := t_w \cdot L_w = 3 \times 10^{-3}$ Area of web (m^2)

$y_1 := \frac{L_w}{2}$ $y_2 := L_w + \frac{t_f}{2}$ Distance to centroid of each rectangle from x axis (m)

$y := \frac{A_1 \cdot y_1 + A_2 \cdot y_2}{A_1 + A_2}$ Location of neutral axis w.r.t x axis (mm)

$y = 0.123$

11.3 Moment of inerita by P.A.T

$I_1 := \frac{w_f \cdot t_f^{\,3}}{12}$ $I_2 := \frac{t_w \cdot L_w^{\,3}}{12}$ Moment of inertia for each rectangle (m)

$d_1 := y - \frac{L_w}{2}$

Distance to centroid of each axis from neutral axis (m)

$d_2 := \left(L_w + \frac{t_f}{2}\right) - y$

$I_T := I_1 + I_2 + A_1 \cdot d_1^{\,2} + A_2 \cdot d_2^{\,2}$ Moment of inertia about neutral axis T section (m^4)

$I_T = 1.583 \times 10^{-5}$

11.4 Bending stress in T section

Table E-9 Shigley number 16 Fixed Fixed beam Page 1178

$V := Q_{bcl}$ Shear force at the lower clamp (N)

$w := \frac{V}{b_g}$ Distributed force on clamp jaw (N/m) $w = 1.689 \times 10^{4}$

$x := \frac{b_g}{2}$ Location of maximum bending stress (m)

$M := \left(\frac{w}{12}\right) \cdot \left(6 b_g \cdot x - 6x^2 - b_g^{\,2}\right)$ Maximum bending moment in T section (Nm)

$M = 821.046$

$y = 0.123$

$\sigma_x := \frac{M \cdot y}{I_T}$ Pure bending stress in the surface of strengthening T section (Pa)

$\sigma_x = 6395970$

11.5 Shear stress due to bending in T section page 122 Shigley

$A_T := A_1 + A_2 = 5.4 \times 10^{-3}$

$\tau_{xy} := \frac{V}{A_T}$ Shear stress due to bending (Pa)

$\tau_{xy} = 3378788$

11.6 Principal Stresses due to Bending page 97 Shigley

$\sigma_y := 0$

$$\sigma_1 := \left(\frac{\sigma_x + \sigma_y}{2}\right) + \left[\left(\frac{\sigma_x - \sigma_y}{2}\right)^2 + \tau_{xy}^2\right]^{0.5}$$

$\sigma_1 = 7850223$

$$\sigma_2 := \frac{\sigma_x + \sigma_y}{2} - \left[\left(\frac{\sigma_x - \sigma_y}{2}\right)^2 + \tau_{xy}^2\right]^{0.5}$$

$\sigma_2 = -1454253$

11.7 Distortion Energy Theory eq 6-9 page 328 Shigley

$$\sigma_{de} := \left(\sigma_1^2 - \sigma_1 \cdot \sigma_2 + \sigma_2^2\right)^{0.5}$$

$\sigma_{de} = 8669317$

11.8 Factors of safety on bending stresses

$$FOS := \frac{\sigma_{yield}}{\sigma_{de}}$$

$FOS = 79.591$

11.9 Shear stress due to blade edges

$$\tau := \frac{\left(\frac{V}{2}\right)}{A_T}$$

Shear stress in the clamp walls at edges of blade (Pa)

$\tau = 1689394$

11.10 Factors of safety on shear stresses

$$FOS := \frac{\tau_{yield}}{\tau}$$

$FOS = 236.89$

11.11 Deflection of T section part of clamp page 1174 figure 7

$$y_{max} := \frac{-w \cdot b_g^4}{384 E_{st} \cdot I_T}$$

Deflection of clamped T section at mid span

$y_{max} = -1.826 \times 10^{-5}$

11.12 Deflection and stresses at the shoulders

3 sections of stub axle
Section 1 is approximated as a rectangle with two ribs
Section 2 is circular
Section 3 is circular

11.13 Moment of inertia Section 3

$$I_3 := \frac{h_{cl} \cdot w_{cl}^{3}}{12} \qquad I_3 = 2.813 \times 10^{-5}$$

$$d := \left(\frac{w_{cl}}{2}\right) + \left(\frac{L_w}{2}\right)$$

$$I_{rect} := 2 \cdot \left(I_2 + A_2 \cdot d^{2}\right) + I_3$$ Moment of inertia for rectangular section (m^4)

$$I_{rect} = 1.744 \times 10^{-4}$$

$$M_1 := \frac{w \cdot b_g^{2}}{12}$$ Moment at end of T section (carry over to stub)

$$M_1 = 1.642 \times 10^{3}$$

$l_a := 10 \cdot 10^{-3}$ Length of Section 1 (m)

$l_b := 100 \cdot 10^{-3}$ Length of Section 2 (m)

$l_c := 228 \cdot 10^{-3}$ Length of Section 3 (m)

$$l_a + l_b + l_c = 0.338$$

$$R_1 := \frac{\left[\frac{V}{2} \cdot \left(l_c\right) + M_1\right]}{l_b}$$ Reaction at DU bush (N)

$$R_1 = 37221$$

$$R_2 := R_1 + \frac{V}{2}$$ Reaction at DU bush (N)

$$R_2 = 46343$$

Use shaft deflection spreadsheet [5] to determine moments and deflections at critical shoulder locations

Shaft deflection calculated from spreadsheet is

$y_{stub} := -3.54 \cdot 10^{-5}$

$y_{total} := y_{stub} + y_{max} = -5.366 \times 10^{-5}$

$M_{s1} := 0$ Moment at shoulder 1 from spreadsheet (Nm)

$M_{s2} := 365($ Moment at shoulder 2 from spreadsheet (Nm)

$$\sigma_{s1} := \frac{\left[M_{s1} \cdot \left(\frac{D_1}{2}\right)\right]}{I_{D1}} \qquad \sigma_{s1} = 0$$

$$\sigma_{s2} := \frac{\left[M_{s2} \cdot \left(\frac{D_2}{2}\right)\right]}{I_{D2}} \qquad \sigma_{s2} = 50999444$$

$V_{s1} := 0$ Shear force at shoulder 1 (N)

$V_{s2} := 912$ Shear force at shoulder 2 (N)

Both from shaft deflection spreadsheet

$\tau_{s1} := \frac{V_{s1}}{A_{D1}}$ Shear stress in shaft at shoulder 1 (Pa)

$\tau_{s1} = 0$

$\tau_{s2} := \frac{V_{s2}}{A_{D2}}$ Shear stress in shaft at shoulder 2 (Pa)

$\tau_{s2} = 1.434 \times 10^{6}$

11.14 Principal stresses shoulder 1

$$\sigma_{1s1} := \left(\frac{\sigma_{s1} + 0}{2}\right) + \left[\left(\frac{\sigma_{s1} - 0}{2}\right)^2 + \tau_{s1}^{\,2}\right]^{0.5}$$

$\sigma_{1s1} = 0$

$$\sigma_{2s1} := \frac{\sigma_{s1} + 0}{2} - \left[\left(\frac{\sigma_{s1} - 0}{2}\right)^2 + \tau_{s1}^{\,2}\right]^{0.5}$$

$\sigma_{2s1} = 0$

$$\sigma_{s1de} := \left(\sigma_{1s1}^{\,2} - \sigma_{1s1}\cdot\sigma_{2s1} + \sigma_{2s1}^{\,2}\right)^{0.5}$$

$\sigma_{s1de} = 0$

11.15 Stress concentration shoulder 1 page 1185 Shigley

$$K_{ts1} := 0.632 + 0.377\left(\frac{D_2}{D_1}\right)^{-4.4} + \left(\frac{r_1}{D_1}\right)^{-0.5}\cdot\left[\frac{-0.14 - 0.363\left(\frac{D_2}{D_1}\right)^2 + 0.503\left(\frac{D_2}{D_1}\right)^4}{1 - 2.39\left(\frac{D_2}{D_1}\right)^2 + 3.368\left(\frac{D_2}{D_1}\right)^4}\right]^{0.5}$$

$K_{ts1} = 1.009$

$\sigma_{s1K} := \sigma_{s1de}\cdot K_{ts1}$ Maximum stress at shoulder 1 (Pa)

$\sigma_{s1K} = 0$

11.16 Principal stress shoulder 2

$$\sigma_{1s2} := \left(\frac{\sigma_{s2} + 0}{2}\right) + \left[\left(\frac{\sigma_{s2} - 0}{2}\right)^2 + \tau_{s2}^{\,2}\right]^{0.5}$$

$\sigma_{1s2} = 51039736$

$$\sigma_{2s2} := \frac{\sigma_{s2} + 0}{2} - \left[\left(\frac{\sigma_{s2} - 0}{2}\right)^2 + \tau_{s2}^{\,2}\right]^{0.5}$$

$\sigma_{2s2} = -40292$

$$\sigma_{s2de} := \left(\sigma_{1s2}^{2} - \sigma_{1s2}\cdot\sigma_{2s2} + \sigma_{2s2}^{2}\right)^{0.5}$$

$\sigma_{s2de} = 51059894$

11.17 Stress concentration shoulder 1 page 1185 Shigley

$$K_{ts2} := 0.632 + 0.377\left(\frac{w_{cl}}{D_2}\right)^{-4.4} + \left(\frac{r_2}{D_2}\right)^{-0.5}\cdot\left[\frac{-0.14 - 0.363\left(\frac{w_{cl}}{D_2}\right)^{2} + 0.503\left(\frac{w_{cl}}{D_2}\right)^{4}}{1 - 2.39\left(\frac{w_{cl}}{D_2}\right)^{2} + 3.368\left(\frac{w_{cl}}{D_2}\right)^{4}}\right]^{0.5}$$

$K_{ts2} = 2.227$

$\sigma_{s2K} := \sigma_{s2de}\cdot K_{ts2}$ Maximum stress at shoulder 1 (Pa)

$\sigma_{s2K} = 113691430$

11.18 Endurance limit modification for first shoulder where highest stress occurs

$a := 4.45$
$b := -0.265$

$S'_e = 3.95\times 10^{8}$

$$k_a := a\cdot\left(\frac{\sigma_{uts}}{1\cdot 10^{6}}\right)^{b}$$ Surface factor Shigley page 375

$k_a = 0.759$

$k_b := 0.859 - 0.000837 D_1$ Size factor Shigley page 376

$k_b = 0.859$

$k_c := 1$ Marin loading factor Shigley page 378

$k_c = 1$

$k_d := 1$ Temperature factor Shigley page 380

$k_d = 1$

$k_e := 0.8$ Miscellaneous effects factor Shigley page 381
0.8 due to outdoor environment

$S_e := k_a\cdot k_b\cdot k_c\cdot k_d\cdot k_e\cdot S'_e$

$S_e = 206125153$

Stresses in FEA and above calculations are below this modified endurance limit - upper clamp shaft is safe in fatigue

$$FOS_{fatigue} := \frac{S_e}{\sigma_{s2K}} = 1.813$$ **THIS IS THE CRITICAL FOS FOR SIZE ON THE SHAFT**

12.0 CARRIAGE FRAME CALCULATIONS (see notes for FBD)

DIMENSIONS FROM SOLIDWORKS [9]

$L_{off} := 0.083$ Offest from centre of frame reactions of the COG (m)

$h_{cg} := 1.018$ Height of the COG from the base of the frame (m)

$L_{car} := 1.600$ Distance between centre of linear bearing frame supports (m)

$h_{pivot} := 1.839$ Height from linear bearing frame supports to upper clamp (m)

$M_{car} := 210($ Mass of carriage (including section of blade material in shuttle) (kg) See solidworks model C11-102a

$$L_{RL} := \left(\frac{L_{car}}{2}\right) + L_{off} = 0.883$$

$$L_{RR} := \left(\frac{L_{car}}{2}\right) - L_{off} = 0.717$$

$$RR := \frac{Q_{g_1} \cdot h_{pivot} + M_{tcl} + M_{car} \cdot a_{g_1} - L_{RL} \cdot \left(M_{car} \cdot g\right)}{L_{car}} \qquad RR = 5.809 \times 10^4$$

$$RL := \frac{Q_{g_1} \cdot h_{pivot} + M_{tcl} + M_{car} \cdot a_{g_1} + L_{RR} \cdot \left(M_{car} \cdot g\right)}{L_{car}} \qquad RL = 7.868 \times 10^4$$

$N_{sup} := 2$ Number of supports per reaction force

$F_{bsRR} := \frac{RR}{N_{sup}}$ Force on bearing support at right reaction (N) $F_{bsRR} = 2.904 \times 10^4$

$F_{bsRL} := \frac{RL}{N_{sup}}$ Force on bearing support at left reaction (N) $F_{bsRL} = 3.934 \times 10^4$

13.0 CRANK ARRANGEMENT BEARING SELECTION

$M_g = 1.108\times 10^3$ Mass of blade (kg) $Q_{g_1} = 2.204\times 10^4$

$M_{car} = 2.1\times 10^3$ Mass of shuttle carriage (kg)

$M_{tot} := M_g + M_{car} = 3.208\times 10^3$

$F_{cr} := M_{car}\cdot a_{g_1} + Q_{g_1} = 63799$ $N_{oscwcs} = 7.936\times 10^3$

$\sigma_{yield} := \sigma_{y4140}$

$\tau_{yield} := 0.58\cdot\sigma_{yield}$

$\sigma_{uts} := \sigma_{uts4140}$

$S'_e := 0.5\cdot\sigma_{uts}$

Page 369 Shigley

13.1 Hinge point pin strength (bolted into frame)

Choose 4140 150mm black round for pin

$l_{pin} := 75\cdot 10^{-3}$ Length of pin between support plates (m)

$d_{pin} := 65\cdot 10^{-3}$ Diameter of pin $D_{pin} := 75\cdot 10^{-3}$

$d_{hole} := 17\cdot 10^{-3}$ Diameter of clearance hole through pin $y_{pin} := \frac{d_{pin}}{2}$

$A_{pin} := \pi\cdot\left(\frac{d_{pin}}{2}\right)^2 - \pi\cdot\left(\frac{d_{hole}}{2}\right)^2$ Area of pin (m^2)

$A_{pin} = 3.091\times 10^{-3}$

$I_{pin} := \frac{\pi\cdot\left(d_{pin}^{\ 4} - d_{hole}^{\ 4}\right)}{64}$ Moment of inertia of pin (m^4)

$I_{pin} = 8.721\times 10^{-7}$

$M_{pin} := \frac{F_{cr}\cdot l_{pin}}{8}$ Bending moment at each end of pin due to bending Page 1177 Shigley (Nm)

$M_{pin} = 598.111$

$M_{midpin} := \left(\frac{F_{cr}}{8}\right)\cdot\left[3\cdot l_{pin} - 4\cdot\left(\frac{l_{pin}}{2}\right)\right] = 598.111$

Checking mid span moment is equal

$M_{mid} := \left(\frac{F_{cr}}{8}\right)\cdot\left[4\cdot\left(\frac{l_{pin}}{2}\right) - l_{pin}\right] = 598.111$

$y_{pinmax} := \frac{F_{cr}\cdot l_{pin}^{\ 3}}{192\cdot E_{st}\cdot I_{pin}}$ Maximum deflection of pin (m)

$y_{pinmax} = 7.765\times 10^{-7}$

$V_{pin} := \frac{F_{cr}}{2}$ Shear force in any cross section of pin (N)

$V = 1.825\times 10^4$

$\tau_{pin} := \frac{4\cdot V_{pin}}{3\cdot A_{pin}}$ Shear stress in pin due to bending (Pa)

$\tau_{pin} = 13758605$

$\sigma_{pin} := \frac{M_{pin}\cdot y_{pin}}{I_{pin}}$

$\sigma_{pin} = 22288391$

$\sigma_y = 0$

Principal stresses for pin (Pa)

$$\sigma_1 := \left(\frac{\sigma_{pin} + \sigma_y}{2}\right) + \left[\left(\frac{\sigma_{pin} - \sigma_y}{2}\right)^2 + \tau_{pin}^2\right]^{0.5} \qquad \sigma_1 = 28849909$$

$$\sigma_2 := \frac{\sigma_{pin} + \sigma_y}{2} - \left[\left(\frac{\sigma_{pin} - \sigma_y}{2}\right)^2 + \tau_{pin}^2\right]^{0.5} \qquad \sigma_2 = -6561518$$

$$\sigma_{pinDE} := \left(\sigma_1^2 - \sigma_1 \cdot \sigma_2 + \sigma_2^2\right)^{0.5} \qquad \sigma_{pinDE} = 3.263 \times 10^7$$

13.2 Stress concentration pin shoulder page 1185 shigley

$r_a := 1.5 \cdot 10^{-3}$ Page 61 Maximum shoulder radius for pin without undercut (m)

$$K_{tpin} := 0.632 + 0.377\left(\frac{D_{pin}}{d_{pin}}\right)^{-4.4} + \left(\frac{r_a}{d_{pin}}\right)^{-0.5} \cdot \left[\frac{-0.14 - 0.363\left(\frac{D_{pin}}{d_{pin}}\right)^2 + 0.503\left(\frac{D_{pin}}{d_{pin}}\right)^4}{1 - 2.39\left(\frac{D_{pin}}{d_{pin}}\right)^2 + 3.368\left(\frac{D_{pin}}{d_{pin}}\right)^4}\right]^{0.5}$$

$K_{tpin} = 2.585$

$\sigma_{pinDEK} := \sigma_{pinDE} \cdot K_{tpin} = 84339911$

This is an alternating stress about a mean 0 MPa since the motion is oscillating

$FOS_{yield} := \frac{\sigma_{y4140}}{\sigma_{pinDEK}}$ Factor of safety on yielding on pin

$FOS_{yield} = 8.3$

13.3 Endurance limit modification for first shoulder where highest stress occurs

$a := 4.45$

$b := -0.265$ $S'_e = 4.25 \times 10^8$

$$k_a := a \cdot \left(\frac{\sigma_{uts}}{1 \cdot 10^6}\right)^b$$ Surface factor Shigley page 375

$k_a = 0.745$

$k_b := 1.24 \cdot d_{pin}^{-0.107}$ Size factor Shigley page 376

$k_b = 1.661$

$k_c := 1$ Marin loading factor Shigley page 378

$k_c = 1$

$k_d := 1$ Temperature factor Shigley page 380

$k_d = 1$

$k_e := 0.8$ Miscellaneous effects factor Shigley page 381
0.8 due to outdoor environment

$S_e := k_a \cdot k_b \cdot k_c \cdot k_d \cdot k_e \cdot S'_e$

$S_e = 420710033$

$FOS_{fatigue} := \frac{S_e}{\sigma_{pinDEK}} = 4.988$ **THIS IS THE CRITICAL FOS FOR SIZE ON THE PIN**

13.4 SKF Spherical Bearing Selection

$F_{cr} = 6.38 \times 10^4$

BEARING 1 - frame to crank

$C := 220$ Basic dynamic load rating (kN) page 60 SKF spherical catalogue

$P_u := 24$ Fatigue load limit (kN) page 60 SKF spherical catalogue

$P := F_{cr}$ Equivalent dynamic bearing load (kN) no axial force, page 18 SKF

$n := 3.6$ Rotational speed of outer ring of bearing from SW simulation RPM

$a_1 := 0.21$ Life adjustment factor SKF catalogue page 18

At this point I've used the SKF online calculator and found that the rotational speed is too low for adequate oil film dispersion inside the bearing. Called salesperson Shane at SKF who confirmed that spherical bearings are correct for the application although not ideal by any means - no other better solution. LGHB grease suggested as this is a high load, heavy impact grease with a more desirable viscosity for oil dispersion. This grease has a viscosity between the regular duty LGEP (200mm^2/s) and heavy duty LGEV (1000mm^2/s) grease. SKF calculator suggested the use of the static safety factor s0 to select bearing - s0=C0/P0>=3. P0 is the radial loading on the bearing therefore, the static load rating should be larger than

$P_0 := F_{cr} = 6.38 \times 10^4$ Page 87-88 SKF Roller Catalogue [11]

$C_0 := 3 \cdot P_0 = 1.914 \times 10^5$

A spherical bearing with d=65mm has a static loading rating of 360kN - this has been selected.

Select bearing 22313 E/VA405 sealed (NoWear coating?) and pre packed with LGHB grease

CRANK SHAFT 2 - crank shaft connecting to drive shaft

This is the bearing where the highest moment loading will occur. Creating a stiff connection here will ensure that the cranks behave as a pinned mechanism.

All forces in the mechanism are lower at the shorter stroke due to less acceleration at the extremes of shuttle travel - see Solidworks simulation [12].

$F1 := F_{cr} = 6.38\times 10^{4}$ Force in the crank arm from frame to connecting pin (N)

$F3 := 7.5\cdot 10^{4}$ Force in the adjusting crank (N)

$\theta := 30deg$ Angle between F1 and F3

$F3R := F3\cdot\cos(\theta)$ F3 component in the same plane as F1

$F3R = 6.495\times 10^{4}$

$d_{sep1} := 75\cdot 10^{-3}$ Distance of separation for F1 and bearing 2 (m)

$d_{sep3} := 75\cdot 10^{-3}$ Distance of separation for F3 and bearing 2 (m)

BEARING 2

$F1 = 6.38\times 10^{4}$ Force in crank 1 (N)

$\omega := 161$ Angular velocity of outer ring of bearing (deg/s)

$N := \omega\cdot 60\cdot\frac{1}{360}$ Speed of outer ring of bearing (RPM)

$N = 26.833$

USE SKF online bearing calculator

Select NNCF5016 double row cylindrical roller bearing - better load distribution on rollers than ball bearings. Can take tilting moments.

BEARING 3

$d_{tp} := 60\cdot 10^{-3}$

$F3 = 7.5\times 10^{4}$ Force in the driving crank (N)

$M1 := F1\cdot d_{sep1} = 4.785\times 10^{3}$ Moments caused by crank 1 and 3 (Nm)

$M2 := F3\cdot d_{sep3} = 5.625\times 10^{3}$

$M_{total} := M1 + M2$ Twisting moment around crank 2

$M_{total} = 10410$

$F_{tp2} := \frac{M_{total}}{d_{tp}}$ Radial force on lower tapered roller resulting from moment (N)

$F_{tp2} = 173498$

13.5 Top bearing selection

Top bearing $p := \frac{10}{3}$ Life exponent p for roller bearings page 64 SKF [11]

Choose tapered roller bearing 30215 J2/Q

$P := F3 = 75000$ Radial load on bearing (N)

$C := 140\cdot 10^{3}$ Dynamic basic load rating (N)

$N_{osc} = 4.299\times 10^{5}$

$L_{10} := \left(\frac{C}{P}\right)^{p}\cdot 1\cdot 10^{6}$ Life of bearing (Revolutions)

$L_{10} = 8.009\times 10^{6}$

$FOS_{life} := \frac{L_{10}}{N_{osc}} = 18.631$

13.6 Bottom bearing selection

Select bearing T2EE 100

$P := F_{tp2} = 1.735\times 10^{5}$

$C := 314\cdot 10^{3}$

$L_{10} := \left(\frac{C}{P}\right)^{p}\cdot 1\cdot 10^{6}$ Life of bearing (Revolutions)

$L_{10} = 7.224\times 10^{6}$

$FOS_{life} := \frac{L_{10}}{N_{osc}} = 16.806$

14.0 DRIVESHAFT STRENGTH CALCULATIONS

14.1 Bearing reaction forces and moments for static overload case (see sketch Fig D7)

$L_{Fs} := 0.2$ Distance from crank arm neutral axis to top bearing (m)

$L_{sep} := 0.4$ Separation of top and bottom bearings (m)

$F_{cr} = 63798.52$

$R_{sB1} := F_{cr}\cdot\frac{\left(L_{Fs} + L_{sep}\right)}{L_{sep}}$ Radial load at top bearing (N)

$R_{sB1} = 103672.6$

$R_{sB2} := \frac{\left(F_{cr}\cdot L_{Fs}\right)}{L_{sep}}$ Radial load at bottom bearing (N)

$R_{sB2} = 39874.08$

Maximum bending moment occurs at the top bearing

$M_a := F_{cr}\cdot L_{Fs}$ Maximum bending moment in shaft (Nm)

$M_a = 15950$

Mean torque in shaft from motor drive (Nm)

$T_m := 198$

$N := N_{g_1}$ Driveshaft speed at third mode swinging (RPM)

$N = 243.619$

14.2 Minimum diameter of shaft by DE criterion page 1117 Shigley

Choose 4140 for the driveshaft material

$\sigma_{yield} := \sigma_{y4140}$

$\tau_{yield} := 0.58\sigma_{yield}$

$\sigma_{uts} := \sigma_{uts4140} = 8.5\times 10^{8}$

$S'_e := 0.5\cdot\sigma_{uts}$

$d_s := 170\cdot 10^{-3}$ Diameter of shaft at critical top bearing (m)

$d_o := 184\cdot 10^{-3}$ Large diameter of shaft at shoulder (m) from SKF catalogue page 839 [11]

$a := 4.45$
$b := -0.265$

$S'_e = 4.25 \times 10^8$

$k_a := a \cdot \left(\frac{\sigma_{uts}}{1 \cdot 10^6} \right)^b$ Surface factor Shigley page 375

$k_a = 0.745$

$k_b := 0.859 - 0.000827 d_s$ Size factor Shigley page 376

$k_b = 0.859$

$k_c := 0.583$ Marin loading factor Shigley page 378 (torsion)

$k_c = 0.583$

$k_d := 1$ Temperature factor Shigley page 380

$k_d = 1$

$k_e := 0.8$ Miscellaneous effects factor Shigley page 381
0.8 due to outdoor environment

$S_e := k_a \cdot k_b \cdot k_c \cdot k_d \cdot k_e \cdot S'_e$

$S_e = 1.268 \times 10^8$

$r_s := 2.5 \cdot 10^{-3}$ Minimum radius for shoulder in tapered roller bearings around 170mm page 839
SKF [11] convert to inches due to Shigley page 384

$$K_t := 0.622 + 0.38 \left(\frac{d_o}{d_s} \right)^{-4.3} + \left(\frac{r_s}{d_s} \right)^{-0.5} \cdot \left[\frac{-0.322 - 0.277 \left(\frac{d_o}{d_s} \right)^2 + 0.599 \left(\frac{d_o}{d_s} \right)^4}{1 - 2.55 \left(\frac{d_o}{d_s} \right)^2 + 5.27 \left(\frac{d_o}{d_s} \right)^4} \right]^{0.5}$$

$K_t = 2.401$

$$K_{ts} := 0.78 + 0.2 \left(\frac{d_o}{d_s} \right)^{-10} + \left(\frac{r_s}{d_s} \right)^{-0.46} \cdot \left[\frac{-0.002 - 0.125 \left(\frac{d_o}{d_s} \right)^2 + 0.123 \left(\frac{d_o}{d_s} \right)^4}{1 - 2.75 \left(\frac{d_o}{d_s} \right)^2 + 2.55 \left(\frac{d_o}{d_s} \right)^4} \right]^{0.5}$$

$K_{ts} = 1.75$

$n := 2$ Factor of safety

$a := \frac{139 \cdot 10^6}{\sigma_{uts}}$ Page 383 Shigley for a shoulder

$r_s := \frac{\left(2.5 \cdot 10^{-3}\right)}{25.4 \cdot 10^{-3}}$ Convert to inches Shigley page 384

$K_f := \frac{K_t}{1 + \left(\frac{2}{\sqrt{r_s}}\right) \cdot \left(\frac{K_t - 1}{K_t}\right) a} = 1.493$ $K_{fs} := \frac{K_{ts}}{1 + \left(\frac{2}{\sqrt{r_s}}\right) \cdot \left(\frac{K_{ts} - 1}{K_{ts}}\right) a} = 1.21$ Page 384 Shigley

$$d_{min} := \left[\left(\frac{16 \cdot n}{\pi}\right) \cdot \left[4 \cdot \left(\frac{K_f \cdot M_a}{S_e}\right)^2 + 3 \cdot \left(\frac{K_{fs} \cdot T_m}{\sigma_{yield}}\right)^2\right]^{0.5}\right]^{\frac{1}{3}}$$

$d_{min} = 0.156$

14.3 Top bearing selection

Top bearing $p := \frac{10}{3}$ Life exponent p for roller bearings page 64 SKF [11]

Choose tapered roller bearing T4DB170 page 836 SKF

$P := R_{sB1} = 103673$ Radial load on bearing (N)

$C := 251 \cdot 10^3$ Dynamic basic load rating (N)

$N_{osc} = 4.299 \times 10^5$

$L_{10} := \left(\frac{C}{P}\right)^p \cdot 1 \cdot 10^6$ Life of bearing (Revolutions) $L_{10} = 1.906 \times 10^7$

$FOS_{life} := \frac{L_{10}}{N_{osc}} = 44.332$

14.4 Bottom bearing selection

Select bearing 32020X/Q page 834 SKF bearing catalogue [11]

$P := R_{sB2} = 3.987 \times 10^4$

$C := 172 \cdot 10^3$

$L_{10} := \left(\frac{C}{P}\right)^p \cdot 1 \cdot 10^6$ Life of bearing (Revolutions) $L_{10} = 1.307 \times 10^8$

$FOS_{life} := \frac{L_{10}}{N_{osc}} = 303.954$

15.0 PLATFORM STRENGTH CALCULATIONS *See sketch Fig D8*

At the centre of rotation (spigot helps to strengthen here)

$w_1 := 1.96$ Width of platform (m)

$d_1 := 30 \cdot 10^{-3}$ Thickness of platform (m)

$w_2 := 0.8$ Diameter of base rotation driveshaft spigot (m)

$d_2 := 50 \cdot 10^{-3}$ Thickness of base rotation driveshaft spigot (m)

$b_o := 100 \cdot 10^{-3}$ Strengthening beam outside short dimension (m)

$d_o := 150 \times 10^{-3}$ Strengthening beam outside long dimension (m)

$t := 10 \cdot 10^{-3}$ Wall thickness of strengthening beam (m)

$b_i := b_o - 2 \cdot t = 0.08$ Strengthening beam inside short dimension (m)

$d_i := d_o - 2 \cdot t = 0.13$ Strengthening beam inside long dimension (m)

Centroid calculation

$A_1 := w_1 \cdot d_1$ Area of platform cross section at rotational axis (m^2) $A_1 = 0.059$

$A_2 := w_2 \cdot d_2$ Area of spigot cross section at rotational axis (m^2) $A_2 = 0.04$

$A_3 := b_o \cdot d_o - b_i \cdot d_i$ Cross section of strengthening beam (m^2) $A_3 = 4.34 \times 10^{-3}$

$y_1 := d_o + 0.5 \cdot d_1$ Distance from x axis to centroid of A1 $y_1 = 0.165$

$y_2 := d_o - 0.5 \cdot d_2$ Distance from x axis to centroid of A2 $y_2 = 0.125$

$y_3 := \frac{d_o}{2}$ Distance from x axis to centroid of A3 $y_3 = 0.075$

$N := 4$ Number of strengthening beams

$$y := \frac{A_1 \cdot y_1 + A_2 \cdot y_2 + N \cdot A_3 \cdot y_3}{A_1 + A_2 + N \cdot A_3} \qquad y = 0.138$$

$I_1 := \frac{w_1 \cdot d_1^{\,3}}{12}$ Moment of inertia of A1 (m^4) $I_1 = 4.424 \times 10^{-6}$

$I_2 := \frac{w_2 \cdot d_2^{\,3}}{12}$ Moment of inertia of A2 (m^4) $I_2 = 8.333 \times 10^{-6}$

$I_3 := \left(\frac{b_o \cdot d_o^{\,3}}{12}\right) - \left(\frac{b_i \cdot d_i^{\,3}}{12}\right)$ Moment of inertia (A3) (m^4) $I_3 = 1.311 \times 10^{-5}$

$d_{y1} := y_1 - y$ Distance of A1 relative to neutral axis (m) $d_{y1} = 0.027$

$d_{y2} := y - y_2$ Distance of A2 relative to neutral axis (m) $d_{y2} = 0.013$

$d_{y3} := y - y_3$ Distance of A3 relative to neutral axis (m) $d_{y3} = 0.063$

$I_y := I_1 + I_2 + N\,I_3 + A_1 \cdot d_{y1}^{\,2} + A_2 \cdot d_{y2}^{\,2} + N \cdot A_3 \cdot d_{y3}^{\,2}$

Moment of inertia of combined sections (m^4) $I_y = 1.839 \times 10^{-4}$

Maximum deflection due to linear guide forces (Shigley page 1171 cantilever)

$F := RL = 7.868 \times 10^{4}$ Maximum end load on platform at the linear guides (N)

$E_{st} = 2.07 \times 10^{11}$ Modulus of steel (Pa)

$L := \frac{L_{car}}{2} = 0.8$ Distance to linear guides from rotational axis (m)

$y_{max} := \frac{F \cdot L}{3 \cdot E_{st} \cdot I_y} = 5.513 \times 10^{-4}$ Maximum deflection at the linear guides (m)

Maximum bending stress

$M := F \cdot L = 6.294 \times 10^{4}$ Bending moment in platform at rotational axis (Nm)

$c := d_1 + d_o - y = 0.042$ Distance from neutral axis to platform surface (m)

$\sigma_{bend} := \frac{M \cdot c}{I_y}$ Bending stress in the platform surface (Pa) $\sigma_{bend} = 14441174$

16.0 BASE ROTATION BEARING SELECTION *See sketch Fig D7*

$a := 112.75 \cdot 10^{-3}$

$b := 32.75 \cdot 10^{-3}$

$L_{sep} = 0.4$

$L_{sepbr} := 250 \cdot 10^{-3}$

$R_{sB1} = 103673$

$R_{sB2} = 39874$

Sum of moments about RbrB2

$$R_{brB1} := \frac{R_{sB1} \cdot (L_{sepbr} + a) + R_{sB2} \cdot (b)}{L_{sepbr}}$$

Reaction at top base rotation bearing (N)

$R_{brB1} = 155652$

$R_{brB2} := -R_{sB1} + R_{brB1} + R_{sB2}$

$R_{brB2} = 91854$

Bending moment at critical top bearing

$M_a := 1200$ Bending moment amplitude from spreadsheet [5] (Nm)

$M_m := 0$

$M_r := 2 \cdot M_a$

$T_m := 198$ Same torque required for resisting blade twist (Nm)

$T_r := 2 \cdot T_m$

$d_i := 195 \cdot 10^{-3}$ Inner diameter of shaft at critical bearing (m)

$D := 377 \cdot 10^{-3}$ SKF catalogue p841 [11]

$d := 360 \cdot 10^{-3}$ Outer diameter of shaft at critical bearings (m)

Distortion energy theory page 339 Deutschmann or use Gooch 440 notes on Shaft Design

Assume that the 800mm rounds are only available in mild steel - google search results in Chinese supplier

$S_y := \sigma_{yC350} = 3.5 \times 10^8$

$\sigma_{uts} := \sigma_{utsC350}$

$d_s := D_o$

$S_{ys} := 0.58 \cdot S_y = 2.03 \times 10^8$

$S'_e := 0.5 \sigma_{utsC350} = 2.15 \times 10^8$

$S'_{es} := 0.29 \sigma_{utsC350} = 1.247 \times 10^8$

Page 107 Deutschmann

Endurance limit in bending

$a := 4.45$

$b := -0.265$

$S'_e = 2.15 \times 10^8$

$$k_a := a \cdot \left(\frac{\sigma_{uts}}{1 \cdot 10^6} \right)^b$$

Surface factor Shigley page 375

$k_a = 0.892$

$k_b := 0.859 - 0.000827 d_s$ Size factor Shigley page 376

$k_b = 0.859$

$k_c := 1$ Marin loading factor Shigley page 378 (bending mainly)

$k_c = 1$

$k_d := 1$ Temperature factor Shigley page 380

$k_d = 1$

$k_e := 0.8$ Miscellaneous effects factor Shigley page 381
0.8 due to outdoor environment

$r_s := 2.5 \cdot 10^{-3}$ Minimum radius for shoulder in tapered roller bearings around 200-360mm page 839 SKF [11]

$a := \frac{139 \cdot 10^6}{\sigma_{uts}}$ Page 383 Shigley for a shoulder

$$K_t := 0.622 + 0.38\left(\frac{D}{d}\right)^{-4.3} + \left(\frac{r_s}{d}\right)^{-0.5} \cdot \left[\frac{-0.322 - 0.277\left(\frac{D}{d}\right)^2 + 0.599\left(\frac{D}{d}\right)^4}{1 - 2.55\left(\frac{D}{d}\right)^2 + 5.27\left(\frac{D}{d}\right)^4}\right]^{0.5}$$

$r_s := \frac{\left(2.5 \cdot 10^{-3}\right)}{25.4 \cdot 10^{-3}}$ converted to inches Shigley 384

$K_t = 2.666$

$$K_f := \frac{K_t}{1 + \left(\frac{2}{\sqrt{r_s}}\right) \cdot \left(\frac{K_t - 1}{K_t}\right)^a} = 1.165$$

$S_e := k_a \cdot k_b \cdot k_c \cdot k_d \cdot k_e \cdot S'_e \cdot \left(\frac{1}{K_f}\right)$ $S_e = 1.131 \times 10^8$

Endurance limit in torsion

$a := 4.45$
$b := -0.265$ $S'_e = 2.15 \times 10^8$

$k_a := a \cdot \left(\frac{\sigma_{uts}}{1 \cdot 10^6}\right)^b$ Surface factor Shigley page 375

$k_a = 0.892$

$k_b := 0.859 - 0.000827 d_s$ Size factor Shigley page 376

$k_b = 0.859$

$k_c := 0.5$ Marin loading factor Shigley page 378 (torsion)

$k_c = 0.5$

$k_d := 1$ Temperature factor Shigley page 380

$k_d = 1$

$k_e := 0.8$ Miscellaneous effects factor Shigley page 381
0.8 due to outdoor environment

$r_s := 4 \cdot 10^{-3}$ Minimum radius for shoulder in tapered roller bearings around 200-360mm page 839 SKF [11]

$a := \frac{139 \cdot 10^6}{\sigma_{uts}} = 0.323$ Page 383 Shigley for a shoulder

$$K_{ts} := 0.78 + 0.2\left(\frac{D}{d}\right)^{-10} + \left(\frac{r_s}{d}\right)^{-0.46} \cdot \left[\frac{-0.002 - 0.125\left(\frac{D}{d}\right)^2 + 0.123\left(\frac{D}{d}\right)^4}{1 - 2.75\left(\frac{D}{d}\right)^2 + 2.55\left(\frac{D}{d}\right)^4}\right]^{0.5}$$

$K_{ts} = 1.633$

$r_s := \frac{\left(4 \cdot 10^{-3}\right)}{25.4 \times 10^{-3}}$ converted to inches Shigley 384

$$K_{fs} := \frac{K_{ts}}{1 + \left(\frac{2}{\sqrt{r_s}}\right) \cdot \left(\frac{K_{ts} - 1}{K_{ts}}\right) \cdot a} = 1.001$$

$S_{es} := k_a \cdot k_b \cdot k_c \cdot k_d \cdot k_e \cdot S'_{es} \cdot \left(\frac{1}{K_{fs}}\right)$

$S_{es} = 3.819 \times 10^7$

Using the diameters entered above the safety factor for the hollow shaft is

$$\tau_{max} := \left[\frac{16}{\pi \cdot d^3 \cdot \left[1 - \left(\frac{d_i}{d}\right)^4\right]}\right] \cdot \sqrt{\left[M_m + \left(\frac{S_y}{S_e}\right) \cdot M_r\right]^2 + \left[T_m + \left(\frac{S_{ys}}{S_{es}}\right) \cdot T_r\right]^2}$$

Deutschmann page 339

$N := \frac{0.5 \cdot S_y}{\tau_{max}} = 18.837$

Select top bearing SKF 32972
Select bottom bearing SKF 32956/C02

16.1 Top bearing selection

Top bearing $p := \frac{10}{3}$ Life exponent p for roller bearings page 64 SKF [11]

Choose tapered roller bearing 32972

$P := R_{brB1} = 155652$ Radial load on bearing (N)

$C := 1120 \cdot 10^3$ Dynamic basic load rating (N)

$N_{osc} = 4.299 \times 10^5$

$L_{10} := \left(\frac{C}{P}\right)^p \cdot 1 \cdot 10^6$ Life of bearing (Revolutions)

$L_{10} = 7.192 \times 10^8$

$FOS_{life} := \frac{L_{10}}{N_{osc}} = 1.673 \times 10^3$

16.2 Bottom bearing selection

Select bearing SKF 32956/C02

$P := R_{brB2} = 9.185 \times 10^4$

$C := 765 \cdot 10^3$

$L_{10} := \left(\frac{C}{P}\right)^p \cdot 1 \cdot 10^6$ Life of bearing (Revolutions)

$L_{10} = 1.171 \times 10^9$

$FOS_{life} := \frac{L_{10}}{N_{osc}} = 2.724 \times 10^3$

17.0 WIND LOADING

$c_d := 2$ Drag coefficient of a flat plate perpendicular to the flow http://en.wikipedia.org/wiki/Drag_coefficient

$\rho_{air} := 1.2$ Density of air (kg/m^3)

$v_{light} := 10 \cdot \left(\frac{1000}{3600}\right) = 2.778$ Velocity of light winds (m/s)

$v_{mod} := 50 \cdot \left(\frac{1000}{3600}\right) = 13.889$ Velocity of moderate winds (m/s)

$v_{strong} := 100 \cdot \left(\frac{1000}{3600}\right) = 27.778$ Velocity of strong winds (m/s)

$A := b_g \cdot L_g$ Area of blade perpendicular to wind (m^2)

$A = 9.098$

$F_{dl} := 0.5 \cdot \rho_{air} \cdot (v_{light})^2 \cdot c_d \cdot A$ Drag force light winds (N)

$F_{dl} = 84.24$

$F_{dm} := 0.5 \cdot \rho_{air} \cdot (v_{mod})^2 \cdot c_d \cdot A$ Drag force moderate winds (N)

$F_{dm} = 2.106 \times 10^3$

$F_{ds} := 0.5 \cdot \rho_{air} \cdot (v_{strong})^2 \cdot c_d \cdot A$ Drag force strong winds (N)

$F_{ds} = 8.424 \times 10^3$

$M_l := \frac{F_{dl} \cdot \left(\frac{L_g}{2}\right) d_{sep}}{d_{sep}}$ Moment in blade at top clamp in light winds (Nm)

$M_l = 354.819$

$M_m := \frac{F_{dm} \cdot \left(\frac{L_g}{2}\right) d_{sep}}{d_{sep}}$ Moment in blade at top clamp in moderate winds (Nm)

$M_m = 8.87 \times 10^3$

$M_s := \frac{F_{ds} \cdot \left(\frac{L_g}{2}\right) d_{sep}}{d_{sep}}$ Moment in blade at top clamp in strong winds (Nm)

$M_s = 3.548 \times 10^4$

$\sigma_l := \frac{M_l \cdot Y_g}{I_g}$ Stress in the blade at top clamp under light wind loads

$\sigma_l = 4.073 \times 10^6$

$\sigma_m := \frac{M_m \cdot Y_g}{I_g}$ Stress in the blade at top clamp under moderate wind loads

$\sigma_m = 101.819 \times 10^6$

$\sigma_s := \frac{M_s \cdot Y_g}{I_g}$ Stress in the blade at top clamp under strong wind loads

$\sigma_s = 407.276 \times 10^6$

18.0 BLADE TWIST AND BRAKING FORCE CALCULATION

$\theta_{twist} := 20deg$ CHECK ON TEST RIG

http://en.wikipedia.org/wiki/Torsion_constant

$\beta := 0.3$ Equation for torsion of a flat plate

$a := b_g$ Beta comes from a/b ratio

$b := d_g$

$J_g := \beta \cdot a \cdot b^3 = 3.795 \times 10^{-6}$

$$J_g := a \cdot b^3 \left[\left(\frac{1}{3} \right) - 0.21 \cdot \left(\frac{b}{a} \right) \cdot \left[1 - \left(\frac{b^4}{12 \cdot a^4} \right) \right] \right] = 3.784 \times 10^{-6}$$

$$T_{twist} := \frac{\theta_{twist} \cdot G_g \cdot J_g}{L_g}$$ Required torque at free end of blade to produce assumed level of twist (Nm)

$T_{twist} = 6.899 \times 10^3$

$$F_{req} := \frac{T_{twist}}{b_g}$$ Force required to produce an equivalent force couple moment at free end of blade (N) THIS IS ALSO THE REACTION FORCES AT THE UPPER CLAMP DUE TO TWIST

$F_{req} = 6.388 \times 10^3$

18.1 Test Rig Blade Check

http://en.wikipedia.org/wiki/Torsion_constant

$\beta := 0.3$ Equation for torsion of a flat plate

$a := b_{tr}$ Beta comes from a/b ratio

$b := d_{tr}$

$J_{tr} := \beta \cdot a \cdot b^3 = 3.849 \times 10^{-10}$

$$J_{tr} := a \cdot b^3 \left[\left(\frac{1}{3} \right) - 0.21 \cdot \left(\frac{b}{a} \right) \cdot \left[1 - \left(\frac{b^4}{12 \cdot a^4} \right) \right] \right] = 3.866 \times 10^{-10}$$

$$T_{req} := \frac{\theta_{twist} \cdot G_{tr} \cdot J_{tr}}{L_{tr}}$$ Required torque at free end of blade to produce assumed level of twist (Nm)

$T_{req} = 6.752$

$$F_{req} := \frac{T_{req}}{b_{tr}}$$ Force required to produce an equivalent force couple moment at free end of blade (N) THIS IS ALSO THE REACTION FORCES AT THE UPPER CLAMP DUE TO TWIST

$F_{req} = 33.758$

FOS := 1

18.2 Braking force required to avoid unloading of belt/chain

$N_{rot} := 0.5$ Maximum rotational speed of table (RPM) (Evan Webb)

$\omega_{rot} := N_{rot} \cdot \frac{2\pi}{60}$ Rotational speed of mechanism (rad/s)

$t_{rot} := 5$ Time taken to reach required angular speed (s)

$\alpha_{rot} := \frac{\omega_{rot}}{t_{rot}}$ Angular acceleration required to reach speed in required time (rad/s^2)

$I_{rot} := 1423.2($ Mass moment of inertia of shuttle structure about rotational axis (kgm^2) from solidworks model - UPDATE AS NECESSARY

$T_{inert} := I_{rot} \cdot \alpha_{rot} = 14.904$

$T_{brake} := T_{twist} = 6.899 \times 10^3$ Brake needs to oppose the twisting torque but not the rotating inertia of the table

$I_{rot} \cdot \alpha_{rot} := T_{pulley} - T_{brake} - T_{twist}$ EOM of rotating system

$T_{pulley} := FOS \cdot \left(I_{rot} \cdot \alpha_{rot} + T_{brake} + T_{twist}\right)$ Torque required at pulley (Nm)

$T_{pulley} = 1.381 \times 10^4$

18.3 Motor Speed/Torque Requirement Calculation http://en.wikipedia.org/wiki/Gear_ratio

$r_{pulley} := 0.6$ Pitch circle radius for teeth on driven pulley (m)

$r_{out} := 0.1$ Pitch circle radius for teeth on driving pulley (m)

Speed Ratio

$\omega_{pulley} := \omega_{rot} = 0.052$ Angular speed of the driven pulley (rad/s)

$\frac{r_{pulley}}{r_{out}} = 6$

$\frac{T_{out}}{T_{pulley}} := \frac{r_{out}}{r_{pulley}} =$ $\frac{T_{out}}{T_{pulley}} := \frac{\omega_{pulley}}{\omega_{out}}$ Torque relationships

$T_{out} := T_{pulley} \cdot \frac{r_{out}}{r_{pulley}}$ Torque required at motor drive (Nm)

$T_{out} = 2.302 \times 10^3$

$\omega_{out} := \omega_{pulley} \cdot \frac{T_{pulley}}{T_{out}}$ Rotational speed required at motor drive (rad/s)

$\omega_{out} = 0.314$

$N_{out} := \omega_{out} \cdot \frac{60}{2\pi}$

$N_{out} = 3$ RPM

Gearbox will definitely be required on the output of the base rotation electric motor

18.4 Belt Power/Tension Calculation

$\eta_{belt} := 0.98$ Factor for losses through the belt (0.98 for Gates synchronous belt)

$P_{pulley} := \omega_{pulley} \cdot T_{pulley}$ Power required at the pulley(W)

These should be the same with no losses in belt $P_{pulley} = 723.27$

$P_{out} := \frac{(\omega_{out} \cdot T_{out})}{\eta_{belt}}$ Power required at the gearbox output shaft accounting for belt losses (W) $P_{out} = 738.03$

$P_{hp} := \frac{P_{out}}{746}$ Power at the output shaft of gearbox (and also at driven pulley assuming no belt losses) (hp) $P_{hp} = 0.989$

Worst case belt tension

$F_{Tpull} := \frac{T_{pulley}}{r_{pulley}}$ Tension force in belt at the pulley side of tight belt segment (N)

$F_{Tpull} = 2.302 \times 10^4$

$F_{Tout} := \frac{T_{out}}{r_{out}}$ Tension force in belt at driving pulley side of tight belt segment (N)

$F_{Tout} = 2.302 \times 10^4$

These will be identical if belt is ideal and has no losses, choose larger value for when the belt efficiency is included in calculation

REFERENCES (see storage media)

[1] Fletchers Special Steel Book

[2] Steel and Tube Catalogue

[3] Fatigue testing carried out August 2013

[4] Big Blade calculations

[5] Shaft deflection calculation spreadsheet

[6] DU Bush Catalogue

[7] Steel and Tube Dimensions and Properties (Design with Steel) Handbook

[8] FEA Results for Shuttle Frame

[9] Solidworks Model of Giant Blade

[10] SKF Spherical Roller Bearings Catalogue

[11] SKF Roller Bearings Catalogue

[12] Variable Stroke Mechanism Motion Study

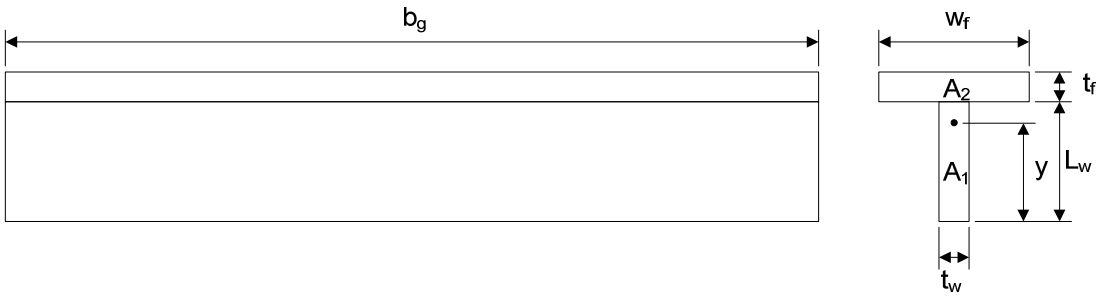

Figure D.1: Cross section of T section in upper pivot clamp showing dimensions used in calculations

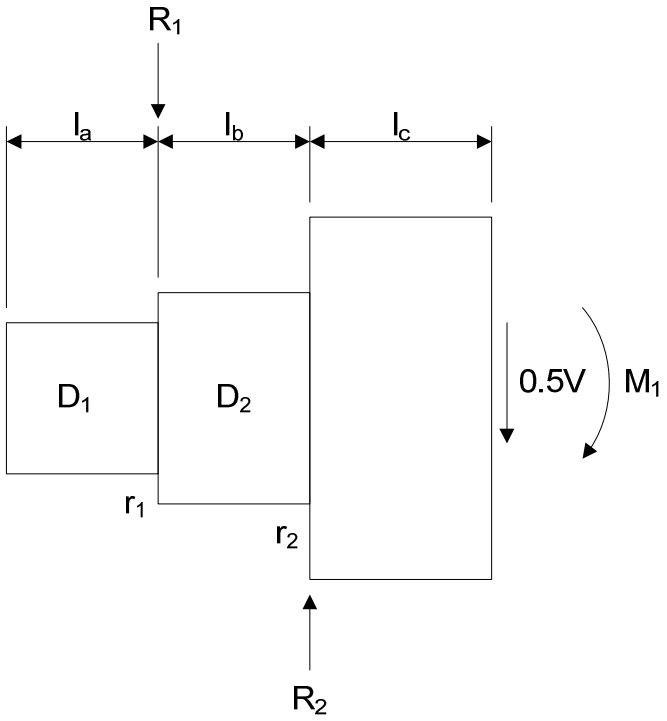

Figure D.2: Free body diagram of the ends of the upper pivot shaft showing dimensions used in calculations

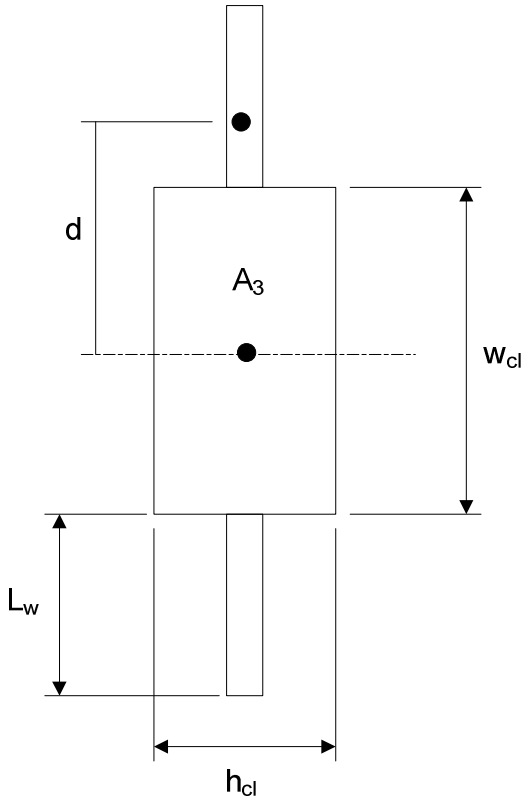

Figure D.3: Cross section of upper pivot clamp between cavity and stub shaft ends showing dimensions used in calculations

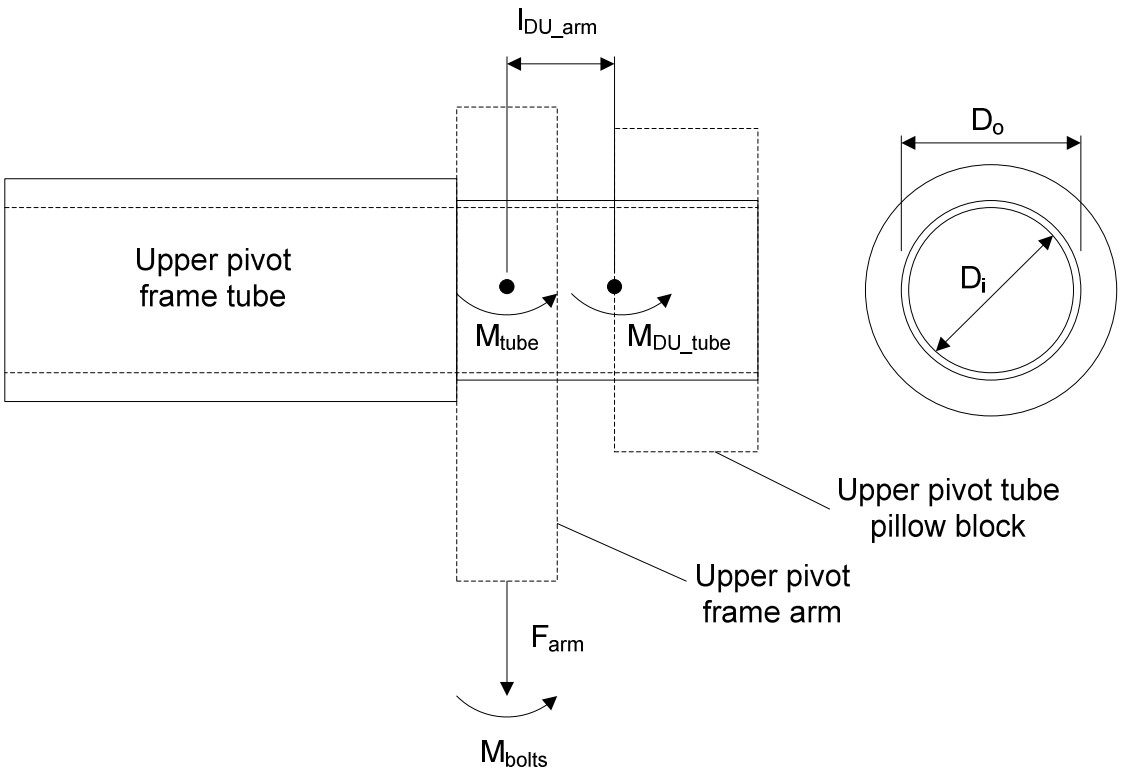

Figure D.4: Free body diagram showing forces and moments acting at upper pivot frame. Dimensions used in calculations also shown.

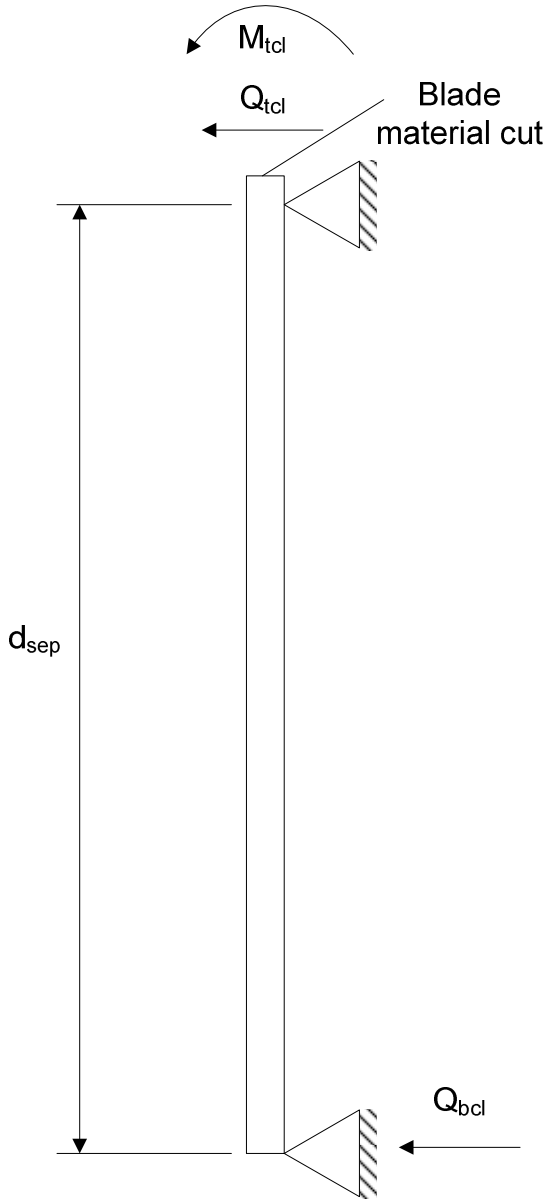

Figure D.5: Free body diagram of blade material in clamp showing cut at upper pivot.

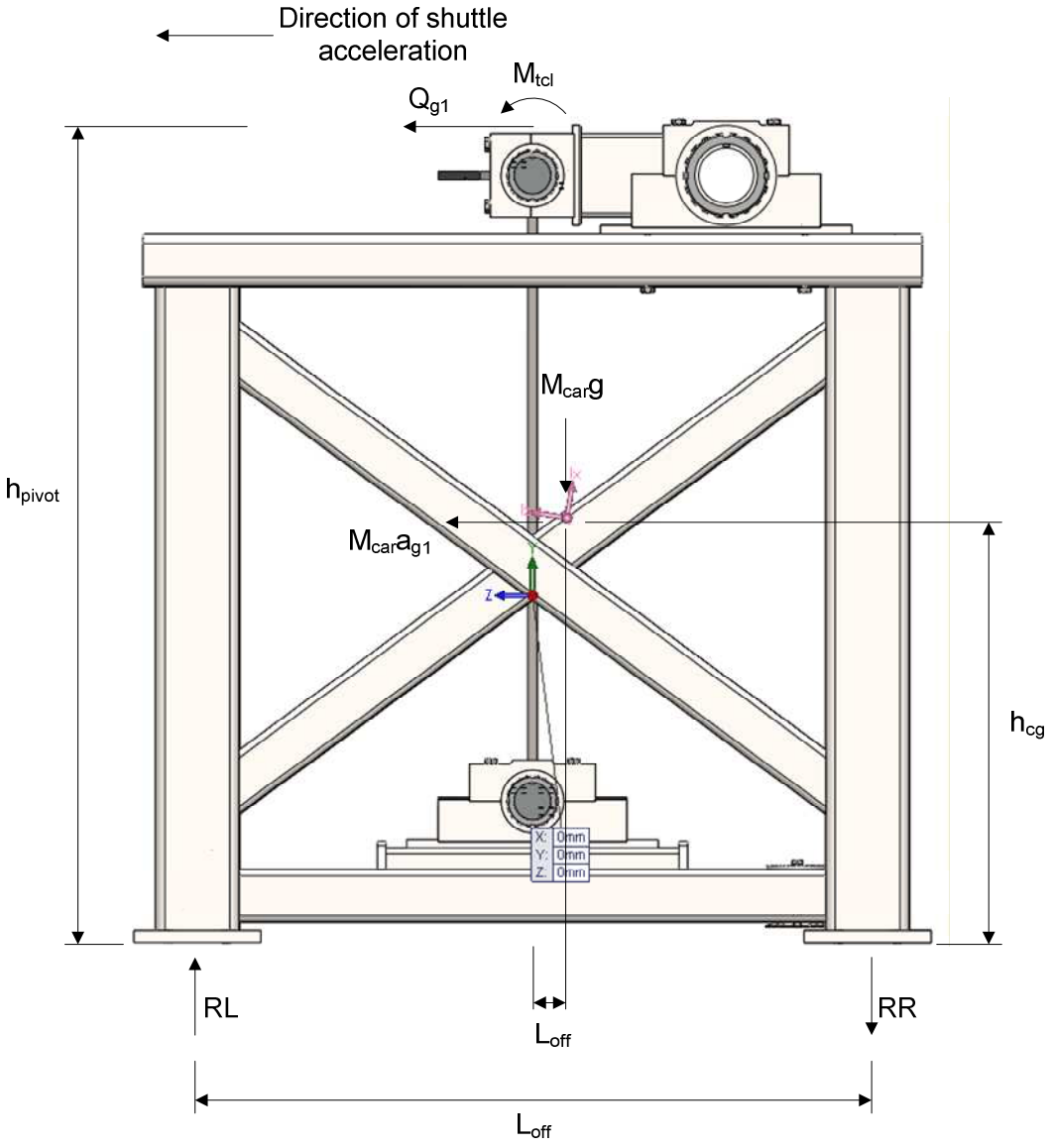

Figure D.6: Free body diagram of shuttle showing reaction forces at bearings as well as body forces due to oscillation accelerations. Centre of gravity is shown in pink.

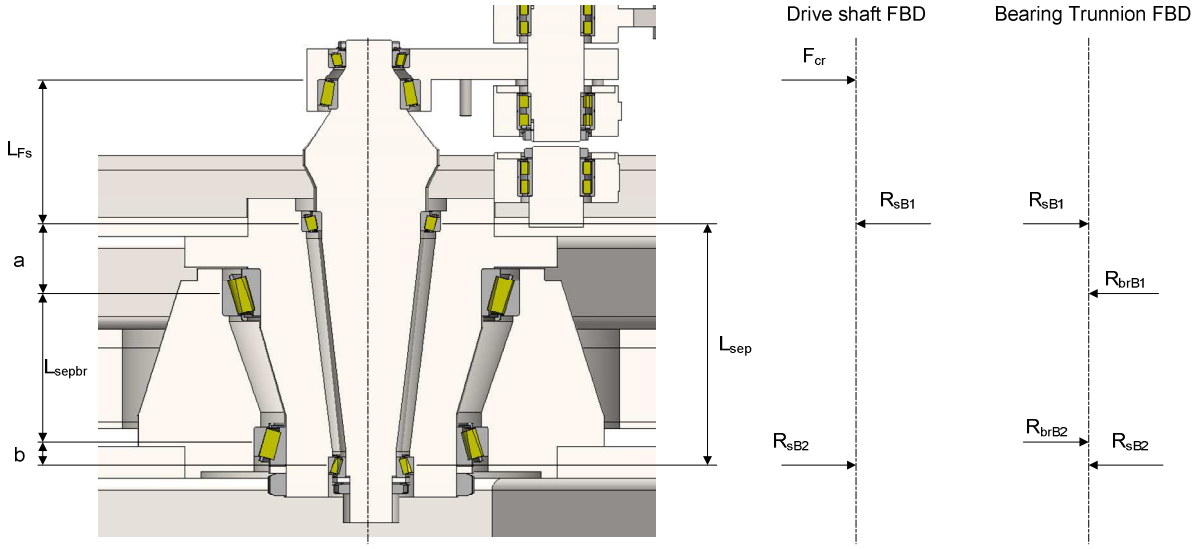

Figure D.7: 3D CAD cross section and corresponding free body diagrams of oscillation drive shaft and base rotation bearing trunnion

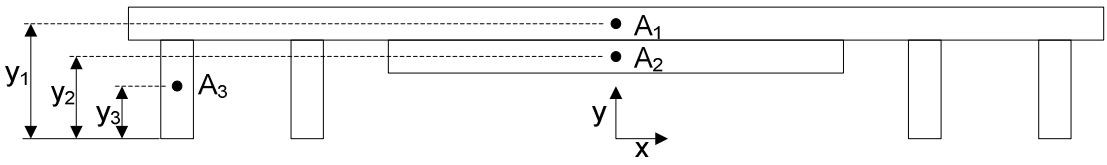

Figure D.8: Cross section of bearing platform indicating the dimensions used in calculations

E. Design Documents

Table E.1: Blade material design requirements specification from (S. D. Gooch, 2001)

Demand/ **W**ish	Blade material requirements (Big Blade)
D	Blade length at least double the prototype size *($l_s \geq 3.26m$)*
D	Minimum *Blade* life of one performance
D	Static similarity to be preserved in changing blade size
D	Double harmonic to feature in the *Blade* performance
D	Sound quality for the blade material of equal quality or better than would be expected from a carbon steel blade *($\eta < 2 \times 10^{-3}$ @ 30°C)*
D	Bright steel-like colour for the blade material
D	Running costs for a nominally *2-2.5* size of prototype to be less than 500NZD/performance.
D	Polished surface finish for blade (surface roughness $R_a < 0.8\ \mu m$)
W	Geometric similarity of the vibratory form to be preserved in changing blade size
W	Running costs of less than 50NZD
W	For the case where the blade material has a finite life then use a readily available blade material *(acquirable within 12 month lead time).*
W	Preserve the sound qualities of the *Original Blade* (η *for the Blade material* $< 10^{-4}$ *@ 30°C)*
W	*Blade* to be resistant to attack by salt water and U-V radiation
W	Bright highly reflective steel-like surface finish for the blade
W	Infinite design life for blade material

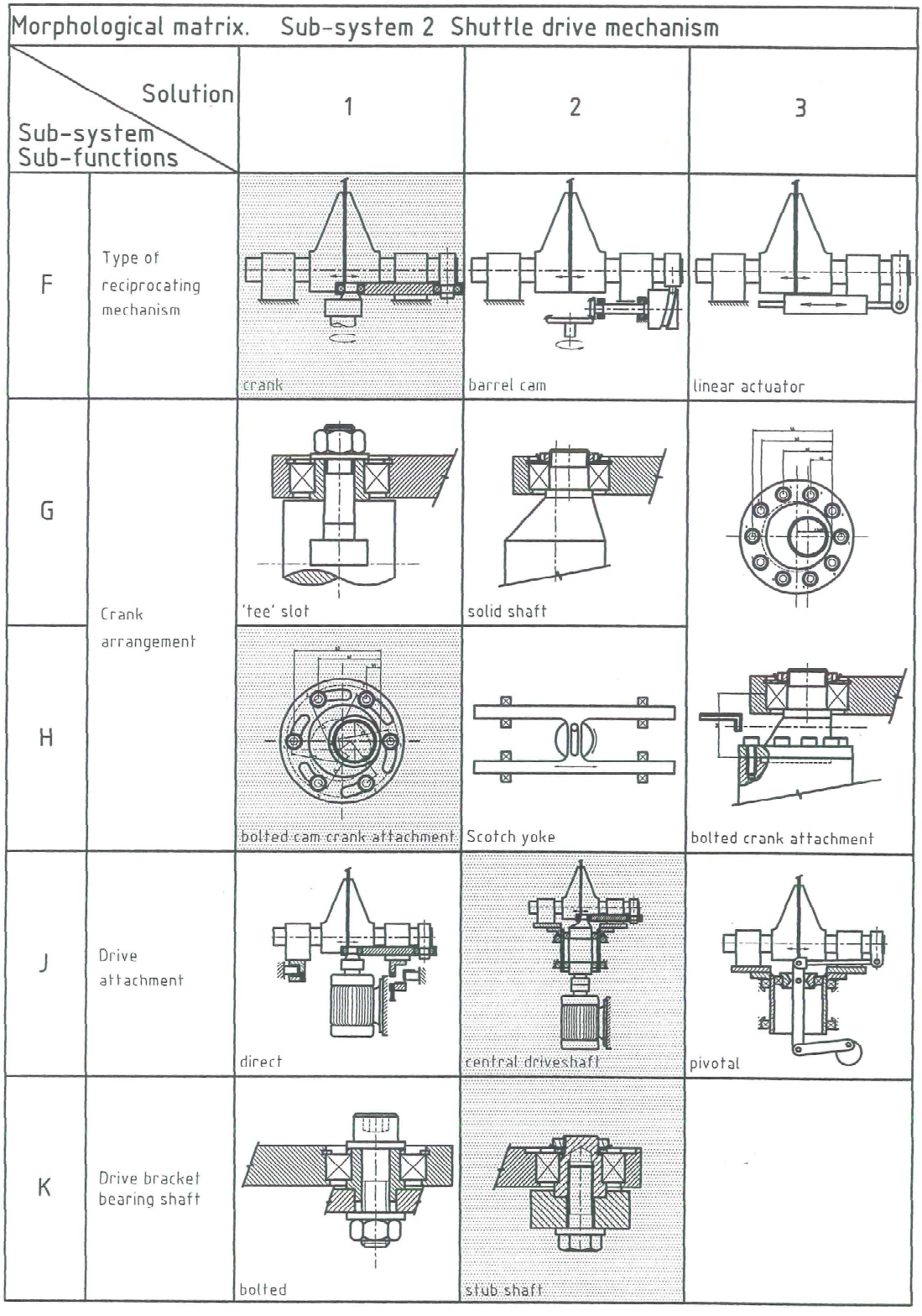

Figure E.1: Working principles considered in the development of a concept for the shuttle drive mechanism in the Giant Blade design [Adapted from Gooch (2001)]

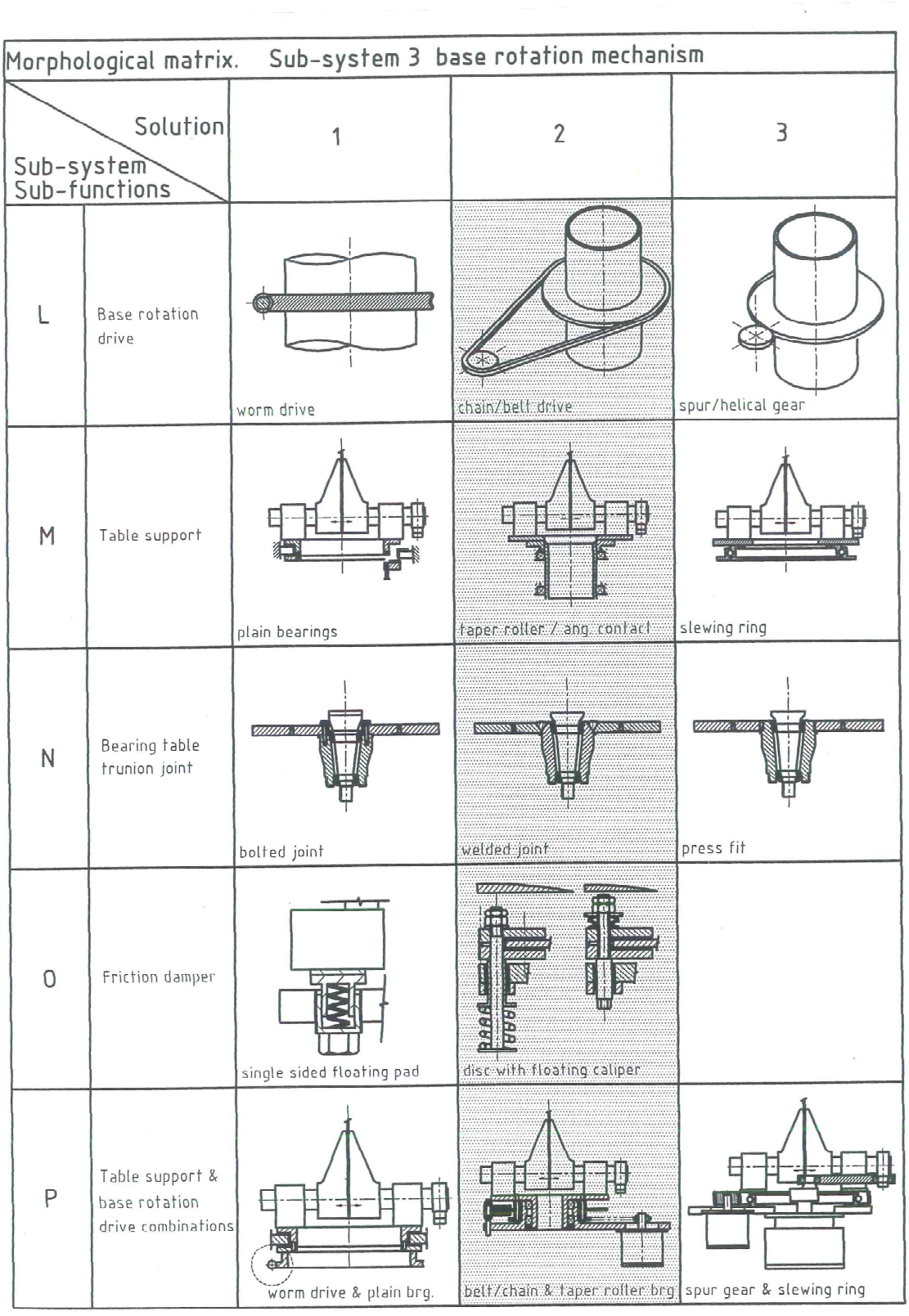

Figure E.2: Working principles considered in the development of a concept for the base rotation mechanism in the Giant Blade design [Adapted from Gooch (2001)]

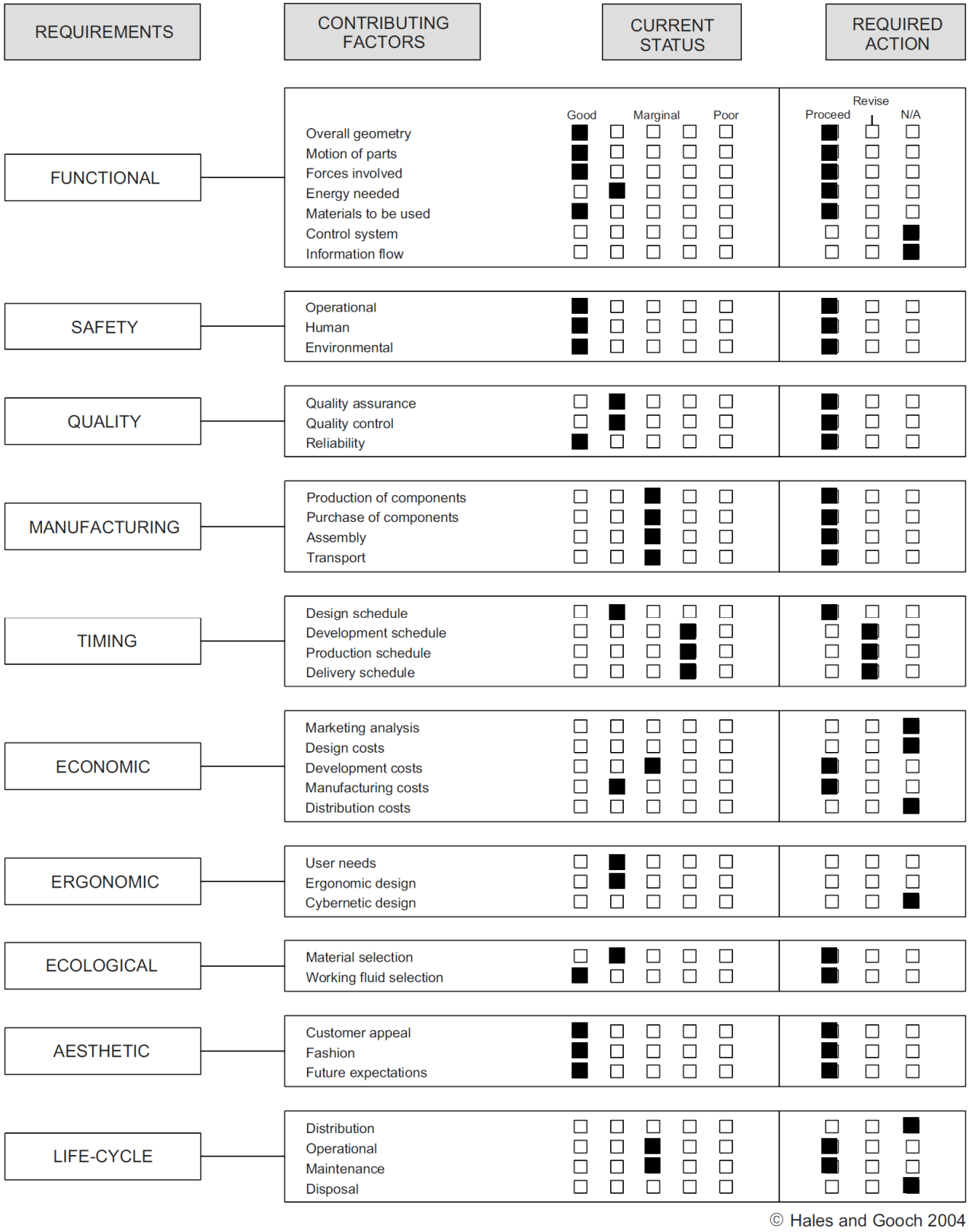

Figure E.3: Conceptual design worksheet for the Giant Blade drive mechanism after (Hales & Gooch, 2004))

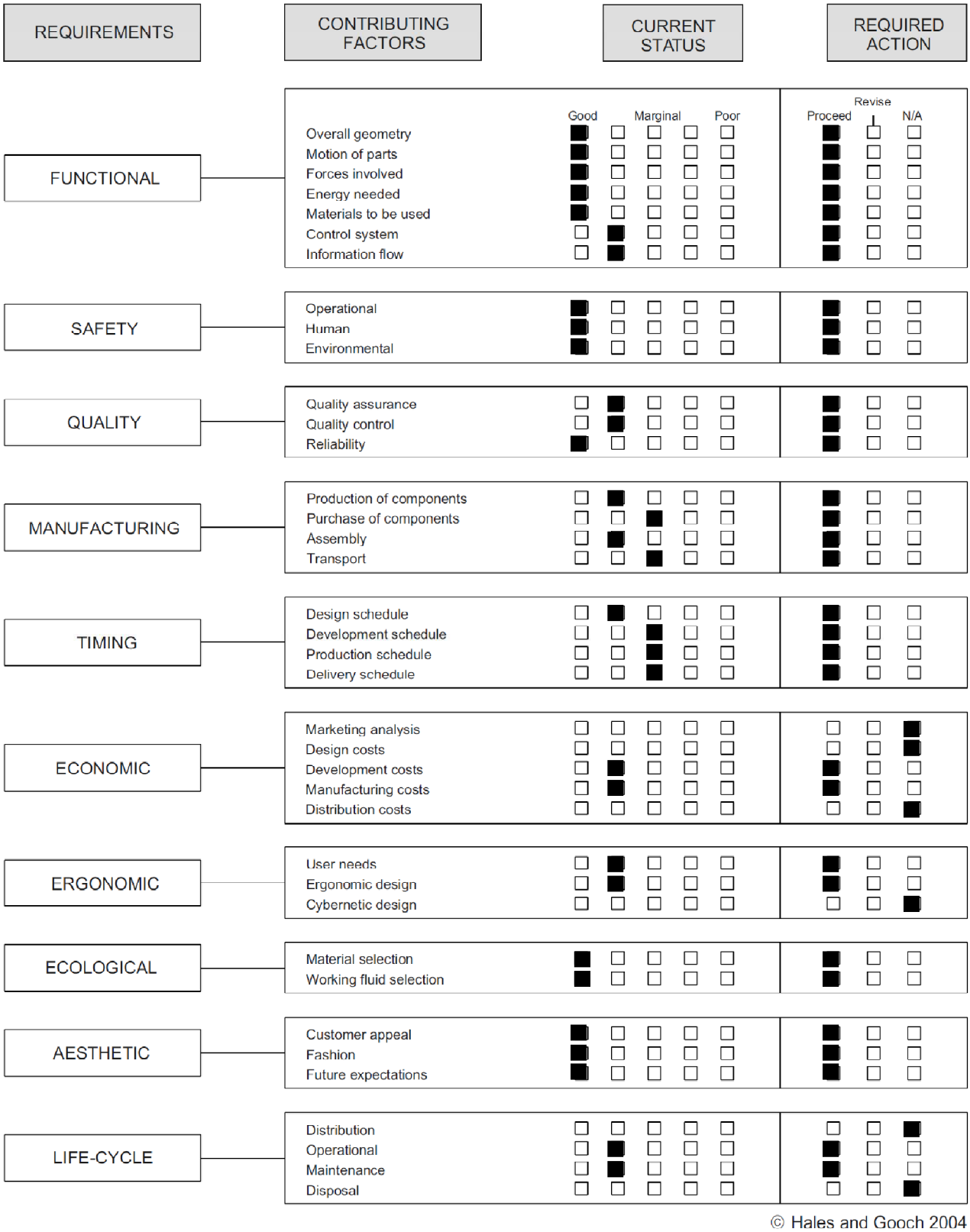

Figure E.4: Embodiment design worksheet for the Giant Blade drive mechanism after (Hales & Gooch, 2004)